

# Nanoparticle assemblies: Order by self-organization and collective magnetism

Von der Fakultät für Mathematik, Informatik und Naturwissenschaften der RWTH Aachen University zur Erlangung des akademischen Grades einer Doktorin der Naturwissenschaften genehmigte Dissertation

vorgelegt von

Master of Science

*Asma Qdemat*

aus

*Jerusalem, Palästina*

Berichter: *Univ. -Prof. Dr. rer. nat. Thomas Brückel*

*Univ. -Prof. Dr. rer. nat. Joachim Mayer*

Tag der mündlichen Prüfung: 17. Dezember 2020

Diese Dissertation ist auf den Internetseiten der Universitätsbibliothek verfügbar.



# Abstract

Assembly of nanoparticles into highly ordered two- or three-dimensional arrays is a prerequisite to achieve their application in novel functional devices. The unique properties of such ensembles differ significantly from those of individual nanoparticles. The assembly techniques have to be able to control the arrangement of nanoparticles over large areas and should be suitable for industrial applications. In the present work, novel, simple and inexpensive assembly approaches used to achieve highly ordered two- and three-dimensional arrangements of nanoparticles, are presented. Also, an extensive determination of the structural and the magnetic correlations of the obtained systems has been performed using advanced scattering methods.

Among a variety of common assembly techniques, drop-casting is one of the prospective approaches because of its simplicity. Although drop casting has shown its potential to form ordered nanoparticle arrangements, the formation of uniform nanoparticle arrays over large areas remains a challenging subject. Here, we introduce an improved variant of the drop-casting method and demonstrate the formation of large-area highly ordered monolayers of silica nanospheres on a silicon substrate. In our method, the addition of stearyl alcohol to the colloidal nanoparticle dispersion assists the assembly of  $\text{SiO}_2$  nanospheres with a size of 50 nm into a highly ordered arrangement. We reveal that the NPs concentration, the stearyl alcohol concentration, the volume of the droplet, and the annealing time are key factors in the self-assembly in our method. The  $\text{SiO}_2$  nanosphere-monolayers contain almost no cracks and voids. Structural characterization of the obtained silica NP monolayer was done locally by Scanning Electron Microscopy (SEM), and globally by X-Ray Reflectivity (XRR) and Grazing Incidence Small-Angle X-ray Scattering (GISAXS), where the data is reproduced by simulation within the Distorted Wave Born Approximation (DWBA). This allows one to make unbiased conclusions that the heat treatment in combination with a compatible additive with a melting point significantly below that of the particles, can be a general method to improve the ordering between particles in monolayers as well as in multilayers.

Also, in this thesis, 2D arrays of cobalt ferrite (COF) nanodots on silicon substrates were used to determine the effects of dipolar interparticle interactions on the magnetic properties of self-assembled structures of magnetic nanoparticles. GISAXS and SEM confirm a close-packed hexagonal order of the NP monolayer. Atomic force microscopy (AFM) provides information about the interparticle distance and XRR provides the depth profile of the 2D nanodots monolayer. Simulation of the GISAXS pattern reveals that the particles have a hemispherical shape with a height of 10 nm, a radius of 8.5 nm and a hexagonal

structure with a lattice constant of 34 nm. Temperature and field dependent magnetization measurements were performed using a superconducting quantum interference device (SQUID). The hysteresis loops in plane and out-of-plane directions reveal an in-plane easy direction. Also, a superparamagnetic behavior is obtained in-plane at room temperature and below while, out-of-plane superparamagnetism with an additional opening at low and large fields is observed at room temperature and below. The blocking temperature has been determined from magnetization measurements after zero- and field-cooled protocols. It was found to be higher than 300 K in both direction. Moreover, a decrease of the in-plane FC magnetization is detected due to the interparticle interaction. The magnetic depth profile of the 2D COF nanodots could be deduced from polarized neutron reflectometry (PNR). Half polarized neutron reflectometry at saturation field shows a small splitting between up and down channels is visible. This is an indication to a small in-plane magnetization component parallel to the applied magnetic field. While the sample magnetization approach a demagnetized state with zero net magnetization at remanence filed.

In addition, trench patterned silicon substrates of 50-100 nm width were fabricated using electron beam lithography and used as a template for assisted self-assembly of nanoparticles in order to reach 3D single crystalline arrangements of nanoparticles and to investigate the magnetostatic interaction between nanoparticles. The trench patterned substrates were characterized locally by SEM and globally by GISAXS and XRR. Three dimensional arrangements of iron oxide nanocubes with an edge length of 14(1) nm were obtained using dip coating method. GISAXS shows a large coherence length in both, in-plane and out of plane arrangement of the nanoparticles. Additionally, no correlation between the structural arrangement of nanoparticles and the geometry of trench-patterned substrates is concluded. The nanoparticles arranged in-plane into 2D hexagonal lattice and into FCC structure oriented in its (111) out-of-plane direction. From the hysteresis loops, an anisotropy in the magnetic properties is observed and an exchange Bias (EB) is visible at low temperature. Moreover, a decrease in the FC magnetization is observed which is an indication of dipolar interaction between nanoparticles. This leads to demonstrate that spatial confinement can be employed to induce nanoparticle assembly in trenches and might provide a promising route toward nanoscale devices with tunable anisotropic properties.

# Zusammenfassung

Die Anordnung von Nanopartikeln zu hochgeordneten zwei- oder dreidimensionalen Strukturen ist für deren Anwendung in neuartigen funktionalen Bauteilen von wesentlicher Bedeutung. Die physikalischen Eigenschaften solcher wechselwirkender Ensembles unterscheiden sich stark von denen einzelner Nanopartikeln. Darüber hinaus sollten die Herstellungsverfahren in der Lage sein, die Anordnung von Nanopartikeln über große Flächen zu ermöglichen und sie sollten möglichst für industrielle Anwendungen geeignet sein. In der vorliegenden Arbeit werden neuartige, einfache und kostengünstige Assemblierungsansätze vorgestellt, die das Erzielen von hochgeordneten zwei- und dreidimensionalen Anordnungen von Nanopartikeln ermöglichen. Außerdem wurde eine Bestimmung der strukturellen und magnetischen Korrelationen der erhaltenen Systeme unter Verwendung unterschiedlicher Streumethoden durchgeführt.

Unter einer Vielzahl gängiger Herstellungsmethoden ist das „drop-casting“ aufgrund seiner Einfachheit einer der vielversprechendsten Ansätze. Obwohl dieses Verfahren gezeigt hat, dass es geordnete Nanopartikel-Arrays bilden kann, bleibt die Herstellung einheitlicher Nanopartikel-Anordnungen über große Flächen ein herausforderndes Thema. Hier stellen wir eine verbesserte Variante des Drop-Casting-Verfahrens vor und demonstrieren die Bildung großflächiger hochgeordneter Monoschichten von Silica-Nanokugeln auf einem Siliziumsubstrat. Bei unserer Methode unterstützt das Hinzufügen von Stearylalkohol zu der kolloidalen Nanopartikeldispersion die Anordnung von SiO<sub>2</sub>-Nanokugeln mit einer Größe von 50 nm zu einer hochgeordneten Struktur. Wir zeigen, dass die NP-Konzentration, die Stearylalkoholkonzentration, das Tröpfchenvolumen und die Temperzeit Schlüsselfaktoren für die Selbstorganisation in unserer Methode sind. Die Silika-Nanokugeln-Monoschichten weisen fast keine Risse und Leerstellen mehr auf. Die strukturelle Charakterisierung der erhaltenen SiO<sub>2</sub>-NP-Monoschicht erfolgte lokal durch Rasterelektronenmikroskopie (SEM) und global durch Röntgenreflexion (XRR) und Kleinwinkel-Röntgenstreuung unter streifendem Einfall (GISAXS). Dabei gelingt es, die Daten durch Simulation innerhalb der Distorted Wave Born Approximation (DWBA) zu reproduzieren. Dies ermöglicht die unvoreingenommene Schlussfolgerung, dass die Wärmebehandlung in Kombination mit einem kompatiblen Additiv mit einem Schmelzpunkt, der deutlich unter dem der Partikel liegt, eine allgemeine Methode zur Verbesserung der Ordnung zwischen Partikeln in Monoschichten und Mehrfachschichten sein kann.

In dieser Arbeit wurden auch 2D-Arrays von Kobaltferrit (COF) -Nanopunkten auf Siliziumsubstraten verwendet, um die Auswirkungen der dipolaren Interpartikelwechselwirkung auf die magnetischen Eigenschaften selbstorganisierter

Strukturen magnetischer Nanopartikel zu bestimmen. GISAXS und SEM belegen eine dicht gepackte hexagonale Ordnung der NP-Monoschicht. Die Rasterkraftmikroskopie (AFM) liefert Informationen über den Abstand zwischen den Partikeln und XRR liefert das Tiefenprofil der 2D-Nanopunkt-Monoschicht. Die Simulation der GISAXS Daten zeigt, dass die Partikel eine halbkugelförmige Gestalt mit einer Höhe von 10 nm, einem Radius von 8.5 nm und einer hexagonalen Struktur mit einer Gitterkonstante von 34 nm aufweisen. Temperatur- und feldabhängige Magnetisierungsmessungen wurden unter Verwendung einer supraleitenden Quanteninterferenzvorrichtung (SQUID) durchgeführt. Die Hystereseschleifen in der Ebene und senkrecht dazu zeigen, dass die leichte magnetische Richtung in der Ebene liegt. In der Substratebene wurde sowohl bei Raumtemperatur als auch darunter ein superparamagnetisches Verhalten gefunden, während senkrecht dazu Superparamagnetisches mit einer zusätzlichen Öffnung bei niedrigen und hohen Feldern auftritt. Die Blockiertemperatur wurde aus Magnetisierungsmessungen nach null- und feldgekühlten Protokollen bestimmt. Es wurde festgestellt, dass es in beiden Richtungen höher als 300 K ist. Darüber hinaus wird aufgrund der Wechselwirkung zwischen den Partikeln eine Abnahme der FC-Magnetisierung in der Ebene festgestellt. Das magnetische Tiefenprofil der 2D-COF-Nanopunkte konnte aus der polarisierten Neutronenreflektometrie (PNR) abgeleitet werden. Die halbpolarisierte Neutronenreflektometrie im Sättigungsfeld zeigt, dass eine kleine Aufteilung zwischen Aufwärts- und Abwärtskanälen sichtbar ist. Dies ist ein Hinweis auf eine kleine Magnetisierungskomponente in der Ebene parallel zum angelegten Magnetfeld. Während sich die Probenmagnetisierung einem entmagnetisierten Zustand mit einer Nettomagnetisierung von Null bei Remanenz nähert.

Zusätzlich wurden grabenstrukturierte Siliziumsubstrate mit einer Grabenbreite von 50 bis 100 nm unter Verwendung von Elektronenstrahlolithographie hergestellt und als Vorlage für die unterstützte Selbstorganisation von Nanopartikeln verwendet. Ziel war die Herstellung einkristalliner 3D-Anordnungen von Nanopartikeln um die magnetostatische Wechselwirkung zwischen diesen Teilchen zu bestimmen. Die mit Gräben strukturierten Substrate wurden lokal durch SEM und global durch GISAXS und XRR charakterisiert. Dreidimensionale Anordnungen von Eisenoxid-Nanowürfeln mit einer Kantenlänge von 14 (1) nm wurden unter Verwendung eines Tauchbeschichtungsverfahrens erhalten. GISAXS zeigt eine große Kohärenzlänge sowohl in der Ebene als auch außerhalb der Ebene der Nanopartikel. Darüber hinaus wird auf keine Korrelation zwischen der strukturellen Anordnung von Nanopartikeln und der Geometrie von Substraten mit Grabenmuster geschlossen. Die Nanopartikel sind in einem hexagonalen 2D-Gitter in der Ebene und in einer FCC-Struktur angeordnet, die in ihrer (111-Richtung) senkrecht zur Ebene ausgerichtet ist. Aus den Hystereseschleifen wird eine Anisotropie der magnetischen Eigenschaften geschlossen

und bei niedriger Temperatur ist ein „Exchange Bias“ (EB) sichtbar. Darüber hinaus wird eine Abnahme der Magnetisierung nach Feldkühlung beobachtet, was ein Hinweis auf eine dipolare Wechselwirkung zwischen den Nanopartikeln ist. Dies führt zu dem Nachweis, dass räumliche Begrenzung verwendet werden kann, um die Anordnung von Nanopartikeln in Gräben zu induzieren, und einen vielversprechenden Weg zu nanoskaligen Bauelementen mit einstellbaren anisotropen Eigenschaften beschreiten zu könnte.



# Contents

<b>1. Introduction</b>	<b>1</b>
<b>2. Theoretical Background</b>	<b>5</b>
2.1. Magnetism	5
2.1.1. Magnetization	7
2.1.1.1. Diamagnetism	8
2.1.1.2. Paramagnetism	8
2.1.2. Magnetic interactions	9
2.1.2.1. Magnetic dipolar interaction	9
2.1.2.2. Exchange interaction	9
2.1.3. Magnetic order	15
2.1.3.1. Ferromagnetism (FM)	16
2.1.3.2. Antiferromagnetism (AF)	17
2.1.3.3. Ferrimagnetism (FiM)	19
2.1.4. Magnetic anisotropy	19
2.1.5. Exchange Bias (EB)	22
2.1.6. Superparamagnetism	24
2.2. Self-assembly	28
2.2.1. Van der Waals force	28
2.2.2. Magnetic interactions	29
2.2.3. Other forces	32
2.2.3.1. Steric repulsion	32
2.2.3.2. Electrostatic force	32
2.2.3.3. Capillary force	32
2.2.3.4. Convective force	33
2.3. Scattering	33
2.3.1. Scattering theory	34
2.3.2. X-ray and neutron matter interaction	37
2.3.3. Bragg diffraction	42
2.3.4. Ewald sphere construction	45
2.4. Small Angle X-ray Scattering (SAXS)	47
2.5. X-ray Reflectometry (XRR)	51
2.6. Polarized neutron reflectometry (PNR)	56
2.7. GISAXS	58

<b>3. Instruments and experimental techniques</b>	<b>64</b>
3.1. Sample preparation	64
3.1.1. Top-down methods	65
3.1.1.1. Electron beam lithography (EBL)	65
3.1.2. Bottom-up methods	66
3.1.2.1. Drop-casting	66
3.1.2.2. Spin-coating	67
3.1.2.3. Dip-coating	67
3.2. Electron microscope	68
3.2.1. Scanning Electron Microscopy (SEM)	69
3.2.1.1. Imaging	71
3.3. Magnetometry	72
3.3.1. Superconducting Quantum Interference Device (SQUID)	72
3.3.1.1. Josephson junction	73
3.3.1.2. Modes of measurements	75
3.3.1.3. Theory of operation	78
3.3.1.4. Measurement Procedures	79
3.4. X-ray instruments	80
3.4.1. Gallium Anode Low-Angle X-ray Instrument (GALAXI)	81
3.4.1.1. Small Angle X-ray Scattering (SAXS)	82
3.4.1.2. Grazing Incidence Small Angle X-ray Scattering (GISAXS)	85
3.4.1.3. X-ray Reflectometry (XRR)	88
3.5. Neutron techniques	90
3.5.1. Magnetic reflectometer MARIA	90
3.5.1.1. Polarized Neutron Reflectometry (PNR)	92
<b>4. Structural characterization of line gratings by grazing incidence small angle x-ray scattering (GISAXS)</b>	<b>94</b>
4.1. GISAXS on grating structures	94
4.2. Direct data analysis and numerical simulation	97
4.3. Dimensional nanometrology of surface gratings	99
4.4. Large pitches close to 300 nm	100
4.4.1. Materials and methods	101
4.4.2. Scanning Electron Microscopy (SEM)	102
4.4.3. Determination the capping layer thickness and the line height by XRR	104
4.4.4. GISAXS	104
4.4.4.1. Perpendicular orientation	106
4.4.4.2. Parallel orientation, Fourier Transform analysis	107
4.4.4.3. Rotation around the surface normal vector	110
4.4.5. Validation by simulation using BornAgain	112

4.5.	Small pitches below 300 nm . . . . .	115
4.5.1.	Sample preparation . . . . .	115
4.5.2.	Scanning Electron Microscopy (SEM) . . . . .	117
4.5.3.	GISAXS . . . . .	122
4.5.3.1.	Parallel orientation, grating parameters determination . . . . .	122
4.5.3.2.	Fourier Transform analysis of GISAXS in parallel orientation . . . . .	129
4.5.4.	XRR results of line height and capping layer thickness . . .	130
4.6.	Summary and Outlook . . . . .	135
<b>5.</b>	<b>Self assembly of silica nanoparticles on flat and patterned silicon substrates</b>	<b>137</b>
5.1.	Current state of research on nanoparticles monolayer self-assembly	137
5.2.	Introduction to silica nanoparticles . . . . .	141
5.3.	Experimental methods . . . . .	141
5.3.1.	Synthesis of stearyl silica nanoparticles . . . . .	141
5.3.2.	Nanoparticles characterization . . . . .	142
5.3.3.	Deposition process of nanoparticles on wafer surface . . . .	145
5.4.	Formation of nanoparticle monolayers and local characterization by SEM . . . . .	155
5.4.1.	Global and depth-resolved characterization by XRR and GISAXS . . . . .	161
5.5.	Self-assembly of nanoparticles on two-dimensional nanometer-scale patterned surfaces . . . . .	174
5.6.	Summary . . . . .	182
<b>6.</b>	<b>Investigation of spin structure of Cobalt ferrite nanodots on Silicon substrate</b>	<b>184</b>
6.1.	Introduction to Cobalt Ferrite . . . . .	185
6.2.	Cobalt Iron Oxide nanopowder . . . . .	187
6.3.	Experimental methods . . . . .	189
6.3.1.	Sample preparation . . . . .	189
6.3.2.	Monolayer structural characterization . . . . .	190
6.3.3.	Monolayer magnetism . . . . .	192
6.4.	Results and discussion . . . . .	193
6.4.1.	Structural characterization . . . . .	193
6.4.1.1.	Morphological characterization . . . . .	193
6.4.1.2.	Vertical structure . . . . .	195
6.4.1.3.	Lateral structure . . . . .	196
6.4.2.	Magnetism . . . . .	201
6.4.2.1.	Macroscopic magnetization . . . . .	201
6.4.2.2.	Depth-resolved magnetization . . . . .	203

6.5. Summary . . . . .	206
<b>7. Directed self-assembly of iron oxides nanoparticles on patterned substrates</b>	<b>207</b>
7.1. Introduction to Iron Oxides . . . . .	207
7.2. Nanoparticles characterization . . . . .	211
7.3. Nanoparticles / pre-structured Silicon substrate . . . . .	216
7.3.1. Sample preparation . . . . .	217
7.3.2. Structural characterization . . . . .	218
7.3.2.1. Vertical Structure from X-Ray Reflectometry . . . . .	218
7.3.2.2. GISAXS . . . . .	219
7.3.3. Magnetic characterization . . . . .	223
7.3.3.1. Macroscopic magnetization . . . . .	223
7.4. Summary and outlook . . . . .	228
<b>8. Conclusion and Outlook</b>	<b>230</b>
8.1. Summary . . . . .	230
8.2. Conclusion . . . . .	232
8.3. Future prospects . . . . .	234
<b>Appendices</b>	<b>236</b>
<b>A. Derivations</b>	<b>237</b>
A.1. Green's function of free Schrödinger equation . . . . .	237
A.2. Scattering theory for electromagnetic waves . . . . .	239
<b>B. Preparation parameters of grating lines by Eulitha company</b>	<b>245</b>
<b>C. The EBL protocol and the preparation parameters of grating lines by HNF</b>	<b>246</b>
<b>D. Absolute calibration of SAXS measurements at GALAXI</b>	<b>247</b>
<b>E. Form Factors</b>	<b>249</b>
E.1. Spherical form factor . . . . .	249
E.2. Spherical Core-Shell form factor . . . . .	249
E.3. Cubic form factor . . . . .	250
<b>F. 2D Ordered Arrays of Ferrimagnetic Cobalt Ferrite Nanodots</b>	<b>252</b>
F.1. Magnetic moment per nanoparticle in Bohr magneton ( $\mu_B$ / NP) . . . . .	252
F.2. Magnetization curves . . . . .	253
F.3. Neutron reflectometry . . . . .	256
<b>Glossary</b>	<b>258</b>

<b>Bibliography</b>	<b>261</b>
<b>Acknowledgements</b>	<b>277</b>
<b>Statutory declaration</b>	<b>280</b>
<b>Personal Bibliography</b>	<b>281</b>
<b>Curriculum Vitae</b>	<b>282</b>



# List of Figures

2.1. Superexchange interaction between two magnetic ions ( $\text{Co}^{+2}$ ) mediated by a non-magnetic ion ( $\text{O}^{-2}$ ). (a) and (b) show the first GKA rule: antiferromagnetic order is favored between two half-filled or two empty orbitals of magnetic ions with $180^\circ$ arrangement. (c) show the second GKA: ferromagnetic order is favored between one half-filled orbital and one empty orbital of magnetic ions with $180^\circ$ arrangement. (d) show the third GKA rule: ferromagnetic order is favored between two half-filled orbitals of magnetic ions with $90^\circ$ arrangement. Inspired from [29] . . . . .	13
2.2. Double exchange interaction between $\text{Mn}^{+3}$ and $\text{Mn}^{+4}$ mediated by an $\text{O}^{-2}$ ion. Inspired from [29]. . . . .	15
2.3. Magnetic spin arrangements of (a) a ferromagnetism, (b) an antiferromagnetism and (c) a ferrimagnet. . . . .	16
2.4. Magnetic susceptibility vs. temperature for ferromagnetic system.	17
2.5. Antiferromagnetic moments configurations can be decomposed into two interpenetrating sublattices. . . . .	18
2.6. Magnetic susceptibility vs. temperature for antiferromagnetic material. . . . .	19
2.7. Phenomenological picture of exchange bias for an AF-FM bilayer and illustration of the spin order during the hysteresis measurement. Inspired from [34] . . . . .	23
2.8. Effect of the external magnetic field on the arrangements of the dipoles. . . . .	31
2.9. Schematic of the general scattering process. An incoming wave with a wave vector $k_i$ (red) interacts with the target (yellow) and produces an outgoing wave with wave vector $k_f$ (green) then it is detected by a detector. . . . .	34
2.10. Geometry of the scattering cross section: number of particle $N$ per unit time $dt$ measured by a detector at a distance $r$ , scattered into an element of solid angle $d\Omega$ in direction $(\theta, \Phi)$ . Adapted from [54] . . . . .	38
2.11. An illustration of a reflection from a sample (a) Bragg reflection from planes separated by a distance $d$ , (b) Laue representation of a Bragg reflection. . . . .	39
2.12. Ewald sphere construction: When the reciprocal lattice point intersecting the sphere, the Bragg condition is satisfied. . . . .	46
2.13. Ewald sphere construction for powder samples. . . . .	47

2.14. Reflection and refraction from a surface. . . . .	52
2.15. Schematic representation of two layers of thickness $d_1$ and $d_2$ on a substrate with a total periodicity $D$ . . . . .	56
2.16. GISAXS geometry with the reciprocal axes. . . . .	60
2.17. Four events involved in the scattering process in GISAXS geometry. The first event corresponds to the simple Born approximation. While the other events shows reflection at the interface . . .	61
3.1. Sketch of the major steps of EBL process. . . . .	65
3.2. Schematics of various methods for NP self-assembly used in this thesis: (a) Drop-casting, (b) Spin coating, (c) Dip coating. . . . .	67
3.3. Interaction of electrons with matter leading to several secondary effects. . . . .	68
3.4. Schematical setup for a scanning electron microscope. . . . .	70
3.5. Diagram explaining different types of signals emitted by the interaction between the incident electron beam and the sample surface and the area from which they originate. . . . .	71
3.6. Superconducting Quantum Interference Device (SQUID) as simple magnetometer. . . . .	73
3.7. Schematic setup of the detection system with second-order gradiometer for an rf-SQUID, the inset shows the response curve versus sample position fitted with a point dipole approximation. Inspired from [65] . . . . .	74
3.8. A Josephson junction: It is made of two superconductors connected through a small insulating layer. . . . .	75
3.9. (a) A DC SQUID is made up of two Josephson junctions a and b connected in parallel, (b) RSO SQUID is made of one Josephson junction superconducting loop in an external magnetic field. . . . .	76
3.10. Schematic diagram of an rf SQUID with one Josephson junction. . .	79
3.11. SQUID = flux to voltage converter . . . . .	80
3.12. Measurement procedures for (a) zero field cooling and (b) field cooling, where green arrows mark the paths along which the magnetization is recorded. . . . .	81
3.13. Schematic drawing of GALAXI showing its main components. . .	82
3.14. Samples of SAXS experiments filled in a samples holder that can move vertically for automatic measurement of multiple samples over a day. . . . .	83
3.15. AgBH calibration to determine the beam center and the sample-to-detector distance. In the left, the measured intensity recorded on the detector. on the right, the transferred measured intensity to polar coordinates, where from the projection on Q, the optimal parameters for beam center and sample-to-detector distance are determined. . . . .	84

3.16. Scattering curve of FEP measured by the ESRF (left) and the vertical scan of the sample holder (right) from which the sample transmission and the width can be determined to scale the data to absolute unit. . . . .	85
3.17. Illustration of SAXS measurement principle, where the beam come from right to left. . . . .	85
3.18. The sample holder for the GISAXS experiment that can be tilted and moved in three dimensions. . . . .	86
3.19. Three dimensional view of the geometry of the GISAXS measurements along the x-axis on the yz plane with the scattering angles. . . . .	87
3.20. Schematic of X-ray reflectometry measurement. . . . .	89
3.21. The MARIA instrument at Heinz Maier-Leibnitz Zentrum used for (polarized) neutron reflectometry. . . . .	91
3.22. Hexapod sample table. . . . .	92
3.23. Typical configuration of specular PNR experiment. Neutrons are polarized, either parallel or antiparallel to the external magnetic field $\vec{H}$ . The $\vec{M}_{\parallel}$ and $\vec{M}_{\perp}$ are the two projections of $\vec{M}$ with respect to $\vec{H}$ . . . . .	93
4.1. Schematic representation of grating lines with period $P$ , mesa width $D$ , groove width $W$ and height $H$ . (a) Cross-sectional view in real space. (b) Reciprocal space representation of grating lines. (c) Scattering of a collimated X-ray beam from grating lines oriented parallel with respect to the incident beam (i.e. $\phi = 0^\circ$ ) . . . .	96
4.2. (a) The parallel orientation between incident beam and grating lines i.e. $\phi = 0^\circ$ . (b) The perpendicular orientation between incident beam and grating lines i.e. $\phi = 90^\circ$ . (c)The intersection of grating truncation rods (orange lines) which are the reciprocal space representation of grating lines and the Ewald sphere (grey mesh) in reciprocal space reconstruction in case of parallel orientation. The intersection leads to semi-circular sharp spots (red spots) on the detector. (d) Misalignment between the incident beam and the grating lines (i.e. the direct beam almost parallel to the grating lines). . . . .	98
4.3. (a) Schematic diagram showing the DTL method. The photoresist coated substrate is moved towards the mask by approximately one Talbot period during the exposure. (b) Schematic representation of the fabrication process of the grating lines by DTL method: (a) exposure and development of photoresist; (b) dry etching into anti-reflective coating (ARC); (c) dry etching into Cr layer; (d) etching of Si substrate. . . . .	102

4.4.	(a) SEM image of the grating lines on Si substrate. (b) A cross-section SEM image of the grating lines. (c) Line profile of the pattern, where the distance between the two red dotted lines represents the gratings period. (d) 3D-SEM image of the pattern.	103
4.5.	(a) X-ray reflectivity as a function of momentum transfer ( $Q$ ) of grating lines. Data shown as red symbols and fits shown as the black solid line. Parameters of the fit are displayed in table 4.1. (b) Modeled scattering length density (SLD) as a function of distance from air interface. (c) Sketch of the model used for fitting XRR data with the relevant parameters that are used to describe it. . . . .	105
4.6.	(a) GISAXS scattering image of grating lines at $\alpha_i = 0.06^\circ$ as the incoming beam perpendicular to the lines. (b) Intensity profile along the vertical specular axis as a function of $Q_z$ . The peak position at $0.1 \text{ nm}^{-1}$ represents the specular peak. . . . .	106
4.7.	Comparison between calculated and measured peak positions in the GISAXS scattering pattern of grating lines. The red and black circles represent the calculated and the measured positions, respectively. The calculated peak positions match the measured one, quite well. . . . .	108
4.8.	(a) GISAXS pattern of grating lines at $\alpha_i = 0.38^\circ$ as the incoming beam parallel to the lines. (b) Intensity profile $I(Q_y)$ along the intersection of the Ewald sphere and GTRs in (a) as a function of $Q_y$ . The peak positions along the semicircle correspond to the diffraction orders of the gratings. (c) PSD of the $I(Q_y)$ profile in (b), the dotted vertical line indicates the nominal values of grating period $P$ and the red solid line represent the fit of the peak using Gaussian function. . . . .	109
4.9.	(a) GISAXS pattern of grating lines for different azimuthal rotation close to the parallel orientation $\phi = 0^\circ$ recorded at $\alpha_i = 0.085^\circ$ . GISAXS pattern at right recorded at $\phi = 6.3^\circ$ while at left recorded at $\phi = 9.5^\circ$ . (b) The extracted average intensity profile $I(Q_y)$ as a function of $Q_y$ , where the violate line represents the right curvature and the pink line represents the left curvature. . .	111
4.10.	Line profile of the gratings (black solid line) fitted with a square wave, where the green and the yellow dotted lines represent 319 nm, 335 nm as a gratings periods, respectively. . . . .	113

4.11. (a) GISAXS pattern of grating lines at $\alpha_i = 0.377^\circ$ as the incoming beam parallel to the lines. (b) Simulation of GISAXS scattering pattern from grating using BornAgain software with a long Lorentz box model. (c) Intensity profile at a constant $Q_z = 0.617nm^{-1}$ of experimental (black solid line) and the simulation (green solid line) data as a function of $Q_y$ . . . . .	114
4.12. Grating lines fabrication by e-beam lithography (EBL) method. . . . .	117
4.13. (a) SEM image for S1_01, (b) SEM image for S1_02, (c) Line profile for S1_01 and (d) Line profile for S1_02. . . . .	119
4.14. (a) SEM image for S2_01, (b) SEM image for S2_02, (c) Line profile for S2_01 and (d) Line profile for S2_02. . . . .	120
4.15. (a) SEM image for S3_01, (b) SEM image for S3_02, (c) SEM image for S3_03, (d) Line profile for S3_01, (e) Line profile for S3_02 and (f) Line profile for S3_03 . . . . .	121
4.16. GISAXS image of gratings. The arc drawn in black indicates the high-intensity Bragg spots (i.e. first main features). The tilted lines drawn in white indicate the diffuse scattering (i.e. second main features). . . . .	123
4.17. A sketch of the grating model which explains and confirms the GISAXS data. . . . .	124
4.18. GISAXS patterns at an incident angle $\alpha_i=0.4^\circ$ for (a) S1_01 and (b) S1_02. The bottom right and left-hand images display the intensity as a function of $Q_y$ along the semicircle for (d) S1_01 and (e) S1_02. . . . .	125
4.19. GISAXS data at an incident angle $\alpha_i=0.3^\circ$ for (a) S2_01 and (b) S2_02. The bottom right and left-hand images display the intensity as a function of $Q_y$ along the semicircle for (d) S2_01 and (e) S2_02. . . . .	126
4.20. GISAXS data at an incident angle $\alpha_i=0.35^\circ$ for (a) S3_01, (b) S3_02 and (c) S3_03. The bottom images displays the intensity as a function of $Q_y$ along the semicircle for (d) S3_01, (e) S3_02 and (f) S3_03. . . . .	128
4.21. PSD of the $I(Q_y)$ profiles shown in figure 4.18 (d) and (e), where (a) for S1_01 and (b) for S1_02. . . . .	130
4.22. PSD of the $I(Q_y)$ profiles shown in figure 4.19 (d) and (e), where (a) for S2_01 and (b) for S2_02. . . . .	131
4.23. PSD of the $I(Q_y)$ profiles shown in figure 4.20 (d), (e) and (f), where (a) for S3_01, (b) for S3_02 and (c) for S3_03. . . . .	131

4.24. X-ray reflectivity as a function of momentum transfer ( $Q_z$ ) of (a) S1_01 and (b) S1_02 grating lines. Data shown as red symbols and fits shown as black solid line. Inset shows the scattering length density (SLD) profile as a function of distance from air interface. . . . .	132
4.25. X-ray reflectivity as a function of momentum transfer ( $Q_z$ ) of (a) S2_01 and (b) S2_02 grating lines. Data shown as red symbols and fits shown as the black solid line. Inset shows the scattering length density (SLD) profile as a function of distance from air interface. . . . .	133
4.26. Left side image : X-ray reflectivity as a function of momentum transfer ( $Q_z$ ) of S3 grating lines. The data are shown as symbols and fits shown as a black solid line; red points correspond to S3_03, blue points for S3_02 and green points for S3_01 points. The XRR curves for S3_03 were multiplied by 10 and S3_01 multiplied by 100. Right side image: SLD profiles as a function of distance from the air interface obtained by fitting XRR data in left side image. . . . .	134
5.1. Schematic diagram of the self-assembly process during the first drying stage according to [100]. First, the NP stabilize on top of the droplet surface as the droplet volume shrinks, where they can still move in two dimensions to obtain long-range order. Second, with the remaining slow evaporation rate, the ordered structure remains. . . . .	140
5.2. Chemical structure of stearyl alcohol molecule. . . . .	142
5.3. SEM image (left) and evaluated size distribution (right) of the silica nanoparticle . . . . .	143
5.4. SAXS data of SiO <sub>2</sub> NPs together with the fit (black line) to the data (red points) assuming a spherical form factor. . . . .	144
5.5. SEM images of SiO <sub>2</sub> NPs with 0.11 vol% concentration (left) and SiO <sub>2</sub> NPs with 5.4vol% concentration (right). Different region of the same samples are shown in (a-c) and (d-f), respectively. For both concentrations, simple drop-casting method was used to deposit the nanoparticles in the wafer surface. . . . .	150

- 
- 5.6. SEM images were taken at different position in the substrate surface of self- assembled nanoparticles using stearyl alcohol as assistance, simple drop-casting method was used to deposit the nanoparticles in the substrate surface. Different nanoparticles and stearyl alcohol concentration were used: (a) The concentration values for NPs and stearyl alcohol, 0.0022 vol% and 0.0022 vol%, respectively, (b) 0.0022 vol% silica and 0.1 vol% stearyl alcohol , (c) 0.1 vol% silica and 0.0022 vol% stearyl alcohol and (d) 0.1 vol% silica and 0.1 vol% stearyl alcohol. . . . . 152
- 5.7. SEM images of self assemble nanoparticles with the same concentration (5.4 vol%) using various preparation methods. (a) spin-coating, (b) drop-casting, (c) dip-coating and (d) slow evaporation method. (without stearyl alcohol) . . . . . 154
- 5.8. Series of SEM images (a)-(d) with various magnifications, taken at different positions of a monolayer of SiO<sub>2</sub> NPs, assembled on a silicon wafer with extra toluene added after drop casting (without stearyl alcohol). . . . . 156
- 5.9. Series of SEM images (a)-(d) with various magnifications, taken at different positions of a monolayer of SiO<sub>2</sub> NPs, assembled on a silicon wafer after using stearyl alcohol as assistant. . . . . 158
- 5.10. SEM images of stearyl silica monolayer with stearyl alcohol as assistant on silicon substrate heated-treated at 70 C° for various period of time: (a) 15min, (b) 2 hours, (c) 29 hours, (d) 10 days. . 159
- 5.11. A line-cut along  $Q_y$  at  $Q_z = 0.34 \text{ nm}^{-1}$  taken from GISAXS data of the same sample after different period in the oven. . . . . 160
- 5.12. SEM image of self-assembled spherical stearyl silica nanoparticles after drop-casted on a silicon substrate and after 10 days in the oven (with stearyl alcohol). The inset shows the two dimensional Fourier transform pattern of the SEM image. . . . . 161
- 5.13. Direct beam width for GALAXI measured with the detector set to a distance of  $L_{SDD} = 3.528 \text{ m}$ . . . . . 163
- 5.14. X-ray reflectivity from a monolayer of SiO<sub>2</sub> NPs (a) without stearyl alcohol. (b) with stearyl alcohol before heat treatment. ((c) with stearyl alcohol after 10 days of heat treatment (red points) along with the fit (black solid line). (d) The model layers structure assumed for fitting the data shown in (c), displaying an ideal in-plane close-packed arrangement of spherical nanoparticles with a parabolic SLD profile of the nanoparticles layer. . . . 165

- 
- 5.15. GISAXS pattern of a monolayer of SiO<sub>2</sub> NPs deposited on silicon substrates (a) before using stearyl alcohol (b) after using stearyl alcohol, before heat treatment and (c) after 10 days heat treatment. (d) Line-cuts from (a), (b) and (c) along  $Q_y$  at a constant  $Q_z = 0.34 \text{ nm}^{-1}$ . The Bragg peaks are indexed by assuming a 2-D hexagonal lattice with a lattice constant  $a = 51.6 \pm 0.4 \text{ nm}$ . . . . . 166
- 5.16. The 2D GISAXS map of the silica monolayer with stearyl alcohol after 10 days of heat treatment. The integrated intensity area of the Bragg rods is presented by a dotted orange rectangle and the integrated intensity area of the diffuse rings is presented by the white dished rectangle. . . . . 168
- 5.17. Integrated intensity of the (a) diffuse rings and (b) Bragg rods as a function of  $Q_y$  determined from the GISAXS maps shown in figure 5.15 (a-c). The Bragg rods intensity is integrated from  $Q_z = 0.17 \text{ nm}^{-1} - 1.4 \text{ nm}^{-1}$  and the diffuse rings intensity is integrated from  $Q_z = -0.38 \text{ nm}^{-1} - 0.15 \text{ nm}^{-1}$ . . . . . 171
- 5.18. Three dimensional vision of the simulated pattern shown in figure 5.19 (b). . . . . 172
- 5.19. (a) GISAXS pattern of SiO<sub>2</sub> monolayer drop-casted onto silicon substrate with stearyl alcohol after 10 days of heat treatment. (b) Simulation of the GISAXS data using Born Again software assuming paracrystalline hexagonal lattice interference function with a lattice constant  $a = 52 \text{ nm}$  and a spherical particle with radius of 25.5 nm. (c) A vertical slice as a function of  $Q_z$  at  $Q_y = 0.14 \text{ nm}^{-1}$ . (d) A horizontal slice as a function of  $Q_y$  at  $Q_z = 0.32 \text{ nm}^{-1}$ . The experimental data shown as black dots and the simulated data are shown as a green solid line. . . . . 172
- 5.20. The resulted SLD profile from the simulation of the GISAXS pattern. The particle layer is sliced into 60 slices. . . . . 173
- 5.21. SEM images of self-assembled silica nanoparticles of  $\approx 50 \text{ nm}$  diameter on the trench-patterned silicon substrate. (a) S1-sample, (b) S2-sample and (c) S3-sample, the inset is a magnified SEM image of a close-packed pattern indicated as the black rectangle in (c). . . . . 175
- 5.22. GISAXS patterns of S1 and S2 samples with the direct beam almost parallel to the lines (right side images) and perpendicular to the lines (left side image). The incident angle in both cases for both samples  $\alpha_i \approx 0.18^\circ$ . The direction of the X-ray beam with respect to the trenches is illustrated on the top-right corner of each figure. A line cut (red solid line) from each image along  $Q_y$  at constant  $Q_z = 0.3 \text{ nm}^{-1}$ . The Bragg peaks were indexed according to a hexagonal lattice with  $a = 51.7 \text{ nm}$ . . . . . 179

5.23. GISAXS patterns of S3 sample with the direct beam almost parallel to the lines (right side images) and perpendicular to the lines (left side image). The incident angle in both cases $\alpha_i \approx 0.18^\circ$ . The direction of the X-ray beam with respect to the trenches is illustrated on the top-right corner of each figure. A line cut (red solid line) from each image along $Q_y$ at constant $Q_z = 0.3 \text{ nm}^{-1}$ . The Bragg peaks were indexed according to a hexagonal lattice with $a = 52 \text{ nm}$ . . . . .	180
5.24. Comparison between self-assembled particles in flat and trench-patterned substrate. (a) GISAXS pattern of self-assembled stearyl silica particles monolayer on flat surface after 10 days in the oven with stearyl alcohol assistant. (b) GISAXS pattern of directed self-assembled stearyl silica particles on trench-patterned silicon substrate after 10 days in the oven with stearyl alcohol assistant. (c) Line-cut from (a) and (b) along $Q_y$ at a fixed $Q_z = 0.3355 \text{ nm}^{-1}$ . . . . .	181
6.1. Crystal structure of $\text{CoFe}_2\text{O}_4$ . The Co atoms sit within the yellow tetrahedral and the Fe atoms sit within the blue octahedral. The red points represents the oxygen ions. . . . .	186
6.2. Magnetization hysteresis curves for cobalt iron nanopowder at 300 K (left) and 5K (right). . . . .	188
6.3. Magnetization-temperature curves recorded in FC and ZFC modes for cobalt ferrite nanopowder in an external magnetic field of 50 Oe (left) and 100 Oe (right). . . . .	189
6.4. Three dimensional visualization of the simulated structure shown in the right plot of Figure 6.9. The visualization was generated using the BornAgain software package. . . . .	191
6.5. A schematic drawing of the model assumed to fit the neutron reflectivity data. The sample can be modeled by a layered system of a silicon substrate (dark gray), silicon dioxide (light gray) and cobalt ferrite layer (brown). The hexagonal array layer of COF NP is modeled by a single slab of trapezoids. . . . .	192
6.6. SEM image (left) and the particle size distribution histogram (right) along with a lognormal (black solid line) fit. It yields a size distribution of 8.7%. . . . .	193
6.7. The (a) 3D (b) 2D AFM Topographical images of $\text{CoFe}_2\text{O}_4$ nanodots and (c) line profile obtained of a selected set of dots. . . . .	194
6.8. X-ray reflectometry of the $\text{CoFe}_2\text{O}_4$ monolayer prepared by a high temperature treatment. . . . .	195

- 6.9. (a) GISAXS pattern of  $\text{CoFe}_2\text{O}_4$  NPs grown on top of Si substrate at  $\alpha_i = 0.17^\circ$ . The indexing of the Bragg rods according to a 2D hexagonal lattice with  $a = 34$  nm is also shown. (b) A horizontal line cut of the GISAXS pattern at a fixed  $Q_z = 0.29$   $\text{nm}^{-1}$  along with Voigt fit (light green line) to (10) Bragg peak. (c) A vertical line cut of the GISAXS pattern at a fixed  $Q_y = 0.21$   $\text{nm}^{-1}$ . . . . . 198
- 6.10. (a) GISAXS pattern of  $\text{CoFe}_2\text{O}_4$  NP monolayer on Si substrate. (b) The simulation of the experimental GISAXS pattern using the BornAgain software assuming hemispherical particles with 10 nm height and 8.5 nm radius. The lattice constant of the hexagonal lattice is 34 nm. (c) A vertical slice as a function of  $Q_z$  at  $Q_y=0.21$   $\text{nm}^{-1}$ .(d) A horizontal slice as a function of  $Q_y$  at  $Q_z=0.28$   $\text{nm}^{-1}$ . The experimental data are shown as black dots and the simulated data are shown as a green solid line. . . . . 199
- 6.11. The resulted SLD profile from the simulation of the GISAXS pattern. . . . . 200
- 6.12. In-plane and out-of-plane magnetization curves of  $\text{CoFe}_2\text{O}_4$  naodots on Si substrate at 300 K (left) and at 5 K (right). . . . . 202
- 6.13. Temperature dependence of the in-plane (left) and out-of-plane (right) magnetization of  $\text{CoFe}_2\text{O}_4$  nanodots on Si substrate at 50 mT. The blue and green curves are the field-cooling and zero-field-cooling curves, respectively. . . . . 203
- 6.14. Neutron reflectivity of cobalt ferrite monolayer deposited directly onto a silicon wafer measured at 300 K. The NR measured first at saturation field (left) with half polarization analysis and at remnant field (right) with full polarization analysis. At saturation,  $R^+$  and  $R^-$  are displayed, together with the fits shown by solid lines. The  $R^+$  and  $R^-$  are correspond to the states of the RF flipper turned off and on, respectively. At saturation, All four reflectivities: two NSF ( $R^{++}, R^{--}$ ) and two SF ( $R^{+-}, R^{-+}$ ) are displayed, together with the fits shown by solid lines. . . . . 204
- 7.1. Representation of iron oxide structure of (a) magnetite, (b) hematite and (c) wüstite. The red spheres represent the close-packed  $\text{O}^{2-}$  ion and the brown spheres indicate the position of the iron cations occupy either the tetrahedral or octahedral interstices. The visualization was produced using VESTA software [167] where the data used here are obtained from the Inorganic Crystal Structure Database (ICSD). . . . . 209
- 7.2. (a) SEM image of cubic iron oxide nanoparticles drop-casted on the silicon substrate. (b) TEM micrographs of the same particles. (c) The particle size distribution histogram. . . . . 212

7.3.	The SAXS data of the iron oxide nanoparticles dispersed in toluene. Spherical (red), core-shell (yellow), cubic (violate) and superball (light blue) form factors were used to fit the data. . . . .	214
7.4.	The glass tube inside drinking straw used for measurements of liquid nanoparticles using MPMS. . . . .	215
7.5.	Field dependent magnetization of cubic iron oxide dispersion measured at 300 K (left) and at 5 K (right). . . . .	216
7.6.	Schematic drawing of the cubic nanoparticles inside trenches. . . . .	217
7.7.	SEM images from high to low magnification of self-assembled cubic iron oxide nanoparticles on the trench-patterned silicon substrate. . . . .	218
7.8.	Schematic drawing of the expected arrangement of the cubic nanoparticles inside the trenches. . . . .	219
7.9.	X-ray reflectivity data from nanoparticle multilayers inside trenches.	220
7.10.	The GISAXS patterns of the cubic iron oxide nanoparticle were deposited on a trench-patterned silicon substrate with different directions of the beam with respect to the lines. (a) as the beam almost parallel to the lines, (b) The azimuthal angle between the direct beam and the line is $\Phi=45^\circ$ and (c) as the incoming beam perpendicular to the lines where the azimuthal angle $\Phi=90^\circ$ . In the parallel case, the azimuthal angle $\Phi$ of the sample was tilted by $1.7^\circ$ to reduce the scattering intensity from the lines. The angle of the incident beam in all cases $\alpha_i \approx 0.2^\circ$ . (d) A line cut from (a), (b) and (c) along $Q_y$ at $Q_z=0.2071 \text{ nm}^{-1}$ . (e) A line cut from (a), (b) and (c) along $Q_z$ at $Q_y=0.4998 \text{ nm}^{-1}$ . The lateral Bragg peaks were indexed according to a hexagonal lattice with $a = 11.2 \text{ nm}$ while the vertical peaks were indexed according to FCC structure with $c = 9.2 \text{ nm}$ . . . . .	222
7.11.	M vs. T curves of the magnetic moment of nanoparticles self-assembled in trench-patterned silicon substrates after ZFC (green) and FC (blue) at two applied fields, i.e. 50 Oe (left) and 100 Oe (right). The magnetic field was applied perpendicular (a), (b) and parallel (c), (d) to the long axis of the trenches. The arrows indicate the peak temperature $T_P$ , which was defined as the first zero value of the derivative of the ZFC curve. . . . .	226
7.12.	Hysteresis loops for the cubic iron oxide nanoparticles on trench-patterned silicon substrate measured at 300 K (left) and at 5 K (right). The brown hysteresis loops in both figures were measured as the filed parallel to the long axis of the trenches, the green ones were measured with the field perpendicular to the trenches. . . . .	227
8.1.	Schematic picture of the film deposited onto nanospheres monolayer.	235

E.1. Schematic representation of core shell particles. . . . .	250
F.1. Schematic representation of a hexagon. . . . .	253
F.2. In-plane and out-of-plane temperature-dependent magnetization of the ordered $\text{CoFe}_2\text{O}_4$ NP monolayers measured at various magnetic fields. . . . .	254
F.3. In-plane and out-of-plane hysteresis loops of the ordered $\text{CoFe}_2\text{O}_4$ NP monolayers measured at various temperature. The downright insets is an expanded low-field curve. . . . .	255
F.4. PNR measurements from COF nanodots onto a silicon substrate measured at 300 K with an applied In-plane field, (upper left) half polarized NR at 50 mT, (upper right) half polarized NR at remnant field. . . . .	256
F.5. PNR measurements from COF nanodots onto a silicon substrate measured at 300 K with an applied Out-of-plane field. The upper plots show a full polarized NR measured at 70 mT, remnant and saturation, respectively. The bottom plots show a half polarized NR measured at 70 mT, remnant and saturation, respectively. . .	257

# List of Tables

4.1.	Parameters obtained from fitting of the XRR data. . . . .	104
4.2.	Grating parameters of S1 samples obtained from SEM. . . . .	118
4.3.	Grating parameters of S2 samples obtained from SEM. . . . .	118
4.4.	Grating parameters of S3 samples obtained from SEM. . . . .	119
4.5.	Gratings parameters obtained from PSD. . . . .	130
5.1.	Parameters obtained from fitted SAXS data with the spherical form factor shown in figure 5.4. The size of the sphere is given in terms of radius R. The respective log-normal size distribution is given as $\sigma_R$ . The $SLD_{solvent}$ , $SLD_{core}$ are the scattering length density of the core and the solvent, respectively. . . . .	145
5.2.	Comparison of nanoparticle length scale as viewed by SAXS and SEM. . . . .	145
5.3.	The parameters obtained from the fitting of the XRR data shown in figure 4 (c) according to the model in Figure 4 (d). . . . .	164
5.4.	The integrated intensity of the Bragg rods and the diffuse ring as calculated by integration over the areas defined by the dotted orange and white angle drawn in the GISAXS map in figure 5.16. The integrated intensity ratio between the GISAXS peaks and the diffuse rings from single defects are listed in column four. . . . .	170
5.5.	Comparison of intraplanar distances measured from GISAXS scattered pattern ( $2^{nd}$ ) column and calculated values by assuming a hexagonal lattice with $a=50.5$ nm ( $3^{rd}$ ) column . . . . .	170
5.6.	Lattice constant (a), coherence length ( $\zeta$ ) of each GISAXS map and the integrated intensity ratio between the GISAXS peaks and the diffuse rings from single defects. . . . .	171
6.1.	Scattering length density values used in the simulation of the GISAXS data. . . . .	191
6.2.	Comparison of intraplanar distances measured from GISAXS scattered pattern ( $2^{nd}$ ) column and calculated values by assuming a hexagonal lattice with $a=34$ nm ( $3^{rd}$ ) column. . . . .	197
7.1.	Particle size and size distribution of iron oxide nanocubes as obtained from the spherical, the core-shell, the cubic and the superball form factors. $\sigma_{R,L}$ is the log-normal size distribution. . . . .	215



# 1. Introduction

**"There's Plenty of Room at the Bottom"**, one of P. Feynman's famous lectures in 1959. What he was referring to at this time is the tremendous potential for technological applications in the nanometer regime and even below. During the decades that followed up to the present day, the emerging field of nanotechnology has claimed more and more of this room. Nowadays, various nanotechnological applications can be found within reach or already in industrial production such as microprocessors using nm-sized functional elements [1] organic photovoltaic devices [2] bioactive nanoparticles [3], carbon nanotubes for energy storage [4, 5], medicine [6, 7], energy production and storage [8, 9] or electronics and information technology [10, 11]. However, the field of applications is exciting, but it is only one side of the coin. The flip side is the ability to prepare or fabricate such systems which are suitable for such applications and to perform useful and accurate measurements of relevant novel properties in the nanometer regime. Typically, recent nanotechnological applications demand, firstly fabrication suitable nanostructure systems with novel properties, secondly, appropriate tools or techniques to understand, characterize, control, and make use of the underlying principles of these systems.

Monodispersed magnetic nanoparticles are of interest for both technological and fundamental reasons. One of the reasons for that trend is that, besides being promising candidates for further increasing the density of magnetic storage devices towards the Terabyte per inch squared [12], the magnetic interaction between neighbouring particles is becoming a more and more important parameter that has to be understood and controlled. The magnetic configurations are best investigated if the nanoparticles are disposed on a regular 2D or 3D lattice. Magnetic nanoparticles are hereby interesting for the study of dipolar interparticle interaction. As dipolar interaction depends on the relative distance and orientation of two magnetic moments, the degree of structural order is directly correlated to the nature of the interparticle interaction. As a matter of fact, the magnetic interaction between atoms in bulk materials is well known (direct and indirect exchange coupling) [13], the magnetostatic interaction between nanoparticles and the magnetic configurations it leads to are not well known. To the best of my knowledge, this interaction and the collective behaviour it leads to have been mainly deduced from macroscopic magnetization measurements [14, 15] on assemblies of nanoparticles showing only short range order.

The development of magnetism is a story of the development of modern civ-

ilization itself. Over the past decades, a significant development of magnetism occurred and the research in magnetism evolved towards the study of nanometre-sized objects, leading to new properties and applications. One of the most applications that added a new dimension to the magnetism application and initiated a boom in the computer industry is using magnetic hard disk drives for data storage in the 20<sup>th</sup> century. Another breakthrough discovery is the giant magnetoresistance (GMR) effect discovered in 1988 simultaneously by A. Fert and P. Grünberg and honored with the Nobel Prize in Physics in 2007 [16, 17], which led to faster and smaller writing area on a hard disk.

Regular arrangements of magnetic nanoparticles over large areas are fundamentally interesting regarding the understanding of magnetic interactions and for a rational design towards potential applications in information technology and spintronics devices that make additional use of the spin degree of freedom in electron currents instead of only the charge [18]. Usually, devices studied in spintronics are layers of different materials with varying physical properties where new emergent physics might appear from the combination of these materials [19].

For the preparation of such nanostructure systems, there are two general approaches, i.e. top-down and bottom-up processes [14]. Top-down methods such as lithography [20], molecular beam epitaxy, or vapor deposition require sophisticated machines, which are costly [21, 22], and additionally, it is considered inflexible in the material selection [21]. Using these methods, one starts with larger structures, and then the size of the structure is reduced using different processes. One of the most known top-down processes is known as photolithography. Here, a photoresist layer is used, and the desired patterns can be transferred from the masks to the substrate after exposure to UV light. This process is complicated, expensive and the structure resolution is limited to  $\approx 10$  nm which can be improved by replacing UV light by an electron beam or x-rays. But, electron beam lithography (EBL) is very expensive and very slow and x-rays might destroy the masks. In order to reach higher resolution below  $\approx 10$  nm, bottom-up processes can be used. The bottom-up processes are an alternative way that mimics nature's way in building materials and have the promise to fabricate structures with precision and cheaper production cost than those conventionally associated with top-down approaches [23]. Here, nanometer sized building blocks with controllable shape and size are synthesized from the atomic or molecular level by chemical processes, for example, thermal decomposition, and higher order nanostructures are prepared by self-assembly methods [23, 24].

In self-assembly, individual components assemble together without any external forces into an ordered structure. This process promises to provide the framework for the future device fabrication process in a cost-effective way. The self-organized nanostructure inherits the properties of their small components and can emerge new, unique, and collective properties from the long-range or-

---

der and interacting forces. Moreover, it allows us to create multi-functional materials by combinations of different physical properties. However, the self-assembly process requires precise control and a deep understanding of the underlying forces and it is still an active field of study [25–27]. Once nanoparticulate building blocks are self-assembled on a substrate a new system is produced and it presents an ideal model to study the interparticle interaction on the length scales defined by the nanostructure.

Various self-assembly methods used in this study will be introduced later in Sec. 3.1.2. Using these methods, nanostructures as 2D to 3D arrangements can be fabricated. There are also approaches combining both top-down and bottom-up methods, such as templated assisted self-assembly, which is an efficient method and will be introduced later in Sec. 3.1.1. The templates used in this study are pre-patterned silicon substrates with rectangular grooves. These substrates are used to reach high coherence of the lateral order of the nanoparticles.

The main aims of this study: first, fabricate a highly ordered two dimensional and three dimensional arrangements of magnetic and non magnetic nanoparticles under suitable conditions. Second, a proper and accurate characterization of these nanostructures with different dimensions using several experimental techniques, among these, scattering techniques played a major role. The present thesis describes three different nanostructures systems obtained from different nanoparticles and using different techniques. The main focus of the first system is how to achieve highly ordered monolayers of stearyl alcohol grafted silica nanoparticles over a large area and how to properly characterize them. Here, the influence of the volume of the droplet, the concentration of silica particles and the stearyl alcohol on the surface coverage and the uniformity of the monolayer is investigated to optimize the proper parameters for the large area monolayers. The second system focuses on two dimensional arrays of cobalt ferrite nanodots with a hemispherical shape where the main aim is how to study the mesoscopic magnetic properties of these nanodots using neutron. The third system focuses on how to achieve highly ordered three dimensional arrangements of cubic magnetic nanoparticles using patterned substrates. Thus, the influence of pattern dimensions and geometry, particle shape and size is systematically investigated by SEM and GISAXS to optimize the sample preparation.

In all systems, the structural characterization is done locally via imaging techniques (SEM and AFM) and globally using X-ray techniques (XRR and GISAXS). Simulations of the GISAXS data based on Distorted-wave Born approximation (DWBA) are carried out to gain a deeper understanding of the sample structure. The macroscopic magnetic properties are investigated using SQUID magnetometer.

## Concept

Three different nanostructures systems are studied in this thesis, where these systems primarily fabricated differently by using different preparation methods as well as different types of nanoparticles. One of these systems is dealing with non-magnetic nanoparticles with a focus on prepare long-range ordered monolayers of nanoparticles in a two-dimensional lattice and the other two systems are dealing with magnetic nanoparticles with focus on determining effects that result from collective magnetism. First, the nanoparticles are studied separately in dispersion to determine the non-interacting state. Subsequently, the obtained nanostructures are characterized structurally to determine the degree of order in the sample.

This thesis is formatted into eight chapters. In **Ch.2**, a brief introduction about magnetism with a focus on a description of various types of interactions relevant for self-assembly at the nanoscale as well as the four types of magnetic orders which are the most frequently mentioned in the following chapters is given. Furthermore, a literature study of the self-assembly process and a brief discussion of the scattering theory is described in this chapter since various scattering techniques are used extensively for the investigation of our systems. **Ch.3** provides a brief review of different characterization techniques and tools used for scattering, imaging, and magnetization measurements. In **Ch.4**, the measurements, and analysis of GISAXS data obtained from surface gratings with structure periodicity ranging from almost 300 nm down to 78 nm are described. Different ‘direct’ data analysis methods were implemented to determine structural parameters such as grating pitch, groove width, and line-height directly from the data, i.e. without numerical modeling. Then, in **Ch.5** a method to prepare long-range ordered monolayers of silica nanoparticles in a two-dimensional lattice is presented and studied. The monolayer study is extended in **Ch.6** to a layer of a hemispherical cobalt ferrite nanoparticles in a two-dimensional lattice that is prepared by high-temperature treatment. And finally, in **Ch.7**, a three-dimensional arrangement of iron oxide nanocubes obtained using templated assisted self-assembly method is discussed. The conclusion and an outlook have been provided in **Ch.8**.

## 2. Theoretical Background

### 2.1. Magnetism

Electrons carry an intrinsic magnetic moment arising from its intrinsic properties of spin and electric charge and it has an orbital angular momentum that comes from it's orbiting around a nucleus in an atom.

Classically, if a current  $I$  flow in a loop of area  $|d\vec{S}|$ , then the magnetic moment  $d\vec{\mu}$  is given:

$$d\vec{\mu} = Id\vec{S} \quad (2.1)$$

The magnetic moment  $\mu$  for a loop with a finite size is equal to the summation of the magnetic moments of equal infinitesimal current loops distributed through the loop area. So, the total magnetic moment is given as:

$$\mu = \int d\vec{\mu} = I \int d\vec{S} \quad (2.2)$$

In atoms the magnetic moment  $\vec{\mu}$  is associated with an orbiting electron lies along the same direction as it's angular momentum  $\vec{L}$ , the relation between the  $\vec{\mu}$  and  $\vec{L}$  is given as:

$$\vec{\mu} = \gamma\vec{L} \quad (2.3)$$

Where  $\gamma$  is a gyromagnetic ratio constant. The energy  $E$  of a magnetic moment  $\vec{\mu}$  in a magnetic field  $\vec{B}$  is given by:

$$E = -\vec{\mu} \cdot \vec{B} \quad (2.4)$$

The minimum energy is achieved when the magnetic moment  $\vec{\mu}$  lies along the magnetic field. The torque  $\vec{G}$  on the magnetic moment is given by:

$$\vec{G} = \vec{\mu} \times \vec{B} \quad (2.5)$$

Since the magnetic moment  $\vec{\mu}$  is associated with the angular momentum  $\vec{L}$  by equation 2.3 and the torque is equal to the change rate of the angular momentum, then, the magnetic moment can be written as:

$$\frac{d\vec{\mu}}{dt} = \gamma\vec{\mu} \times \vec{B} \quad (2.6)$$

This means that the magnetic moment precesses around the magnetic field with a Larmor precession:

$$\omega_L = \gamma B \quad (2.7)$$

The magnetic moment for an electron with a charge  $e$  and mass  $m_e$  moving in an orbit of radius  $r$  and speed  $v$ :

$$\mu_L = \pi r^2 I = -\frac{e}{2m_e} L \quad (2.8)$$

The current  $I = \frac{e}{\tau} = \frac{ev}{2\pi r}$ , where  $\tau$  is the orbital period,  $v$  is the speed and  $r$  is the radius of the circular orbit. The angular momentum  $L = m_e v r$ .

In quantum mechanics, the angular momentum is conserved only if the symmetry allows (i.e.  $[H, L] = 0$ ), then the magnetic moment can be written as:

$$\mu_L = -g\mu_B \frac{L}{\hbar} \quad (2.9)$$

Where  $g$  is known as the g-factor of the electron has an approximate value of 2,  $L$  is electron orbital angular momentum and  $\mu_B$  is the Bohr magneton, defined by:

$$\mu_B = \frac{e\hbar}{2m_e} \quad (2.10)$$

Bohr magneton takes the value  $9.274 \times 10^{-24} \text{ Am}^2$  and it describe the size of the atomic magnetic moments.

The magnetic moment due to the electron spin  $s$  is given by:

$$\mu_s = -g\mu_B \frac{S}{\hbar} \quad (2.11)$$

Where  $S$  is the electron spin angular momentum. The energy of an electron in magnetic field given as:

$$E = -\vec{\mu} \cdot \vec{B} = g\mu_B m_s B \quad (2.12)$$

In a magnetic field, the energy level of an electron will split by an amount of  $g\mu_B B$  which is known as Zeeman splitting. For an electron with spin  $\frac{1}{2}$ ,  $m_s$  can take values  $\pm\frac{1}{2}$  and the electron energy level split into two levels with an energy:

$$E \approx \pm\mu_B \quad (2.13)$$

### 2.1.1. Magnetization

The magnetization  $M$  of magnetic solid consists of a large number of atoms is defined as the magnetic moment ( $m$ ) per unit volume ( $V$ ).

$$\vec{M} = \frac{\vec{m}}{V} \quad (2.14)$$

In the presence of an external magnetic field  $\vec{H}$ , the magnetic induction  $\vec{B}$  induced inside the magnetic material with magnetization  $M$  given as:

$$\vec{B} = \mu_0(\vec{H} + \vec{M}) \quad (2.15)$$

Where  $\mu_0 = 4\pi \times 10^{-7} \text{Hm}^{-1}$  is the permeability of the free space.

In the free space (vacuum), there is no magnetization, so equation 2.15 becomes:

$$\vec{B} = \mu_0 \vec{H} \quad (2.16)$$

For the case for the linear materials i.e. the magnetization  $\vec{M}$  is linearly related to the magnetic field  $\vec{H}$  and it is given as:

$$\vec{M} = \chi \vec{H} \quad (2.17)$$

Where  $\chi$  is the magnetic susceptibility, which is a dimensionless quantity. The  $\chi$  values distinguish between two different types of magnetic materials.

- 1) Diamagnetic material with  $\chi < 0$
- 2) Paramagnetic material with  $\chi > 0$

### 2.1.1.1. Diamagnetism

All materials show diamagnetism, which is weak and has negative magnetic susceptibility. Diamagnetism means that the magnetic field induces a magnetic moment, which opposes the applied magnetic field. Diamagnetism can be explained classically via Lenz's law, but it is a purely quantum phenomenon. The diamagnetic susceptibility using first-order perturbation theory is given by [28]:

$$\chi_{dia} = -\frac{Ne^2\mu_0}{6Vm_e} \sum_{i=1}^Z \langle r_i^2 \rangle \quad (2.18)$$

Where, N is the ions number, V is the volume,  $m_e$  is the electron mass and  $\mu_0$  is the vacuum permeability. The diamagnetic susceptibility are largely temperature independent.

### 2.1.1.2. Paramagnetism

In paramagnetism, the applied magnetic field induces a magnetization aligned parallel to the applied magnetic field. The paramagnetic susceptibility is positive, but very small and it depends on the strength of the applied magnetic field. Paramagnetism phenomena are observed in materials with unpaired electrons. At finite temperature, the spins are randomly oriented due to the thermal fluctuations (i.e. there's no interaction between the magnetic moments). The magnetization depends on the total angular momentum  $\vec{J}$  which is a sum of the orbital angular momentum  $\vec{L}$  and the spin angular momentum  $\vec{S}$ .

$$\vec{J} = \vec{L} + \vec{S} \quad (2.19)$$

The paramagnetic susceptibility is given by [28]:

$$\chi_{para} = \frac{M}{H} \approx \frac{\mu_0 M}{B} = \frac{n\mu_0\mu_{eff}^2}{3k_B T} \quad (2.20)$$

Where  $\mu_{eff}$  is the effective moment given by:

$$\mu_{eff} = gJ\mu_B\sqrt{J(J+1)} \quad (2.21)$$

Equation 2.20 demonstrates that the magnetic susceptibility is inversely proportional to the temperature T, which is known as **Curie's law**.

### 2.1.2. Magnetic interactions

Long range ordering like Ferromagnetic (FM), Antiferromagnetic (AFM) and Ferrimagnetic (FIM) arises due to the interactions between the magnetic moments. These interactions will be discussed briefly in this section.

#### 2.1.2.1. Magnetic dipolar interaction

The first interaction that plays a role in magnetic ordering is the magnetic dipolar interaction. Generally, the magnetic moments are similar to the magnetic dipoles and can show dipole-dipole interaction amongst them. A magnetic field produced by one dipole can interact with the neighboring magnetic dipole, and vice versa. The dipole-dipole interaction energy between two dipoles  $\vec{\mu}_1$  and  $\vec{\mu}_2$  separated by a distance  $\vec{r}$  is given by:

$$E_{dd} = \frac{\mu_0}{4\pi r^3} [\vec{\mu}_1 \cdot \vec{\mu}_2 - \frac{3}{r^2} [(\vec{\mu}_1 \cdot \vec{r})(\vec{\mu}_2 \cdot \vec{r})]] \quad (2.22)$$

The dipole-dipole energy depends on the separation between the two dipoles and the orientation of its moments. The behaviour of this interaction, either repulsive or attractive depends on the orientation of the nanoparticles spin. For atomic moments with  $\mu \sim 1\mu_B$  separated by  $|\vec{r}| = 0.1$  nm, the ordering temperature is usually of the order of 1 K, which is quite weak compared to the normal thermal energy. Therefore the magnetic dipolar interaction is too weak to account for the ordering at high temperature in solids because it can easily be overcome by thermal fluctuations at a temperature of a few Kelvin. For particles with large magnetic moments separated by a distance in the nm range, the magnetic dipolar interaction can be a hundred orders of magnitude stronger. Therefore, magnetic dipolar interactions are important in the ordering of nanoparticles.

#### 2.1.2.2. Exchange interaction

Exchange interaction plays a significant role in the long-range magnetic order phenomena such as ferromagnetic (FM), antiferromagnetic (AF) and ferrimagnetic (FiM). Exchange interaction is a result of Coulomb interaction and the Pauli principle. Where Coulomb repulsion tries to repel electrons from each other when they are together, while Pauli principle state that two electrons with the same spin quantum number can not occupy the same state, therefore they have to align antiparallel. So, the total spin state can be 0 or 1, which is known as singlet (S=0) and triplet (S=1) states, respectively.

### Origin

Consider a simple system with two electrons. In first order perturbation theory, the total wavefunction  $\Psi(\vec{r})$  of the state can be constructed from a product of the two electron states  $\psi_a(\vec{r}_1)\psi_b(\vec{r}_2)$ , where  $\psi_a(\vec{r}_1)$  is the wavefunction for the first electron at position  $\vec{r}_1$  and  $\psi_b(\vec{r}_2)$  is the wave function for the second electron at position  $\vec{r}_2$ . The product state doesn't follow the exchange symmetry, it has to be consistent under electrons exchange, and it has to be a linear combination of  $\psi_a(\vec{r}_1)\psi_b(\vec{r}_2)$  and  $\psi_a(\vec{r}_2)\psi_b(\vec{r}_1)$ .

For electrons (fermion), the overall wave function which is a product of the spatial and spin states has to be antisymmetric. If the spin state is antisymmetric singlet state  $\chi_S$ , then the spatial state has to be symmetric, while if the spin state is symmetric triplet state  $\chi_T$ , then the spatial part has to be antisymmetric. The wave functions of the singlet state  $\chi_S$  and the triplet state  $\chi_S$  can be written as [28]:

$$\begin{aligned}\Psi_S &= \frac{1}{\sqrt{2}}[\psi_a(\vec{r}_1)\psi_b(\vec{r}_2) + \psi_a(\vec{r}_2)\psi_b(\vec{r}_1)]\chi_S \\ \Psi_T &= \frac{1}{\sqrt{2}}[\psi_a(\vec{r}_1)\psi_b(\vec{r}_2) - \psi_a(\vec{r}_2)\psi_b(\vec{r}_1)]\chi_T\end{aligned}\quad (2.23)$$

The eigen values (energies) of the two states by assuming the spin states  $\chi_S$  and  $\chi_T$  are normalized.

$$\begin{aligned}E_S &= \int \Psi_S^* \hat{H} \Psi_S d\vec{r}_1 d\vec{r}_2 \\ E_T &= \int \Psi_T^* \hat{H} \Psi_T d\vec{r}_1 d\vec{r}_2\end{aligned}\quad (2.24)$$

The difference between the singlet and the triplet energies states are

$$E_S - E_T = 2 \int \psi_a^*(\vec{r}_1)\psi_b^*(\vec{r}_2)\hat{H}\psi_a(\vec{r}_2)\psi_b(\vec{r}_1)d\vec{r}_1 d\vec{r}_2\quad (2.25)$$

The **exchange integral J** is defined as the difference between the singlet and the triplet states energies

$$J = \frac{E_S - E_T}{2} = \int \psi_a^*(\vec{r}_1)\psi_b^*(\vec{r}_2)\hat{H}\psi_a(\vec{r}_2)\psi_b(\vec{r}_1)d\vec{r}_1 d\vec{r}_2\quad (2.26)$$

Where the Hamiltonian  $\hat{H}$  is given as

$$\hat{H} = \frac{1}{4}(E_S + 3E_T) - (E_S - E_T)\vec{S}_1 \cdot \vec{S}_2 \quad (2.27)$$

Where  $S_1 \cdot S_2 = -\frac{3}{4}$  for the singlet state and  $S_1 \cdot S_2 = \frac{1}{4}$  for the triplet state. The spin part in the Hamiltonian (equation 2.27) describing the exchange interaction between two neighbouring spins  $\vec{S}_1$  and  $\vec{S}_2$  and can be written as:

$$\hat{H}^{spin} = -2J\vec{S}_1 \cdot \vec{S}_2 \quad (2.28)$$

If  $J > 0$ ,  $E_s > E_T$ , then the triplet state is favored and the two spins prefer to align parallel to each other, while if  $J < 0$ ,  $E_S < E_T$ , the singlet state is favored and the two spins prefer to align antiparallel to each other. The Hamiltonian for many electrons system is described by *Heisenberg model*:

$$\hat{H} = -2 \sum_{i < j} J_{ij} \vec{S}_i \cdot \vec{S}_j \quad (2.29)$$

Where  $J_{ij}$  is the exchange constant between  $\vec{S}_i$  and  $\vec{S}_j$ , the summation  $i < j$  to avoid the double counting of the interaction between  $\vec{S}_i$  and  $\vec{S}_j$ .

The exchange integral has some general features, such as if the two electrons belong to the same atom, then the exchange integral is positive and the triplet state is more favored with the antisymmetric spatial state. This minimizes the Coulomb repulsion between the two electrons by keeping them apart, which is consistent with Hund's first rule. While if the two electrons belong to different atoms, in this case, it is more favorable if the electron states (joint state) are shared between the two atoms, which leads to bonds formation. In this case, molecular orbitals have to be considered rather than atomic orbitals. The molecular orbitals can be bonding (spatially symmetric) or antibonding (spatially antisymmetric), with the antibonding state having higher energy compared to the bonding state. This leads to a singlet antisymmetric states and the exchange integral is negative.

The exchange interaction can be further subdivided into the following forms.

### Direct exchange

If two magnetic atoms are close enough to each other, then their magnetic orbitals overlap directly without the need for an intermediary, which means the

electron of one atom can hop easily to its neighboring atom. This kind of exchange interaction is known as a direct exchange interaction. This interaction is quite rare in rare earth elements where 4f electrons are strongly localized and lying close to the nucleus and for transition metals where 3d electrons are also localized. In these cases, to explain the exchange interaction, the band character should be taken into account in addition to the localized electrons. Therefore, in some kind of magnetic materials, it is crucial to consider indirect exchange interaction.

### Indirect exchange

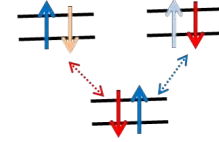
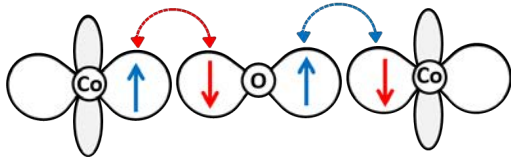
In most magnetic materials usually in ionic solids such as MnO and MnF<sub>2</sub>, the direct exchange interaction is impossible. But it shows an indirect exchange interaction where the non-neighboring magnetic ions interact via a nonmagnetic ion like oxygen which is placed in between the magnetic ions. The exchange interaction is given by:

$$J \sim \frac{-t^2}{U} \tag{2.30}$$

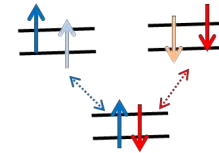
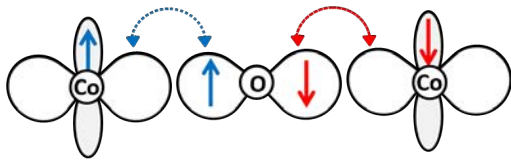
The above equation describes the kinetic exchange in the Hubbard model, where  $t$  known as the hopping integral and  $U$  is the Coulomb energy. This equation explains the virtual hopping processes shown in figure 2.1. It is crucial to remember that hopping does not involve spin-flip.

Indirect exchange interaction consists of several types which will be introduced in the following paragraph.

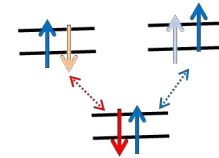
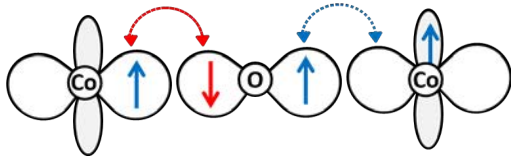
(a) 180°- exchange between half-filled orbitals



(b) 180°- exchange between empty orbitals



(c) 180°- exchange between half-filled orbital and empty orbital



(d) 90°- exchange

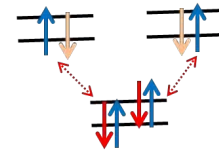
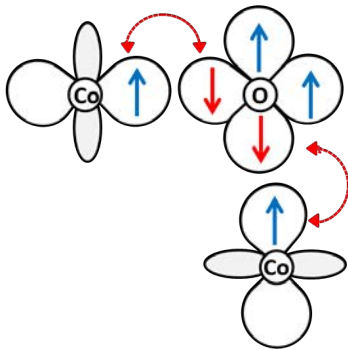


Figure 2.1.: Superexchange interaction between two magnetic ions ( $\text{Co}^{+2}$ ) mediated by a non-magnetic ion ( $\text{O}^{-2}$ ). (a) and (b) show the first GKA rule: antiferromagnetic order is favored between two half-filled or two empty orbitals of magnetic ions with 180° arrangement. (c) show the second GKA: ferromagnetic order is favored between one half-filled orbital and one empty orbital of magnetic ions with 180° arrangement. (d) show the third GKA rule: ferromagnetic order is favored between two half-filled orbitals of magnetic ions with 90° arrangement. Inspired from [29]

Consider a transition metal oxide like CoO, an exchange interaction between two 3d-metal ions ( $\text{Co}^{+2}$ ) mediated via an oxygen 2p-orbital ( $\text{O}^{-2}$ ) is known as indirect **superexchange interaction** which is longer ranged than the direct exchange interaction. Superexchange interaction depends strongly on the occupation of the metal orbitals as well as on the angle between the metal ions and the mediating oxygen atom. The sign of the superexchange interaction can be determined via **Goodenough-Kanamori-Anderson rules (GKA)**. Figure 2.1 shows the Goodenough-Kanamori-Anderson rules. For the two  $\text{Co}^{+2}$  metals and the  $\text{O}^{-2}$  atom lying on one line ( $180^\circ$ ), one obtain antiferromagnetic order between two half-filled orbitals or two empty orbitals as shown in figure 2.1 (a) and (b) because only antiparallel spin alignment allows electrons to hop between the p-orbital in the non magnetic ion  $\text{O}^{-2}$  and the d-orbitals in the both  $\text{Co}^{+2}$  magnetic ions, thus reducing the kinetic energy. With parallel arrangements, electrons are only allowed to hop between the non magnetic ion  $\text{O}^{-2}$  and one  $\text{Co}^{+2}$  magnetic ion, due to Pauli principle which states that two electrons with the same quantum state can't occupy the same orbital. This kind of interaction is known as the first **GKA** rule. The second **GKA** rules explain the case for superexchange interaction between one half-filled orbital and one empty orbital where the spins prefer to align parallel in neighboring magnetic ions (figure 2.1 (c)) because according to the first Hund's rule the total spin angular momentum is maximized. The third **GKA** explain the  $90^\circ$  superexchange (figure 2.1(d)) for two half-filled metal orbitals, ferromagnetic order is more favored in this case, because of the reduction of the Coulomb repulsion of parallel spin orientations of electrons within atoms, which leads to Hund's first rule.

For superexchange interaction, both magnetic ions have the same valence, only virtual charge transfer is involved in this case. If the magnetic ions are in mixed-valence state then during the exchange interaction, real charge transfer may take place. This kind of exchange interaction known as **double exchange interaction** which is depicted schematically in figure 2.2. Consider MnO oxide, where Mn ion exist in oxidation state 3 or 4 ( $\text{Mn}^{+3}$  or  $\text{Mn}^{+4}$ ), double interaction takes place when an electron from  $\text{Mn}^{+3}$  ion hops into the oxygen 2p orbital, while simultaneously an oxygen 2p orbital hops on the  $\text{Mn}^{+4}$  site. The hopping of an electron between  $\text{Mn}^{+3}$  and  $\text{Mn}^{+4}$  is possible if the spins of the electrons of the two neighboring metal ions are parallel. Therefore, double exchange interaction between  $\text{Mn}^{+3}$  and  $\text{Mn}^{+4}$  ions is ferromagnetic, because ferromagnetic lowers the energy of the system.

In certain metals, the exchange interaction between magnetic ions can be mediated by the conduction electrons. These electrons are polarized by a localized magnetic moment and then coupled to another localized magnetic moment. This kind of indirect exchange interaction known as **Ruderman, Kittel, Kasuya and Yosida (RKKY) interaction**. The coupling depends on the distance between the localized magnetic moments and it is given by:

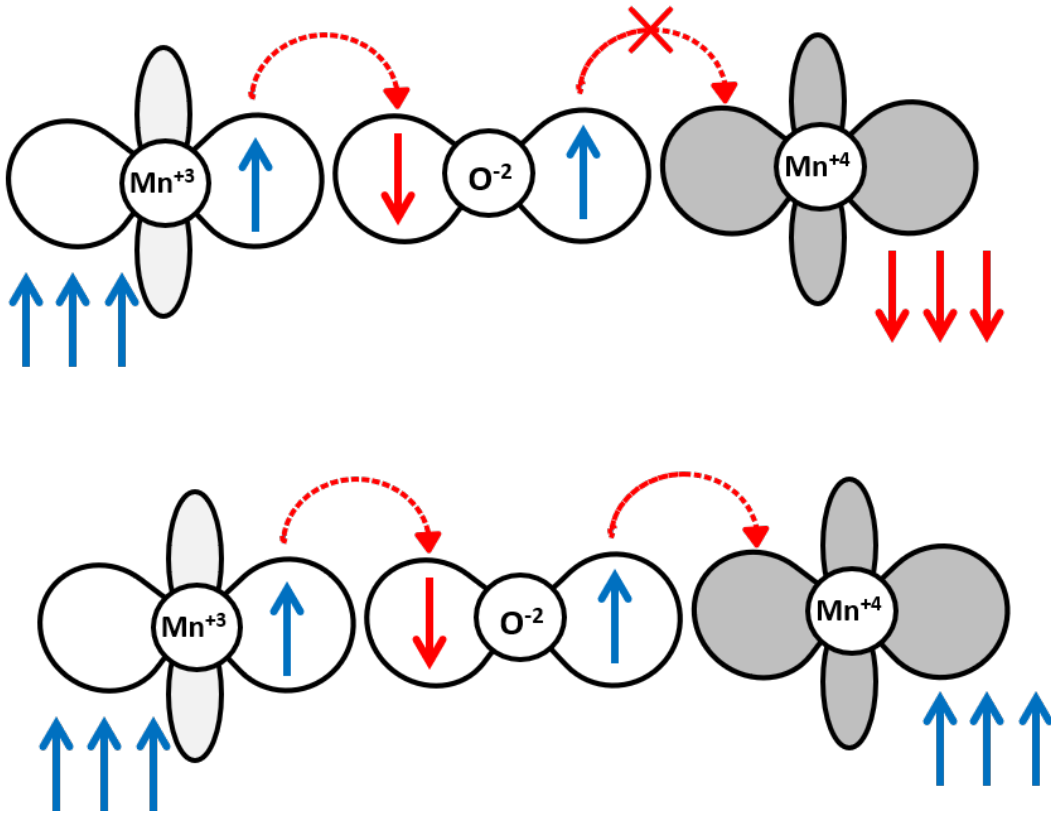


Figure 2.2.: Double exchange interaction between  $\text{Mn}^{+3}$  and  $\text{Mn}^{+4}$  mediated by an  $\text{O}^{-2}$  ion. Inspired from [29].

$$J_{RKKY}(r) \propto \frac{\cos 2k_F r}{r^3} \quad (2.31)$$

Where  $r$  is the distance and  $k_F$  is the radius of the Fermi surface. RKKY interaction is a long range interaction and oscillatory in nature with the oscillation wavelength of  $\frac{\pi}{k_F}$ . The interaction can be ferromagnetic, antiferromagnetic depending on the distance.

### 2.1.3. Magnetic order

Depending on the interactions between the magnetic moments in a solid, it can show long-range magnetic order. The ordering can lead to ferromagnetism order in which all the magnetic moments align parallel to each other and antiferromagnetism in which all the magnetic moments align antiparallel to each other. In this section, we will consider different types of the magnetic ground state

(figure 2.3) which can be produced due to the interactions explained in Sec. 2.1.2.

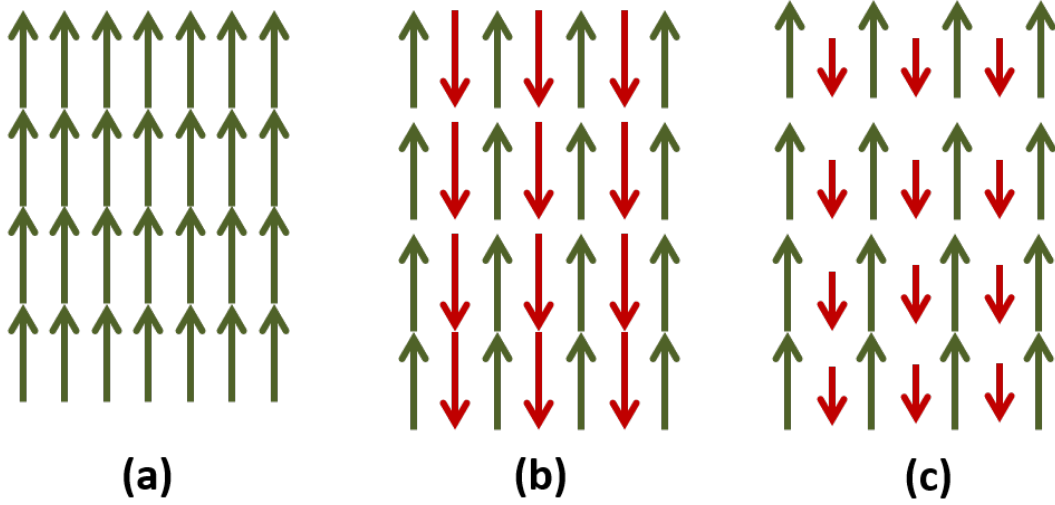


Figure 2.3.: Magnetic spin arrangements of (a) a ferromagnetism, (b) an antiferromagnetism and (c) a ferrimagnet.

### 2.1.3.1. Ferromagnetism (FM)

In a ferromagnet, the magnetic moments are aligned parallel to each other as shown in figure 2.3(a). It has a spontaneous magnetization even in the absence of applied field, which arises due to the exchange interaction which was described in more detail in Sec. 2.1.2.2. FM order is usually found in systems with itinerant electrons. The appropriate Hamiltonian for a ferromagnet in an applied field  $\vec{B}$  given as:

$$\hat{H} = - \sum_{ij} J_{ij} \vec{S}_i \cdot \vec{S}_j + g\mu_B \sum_j \vec{S}_j \cdot \vec{B} \quad (2.32)$$

The first term on the right side is known as the Heisenberg exchange energy where  $J_{ij}$  is the exchange constant which is positive for FM. The second term on the right side known as the Zeeman energy term in the presence of a field. The origin of FM was explained by the Weiss model. He assumed that each magnetic moment experiences a mean-field or molecular field given by:

$$\vec{B}_{mf} = \lambda \vec{M} \quad (2.33)$$

Where  $\lambda$  is a constant known as Weiss coefficient which parametrizes the strength of the molecular field as a function of the magnetization and  $\vec{M}$  is the magnetization. Now, we can treat the problem as a paramagnet placed in a magnetic field  $\vec{B} + \vec{B}_{mf}$ . At low temperatures, the magnetic moments are aligned by the internal mean-field even without the external magnetic field. While, at higher temperatures, thermal fluctuations begin to destroy the aligned magnetic moments and finally at the critical temperature  $T_C$ , the order becomes destroyed. The magnetic susceptibility for FM is given by:

$$\chi \propto \frac{1}{T - T_C} \quad (2.34)$$

Where  $T_C$  is the Curie temperature.

Equation 2.34 known as Curie-Weiss law explains the inverse relation between the magnetic susceptibility and the temperature as shown in figure 2.4.

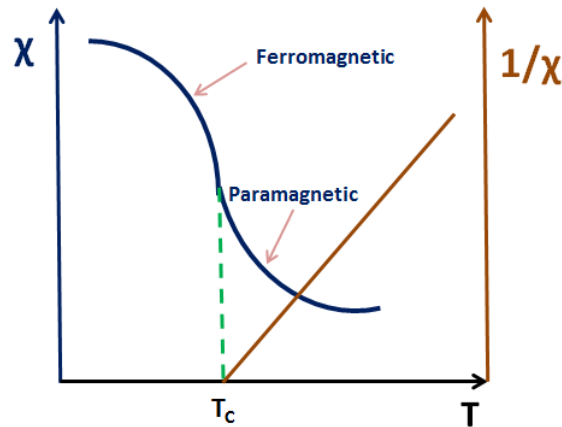


Figure 2.4.: Magnetic susceptibility vs. temperature for ferromagnetic system.

### 2.1.3.2. Antiferromagnetism (AF)

For simple cases, the system called antiferromagnetism if the nearest neighbor magnetic moments aligned antiparallel to each other (figure 2.3 (b)). The exchange interaction is negative  $J < 0$ . Very often, it is considered as two interpenetrating sublattices (green and red), where the magnetic moments in one sublattice points up (+) (green lattice) and on the other sublattice points down (-) (red lattice) (see figure 2.5). Similar to a ferromagnet, the Weiss model is used to find the solution for Curie temperature. Consider the assumption that

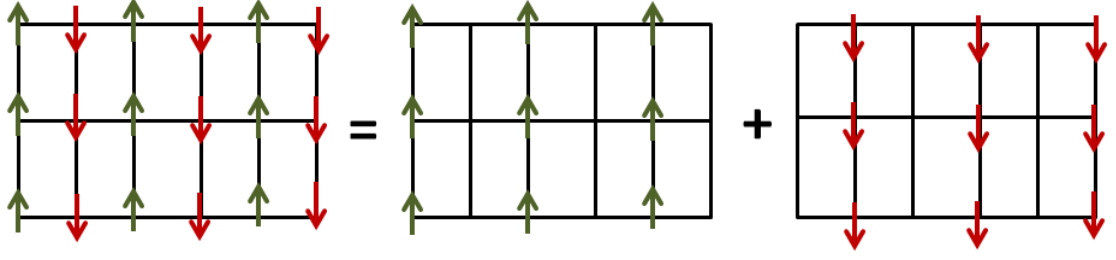


Figure 2.5.: Antiferromagnetic moments configurations can be decomposed into two interpenetrating sublattices.

the molecular field experienced by one sublattice is proportional to the magnetization of the other sublattice. The molecular fields of the two sublattices can be written as:

$$B_+ = -|\lambda|M_- \quad (2.35)$$

$$B_- = -|\lambda|M_+ \quad (2.36)$$

Then the magnetization of each sublattice can be written as:

$$M_{\pm} = M_s B_j \left( \frac{gJ\mu_B J |\lambda| M_{\mp}}{K_B T} \right) \quad (2.37)$$

Where  $B_j$  is the Brillouin function

The two sublattices are equivalent in magnitude and have different direction. So,

$$|M_+| = |M_-| = |M| \quad (2.38)$$

The molecular field on each sublattice is similar to the one for FM. It disappears above a transition temperature known as *Neel* temperature  $T_N$ . The antiferromagnetic susceptibility can be written as:

$$\chi \propto \frac{1}{T + T_N} \quad (2.39)$$

It is important to know the direction of the applied field with respect to the direction of the sublattice magnetization when the magnetic field applied below  $T_N$ . At 0 K, if the field applied parallel to the magnetization then the susceptibility is zero ( $\chi_{\parallel}$ ), while if the field applied perpendicular to the magnetization direction then the susceptibility is non zero ( $\chi_{\perp}$ ). Figure 2.6 shows the variation of  $\chi_{\parallel}$  and  $\chi_{\perp}$  with temperature.

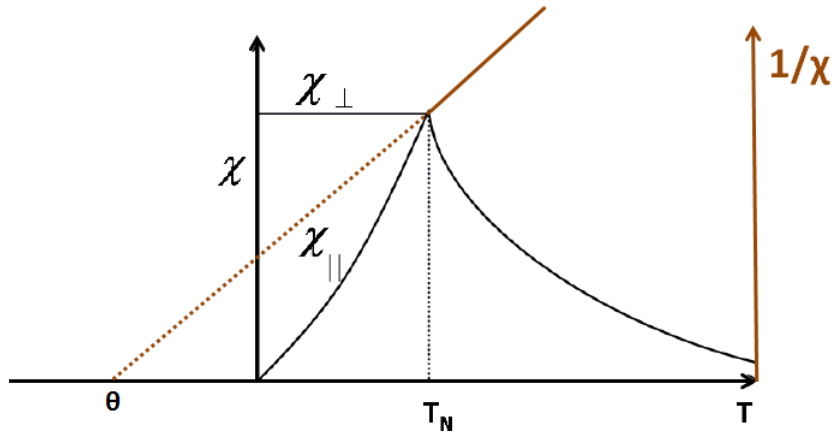


Figure 2.6.: Magnetic susceptibility vs. temperature for antiferromagnetic material.

A spin-flop transition is observed when a strong field is applied parallel to the magnetization direction, where the sublattice with the opposite moment becomes parallel to the applied field. In this case, the Zeeman energy dominates and can overcome the exchange interaction.

### 2.1.3.3. Ferrimagnetism (FiM)

The system called Ferrimagnetism if the two sublattices described in the antiferromagnet case have different magnitude,  $|M_+| \neq |M_-|$ , then they don't cancel out and a net magnetization is expected. (see figure 2.3 (c)). Ferrimagnetism depends on the crystal structure of the material and its magnetic susceptibility does not follow the Curie Weiss law.

### 2.1.4. Magnetic anisotropy

In some materials, it is easier to be magnetized in one direction than the others. This preferred direction of the spontaneous magnetization known as *easy axes* determined by internal energy known as magnetic anisotropy. In the material, one can observe two different directions known as *easy axes* with the lowest energy cost and *hard axes* with the maximum energy cost. The materials have the lowest energy when the magnetization aligns along the easy axes, and a

smaller field is required to align the magnetization along the easy axes during a reversal process. The magnetic anisotropy comes firstly from spin-orbit coupling which is responsible for magnetocrystalline anisotropy, surface anisotropy and magnetostriction and secondly from long-range dipolar interaction between the moments which originates from the shape of the system [28]. Magnetocrystalline and magnetostatic anisotropy should be taken into consideration for determining the anisotropy in bulk materials, while shape, strain and surface anisotropy needs to be considered in nanostructured materials [30]. Depending on the orientation directions of the magnetic moment, the magnetic anisotropy energy can be written as:

$$E_a = KV \sin^2 \theta \quad (2.40)$$

Where  $\theta$  is the angle between the easy axis and the magnetization. Magnetic anisotropy originate from various sources as explained in the following.

### Shape anisotropy

The shape anisotropy is related to the shape of the material as the name expresses and it is not an intrinsic property of the material. Due to the demagnetization energy, the shape of the material can create an additional anisotropy known as shape anisotropy. The demagnetization energy or demagnetization field originates from the charges or poles at the surface which produced by a magnetized body will act in opposition to the magnetization that produces it. The demagnetization energy  $E_d$  can be written as:

$$E_d = -\frac{\mu_0}{2} \int \vec{M} \cdot \vec{H}_{dm} dV \quad (2.41)$$

Where  $\vec{M}$  is the magnetization and  $\vec{H}_{dm}$  is the demagnetization field induced by the magnetic moment inside the material given as  $\vec{H}_{dm} = -\vec{N} \cdot \vec{M}$  with  $N$  is the demagnetization tensor which may vary along different directions due to the shape anisotropy. For example, a spherical body has zero shape anisotropy, because the demagnetization field is isotropic in all direction, and the demagnetization factor  $N_x=N_y= N_z=\frac{1}{3}$ . While, in the case of an ellipse body, the demagnetization energy is smaller if the magnetization lies along the major axes than along the minor axes, which gives easy axes of magnetization along the major axes. The shape anisotropy energy of the ellipsoidal body given as [31]:

$$E_{shape} = \frac{1}{2} \mu_0 V (N_x M_x^2 + N_y M_y^2 + N_z M_z^2) \quad (2.42)$$

Where  $M_x, M_y, M_z$  and  $N_x, N_y, N_z$  are the components of the magnetization and the demagnetization factors along X, Y, Z directions. The demagnetization factor always satisfies:

$$N_x + N_y + N_z = 1 \quad (2.43)$$

The energy barrier between two minima caused by the shape anisotropy can be calculated by the difference between the easy and hard axes [32]:

$$\Delta E = -\frac{1}{2}\mu_0 V M^2 (N_{easy} - N_{hard}) \quad (2.44)$$

Magnetic moments prefer to lie along the easy axes if the anisotropy energy cannot be overcome.

### Magnetocrystalline anisotropy

It is an intrinsic property of the material. For different orbitals, energy splits into various levels due to the electrostatic interaction between the electron orbitals and its environment, known as the *crystal field effect*. Due to the crystalline symmetry of the lattice, the wavefunctions of the neighboring orbitals exhibit different overlap energies for different orbital orientations which, together with the spin-orbit interaction, is the cause of the magnetocrystalline anisotropy. The direction of the spontaneous magnetization inside a solid is influenced by the crystalline symmetry. Due to the spin-orbit interaction or quenching of the orbital angular momentum, some crystallographic directions of the magnetization are preferred than the others.

For a hexagonal lattice, the easy axes are along the c-axes of the unit cell, which known as uniaxial anisotropy. The energy associated with it given as:

$$E_{uni} = K_1 V \sin^2 \theta + K_2 V \sin^4 \theta + \dots \quad (2.45)$$

Where,  $K_1, K_2$ , etc. are the anisotropy constant,  $V$  is the volume and  $\theta$  is the angle between the c-axes (easy axes) and the magnetization direction. The anisotropy constant have a strong temperature dependence, it is considered as a constant below  $T_c$ . In most cases,  $K_1$  is much larger than the other higher-order terms which can then be neglected. Therefore, the magnetocrystalline anisotropy energy can be written as:

$$E_{uni} = KV \sin^2 \theta \quad (2.46)$$

For a cubic system, the cubic anisotropy is given as:

$$E_{cubic} = K_1 \left( \frac{1}{4} \sin^2 \theta \sin^2 2\phi + \cos^2 \theta \right) \sin^2 \theta + \frac{K^2}{16} \sin^2 2\phi \sin^2 2\theta \sin^2 \theta + \dots \quad (2.47)$$

Where  $\theta$  and  $\phi$  are the polar and the azimuthal angles between the preferred direction and the magnetization.

### Surface anisotropy

Besides these two anisotropy types discussed above, a surface anisotropy originates from atoms at surfaces which are not saturated. Surface anisotropy plays an important role over magnetocrystalline anisotropy and magnetostatic energies, especially in reduced dimensional systems. The effective surface anisotropy for small spherical particles is given as:

$$K_{eff} = K_V + \frac{S}{V} K_S = K_V + \frac{6}{d} K_S \quad (2.48)$$

Where  $\frac{S}{V}$  is the surface to volume ratio with  $S = \pi d^2$  and  $V = \frac{\pi d^3}{6}$ ,  $d$  is the diameter of the particle.  $K_V$  is the volume anisotropy consisting of the magnetocrystalline, magnetostriction and shape anisotropy terms.  $K_S$  is the surface anisotropies.

#### 2.1.5. Exchange Bias (EB)

Exchange bias is a new type of magnetic anisotropy known as exchange anisotropy was first discovered in the study of ferromagnetic cobalt with antiferromagnetic cobalt oxide shell by Meiklejohn and Bean [25]. Exchange anisotropy or unidirectional anisotropy is observed in torque measurement after the sample (bilayer system) cooled below the Ne'el temperature of the antiferromagnetic cobalt oxide within a magnetic field, starting at temperature  $T$  ( $T_N < T < T_C$ , where  $T_C$  is the ferromagnetic Curie temperature). The measured hysteresis loop observed at  $T \ll T_N$  appears to be shifted as if there's another magnetic field that was present in addition to the applied magnetic field due to the exchange coupling between the ferromagnetic and antiferromagnetic materials at the interface[33]. Figure 2.7 explains the typical model to understand the EB phenomena. Consider that the Ne'el temperature of the antiferromagnetic material is smaller than the Curie temperature for the ferromagnetic material. Usually, an external field is applied to fix the direction of the ferromagnetic material during cooling the system, at  $T > T_N$ , the magnetic moments in the ferromagnetic layer are aligned along the applied magnetic field, while it is randomly ordered

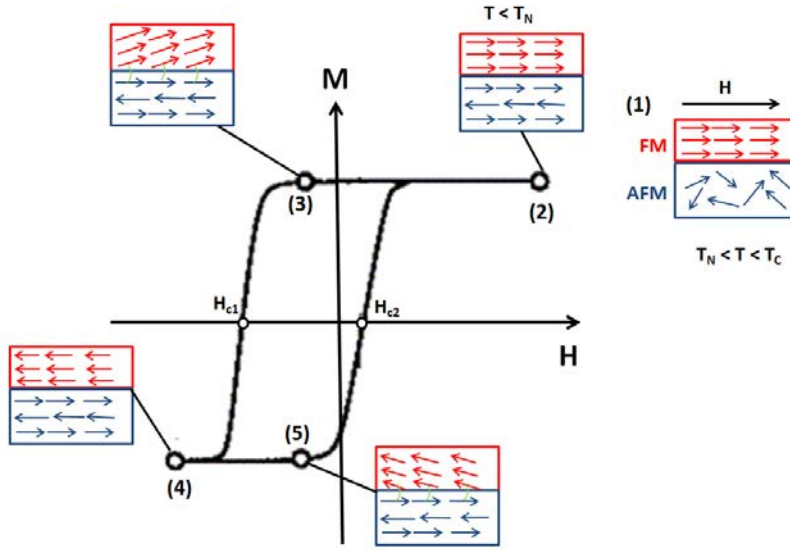


Figure 2.7.: Phenomenological picture of exchange bias for an AF-FM bilayer and illustration of the spin order during the hysteresis measurement. Inspired from [34]

in the antiferromagnetic layer (1). After the system cooled below Ne'el temperature the antiferromagnetic moment at the interface chooses the state that minimizes the energy due to the coupling to the interfacial magnetic moments of the ferromagnetic via exchange interaction. They align parallel or antiparallel to each other depending on the exchange constant  $J_{AF-FM}$  (2). The ferromagnetic moments start to rotate when the magnetic field starts to decrease. Therefore, the coupling between the interfacial the ferromagnetic moment and the antiferromagnetic moments stabilize the parallel order of the ferromagnetic interfacial moments to the direction of the cooling field. When the external field reverses the ferromagnet moments, the antiferromagnetic moments do not switch if the assumption of sufficiently high anisotropy is fulfilled (3-4). The antiferromagnetic moments at the interface try to keep the ferromagnetic moments in their original direction. Consequently, the magnetic field  $H_{c1}$  needed to reverse the ferromagnet moments is larger than the coercive field  $H_c$  for single ferromagnetic layers. Further decrease of the magnetic field (i.e. increase in the negative direction), at this point all ferromagnetic moments align in the opposite direction. The antiferromagnetic order remains the same even when the magnetic field switches all ferromagnetic moments due to the large anisotropy of the antiferromagnetic. For increasing the magnetic filed the interfacial ferromagnetic and antiferromagnetic moments are satisfied to align antiparallel to each other for  $J_{AF-FM} < 0$  or parallel to each other for  $J_{AF-FM} > 0$  again due to the exchange interaction (5-2). Therefore, the magnetic field  $H_{c2}$  needed to

reverse the ferromagnetic moments back along the positive direction is smaller than the coercive field  $H_c$ . So, the center of the hysteresis is shifted towards the negative direction (i.e. exchange bias). The EB field can be calculated as  $H_{ex} = \frac{1}{2}(H_{c1} + H_{c2})$ .

Practically, due to the thermal fluctuation, interface roughness, etc, the magnetic moments in the ferromagnetic layer may not align perfectly as shown in figure 2.7. Also, if the antiferromagnetic layer has a small anisotropy, the antiferromagnetic moment may switch when the interfacial ferromagnetic moments are aligned. Therefore, an increase of  $H_{c2}$  is expected as well as an increase in the coercive field.

EB has attracted much interests in thin-film systems due to their applications in industrial devices as well as on control the thickness of the antiferromagnetic and ferromagnetic layer and the roughness at the ferromagnetic-antiferromagnetic interface and in nanostructured systems because of its possibility to overcome the superparamagnetic limit due to the finite size effect, so it makes the application of nanoparticle in high-density data storage suitable [35].

### 2.1.6. Superparamagnetism

Superparamagnetism explains a form of magnetism, which appears in small ferromagnetic or ferrimagnetic nanoparticles. It occurs in nanoparticles composed of a single magnetic domain.

Formation of domain walls in ferromagnetic materials is controlled by the competition between the energy cost for domain wall formation and the energy gain from the magnetostatic energy which is known as demagnetizing energy density  $E_D$  and is given by:

$$E_D = -\frac{1}{2}\mu_0 N M_s^2 \quad (2.49)$$

Where  $\mu_0$  is the vacuum permeability,  $N$  is the shape dependent demagnetization tensor and  $M_s$  is the saturation magnetization. The domain wall energy becomes more important compared with the demagnetization energy with decreasing grain size. Below a certain critical diameter, the ferromagnetic nanoparticles become single magnetic domain and behave as a permanent magnet. This critical diameter is given as:

$$d_c \approx 18 \frac{\sqrt{AK_{eff}}}{\mu_0 M_s^2} \quad (2.50)$$

Where  $A$  is the exchange constant, proportional to  $J$ ,  $K_{eff}$  is the effective magnetic anisotropy constant, and  $M_s$  the saturation magnetization.

The magnetization in a single magnetic domain nanoparticle is preferably oriented along an easy axis, and an energy barrier  $\Delta E = KV$  (where  $K$  is the anisotropy constant and  $V$  is the volume) has to overcome for the magnetization reversal.

If the nanoparticles are separated enough to prevent any interparticle interactions, the directions of the superspins in the absence of a magnetic field are only a result of the competition between thermal fluctuation and anisotropy. For large particles, the energy barrier  $\Delta E$  is large, and can't be overcome by the thermal energy, so the superspins stay along their easy axis below the critical temperature of the material. While for very small particles, where the energy barrier  $\Delta E = KV$  decreases below the thermal energy  $k_B T \gtrsim KV$ , the nanoparticle superspin can thermally fluctuate with time in analogy to the spins in a paramagnetic even below its critical temperature. This magnetic state is called *superparamagnetism* (SPM) [36, 37]. The curve of a superparamagnetic system follows the classical Langevin behavior

$$M(H, T) = \mu M \left[ \coth \left( \frac{\mu H}{k_B T} \right) - \frac{k_B T}{\mu H} \right] = N \mu L \left( \frac{\mu H}{k_B T} \right) \quad (2.51)$$

Where  $N$  is the number of particles,  $\mu$  is the integral particle moment, and  $L(x)$  the Langevin function.

The magnetic moment has usually only two stable orientations antiparallel to each other due to the nanoparticles anisotropy, separated by an energy barrier  $\Delta E$ . These orientations define the nanoparticle's easy axis. At finite temperature, the magnetization starts to flip and reverse its direction. The mean time between two flips of superspins is called as *Neel-Brown* relaxation time  $\tau$ , and is given by *Neel-Arrhenius* equation [28, 38, 39]:

$$\tau_N = \tau_0 \exp \left( \frac{KV}{k_B T} \right) \quad (2.52)$$

Where  $\tau_N$  is the average time of the randomly flip of the magnetization of the nanoparticles as a result of the thermal fluctuations,  $\tau_0$  is a pre-factor, characteristic of the material called the attempt time which is usually  $\sim 10^{-9}$  second [38, 40].

The magnetization of a single superparamagnetic nanoparticle goes to zero if the average measurement time  $t \gg \tau_N$  because the nanoparticle magnetization will flip several time during the measurement (superparamagnetic state), while for  $t \ll \tau_N$ , the measured magnetization will be similar to the instantaneous magnetization was at the beginning of the measurement (blocked state). The transition

between superparamagnetic and blocked state occurs at  $t = \tau_N$ . The transition between these two states is temperature-dependent as given in equation 2.53 [28, 38] because the measurement time is kept constant and the temperature is varied.

$$t = \tau(T_B) = \tau_0 \exp\left(\frac{KV}{k_B T_B}\right) \rightarrow T_B = \frac{KV}{k_B \ln\left(\frac{t}{\tau_0}\right)} \quad (2.53)$$

When the temperature decrease (decreasing in the thermal energy), the  $\tau_N$  increases.  $\tau_N$  becomes comparable to  $t$  below a characteristic temperature known as blocking temperature ( $T_B$ ). In this case, the superspins are blocked in one of the energy minima during the measurement. The blocked state can only be observed when  $\tau_N \geq t$ .  $T_B$  depends on the measurement time  $t$ . For  $T > T_B$ , the superspins can easily be flipped by thermal fluctuations, while for  $T < T_B$ , the superspins are in the blocked state.

The blocking temperature depends on measurement time and it is not an intrinsic temperature like the Curie temperature. To study the magnetization in superparamagnetic particles, different measurements were carried out. In a magnetization versus field measurement at a fixed temperature (hysteresis), if the hysteresis cycle  $\tau_{M-H} \gg$  relaxation time  $\tau(T)$ , then a closed S-shape is observed similar to a paramagnet with a high magnetic moment. While if  $\tau_{M-H} \ll$  relaxation time  $\tau(T)$ , then an open loop is observed similar to a ferromagnetic system. Another unique measurement is the magnetization versus temperature at a fixed field known as zero field cooling (ZFC) and field cooling (FC). In ZFC, the sample is cooled from a high temperature usually from above the blocking temperature to a very low temperature in zero field, then a small field is applied and the magnetization is recorded. In FC measurement, the sample is cooled in a field and the magnetization is recorded. The ZFC and FC curves split at a temperature  $T_s$ . The ZFC shows a maximum at the blocking temperature ( $T_B$ ). If the volume of all the particles is the same, which means there's no distribution in the energy barriers, then  $T_s = T_B$  but for polydisperse system  $T_s > T_B$ .

In most practical cases an ensemble of particles is taken without any interparticle interactions which are known as a superparamagnetic ensemble. Above  $T_B$  one can observe a zero net magnetization because the superspins fluctuate like in a paramagnet. After cooling the ensemble below  $T_B$  in a zero field, the superspins are blocked and the magnetization still zero. When a small field applied then it can lead to align few of the blocked superspins along the field direction and a small magnetization is recorded. By increasing the temperature, more and more superspins start to align along the applied field direction. Therefore, the magnetization increase with increasing temperature. The highest value of the magnetization observed at  $T = T_B$ , where all the superspins go to

unblocked state. Above  $T_B$ , thermal fluctuation dominates, the magnetization decrease following  $\frac{1}{T}$  and the system becomes in a reversible state. In FC, applying a field then cooling down, the magnetization follows the same behaviour as for the ZFC case. But below  $T_B$ , the system goes into an irreversible state, the superspins are blocked in a way that the net magnetization is higher than the ZFC net magnetization. In this case, the superspins are blocked along the applied field direction, as the temperature decrease, the magnetization increase. But usually in many systems, the interparticle interactions cannot be neglected. For example in nanoparticles, dipolar interaction is the most dominant interaction. Therefore, the energy of  $i^{th}$  particle can be written as:

$$E_i = -K_i V_i (\hat{K}_i \cdot \hat{m}_i)^2 - \mu_0 M_s V_i \vec{H} \cdot \hat{m}_i + \frac{\mu_0 M_s^2}{4\pi} \sum_j V_i V_j \frac{\hat{m}_i \cdot \hat{m}_j - 3(\hat{m}_i \cdot \hat{r}_{ij})(\hat{m}_j \cdot \hat{r}_{ij})}{r_{ij}^3} \quad (2.54)$$

Depending on the strength of the interactions, different magnetic states can be observed for an ensemble of nanoparticles which are characterized by the relaxation time of nanoparticle ensembles [38].

- (i) Superparamagnetism (SPM):  $\tau = \tau_0 \exp\left(\frac{KV}{k_B T}\right)$
- (ii) Modified superparamagnetism:  $\tau = \tau_0 \exp\left(\frac{\Delta E^*}{k_B T}\right)$
- (iii) Glass like freezing:  $\tau = \tau_0 \exp\left(\frac{\Delta E^*}{k_B (T - T_0)}\right)$
- (iv) superspin glass (SSG):  $\tau = \tau_0^* \left(\frac{T - T_g}{T_g}\right)^{-zv}$
- (v) Superferromagnetism (SFM):  $\tau = \tau_0^* \left(\frac{T - T_c}{T_c}\right)^{-zv}$

For the non-interacting nanoparticles,  $\tau$  is described by equation 2.52. When the nanoparticles start to interact with each other, a modified energy barrier introduced as in case (ii). The first and the second model have similar behavior except the energy barrier is different. As the interaction strength increase, they start to behave glass-like as in case (iii), where  $T_0$  is the glass temperature. This case is known as Vogel-Fulcher law. For strong interactions, SSG behavior is obtained,  $\tau$  can be explained by the case (iv), where  $T_g$  is the critical temperature and  $v$  is the critical exponent of the correlation length  $\xi$  given as:

$$\xi \propto \left(\frac{T - T_g}{T_g}\right)^{-v} \quad (2.55)$$

$$\tau \propto \xi^z \tag{2.56}$$

If the nanoparticle interacts strongly with each other, then a ferromagnetic like ordering can be observed, which is known as Superferromagnet, then  $\tau$  can be described as the case (v) with  $T_c$  is the Curie temperature.

Experimentally, the different states can be distinguished by measuring AC-susceptibility and fitting the data by one of these models to describe their magnetic behavior.

## 2.2. Self-assembly

Self-assembly works as a tool for assembling the components of a system into a larger, functional unit and it is a manifestation of a spontaneous arrangement of the disordered components into an ordered form by controlling the interactions between the components and the environment. Self-assembly is a widespread phenomena in nature on all different length scales, such as the formation of galaxies, weather system and atoms arranging in crystal structure [24, 41]

Self-assembly of individual building blocks (atoms, molecules, nanoparticles) into nano dimensional unit has shown novel properties, which is very different than its bulk form.

Assembling of these building blocks, particularly NPs into two- and three dimensional ordered form, play a major role in different applications such as magnetic data storage media[12], bandgap engineering [42] and electronic devices [43, 44]. Furthermore, it leads to fabricate materials with novel properties. The spontaneous arrangements of the NPs into ordered form arises due to the interaction between their superspins via different inter-particle interactions and thus show a collective effect. Furthermore, the interaction forces are also fundamental and important for understanding the existence of nanoparticles in solutions without agglomeration.

Understanding self-assembly of NPs requires a comprehensive knowledge of different interactions that drive this process. NPs may self-assemble into different lattice structures depending on the interactions between the particles at the nanoscale (1 - 100 nm).

This section will focus on the inter-particle interactions leading to the formation of ordered structure from solution and the strength of the interaction.

### 2.2.1. Van der Waals force

Van der Waals (vdW) force is the most widespread force existing at the nanoscale. It is a term explaining the electromagnetic fluctuations arising due to the random motion of negative and positive charges present in an atom, molecule, or

bulk. It is the weakest of the chemical forces which contribute to the intermolecular interaction. It acts only over a very short range. It can be attractive or repulsion depending on the distance between the molecules. Usually, it is an attractive force in the NP solution, which tries to aggregate particles in the solution. But a proper ligand surrounding the particles can be used to harness this interaction in guiding two- and three-dimensional self-assembly of NPs. The vdW interaction can be quantified by various theoretical approaches: Hamaker integral approximation which neglects the many-body effects between the atoms, Dzyaloshinskii Lifshitz Pitaevskii (DLP) which is derived from continuum approach and Coupled-dipole method (CDM) which take a discrete pairwise summation plus the many-body effects [45].

### 2.2.2. Magnetic interactions

Some magnetic materials, like diamagnetic or paramagnetic, in the absence of a magnetic field, their magnetic moments behave independently and weak magnetic interactions exist between their magnetic moments. However, there are several magnetic materials which show a spontaneous magnetic order even in the absence of a magnetic field due to the magnetic interactions between their magnetic moments, such as ferromagnetic, antiferromagnetic and ferrimagnetic materials. Basically, in magnetic nanoparticles, the magnetic moments lie along the preferred direction "easy axis" with a huge value known as "superspin". Below a certain temperature, The superspin undergoes thermal fluctuation according to *Neel*-Brown model (*Neel*-Arrhenius model) where the mean fluctuation time is given in equation 2.52.

Each nanoparticle behaves like a single magnetic dipole with a magnetic moment:

$$m = VM \quad (2.57)$$

Where  $V$  is the volume of the NP and  $M$  is the saturation magnetization. The field generated by each dipole at point  $\vec{r}$  is given by:

$$\vec{H}(\vec{r}) = \frac{1}{4\pi\mu_0} \frac{3(\vec{m} \cdot \hat{r}) - \vec{m}}{r^3} \quad (2.58)$$

Where  $\hat{r}$  is the unit vector in the direction of  $\vec{r}$ .

The magnetic energy and the corresponding force is given by:

$$U_m = -\vec{m} \cdot \vec{H} \quad (2.59)$$

$$\vec{F} = -\vec{\nabla}U_m \quad (2.60)$$

The **dipole-dipole interaction** is given by:

$$E_{dd} = \frac{\vec{m}_1 \cdot \vec{m}_2 - 3(\vec{m}_1 \cdot \hat{r})(\vec{m}_2 \cdot \hat{r})}{4\pi\mu_0 r^3} \quad (2.61)$$

From equation 2.61, the magnetic dipolar interactions depend on the separation between the two dipoles and the orientation of the nanoparticle spin. Magnetic dipolar interaction is a long range interaction compared with vdW interaction as mentioned in Sec. 2.2.1. The magnetic dipolar interaction becomes attractive in nature for in-line dipoles where  $\vec{m}_1 \cdot \vec{m}_2 = m^2$  and  $\vec{m}_1 \cdot \hat{r} = \vec{m}_2 \cdot \hat{r} = m$ , so  $E_{dd} = \frac{-m^2}{2\pi\mu_0 r^3}$ . Also, it is attractive when the two dipoles are oriented antiparallel to each other where  $\vec{m}_1 \cdot \vec{m}_2 = -m^2$ ,  $\vec{m}_1 \cdot \hat{r} = \vec{m}_2 \cdot \hat{r} = 0$  so,  $E_{dd} = \frac{-m^2}{4\pi\mu_0 r^3}$ . While, magnetic dipolar interaction becomes repulsive, if the two dipoles are oriented parallel to each other, where  $\vec{m}_1 \cdot \vec{m}_2 = m^2$  and  $\vec{m}_1 \cdot \hat{r} = \vec{m}_2 \cdot \hat{r} = 0$  so,  $E_{dd} = \frac{m^2}{4\pi\mu_0 r^3}$ . The dipolar arrangements depends on the external magnetic field as shown in figure 2.8.

For most magnetic materials, the dipolar interaction does not play an important role in the magnetic ordering for atomic spins  $m = 1\mu_B$  which corresponds to a dipolar energy  $E_{dd} \approx 10^{-23}$  J or an ordering temperature  $T \approx 1$  K, while it plays a role in the assembly of the nanoparticles, where  $m = 10^3 - 10^5 \mu_B$ , which corresponds to an ordering temperature  $T \approx 10 - 10^3$  K [30]. But this interaction holds good for static dipoles (i.e. when the superspins are in a "blocked" state). But for superparamagnetic (SPM) nanoparticles, the magnetic moment or superspins fluctuate over time. This fluctuation leads to weak dipolar interaction given as [46, 47]:

$$E_{ddfluc} = \frac{-1}{3k_B T} \left( \frac{m_1 m_2}{4\pi\mu_0 r^3} \right)^2 \quad (2.62)$$

Where  $m_1$  and  $m_2$  are the two fluctuating dipoles separated by a distance  $r$ ,  $K_B$  is the Boltzmann constant,  $T$  is the temperature and  $\mu_0$  is the vacuum permeability. From equation 2.62, the dipolar interaction due to the fluctuations is proportional to  $\approx \frac{1}{r^6}$  which is much weaker than the static dipolar interaction, equation 2.1.2 ( $\approx \frac{1}{r^3}$ ). The dipolar interaction becomes weaker when the average distance between the nanoparticles very large, while it becomes stronger for smaller distances between the nanoparticles. For the complex and anisotropic shape of the nanoparticles, higher-order terms or multipole interaction have to

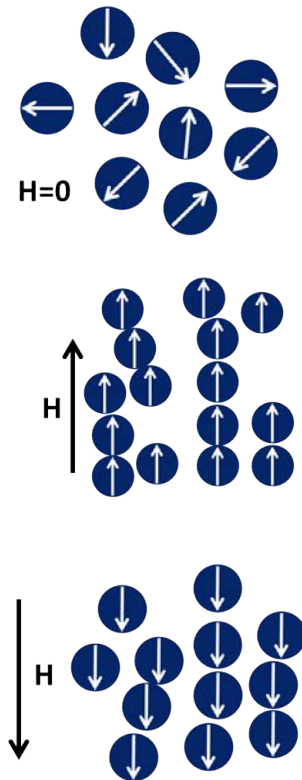


Figure 2.8.: Effect of the external magnetic field on the arrangements of the dipoles.

be added to the total interaction.

The nanoparticles can self-assemble in different structures such as chains or rings due to the magnetic dipolar interaction which provides a directional orientation. For the larger diameter of nanoparticles, the dipolar interaction is stronger and leads to the formation of connected networks over a certain area. The nanoparticles tend to self-assembled in superlattices at high dipolar interaction (at the high magnetic field). For nanoparticles with high volume fraction, it tends to form hexagonal close-packed (HCP) or face-centered cubic structures due to entropic effects.

The self-assembly has two main effects at a higher magnetic field [48]: Firstly, it includes smaller magnetic nanoparticles in deciding the self-assembly, which had a weak interaction due to the SPM effects. Second, the phases are oriented along with the applied field directions, which provides an anisotropic effect due to the self-assembly.

Self-assembly of nanoparticles can be driven by many other forces, which will be explained in Sec. 2.2.3. But the important point is to decide which interactions dominate at that size, shape, separation, and external parameters like the

magnetic field.

### 2.2.3. Other forces

There are several types of forces that play a major role in the ordering of nanoparticles. Most of these forces arise from static or transient electromagnetic interactions between atoms or molecules. Though the importance of the forces in the self-assembly of nanoparticles, but still possible to self-assemble these particles in absence of these forces, such as, at low concentration, the depletion force or the confinement effects could lead to some order, which arise from entropic effects and at high concentrations, ordering forms arises from pure entropic effect. In this section, a brief explanation about the forces leading to the ordering of the nanoparticles is given .

#### 2.2.3.1. Steric repulsion

To minimize the surface energy, the nanoparticles in solutions tend to aggregate due to the attractive vdW, or dipolar interactions. In order to avert this effect, there should be some kind of repulsive force. This can be provided by electrostatic repulsion which is activated in some aqueous or ionic solution by adjusting the pH value or by steric repulsion which is activated in organic solvents by coating the particles by some surfactant or ligand chains. Usually, these chains have grafted the particle from one end and the other one is kept free. When this particle approaches another particle, the free end of the chains repels each other due to the steric repulsion. Therefore, the nanoparticle is kept separate.

#### 2.2.3.2. Electrostatic force

It is an attractive or repulsive interaction between objects having electric charges. It is usually observed in colloids or ionic particles, to stabilizing the particles from agglomeration. By changing the pH value for the solvent, the particles become charged. The charged ligand shells can be attached to the charged particles giving rise to electrostatic interaction which depends on the geometry of the particle that determines the surface charge distribution. The strength of this force depends on the number of positive and negative ions surrounding the charged particles.

#### 2.2.3.3. Capillary force

It is a kind of pressure exerted on the two surfaces due to the solvent meniscus between two adjacent particles or curved surfaces. The capillary force acts as an adhesive force. It is used to self-assemble the nanoparticles into 1- 2- or

3-dimensional structure [49, 50]. In some cases, if the surfactant covered the particles have an ionic head or electric dipole, then water can penetrate to the interface between the particle and the substrate, which left the particles above the surface and can help in ordering or aggregation of the particles [51, 52]. The solvent between two freely moving nanoparticles separated by a small distance tends to adhere to the particles. The particles are brought closer together to reduce surface tension.

#### 2.2.3.4. Convective force

It can control the self-assembly in the bulk or surfaces and it acts like an external magnetic and electric field [52]. Also, it is aided by directional fluid motion. Typically, nanoparticles confined in two-dimensional structures due to the hydrodynamic and capillary forces [53].

## 2.3. Scattering

Scattering describes the general physical process, where it can be defined broadly as the redirection of radiation out of the original direction of propagation, due to the interaction with another object. In a broad perspective, scattering includes the different types of radiation - light, X-ray, electron, neutron, etc. Scattering includes simple processes such as the daily seeing process, where after the light wave is emitted from a light source like a light bulb or the sun, it is scattered from an object in the surrounding before it finally detected with the eyes. Also, scattering includes the process where after the x-rays are produced when the electrons are suddenly decelerated upon collision with the metal target; it interacts with the sample before it is detected with a detector. Moreover, neutrons are including in the scattering techniques, where after the neutrons are generated in a nuclear reactor, it interacts with the sample located in the instrumental hall before it is measured with a detector.

In this study, multiple X-ray and neutron scattering techniques are applied to study the nuclear and magnetic structure of nanoparticles and their assemblies. In order to understand the rich information that can be gained using these techniques, a brief introduction of the general scattering theory is presented in Sec.2.3.1 and in Sec. 2.3.2 the interaction of X-rays and neutron with matter is given. Then the theory behind the main techniques used in this study is discussed: small-angle X-ray scattering in Sec. 2.4, X-ray reflectometry in Sec. 2.5, neutron reflectometry in Sec. 2.6 and grazing-incidence small-angle X-ray scattering in Sec. 2.7.

### 2.3.1. Scattering theory

Generally, in our study, the scattering process describes the scattering of neutrons or X-ray photons, after interacting with the sample as depicted in figure 2.9. An incoming wave  $\vec{k}_i$  with defined direction can interact with the sample and due to this it deviates from its direct path, exiting as outgoing wave  $\vec{k}_f$ . The process is called elastic scattering if there is no change in the energy between incident and scattered wave (i.e.  $E_i = E_f$ ) and  $|\vec{k}_i| = |\vec{k}_f|$  and otherwise it is called inelastic scattering process. The scattering vector describing the momentum transfer during scattering process is defined as

$$\vec{Q} = \vec{k}_f - \vec{k}_i \quad (2.63)$$

For elastic scattering, the magnitude of the scattering vector  $\vec{Q}$  can be directly calculated from the wavelength  $\lambda$  and scattering angle  $2\theta$  between  $\vec{k}_i$  and  $\vec{k}_f$  as:

$$Q = |\vec{Q}| = \sqrt{k_i^2 + k_f^2 - 2k_i k_f \cos 2\theta} = \sqrt{2k^2(1 - \cos(2\theta))} = \frac{4\pi}{\lambda} \sin \theta \quad (2.64)$$

where it is used that  $|\vec{k}_i| = |\vec{k}_f| = k = \frac{2\pi}{\lambda}$ .

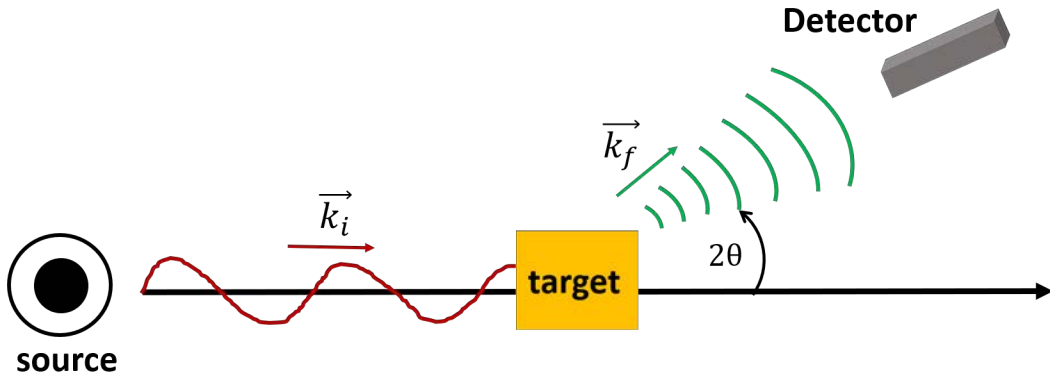


Figure 2.9.: Schematic of the general scattering process. An incoming wave with a wave vector  $k_i$  (red) interacts with the target (yellow) and produces an outgoing wave with wave vector  $k_f$  (green) then it is detected by a detector.

From a broad perspective, scattering theory determines the probabilities for a transition of a particle to go from an initial state to a final state determined by their energy and momentum. Thereby, it provides a method to calculate from

a model the expected scattering intensity, which can be compared to an actual scattering experiment. Moreover, it allows predicting experimental observations from the fundamental interactions postulated by the theory.

The problem that needs to be solved in non-relativistic physics, e.g. for neutrons, is the time-independent Schrödinger equation (equation 2.65). Also, for electromagnetic waves such as X-rays, the propagation and interaction with matter are described better by quantum electrodynamics. However, classical electrodynamics in some cases is sufficient and the scattering theory from Maxwell's equations leads to the same type of problem as for the Schrödinger equation, more details are discussed in App. A.2.

$$\left[ -\frac{\hbar^2}{2m}\Delta^2 + V(\vec{r}) \right] \psi_k(\vec{r}) = E\psi_k(\vec{r}) \quad (2.65)$$

Where  $V(\vec{r})$  is the potential with the boundary condition  $V(\vec{r}) = 0$  for  $\vec{r}$  outside the scattering region.

The energy  $E$  is determined by the energy of the incident plane wave  $E_k = \frac{\hbar^2}{2m}k^2$ . Introducing  $G_0$  as a Green function,

$$\left[ \frac{\hbar^2}{2m}\Delta^2 + E \right] G_0(\vec{r}, \vec{r}'|E) = \delta(\vec{r} - \vec{r}') \quad (2.66)$$

Now, for the free potential Schrödinger equation, equation 2.65 is given as,

$$\left[ \frac{\hbar^2}{2m}\Delta^2 + E \right] \psi_k(\vec{r}) = V(\vec{r})\psi_k(\vec{r}) \quad (2.67)$$

The above equation can be transferred into an integral equation,

$$\psi'_k(\vec{r}) = \psi_k(\vec{r}) + \int d^3r' G_0(\vec{r}, \vec{r}'|E) V(\vec{r}') \psi'_k(\vec{r}') \quad (2.68)$$

Where  $V(\vec{r}')$   $\psi'_k(\vec{r})$  are conceived as inhomogeneity of the differential equation (equation 2.66) and  $\psi_k(\vec{r})$  is the plane wave solution of the free potential Schrödinger equation. The above equation is known as *Lippmann-Schwinger equation*.

The Green function  $G_0(\vec{r}, \vec{r}'|E)$  is not uniquely determined by the Schrödinger equation 2.65. The unique solution requires a boundary condition, which is chosen such that the solution  $\psi'_k(r)$  describes outgoing scattered wave. Then, the Green function can be written as as explained in details in APP. A.1,

$$G_0(\vec{r}, \vec{r}'|E) = -\frac{2m}{\hbar^2} \frac{1}{4\pi} \frac{e^{ik|\vec{r}-\vec{r}'|}}{|\vec{r}-\vec{r}'|} \quad (2.69)$$

Where  $k = \sqrt{\frac{2m}{\hbar^2}} E$ .

The Green function describes the stationary radiation of a particle with energy  $E$  generated at  $\vec{r}'$  by a spherical wave outgoing from the target. Also, the Green function gives the wave amplitude at location  $\vec{r}$  under the condition that the wave is not further scattered during the propagation from  $\vec{r}$  to  $\vec{r}'$ .

In a standard experiment setup, the distance between target and detector is significantly larger than the size of the sample  $|\vec{r}| \gg |\vec{r}'|$ , for large distances between  $\vec{r}$  and the scattering center  $\vec{r}'$ , a good approximation in calculation is,

$$|\vec{r}-\vec{r}'| = \vec{r} - \frac{\vec{r} \cdot \vec{r}'}{r} \quad (2.70)$$

$$\frac{1}{|\vec{r}-\vec{r}'|} = \frac{1}{r} + \mathcal{O}\left(\frac{1}{r^2}\right) \quad (2.71)$$

Inserting the above approximations in equation 2.69, the asymptotic form as well as the far field limit of the Green function can be obtained,

$$G_0(\vec{r}, \vec{r}'|E) = -\frac{2m}{\hbar^2} \frac{1}{4\pi} \frac{e^{ik\vec{r}}}{r} e^{-ik\hat{r} \cdot \vec{r}'} + \mathcal{O}\left(\frac{1}{r^2}\right) \quad (2.72)$$

Inserting the above equation into equation 2.68, then the asymptotic solution of the wave function  $\psi'_k(\vec{r})$  for large distance  $\vec{r}$ ,

$$\psi'_k(\vec{r}) = e^{ik\vec{r}} + \frac{1}{r} e^{ik\vec{r}} f_k(\hat{r}) \quad (2.73)$$

Where  $f(\hat{r}) = f(\theta, \phi)$  is the scattering amplitude and is given by,

$$f_k(\hat{r}) = -\frac{2m}{\hbar^2} \frac{1}{4} \int d^3\vec{r}' e^{-i\vec{k}' \cdot \vec{r}'} V(\vec{r}') \psi'_k(\vec{r}') = -4\pi \frac{\hbar^2}{2m} T(\vec{k}', \vec{k}) \quad (2.74)$$

Where  $T(\vec{k}', \vec{k})$  is the transmission matrix which is proportional to the scattering amplitude.

At  $V = 0$ , the scattering wave function is specified by the unperturbed incident plane wave,

$$\psi_k^{(0)}(\vec{r}) = e^{i\vec{k}\vec{r}} \quad (2.75)$$

In Born approximation, the equation of the scattering amplitude (equation 2.74) given as,

$$f_k(\hat{r}) = -\frac{2m}{\hbar^2} \frac{1}{4\pi} \int d^3\vec{r}' e^{-i\vec{k}'\vec{r}'} V(\vec{r}') e^{i\vec{k}\vec{r}'} = -\frac{2m}{\hbar^2} \frac{1}{4\pi} V(\vec{Q}) \quad (2.76)$$

Where  $V(\vec{Q})$  denotes the Fourier transform of the potential with the momentum transfer  $\vec{Q}$ .

In Born approximation, the incoming wave scatters only once inside the target potential before forming the scattered wave. This is the concept behind the kinematic theory of scattering, that simplifies the interpretation of the scattering experiment.

The differential cross section is given as,

$$\frac{d\sigma}{d\Omega} = \left( \frac{2m}{\hbar^2} \right)^2 \frac{\pi}{2} |V(\vec{Q})|^2 \quad (2.77)$$

The geometry of the scattering cross section is shown in figure 2.10. The scattered intensity is observed by a detector, which covers a small solid angle  $d\Omega = \frac{dS}{r^2}$  with  $dS$  is the detector area and  $r$  is the sample-to-detector distance. A general measure of the scattered intensity  $I(\vec{Q})$  is the differential cross section  $\frac{d\sigma}{d\Omega}$  if the change of the energy of the radiation during the scattering process neglected, which is defined by the number of particle  $dN$  counted per unit time  $dt$  scattered into a cone of solid angle  $d\Omega$  in the detector located at a distance  $r$  under scattering angle  $\theta$ .

### 2.3.2. X-ray and neutron matter interaction

X-ray and neutron scattering are complementary techniques. X-rays are electromagnetic radiation that is mostly scattered at the electrons of the atomic shell. The photon energy is given by  $E = h\nu = \frac{hc}{\lambda} = \hbar ck$ , the charge is zero, the magnetic

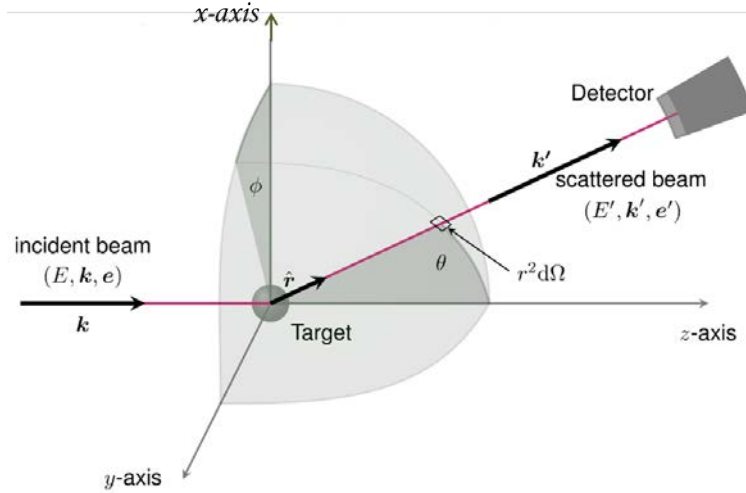


Figure 2.10.: Geometry of the scattering cross section: number of particle  $N$  per unit time  $dt$  measured by a detector at a distance  $r$ , scattered into an element of solid angle  $d\Omega$  in direction  $(\theta, \Phi)$ . Adapted from[54]

moment is zero and the spin is 1. X-rays show particle as well as wave properties. Neutrons are an elementary particle with a mass of  $m_n = 1.675 \cdot 10^{-27} kg$ , charge is zero, spin is  $\frac{1}{2}$ , the magnetic moment is  $\mu_n = 1.913\mu_N$ , the nuclear magneton is  $\mu_n = \frac{eh}{4\pi m_p} = 5.05 \cdot 10^{-27} JT^{-1}$ , the kinetic energy is  $E = \frac{m_n v^2}{2} = k_B T = \left(\frac{\hbar k}{2\pi}\right)^2$ , with  $k = \frac{2\pi}{\lambda}$ . It has a particle as well as wave properties. The neutron has several factors that make it a powerful experimental probe for matter investigation. First, neutrons are highly penetrating, they have no charge and interact with matter via the relatively weak neutron-nucleus interaction. The highly penetrating capability of neutrons ensures that the results obtained from neutron scattering measurements are representative of the bulk, rather than surface layers. Second, the neutron scattering cross-section for a given element is not related to the atomic number, meaning that neutron scattering is an ideal method to study materials containing light elements such as oxygen and hydrogen. Third, neutron possesses a magnetic moment, therefore neutron scattering is used to study magnetic materials.

Similarities between the scattering of neutrons and x-rays from the surface are obvious. When an x-ray or neutron beam is incident on a material, reflections occur due to the interaction between the incident beam and the atoms. The scattering process is schematically shown in figure 2.11(a). The condition for reflection to occur given as:

$$n\lambda = 2d \sin \theta \quad (2.78)$$

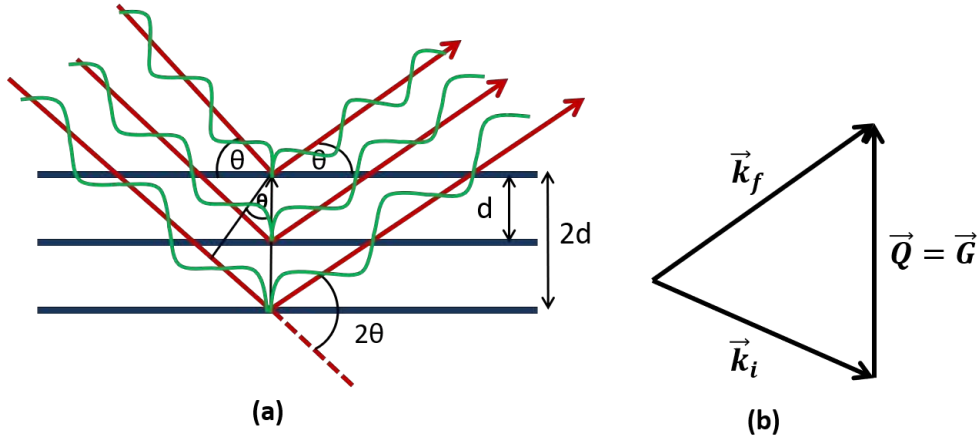


Figure 2.11.: An illustration of a reflection from a sample (a) Bragg reflection from planes separated by a distance  $d$ , (b) Laue representation of a Bragg reflection.

Equation.2.78 is known as *Bragg's law*, where  $\lambda$  is the x-ray or neutron wavelength,  $d$  is the spacing of the reflecting plane as shown in figure 2.11 (a),  $\theta$  is the diffraction angle measured with respect to the incident beam, and  $n$  is an integer known as the order of the corresponding reflection. From equation.2.78, the peak position can be determined, while the intensity of the peak can be determined by the coherent interference of the individual atoms, and is usually described in terms of the unit cell structure factor [55].

$$F(\vec{Q}) = \sum_m b_i e^{i\vec{Q} \cdot \vec{r}_i} e^{-w_i} \quad (2.79)$$

Where  $\vec{r}_i$  is the position of atom  $i$  with respect to the origin of the unit cell,  $w_i$  is the Debye-Waller factor, which describes the attenuation of x-ray scattering or coherent neutron scattering by thermal motion (i.e. a measure of the thermal vibration of atom  $i$ ). The scattering amplitude of atom  $i$  is given as  $b_i$  which is known as the neutron scattering length in the neutron scattering field, where in this case, does not depend on the  $\vec{Q}$  and appears to vary randomly with the atomic number  $Z$ . In x-ray scattering field,  $b_i$  is known as atomic scattering factor, where in this case proportional to the atomic number  $Z$  and decreases rapidly with increasing  $\vec{Q}$ .

The *Bragg's law* in equation.2.78 requires that the scattering vectors  $\vec{Q}$  equal the reciprocal lattice vector  $\vec{G}$ .

$$\vec{Q} = \vec{k}_f - \vec{k}_i = \vec{G} \quad (2.80)$$

The above equation is known as *Laue's* representation of *Bragg's* law, illustrated in figure 2.11 (b).

To calculate the differential cross-section, it is important to know how the scattering wave and the sample interact with each other, which is represented by the potential  $V$ . The derivation of the differential cross-section for quantum mechanical particles is shown in Sec.2.3.1 and in App. A.2 it is shown that a similar formula results for X-rays from classical electrodynamics. The dominant coupling to consider in the case of X-rays is the electromagnetic interaction of the X-ray photons with the electron shells of the atoms forming the material. When considering an electron cloud to oscillate in phase with the incoming X-ray, the differential cross-section is given as

$$\frac{d\sigma}{d\Omega} = |\hat{e}_i \cdot \hat{e}_f|^2 \left| \int dV e^{-i\vec{q}\vec{r}} r_e \rho_e(\vec{r}) \right|^2 \quad (2.81)$$

Where  $|\hat{e}_i \cdot \hat{e}_f|^2$  is a polarization factor depending on the experiment geometry and the source,  $r_e$  is the classical electron radius which is in the order of 2.8 fm and  $\rho_e$  is the density distribution of the electron cloud. The above equation is known as Thomson scattering, which is derived by assuming that the electron cloud follows the incoming wave via Newton's second law  $\vec{F} = m\vec{a} = -\vec{E}e$ . From the above assumption, the resonance, absorption and dispersion effects are neglected. The previous effects become important when the energy of the X-rays is close to the material electronic transitions or is high enough that it ejects electrons from their respective positions. However, such effects in this work are slight and more discussion about it can be found in [56].

For neutrons, there are two main interactions that occur with the material. One is the scattering of neutron via the short-ranged residual strong interaction with the atomic nuclei and the other one is scattering via the electromagnetic interaction with the internal magnetic field of the sample due to the magnetic moment of the neutron. For the nuclear scattering, the length scale of the residual strong force is on the order of ( $10^{-15}m$ ), whereas the wavelength of thermal neutrons ( $10^{-10}m$ ) is much larger. Therefore, the nucleus can be considered point-like and the potential for the scattering of a free neutron from a collection of nuclei positioned at  $\vec{r}_i$  can be modeled by a sum of Fermi pseudopotentials

$$V(\vec{r}) = \frac{2\pi\hbar^2}{m} \sum_i b_i \delta(\vec{r} - \vec{r}_i) \quad (2.82)$$

Where  $b_i$  is the nucleus scattering length, which is different for every element and isotope and it includes the information to distinguish between them. The experimental values of the scattering length have been tabulated for most isotopes [57]. In general, the scattering length is a complex number  $b = b' - ib''$ , where the complex part ( $b''$ ) describes the neutron absorption due to nuclear reactions. Moreover, the scattering length includes a coherent  $b_c$  and incoherent  $b_i$  cross section, where  $b_i$  depends on the relative orientation of the neutron spin  $\vec{s}$  to the nucleus angular momentum  $\vec{I}$

$$b = b_c + \frac{2b_i}{\sqrt{I(I+1)}} \vec{s} \cdot \vec{I} \quad (2.83)$$

In equation.2.82 the sum can be replaced by a scattering length density when the exact atomic structure of a material is not of interest

$$\sum_i b_i \delta(\vec{r} - \vec{r}_i) \rightarrow \rho(\vec{r}) \quad (2.84)$$

The value of  $\rho(\vec{r})$  is determined by summing over the scattering lengths of all atoms in a unit cell of volume  $V_{uc}$  for a given material at position  $i$ ,

$$\rho(\vec{r}) = \frac{1}{V_{uc}} \sum_i^n b_i \quad (2.85)$$

Thus, the differential cross section of neutrons is given as

$$\frac{d\sigma}{d\Omega} = \left| \int d\vec{r} e^{-i\vec{Q}\vec{r}} \rho(\vec{r}) \right|^2 \quad (2.86)$$

It is necessary to mention here that for X-rays, the same formula applies when the X-ray scattering length density is identified from the electron density as  $\rho = r_e \rho_e$ . Therefore, all the following discussion includes both the scattering of X-rays from the electron clouds of matter and the scattering of neutrons from the nuclear structure. The magnetic scattering of neutron from the magnetic structure of a material can be defined by adding a Zeeman potential to the Hamiltonian

$$V_m(\vec{r}) = -\vec{\mu}_n \cdot \vec{B} \quad (2.87)$$

Where  $\vec{\mu}_n = \mu_n \hat{\sigma}$  is the neutron magnetic moment which is in the order of  $\mu_n = 9.662 \cdot 10^{-27} JT^{-1}$  and quantum mechanically is given by the spin operator  $\hat{\sigma}$ , and  $\vec{B}$  is the magnetic field produced by the sample due to the bound electron orbital motion and spins.

The formula for the magnetic scattering amplitude contribution (i.e. contribution by the spin) to the differential cross section is similar to the nuclear scattering contribution as Fourier transform over a magnetic scattering length density

$$f_M(\vec{Q}) = \hat{\mu}_n \cdot \hat{s}_\perp \int d\vec{r} e^{-i\vec{Q}\cdot\vec{r}} \rho_{mag}(\vec{r}) \quad (2.88)$$

The  $\hat{s}_\perp$  is the part of the spins that are directed in the plane perpendicular to the scattering vector  $\vec{Q}$ . So, polarized neutron scattering allows to measure the spin density of a sample in that plane and the magnetic scattering length density ( $\rho_{mag}(\vec{r})$ ) is given by the spin density as

$$\rho_{mag}(\vec{r}) = \frac{m_n \mu_0}{\hbar^2} \frac{\mu_B \mu_n}{2\pi} S_e(\vec{r}) \quad (2.89)$$

In an experiment, the polarization of the incoming neutron beam is defined by a polarizer and stabilized by a weak magnetic guide field. When  $\hat{s}_\perp$  is parallel (anti-parallel) to this direction,  $f_M$  contributes with a positive(negative) sign to the differential cross section and the direction of the spin is conserved during the scattering. While, when  $\hat{s}_\perp$  is perpendicular to this direction, the spin operator results in a flip of the neutron spin (i.e. spin is not conserved) during the scattering process. This allows one to measure additionally the direction of the magnetization in the plane perpendicular to the scattering vector through careful analysis of the non-spin flip and spin flip channels.

### 2.3.3. Bragg diffraction

A crystal or crystalline material is a solid material whose constituents, such as atoms, molecules, or ions, are arranged in a highly ordered microscopic structure, forming a crystal lattice that extends in all directions. To find the crystal structure for any crystalline materials, Bragg diffraction is a suitable technique. In addition, the crystal is defined as a periodic repetition of elementary building blocks known as unit cells, which are described by the lattice vectors  $\vec{b}_1, \vec{b}_2, \vec{b}_3$  along the edges of the unit cell. The crystal is represented by a translation vector  $\vec{T}$  defined as:

$$\vec{T} = A\vec{b}_1 + B\vec{b}_2 + C\vec{b}_3 \quad (2.90)$$

Where A, B and C are integers. Each lattice site occupied by atoms or molecules known as basis. Therefore, the crystal is a combination of lattice and basis. The total scattering amplitude of a crystal is a summation of scattering factors of all the basis present, which is defined as:

$$S(\vec{Q}) = \sum_i f_i(\vec{Q}) e^{i\vec{Q} \cdot \vec{r}_i} \quad (2.91)$$

Where  $f_i(\vec{Q})$  is the form factor of the basis positioned at  $\vec{r}_i$ . Equation 2.91 can be written as a combination of summation over all the lattice point and summation over all basis vectors in a unit cell:

$$S(\vec{Q}) = \sum_{\vec{T} + \vec{r}_j} f_j(\vec{Q}) e^{i\vec{Q} \cdot (\vec{T} + \vec{r}_j)} = \sum_j f_j(\vec{Q}) e^{i\vec{Q} \cdot \vec{r}_j} \sum_t e^{i\vec{Q} \cdot \vec{T}} \quad (2.92)$$

Where the first term  $\sum_j f_j(\vec{Q}) e^{i\vec{Q} \cdot \vec{r}_j}$  is known as structure factor. In a real diffraction measurement, the square of the total scattering amplitude is measured, which is known as the scattering function defined as:

$$W(\vec{Q}) = |S(\vec{Q})|^2 = \left| \sum_j f_j(\vec{Q}) e^{i\vec{Q} \cdot \vec{r}_j} \right|^2 \left| \sum_t e^{i\vec{Q} \cdot \vec{T}} \right|^2 \quad (2.93)$$

The second term  $\sum_t e^{i\vec{Q} \cdot \vec{T}}$  in equation 2.91 can be written as:

$$\sum_t e^{i\vec{Q} \cdot \vec{T}} = \sum_{A=0}^{N_{b_1}} e^{i\vec{Q} \cdot A\vec{b}_1} + \sum_{B=0}^{N_{b_2}} e^{i\vec{Q} \cdot B\vec{b}_2} + \sum_{C=0}^{N_{b_3}} e^{i\vec{Q} \cdot C\vec{b}_3} \quad (2.94)$$

Where  $N_{b_1}, N_{b_2}, N_{b_3}$  is the number of lattice planes in the crystal. The modulus of the three Cartesian coordinates in equation 2.94 are given as:

$$\left| \sum_{A=0}^{N_{b_1}} e^{i\vec{Q} \cdot A\vec{b}_1} \right|^2 = \frac{\sin^2 \left( \frac{N_{b_1} \vec{Q} \cdot \vec{b}_1}{2} \right)}{\sin^2 \left( \frac{\vec{Q} \cdot \vec{b}_1}{2} \right)} \quad (2.95)$$

$$\left| \sum_{B=0}^{N_{b_2}} e^{i\vec{Q} \cdot B\vec{b}_2} \right|^2 = \frac{\sin^2 \left( \frac{N_{b_2} \vec{Q} \cdot \vec{b}_2}{2} \right)}{\sin^2 \left( \frac{\vec{Q} \cdot \vec{b}_2}{2} \right)} \quad (2.96)$$

$$\left| \sum_{C=0}^{N_{b_3}} e^{i\vec{Q} \cdot A\vec{b}_3} \right|^2 = \frac{\sin^2 \left( \frac{N_{b_3} \vec{Q} \cdot \vec{b}_3}{2} \right)}{\sin^2 \left( \frac{\vec{Q} \cdot \vec{b}_3}{2} \right)} \quad (2.97)$$

When the denominator is zero in equations 2.95, 2.96 and 2.97, then the  $W(\vec{Q})$  has a peak. Therefore,  $\vec{Q} \cdot \vec{b}_1 = 2\pi h$ ,  $\vec{Q} \cdot \vec{b}_2 = 2\pi k$  and  $\vec{Q} \cdot \vec{b}_3 = 2\pi l$  or  $Q_x = (\frac{2\pi}{b_1})h$ ,  $Q_y = (\frac{2\pi}{b_2})k$ ,  $Q_z = (\frac{2\pi}{b_3})l$ , which is equal to the reciprocal lattice vectors  $\vec{b}_1^*$ ,  $\vec{b}_2^*$  and  $\vec{b}_3^*$ . The intensity is maximal, when the scattering vector  $\vec{Q}$  is equal to the reciprocal lattice vector  $\vec{G}$  as shown previously in figure 2.11 (b):

$$\vec{Q} = \vec{G} \quad (2.98)$$

$\vec{G}$  is defined as:

$$\vec{G} = h\vec{b}_1^* + k\vec{b}_2^* + l\vec{b}_3^* \quad (2.99)$$

Where h, k and l is the Miller indices. The reciprocal lattice vectors  $\vec{b}_1^*$ ,  $\vec{b}_2^*$  and  $\vec{b}_3^*$  are given as:

$$\vec{b}_1^* = 2\pi \frac{\vec{b} \times \vec{c}}{\vec{a} \cdot (\vec{b} \times \vec{c})} \quad (2.100)$$

$$\vec{b}_2^* = 2\pi \frac{\vec{c} \times \vec{a}}{\vec{a} \cdot (\vec{b} \times \vec{c})} \quad (2.101)$$

$$\vec{b}_3^* = 2\pi \frac{\vec{a} \times \vec{b}}{\vec{a} \cdot (\vec{b} \times \vec{c})} \quad (2.102)$$

The above equations lead to the following identities,

$$\vec{b}_i \cdot \vec{b}_j^* = 2\pi \delta_{ij} \quad (2.103)$$

Where  $\delta_{ij}=1$  in case  $i=j$  and 0 in case  $i \neq j$ .

Equation 2.98 is known as the Laue condition, which is equivalent to Bragg's law of diffraction.

The Bragg's law state that the path difference should be integer multiple of  $\lambda$  for the constructive interference or for Bragg peaks as shown in figure 2.11 (a). Each point in the reciprocal space is related to a set of planes in the real space, where  $\vec{G}_{hkl}$  is perpendicular to the planes with Miller indices (hkl) and the magnitude of the reciprocal lattice vector given as:

$$|\vec{G}_{hkl}| = \frac{2\pi}{d_{hkl}} \quad (2.104)$$

Where  $d_{hkl}$  is the distance between lattice planes with Miller indices (hkl).

The equivalence of Laue condition and Bragg law rise from the relation between reciprocal lattice points and real space lattice planes. To show this equivalence equation 2.98 can be written as:

$$\vec{k}_f = \vec{G} + \vec{k}_i$$

By taking the square of the above equation:

$$k_f^2 = G^2 + 2\vec{G} \cdot \vec{k}_i + k_i^2$$

The above equation becomes  $G^2 = -2\vec{G} \cdot \vec{k}_i$  because  $|\vec{k}_i| = |\vec{k}_f|$ .

$\vec{G} \cdot \vec{k}_i = Gk \sin \theta$ . By substituting  $G = \frac{2\pi}{d}$  and  $k = \frac{2\pi}{\lambda}$ , the Bragg law can be created from Laue equation as follows.

$$G = 2k \sin \theta \rightarrow \frac{2\pi}{d} = 2 \frac{2\pi}{\lambda} \sin \theta \rightarrow n\lambda = 2d \sin \theta$$

### 2.3.4. Ewald sphere construction

The most useful way of imagining the possible Bragg reflections and understanding the occurrence of the diffraction spot is the Ewald sphere construction. The incident beam with a wave vector  $\vec{k}_i$  is assumed to strike the reciprocal lattice at some arbitrary points. Ewald sphere is a sphere of radius  $\frac{2\pi}{\lambda}$  where the origin of the reciprocal lattice lies at the edge of the Ewald sphere in the transmitted

beam as shown in figure 2.12. Whenever the reciprocal lattice points intersecting Ewald sphere or lie exactly on it, Bragg's condition will be satisfied and the corresponding (hkl) plane will appear in the scattering pattern. Ewald sphere construction does not ensure that the reciprocal lattice will intersect it. Therefore, the crystal has to be rotated in order to move more reciprocal lattice points through the Ewald sphere.

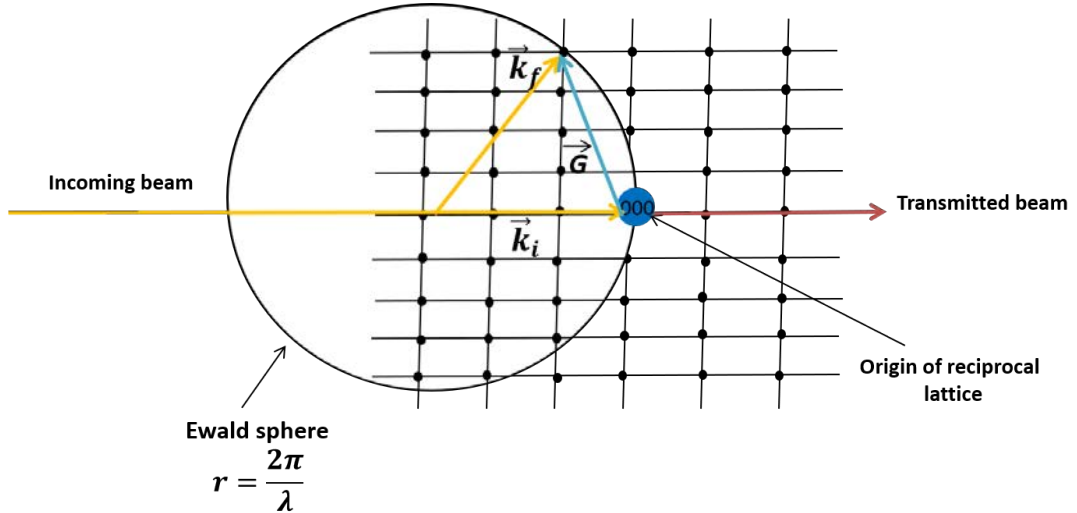


Figure 2.12.: Ewald sphere construction: When the reciprocal lattice point intersecting the sphere, the Bragg condition is satisfied.

For the observations of the Bragg peaks for single crystal. The single crystal has to be rotated for exact alignment of the reciprocal lattice with respect to the incident beam. When the sample is rotated, the reciprocal lattice is also rotated and in this case the scattering vector  $\vec{Q}$  becomes larger than the reciprocal vector  $\vec{G}$ , then the Bragg peaks will disappear. But for powder samples the reciprocal lattice is described by concentric spheres instead of points as shown in figure 2.13, because powder sample consists of all possible lattice planes randomly oriented in all possible directions. The Ewald sphere will cut all the concentric spheres, which appears as Debye-Scherrer rings instead of points. All scattering wave vectors  $\vec{k}_f$  shown in figure 2.13 satisfy the Bragg condition simultaneously. It is possible to do this scan in transmission geometry or for scattering under grazing incidence. Each ring appears at different scattering angle ( $2\theta$ ). These different ( $2\theta$ ) values can be obtained via a detector scan over the whole angular range.

In nanoparticle system, each nanoparticle could be a single crystal. But there may they arranged in a random way, which look like a powder pattern. Therefore to capture all possible reflections from nanoparticle films, scattering under grazing incidence is a sufficient technique by scanning the exit beam over ar-

bitrary wide angles and keeping the incident beam close to the total reflection condition.

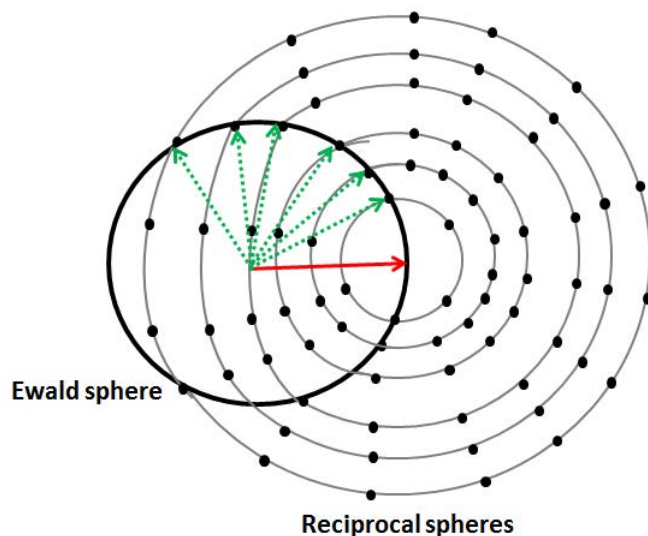


Figure 2.13.: Ewald sphere construction for powder samples.

## 2.4. Small Angle X-ray Scattering (SAXS)

Small-angle scattering (SAS) is a technique to study nanometer-sized objects when the wavelength of the scattered particle is in the order of a few Ångström ångström. SAS experiment arises from two primary sources, known as x-ray source (small-angle x-ray scattering (SAXS)) and neutron source (small-angle neutron scattering (SANS)), but only SAXS will be the main focus of this study. Here, the forward scattering of a collimated beam through a sample is measured on a position-sensitive detector around an opening angle in the order of  $2\theta = 0.1^\circ - 10^\circ$ . Also, in this experiment geometry, the sample-to-detector distance needs to be large to observe the scattering pattern with reasonable resolution due to the small-angle scattering. As the magnitude of the scattering vector  $Q$  is proportional to  $\sin(\theta)$  and  $Q$  is inversely proportional to the probed length scale, as introduced in previous sections,  $\vec{Q} = \frac{4\pi}{\lambda} \sin \theta$ . This means that scattering at small angles ( $\theta$ ), larger length scales are probed from this scattering technique.

SAS measurements are based on the interference of coherent radiations. For objects has to be investigated by SAS, its microscopic characteristic length has to be of the same order of magnitude as the wavelength of the incoming radiation. Usually, the samples measured with SAS technique are dispersed in a solvent

with random orientations like nanoparticles, which is the main interest in our study. The scattering intensity in SAS is measured in transmission geometry, where the size, size distribution and shape of the particles can be determined. In order to avoid multiple scattering, mostly thin samples with a high transmission rate are investigated by this technique.

In general, the local interaction of radiations with matter is characterized by a scattering length  $b_i$ , and its density  $\rho(r) = \rho_i(r)b_i$ , with  $\rho_i(r)$  being the local density of scatterers. Thus the scattering length density (SLD) is give by:

$$\rho(\vec{r}) = \frac{\sum_{i=1}^N b_i(\vec{r})}{V} \quad (2.105)$$

Where V is the volume.

In the following, the application of small-angle scattering to study nanoparticles in dispersion is explained. First step, will consider a dispersion that consists of monodisperse and equally oriented nanoparticles. Here in this case, the scattering length density is given as a constant background value given by the solvent  $\rho_s$  and parts in the solvent where it is replaced by the nanoparticles. The latter is given as a summation over  $\rho_p(\vec{r})$  because all particles are equally oriented and of the same shape.  $\rho_p(\vec{r})$  contains the complete description of the particle shape and it's composition. Also,  $\rho_p(\vec{r})$  is shifted to the different center positions  $\vec{r}_i$  of the nanoparticles

$$\rho(\vec{r}) = \rho_s + \sum_{i=1}^N \Delta\rho_p(\vec{r} - \vec{r}_i) \quad (2.106)$$

The nanoparticle scattering length density can be written as convolution of two functions: a function  $\Delta\rho_p(\vec{r})$ , which describes the shape and composition of a single nanoparticle, and a function  $S(\vec{r})$  describing the exact position of N nanoparticles in the solvent

$$\rho(\vec{r}) = \rho_s + (S * \Delta\rho_p)(\vec{r}) \quad (2.107)$$

Where  $S(\vec{r})$  is given as

$$S(\vec{r}) = \sum_{j=1}^N \delta(\vec{r} - \vec{r}_j) \quad (2.108)$$

The macroscopic differential cross section, which is the differential cross section scaled to the integrated volume given as

$$\frac{d\Sigma}{d\Omega} = \frac{d\sigma}{d\Omega} \frac{1}{V} \quad (2.109)$$

can be evaluated in the Born approximation by inserting the scattering length density (equation 2.107) in equation 2.86

$$\frac{d\Sigma}{d\Omega} = \frac{1}{V} \left| \int_V d\vec{r}' e^{-i\vec{Q}\cdot\vec{r}'} \rho(\vec{r}') \right|^2 = \frac{1}{V} \left| \int_V d\vec{r}' e^{-i\vec{Q}\cdot\vec{r}'} (S * \Delta\rho_p)(\vec{r}') + \int_V d\vec{r}' e^{-i\vec{Q}\cdot\vec{r}'} \rho_s \right|^2 \quad (2.110)$$

The integral over the constant solvent scattering length density equal  $2\pi\delta(\vec{Q})\rho_s$  is evaluated to zero for  $\vec{Q} \neq 0$ . The case of  $\vec{Q} = 0$  corresponds to forward scattering, which is not studied in small-angle x-ray scattering as the direct beam is blocked to protect the detector. The convolution theorem turns the remaining integral to a product of two integrals

$$\frac{d\Sigma}{d\Omega} = \frac{N}{V} \frac{1}{N} \left| \left( \int d\vec{r} e^{-i\vec{Q}\cdot\vec{r}} S(\vec{r}) \right) \left( \int_{V_p} d\vec{r} e^{-i\vec{Q}\cdot\vec{r}} (\rho_p(\vec{r}) - \rho_s) \right) \right|^2 \quad (2.111)$$

The above equation means that the macroscopic differential cross-section is described by two factors. The first integral is known as the structure factor  $S(\vec{Q})$  and the second integral is called the form factor  $F(\vec{Q})$ . The structure factor arises from the arrangement of particles and it becomes relevant when the nanoparticles solvent is too dense, therefore the nanoparticles tend to attract each other and aggregate. Therefore, the interactions between the nanoparticles in solvent can be described by the structure factor  $S(\vec{Q})$ . The structure factor  $S(\vec{Q}) = 1$  for an ensemble with identical, uncorrelated particles. While  $S(\vec{Q}) \neq 1$  for the correlated particles, due to the interactions between the particles. Structure factor is most prominent at small Q values, while at large Q values only the inner particle structure is visible, not the arrangements of the particles in space. The form factor describes the scattering due to the shape and properties of a single nanoparticle. In the definition of the volume integral for the form factor, it is enough to integrate over the volume of a single particle  $V_p$  as the integration is 0 outside. The integral, before applying the magnitude square, is called the form factor amplitude and is denoted by a lower case  $f(\vec{Q})$ , because

the magnitude removes the phase of the amplitude.

The case  $S(\vec{Q}) = 1$  is most often the desired one in a small-angle scattering experiment on nanoparticles as it eliminates the need to model a structure factor. Therefore, in an experiment, the sample is diluted such that the structure factor is approximately 1, but the measured intensity is still strong enough to be counted in a reasonable amount of measurement time. In this case, only the form factor  $F(\vec{Q})$  for a specific sample needs to be modeled.

For a form factor, the simplest model to solve of a nanoparticle is a sphere due to its high symmetry. The scattering length density is then just a constant within the volume of the sphere and the form factor  $F_{sph}(\vec{Q})$  can be solved analytically to

$$\begin{aligned}
 F_{sph}(\vec{Q}) &= \left| \int_{V_p} d\vec{r} e^{-i\vec{Q}\vec{r}} (\rho_p - \rho_s) \right|^2 & (2.112) \\
 &= \left| (\rho_p - \rho_s) \int_0^R dr \int_0^{2\pi} d\phi \int_0^\pi d\theta r^2 \sin(\theta) e^{-iQr \cos(\theta)} \right|^2 \\
 &= \left| 4\pi R^3 (\rho_p - \rho_s) \frac{\sin(QR) - QR \cos(QR)}{(QR)^3} \right|^2 \\
 &= V_{sph}^2 (\rho_p - \rho_s)^2 \left| 3 \frac{\sin(QR) - QR \cos(QR)}{(QR)^3} \right|^2 & (2.113)
 \end{aligned}$$

where  $V_{sph}$  is the volume of the sphere. Thus, the macroscopic differential cross section for diluted nanospheres in a solvent is given as

$$\frac{d\Sigma}{d\Omega} = \alpha V_{sph} (\rho_p - \rho_s)^2 \left| 3 \frac{\sin(QR) - QR \cos(QR)}{(QR)^3} \right|^2 \quad (2.114)$$

with  $\alpha = \frac{NV_{sph}}{V}$  is the volume concentration of the particles in the solvent. The above equation shows that the differential cross section depends on the particle concentration, volume and contrast to the solvent which is mainly used for contrast variation techniques in neutron scattering experiment. The derivation of

further form factors such as a cube or core shell is described briefly in App.E.

The size, size distribution and shape of the particles can be determined by fitting the measured intensity with the calculated intensity. Mostly, there are distributions of different sizes in real systems. Therefore, the scattered intensity  $I(\vec{Q}, \vec{r})$  is folded with the size distribution function  $\chi(\vec{r})$ :

$$I_{real}(\vec{Q}) = I_{ideal}(\vec{Q}, \vec{r}) \otimes \chi(\vec{r}) \quad (2.115)$$

Where  $I_{real}$  and  $I_{ideal}$  represents the real measured intensity and the ideal intensity for any calculated particulate size and form, respectively. The magnitude of the polydispersity is described by a constant know as *polydispersity index (PDI)* given as:

$$PDI = \frac{\sigma(\chi(\vec{r}))}{\mu(\chi(\vec{r}))} \quad (2.116)$$

Where  $\sigma(\chi(\vec{r}))$  is the standard deviation of the size distribution function and  $\mu(\chi(\vec{r}))$  is the mean of the size distribution function. In this study, the size distribution of the nanoparticles is described by a log-normal function:

$$d(R, R_0, \sigma) = \frac{1}{\sqrt{2\pi}\sigma R} \exp\left(-\frac{(\ln \frac{R}{R_0})^2}{2\sigma^2}\right) \quad (2.117)$$

Where  $R$  is the spherical nanoparticle radius,  $R_0$  is the mean value of the radius, and  $\sigma$  is the lognormal standard deviation.

## 2.5. X-ray Reflectometry (XRR)

Reflectometry is a surface-sensitive analytical technique to study the structure of a thin films or multilayers perpendicular to the substrate. In particular, X-ray reflectometry allows to study the average electron density in a sample with depth resolution. The basic principle behind this technique is that the reflected beam is collected at a reflected angle equal to incident angle (specular reflectivity). The scattering vector is parallel to the z-axis, perpendicular to the substrate. It has the effect that the integral over the scattering potential in the previously discussed BA (equation 2.74) reduces to a one dimensional problem

$$\int d\vec{r} e^{-i\vec{Q}\cdot\vec{r}} V(\vec{r}) = \int dZ e^{-iQ_z \cdot Z} \bar{V}(Z) \quad (2.118)$$

where  $\bar{V}$  is the laterally integrated potential

$$\bar{V}(Z) = \int dX \int dY V(\vec{r})$$

(2.119)

Then, reflectometry is a one dimensional problem, where the sample is completely modeled by the laterally averaged scattering potential with respect to the Z axis.

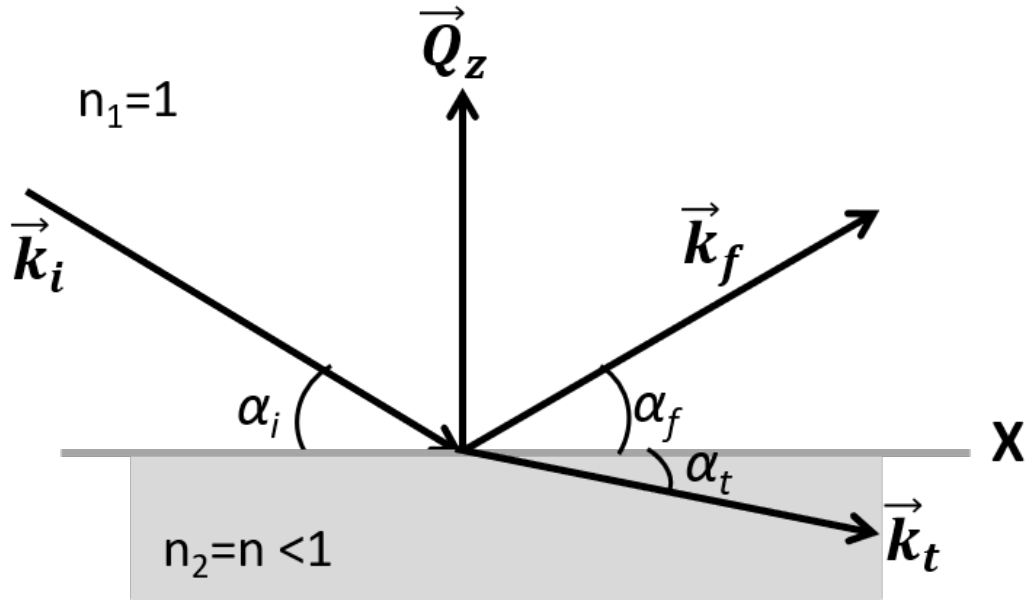


Figure 2.14.: Reflection and refraction from a surface.

**Reflection from a surface:** A simple approach will be considered here in order to understand reflectivity from a laterally homogeneous medium. Figure 2.14 shows the reflection geometry, where a monochromatic, well collimated beam impinges from the vacuum side onto a flat surface under a small incidence angle  $\alpha_i$  and the scattering vector  $\vec{Q}$  is perpendicular to the sample surface. Afterwards, the x-ray beam is partly reflected from a sample surface. The reflected intensity of x-rays is measured in the specular direction ( $\alpha_i = \alpha_f = \alpha$ ). The transmitted wave makes an angle  $\alpha_t$  with the surface. The scattering vector  $Q$  is along Z-axis and is given by:

$$Q = Q_z = 2k \sin \alpha \quad (2.120)$$

According to Snell's law,

$$n_1 \sin \alpha = n_2 \sin \alpha_t$$

and with the refractive indices  $n_1 = 1$  (vacuum) and  $n_2 = n$ :

$$\Rightarrow \sin \alpha = n \sin \alpha_t \quad (2.121)$$

At an incident angle ( $\alpha_i$ ) = critical angle ( $\alpha_c$ ), all the beam is reflected and no beam transmitted into the sample, i.e.  $\alpha_t = 0$ . Therefore, the refractive index can be written as:

$$n = \sin \alpha_c \quad (2.122)$$

The refractive index  $n = 1 - \delta + i\beta$  depends on the material and beam type. For x-ray, the value of the dispersion  $\delta$  and the absorption  $\beta$  terms are give as:

$$\delta = \frac{2\pi r_0 \rho_e}{k_i^2 Z} \sum_j f_j(\vec{Q}) + f'_j(E) \simeq \frac{\lambda^2 r_0 \rho_e}{2\pi} \simeq \frac{2\pi r_0 \rho_e}{k_i^2} \quad (2.123)$$

$$\beta = \frac{2\pi r_0 \rho_e}{k_i^2 Z} \sum_j f''_j(E) = \mu \frac{\lambda}{4\pi} = \frac{\mu}{2k_i} \quad (2.124)$$

Where  $f'$  is the dispersion correction term,  $\mu$  is the absorption coefficient of the material,  $\rho_e$  is the electron density and  $r_0$  is the classical electron radius. Both coefficients are energy dependent, which is neglected in the above equations. For very small incident angles and far away from resonance edges, the refractive index can be written as:

$$n = 1 - \delta = 1 - \frac{\lambda^2 r_0 \rho_e}{2\pi} = 1 - \frac{\alpha_c^2}{2}$$

$$\Rightarrow \alpha_c = \sqrt{\frac{\lambda^2 r_0 \rho_e}{\pi}} = \sqrt{\frac{4\pi r_0 \rho_e}{k^2}} \quad (2.125)$$

Equation 2.125 becomes in Q-space:

$$Q_c = 2k \sin \alpha_c \simeq 2k\alpha_c = \sqrt{16\pi r_0 \rho_e} \quad (2.126)$$

Equation 2.126 shows that the critical scattering vector  $\vec{Q}_c$  is in this approximation independent on the wavelength  $\lambda$ . It depends on the classical electron radius and the electron density which is a function of the atomic number  $Z$  (i.e. is a function of material properties).

From the refractive index definition:

$$n = \frac{k_t}{k} = \frac{\sin \alpha}{\sin \alpha_t} \quad (2.127)$$

For small angle the transmitted wave vector  $k_t = nk$  and the transmitted angle  $\alpha_t = \sqrt{\alpha^2 - \alpha_c^2}$ .

At an incident angle below  $\alpha_c$  an evanescent wave propagates parallel to the sample surface and decreases exponentially from the sample surface to the bottom of the sample. This wave provides information about the in-plane lattice parameter which can be determined by grazing incidence diffraction method. One has to go to an angles higher than the  $\alpha_c$  in order to extract the electron density variation of the sample.

The reflection and the transmission coefficients can be written as:

$$r(\alpha) = \frac{E_{R0}}{E_{I0}} = \frac{\alpha - \alpha_t}{\alpha + \alpha_t} \quad (2.128)$$

$$t(\alpha) = \frac{E_{T0}}{E_{I0}} = \frac{2\alpha}{\alpha + \alpha_t} \quad (2.129)$$

Where  $E_{I0}$ ,  $E_{R0}$  and  $E_{T0}$  are the incident, reflected and transmitted amplitudes, respectively.

Transformation of equations 2.128 and 2.129 into Q-space can be written as:

$$r(Q) = \frac{Q - Q_t}{Q + Q_t} \quad (2.130)$$

$$t(Q) = \frac{2Q}{Q + Q_t} \quad (2.131)$$

Where  $Q = \frac{Q}{Q_c} = \alpha \frac{2k}{Q_c}$  and  $Q_t = \frac{Q_t}{Q_c} = \alpha_t \frac{2k}{Q_c}$ .

The reflectivity ( $R$ ) is defined as the modulus squared of the ratio of the reflected and incoming waves, while the transmissivity ( $T$ ) is defined as the modulus squared of the ratio of the transmitted and incoming waves.

$$R = |r|^2 \Rightarrow R = \left| \frac{\alpha - \alpha_t}{\alpha + \alpha_t} \right|^2 = \left| \frac{Q - Q_t}{Q + Q_t} \right|^2 \quad (2.132)$$

$$T = |t|^2 \Rightarrow T = \left| \frac{2\alpha}{\alpha + \alpha_t} \right|^2 = \left| \frac{2Q}{Q + Q_t} \right|^2 \quad (2.133)$$

In case  $Q \gg 1$ , then  $Q^2 - Q_t^2 = 1$  and  $Q + Q_t \approx Q$ . Therefore the reflectivity and the transmissivity becomes:

$$R_F \propto Q^{-4} \quad (2.134)$$

$$T_F = 1 \quad (2.135)$$

Equation 2.134 known as the Fresnel reflectivity. Means the reflected wave in phase with the incident wave.

In case  $Q \ll 1$ , the reflected wave is out of phase with the incident wave and an evanescent waves are observed.

In the case of reflection from layers on a substrate, multiple transmissions and reflections take place at both surface and interface before the beam exits the sample. Then, the reflected beams from the different interfaces interfere with each other. The maximum intensity is obtained, when the path length difference between two reflected beams is an integer multiple of the wavelength (Bragg's law).

For a simple system consider one layer added on top of the substrate. Here, one has to deal with two interfaces. The first one between the vacuum and the layer and the other one between the layer and the substrate. The phase difference between the reflected intensities from the two interfaces are varied by changing the incident angle  $\alpha_i$ . Therefore, the beams that are reflected from the two interfaces interfere with each other, which gives an oscillation in the reflectivity measurement known as Kiessig oscillations. At large  $Q(z)$ , the thickness of the layer is related to the oscillation period by the following relation:

$$\Delta Q_z = \frac{2\pi}{d} \Rightarrow d = \frac{2\pi}{\Delta Q_z} \quad (2.136)$$

Where  $\Delta Q_z$  is the difference between two successive maxima or minima. Using the relation between Q-space and  $\alpha$ ,  $Q_z = 2k \sin \alpha = (\frac{4\pi}{\lambda}) \sin \alpha \approx (\frac{4\pi}{\lambda}) \alpha$ , then equation 4.6 becomes in angular term:

$$d = \frac{\pi}{k\Delta\alpha} = \frac{\lambda}{\Delta\alpha} \quad (2.137)$$

Where  $\Delta\alpha$  is the difference between two maxima or minima in radian.

In case more than one layer on the substrate exists, such as superlattices with two different layers with thicknesses  $d_1$  and  $d_2$ , and these two layers are repeated several times. The combined periodicity is given by  $D = d_1 + d_2$  as shown in figure 2.15. One can observe that the reflectivity measurement shows some maxima Kiessig fringes which appear with a periodicity of  $\frac{2\pi}{D}$ . In addition, one can observe much weaker oscillation with a period given by the thickness of the total layer. In order to calculate the reflectivity for a multilayer system, Parratt formulated an approach to add all the reflected and transmitted beam amplitudes to the total reflected beam [56, 58].

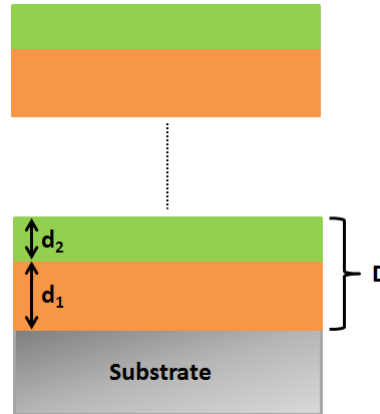


Figure 2.15.: Schematic representation of two layers of thickness  $d_1$  and  $d_2$  on a substrate with a total periodicity  $D$ .

## 2.6. Polarized neutron reflectometry (PNR)

Similarities between x-ray and neutron reflectivity are obvious. X-ray reflectometry allows one to study the average electron density in a sample with depth

resolution as mentioned in the previous section, whereas neutron reflectometry allows one to probe the nuclear structure. Additionally, polarized neutron reflectometry (PNR) allows in principle to resolve the magnetic density with depth resolution [59]. Neutron basically interacts with the nuclear potential and it interacts with the local magnetic induction  $\vec{B}$  in the sample due to the magnetic moment  $\vec{\mu}$  generated by the unpaired electrons inside the atoms for the magnetic materials.

Due to the pronounced differences in the neutron scattering length density of different isotopes, neutrons often provide better contrast and don't damage samples. On the other hand, x-rays provide better Q resolution and higher Q values. In contrast to x-rays, magnetic systems are easily probed by polarized neutron reflectometry due to magnetic dipole interaction with unpaired electrons.

When neutrons interact with matter, an interaction potential is added, which is described as a Fermi pseudo potential

$$V_F = \frac{2\pi\hbar^2}{m_N}\rho_N b \quad (2.138)$$

Where  $m_N$  is the neutron mass,  $\rho_N$  is the nuclear density and  $b$  is the scattering length. Solving the Schrödinger equation for the interaction given in above equation

$$\frac{\hbar^2}{2m} \frac{d^2\psi}{dr^2} + (E_0 - V_F)\psi = 0 \quad (2.139)$$

with  $\psi(r) = \psi_+(r)|+ \rangle + \psi_-(r)|- \rangle$  for the two spin states of the neutron. It follows with

$$k^2 = \frac{2m}{\hbar^2}(E_0 - V_F) \quad (2.140)$$

$$\frac{d^2\psi}{dr^2} + k^2\psi = 0 \quad (2.141)$$

If the interaction of the neutron wave is with a magnetic material, then the interaction potential is modified with a magnetic interaction by

$$V_M = V_F - \gamma_n \mu_N \vec{\sigma} \vec{B} \quad (2.142)$$

Where  $\gamma_n$  is the gyromagnetic factor,  $\mu_N$  is the nuclear magneton and  $\vec{\sigma} = (\sigma_x, \sigma_y, \sigma_z)$ .

$$k_j^{\pm 2} = \frac{2m}{\hbar^2} E_0 - 4\pi\rho_N b_j \pm \frac{2m}{\hbar^2} \gamma_n \mu_N \vec{\sigma} \vec{B} \quad (2.143)$$

which gives four wavevectors for the four spin states  $k_j^{++2}, k_j^{+-2}, k_j^{-+2}, k_j^{--2}$  and four reflectivities  $R^{++}, R^{+-}, R^{-+}, R^{--}$ . Where  $R^{++}$  and  $R^{--}$  are produced when the neutron spin direction is not changed after it is scattered at the sample, which is known as the non spin flip (NSF) scattering, which happens when  $\vec{M}$  align parallel to the applied field. While if the spin direction of the neutron is flipped after scattering,  $R^{+-}, R^{-+}$  are produced, which is known as spin flip (SF) scattering which happens when  $\vec{M}$  oriented perpendicular to the applied field. PNR is not sensitive to the magnetization parallel to the scattering vector  $\vec{Q}$  (Z-component).

The Schrödinger equation for the potential of neutron states (i.e up and down states) can be simplified into two coupled one-dimensional linear differential equations

$$\psi_+''(z) + \left[ k_z^2 - 4\pi b \rho_N + \frac{2m\gamma_n \mu_n}{\hbar^2} B_{\parallel} \right] \psi_+(z) + \frac{2m\gamma_n \mu_n}{\hbar^2} B_{\perp} \psi_-(z) = 0 \quad (2.144)$$

$$\psi_-''(z) + \left[ k_z^2 - 4\pi b \rho_N - \frac{2m\gamma_n \mu_n}{\hbar^2} B_{\parallel} \right] \psi_-(z) + \frac{2m\gamma_n \mu_n}{\hbar^2} B_{\perp} \psi_+(z) = 0 \quad (2.145)$$

## 2.7. GISAXS

Additionally to the perpendicular structure, as described in the previous section, it is interesting to study the lateral structure of nanoparticle assemblies to gain the complete three-dimensional information. For this purpose grazing-incidence small-angle x-ray scattering (GISAS) has assured as an efficient technique to measure the off-specular scattering from which in-plane order within a sample can be extracted with high resolution. GISAXS is a surface-sensitive scattering technique with minimum penetration depth 10 nm used to probe the nanostructure of thin films. Also, it is a versatile and powerful tool, which enables characterization of nanoscale objects deposited on surfaces such as nanoparticles and nanostructured surfaces such as lithographic patterns, which is the main focus of this study. Furthermore, GISAXS enables studies of nanoscale density correlations and/or the shape of nanoscopic objects at surfaces, at buried interfaces, or in thin films.

GISAXS technique combines features of the small-Angle X-ray Scattering and the diffuse X-ray Reflectivity.

The geometry of a GISAXS experiment along with the reciprocal axes is illustrated in figure 2.16. The incoming x-ray beam enters the sample along  $\vec{k}_i$  under a very small angle  $\alpha_i$  with respect to the surface, which results in a large footprint on the sample, and scattered along  $\vec{k}_f$  in the direction  $(\alpha_f, 2\theta_f)$ . The Cartesian z-axis is the normal to the surface plane, the x-axis is the direction along the surface parallel to the beam and the y-axis perpendicular to it. The reciprocal coordinates are related to the scattering angles in real space throughout the following relations:

$$Q_z = k(\sin \alpha_f + \sin \alpha_i) \quad (2.146)$$

$$Q_y = k(\sin 2\theta_f \cos \alpha_f) \quad (2.147)$$

$$Q_x = k(\cos 2\theta_f \cos \alpha_f - \cos \alpha_i) \quad (2.148)$$

Where  $k = \frac{2\pi}{\lambda}$  with  $\lambda$  is the wavelength of the x-ray,  $\alpha_i$  is the incident angle,  $\alpha_f$  is the exit angle and  $2\theta_f$  is the in-plane angle. From GISAXS pattern, the reflected beam observed above the horizon, and the transmitted beam observed below the horizon as shown in figure 2.16.

GISAXS has various cases that provides different information: first case, as the in-plane angle  $2\theta_f = 0$ ,  $\alpha_f = \alpha_i$ , and  $Q_x = Q_y = 0$  and  $Q_z \neq 0$ , then **specular reflectivity** can be observed which depends on the incident angle  $\alpha_i$ . From specular reflectivity, depth-sensitive information like information about layer thickness and surface roughness can be obtained. Second case, if  $2\theta_f = 0$ , and  $\alpha_f \neq \alpha_i$ , then **off specular reflectivity** is obtained. Third case, If  $2\theta_f \neq 0$  and  $\alpha_f \neq \alpha_i$ , then scattering patterns containing information about the lateral ordering can be obtained.

The GISAXS measurement is performed in different geometry than SAXS as shown in figure 2.16. In GISAXS, the incident angle is chosen to be close to the critical angle of the sample, where the Born approximation (BA), which is not taken into account the reflection-refraction effects at the surface of the substrate (i.e. is not accurate enough to reliably calculate the scattering). It has to be modified to account for reflection and refraction effects at the interfaces of a sample. This is provided by the distorted-wave Born approximation (DWBA),

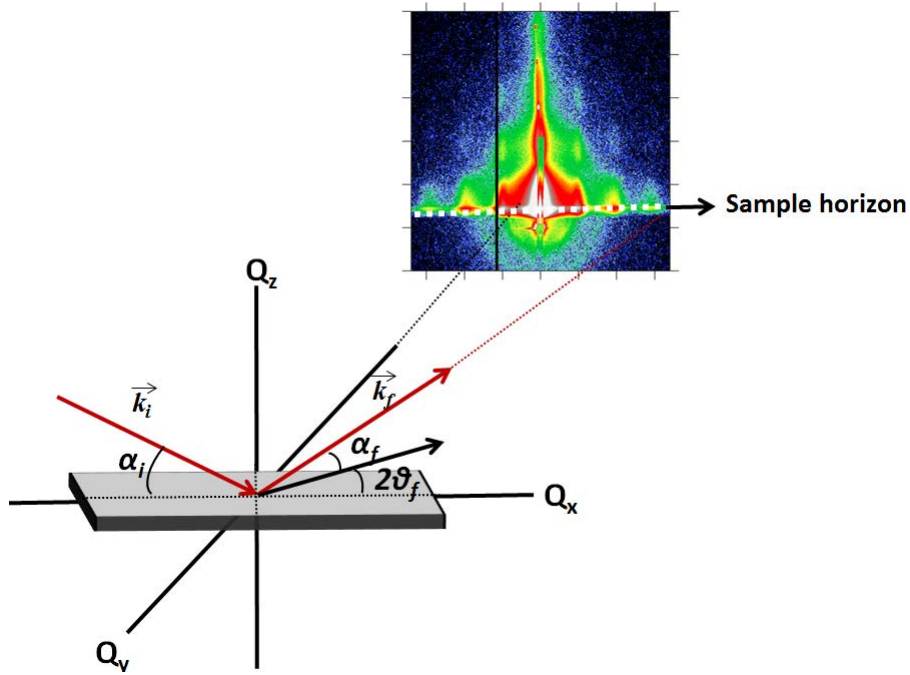


Figure 2.16.: GISAXS geometry with the reciprocal axes.

where the scattering wave function is no longer assumed to be a plane wave within the sample such as in the Born approximation. In DWBA, in addition to the normal scattering event as assumed in (BA), the other three events, a reflection followed by scattering, or a reflection after the scattering, or reflection followed by scattering and a second reflection are taken into consideration. Figure 2.17 shows the four different scattering events encountered in DWBA and involved in GISAXS geometry.

Born approximation is accurate in case if the scattered field is small, compared to the incident field, in the scatterer, where it is treated as a perturbation of free space or of a homogeneous medium. Also, in this case, the incident wave is considered as a plane wave. When the previous mentioned criteria is not satisfied, BA has to be modified to so called DWBA due to the perturbative potential  $\delta V(\vec{r})$  in equation 2.149. In general, the free space zero-potential in BA,  $V_0(\vec{r}) = 0$ , is replaced by a non-trivial reference potential  $V_1(\vec{r})$  of a known scattered field  $\psi(\vec{r})$  obtained from the solution of the Lippmann-Schwinger equation (equation 2.68). In the DWBA, the scattering potential is split as

$$V(\vec{r}) = V_1(\vec{r}) + \delta V(\vec{r}) \quad (2.149)$$

Where the potential  $V_1(\vec{r})$  can be treated exactly to determine the wave function

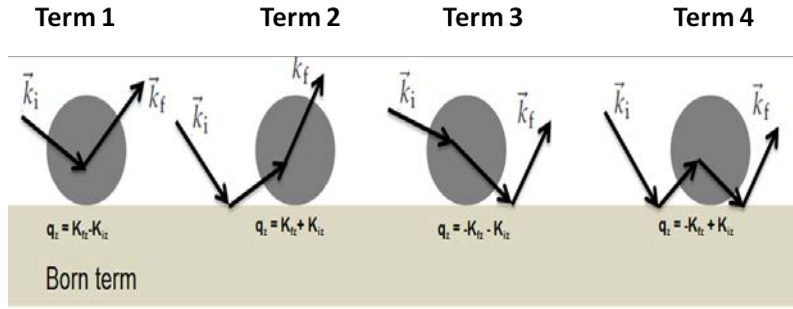


Figure 2.17.: Four events involved in the scattering process in GISAXS geometry. The first event corresponds to the simple Born approximation. While the other events shows reflection at the interface

of the scattering problem for the case  $\delta V(\vec{r}) = 0$  and the perturbation  $\delta V < V_1$  is treated analogue to the Born approximation, but instead of plane waves, the previously determined wave function is used. In GISAXS,  $V_1$  represents the one dimensional description of the layered structure for the sample, and  $\delta V$  collects all fluctuations in x and y direction.

In DWBA, the scattering field  $\psi'(\vec{r})$  due to the potential  $V$  is determined via applying BA to the scattering of the incident wave  $\psi(\vec{r})$

$$\psi'(\vec{r}) = \psi(\vec{r}) + \int d^3r' G_1(\vec{r}, \vec{r}'|E) (\vec{r}') \psi(\vec{r}') \quad (2.150)$$

The distorted incident wave is the outgoing wave solution and  $G_1(\vec{r}, \vec{r}'|E)$  is the Green function with the outgoing boundary condition for the same potential

$$\left[ \frac{\hbar^2}{2m} \nabla^2 - V_1(\vec{r}) + E \right] \psi(\vec{r}) = 0 \quad (2.151)$$

$$\left[ \frac{\hbar^2}{2m} \nabla^2 - V_1(\vec{r}) + E \right] G_1(\vec{r}, \vec{r}'|E) = \delta(\vec{r} - \vec{r}') \quad (2.152)$$

To satisfy the boundary conditions, it is required that the distorted wave function behaves in the asymptotic limit as a plane wave plus an outgoing wave

$$\psi(\vec{r}) \rightarrow e^{ikr} + \frac{1}{r} e^{ikr} f_k^1(\theta, \phi) \quad (2.153)$$

Thus, the total scattering amplitude  $f_k(\theta, \phi)$  in DWBA is given as

$$f_k(\theta, \phi) = f_k^1(\theta, \phi) + \delta f_k(\theta, \phi) \quad (2.154)$$

where  $f_k^1(\theta, \phi)$  is the scattering amplitude for the potential  $V_1(\vec{r})$

$$f_k^1(\theta, \phi) = -\frac{2m}{\hbar^2} \frac{1}{4\pi} \int d^3\vec{r}' e^{-ik'r'} V_1(\vec{r}') \psi(\vec{r}') \quad (2.155)$$

and  $\delta f_k(\theta, \phi)$  is calculated in BA  $\psi(\vec{r}) = \psi'(\vec{r})$

$$\delta f_k(\theta, \phi) = -\frac{2m}{\hbar^2} \frac{1}{4\pi} \int d^3\vec{r}' \psi'^*(\vec{r}') \delta V(\vec{r}') \psi'(\vec{r}') \quad (2.156)$$

In the following, the simplest DWBA formalism will be discussed. Here, the sample is assumed to be a flat interface, with a variety of nanoscale scattering objects distributed over it. Thus, the scattering intensity can be split into a Form Factor  $f(\vec{Q})$  and Structure Factor  $S(\vec{Q})$

$$I(\vec{Q}) = \left\langle |f(\vec{Q})|^2 \right\rangle S(\vec{Q}_{\parallel}) \quad (2.157)$$

In the BA, the Form Factor is simply given as

$$f(\vec{Q}) = \Delta\rho \int_V e^{i\vec{Q}\vec{r}} dV \quad (2.158)$$

The DWBA introduces additional terms to account for reflection and refraction effects. Figure 2.17 shows the four events involved in GISAXS scattering process. The first term is the BA, while the next three terms describe various specific multiple-scattering events. The various terms interfere coherently; thus the final scattering that is measured on the detector comes from their combination:

$$\begin{aligned}
F_{DWBA}(Q_{\parallel}, k_{iz}, k_{fz}) = & F(Q_{\parallel}, k_{iz} - k_{fz}) \\
& + r_F(\alpha_i)F(Q_{\parallel}, k_{iz} + k_{fz}) \\
& + r_F(\alpha_f)F(Q_{\parallel}, -k_{fz} - k_{iz}) \\
& + r_F(\alpha_i)r_F(\alpha_f)F(Q_{\parallel}, -k_{fz} + k_{iz})
\end{aligned} \tag{2.159}$$

The first term in the right side in the above equation belongs to (BA), while the other three terms belongs to (DWBA). It is obvious from the above equation that the higher-order contributions to the form factor are multiplied by the Fresnel reflectivity  $r_F$  because these terms involve reflection events.

$$r_F = \frac{k_z - \tilde{k}_z}{k_z + \tilde{k}_z} \tag{2.160}$$

where  $\tilde{k}_z = -\sqrt{n^2 k_0^2 - |k_{\parallel}|^2}$  and  $n$  is the complex refractive index of the substrate.

Using the effective form factor (equation 2.159), the total incoherent cross-section becomes:

$$\frac{d\sigma}{d\Omega} = \left\langle |f_{DWBA}(\vec{Q}_{\parallel}, k_{iz}, k_{fz})|^2 \right\rangle S(\vec{Q}_{\parallel}) \tag{2.161}$$

The detailed implementation of the DWBA for nanostructures is well discussed in the manual of the software package BornAgain [60], which is used for the simulation of GISAXS data in this work.

## 3. Instruments and experimental techniques

Methods for samples preparation and the characteristics of all instruments used for investigations in the framework of this thesis are briefly introduced in this chapter.

### 3.1. Sample preparation

The sample preparation and the NP assembly methods to create nano-structures or nano-crystalline objects can be divided into three categories depending on the growth strategy [1]. These are **(i) top-down**, **(ii) bottom-up**, and **(iii) virtual fab**. The **top-down** category is the most traditional way of miniaturization by breaking a large structure "manually" or via kind of self-structuring process into smaller structures until the dimensions reach the nanometer range. These processes include deposition and lithographic techniques. In all of these techniques, one needs external tools to get nano-sized structures. This approach is undesirable in industries because with decreasing size the manufacturing cost grows up.

An alternate way to the top-down approach is the **bottom-up** approach, where the structure is created by assembling nanostructure units into desired structures via interaction forces. For example, NPs having a size between 1 nm to 100 nm can be used to build monolayer or multilayer structures by controlling the aggregation process. The bottom-up methods include self-assembly or self-organization of nanostructures on templates, these methods are easier to access and cheaper compared with the top-down methods. Also, via these methods, one can produce uniform nanostructures with few defects and long-range orders. **Virtual fab** is the last category technique to create nano structures or nano-crystalline objects which is based on simulation and theoretical works in a virtual world as explained by Bader et al [61].

Self-assembly methods of nanostructure units like NPs into two- and three-dimensional ordered NPs are the simplest methods. In this thesis, various self-assembly methods have been used, as shown in figure 3.2.

### 3.1.1. Top-down methods

#### 3.1.1.1. Electron beam lithography (EBL)

One application of electrons beam is to create nanostructure by electron beam lithography technique and another application is imaging as will discuss later. EBL is a fundamental technique in nanofabrication, allowing the direct writing of structures down to sub-10 nm dimensions. Derived from the early Scanning Electron Microscopes (SEM), the technique briefly consists of scanning an electron beam over a surface covered by an electron sensitive material (e-beam resist) that changes its solubility properties according to the energy deposited by the electron beam. Here, in this section, just the writing process will be explained and the details of templates preparation for nanoparticles deposition will be explained later in chapter 4. Figure 3.1 shows the main steps involved in the EBL process. In the development step, the exposed or unexposed regions

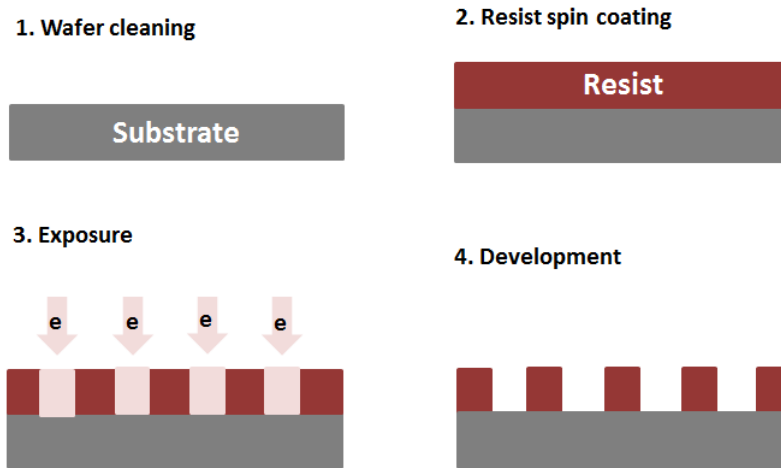


Figure 3.1.: Sketch of the major steps of EBL process.

are removed depending on the resist nature, either positive or negative tone. For negative resist, the portion exposed to the electron beam is insoluble in the developer due to the polymerization of the chemical structure of the photoresist when it is exposed to the e-beam, while for positive resist, the portion exposed to the electron beam is soluble in the developer due to the change in the chemical structure when the photoresist is exposed to the e-beam. By using negative resist, the material is first deposited and then the structure is created, while by using positive resist, the structure is created then the material is deposited. In the present study, only the positive photoresist was used. The common positive e-beam resists are Polymethylmethacrylate (PMMA) with 200K as a molecular weight and 4% dilution in chlorobenzene, PMMA with 950K molecular weight and 2% dilution in chlorobenzene, and CSAR 62 (AR-P 6200). The photoresist

is deposited on the substrate via the spin-coating method to ensure a homogeneous and uniform thickness of the resist over the whole sample area such that the focus does not change laterally while scanning the electron beam over the sample, especially while writing structures near or below 100 nm. The photoresist layer thickness depends on the rotational speed, time of rotation, and the atomic weight. However, the thickness becomes less by increasing the rotational speed and the time. It's crucial to mention that the corners and the edges of the sample should be avoided for lithography.

The patterns can be created by GDSII, DXF, ELM and ASCII text-editor database provided by the Raith Turnkey 150 software or Elphy software. The exact dimensions and the shape of the structure (lines, rectangles, circles...etc) can be drawn by these programs. For example, to make a rectangular pattern of groove width  $W$  and depth  $L$ , the electron beam is scanned over the length  $L$  along the width  $W$  with a step size  $d$ . The final dimension of the structure is determined by different parameters: **Dose factor**  $D$ , **beam current**  $I$ , and the time for writing each step (**dwelling time**  $\tau$ ) which is the same as the exposure time. The previous parameters are related by this relation:

$$\tau = \frac{Dd^2}{I} \quad (3.1)$$

The dwelling time is related to the fact that when electron beams impinge on the polymer chain (resist), try to break the bond and shorten it by transferring the energy. The broken polymer chains have smaller molecular weights and can be washed away in the subsequent development step. For a chemical change to happen in the polymer chain, certain exposure time is required. As developers used for positive resist are AR 600-546 for 60s, Isopropyl alcohol (IPA) for 30s to stop the development process and then Deionized water (DI) for 30s. From the previous equation, the development time is decided by the Dose factor, the beam current and the size of the nanostructures.

In this thesis, trenches were prepared using EBL, which were used as a template for nanoparticle self-assembly. This will be discussed in detail in chapter 4.

### 3.1.2. Bottom-up methods

#### 3.1.2.1. Drop-casting

The drop-casting method is one of the simplest techniques that can be used for sample preparation. Here, a certain volume of NP dispersion is dropped onto Si(100) substrates where it assembles on the substrate with different thicknesses. The obtained morphology of the NP assemblies using this method depends on the evaporation rate of the solvent as well as the amount of the NPs dropped on the substrate. The schematic picture for this method is shown in figure 3.2 (a).

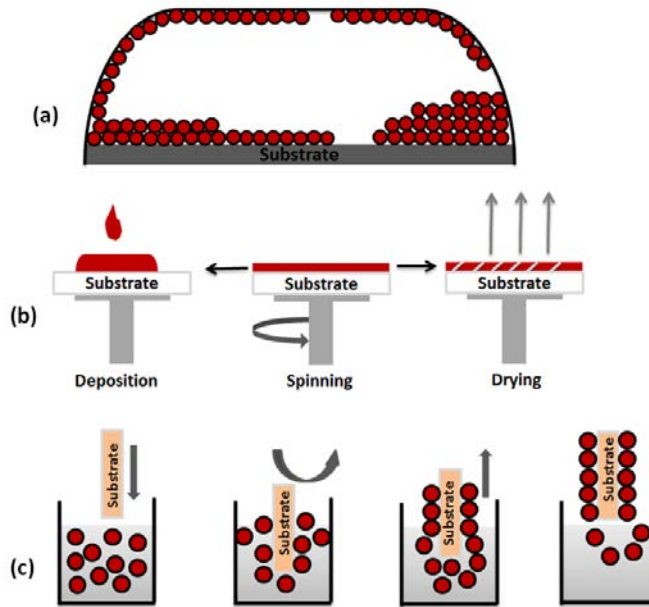


Figure 3.2.: Schematics of various methods for NP self-assembly used in this thesis: (a) Drop-casting, (b) Spin coating, (c) Dip coating.

### 3.1.2.2. Spin-coating

Here, the substrate is fixed on a rotating stage of a spin coating device, after that, the NP dispersion is dropped in the middle of the substrate, subsequently, it starts to rotate with suitable rotation speed and time. The thickness of the NP layer depends on the rotation speed, time and concentration of the NP dispersion. Figure 3.2 (b) shows the schematic picture for this method.

### 3.1.2.3. Dip-coating

The third method used in this study is dip coating. It consists of a few steps carried out directly after each other as shown in figure 3.2 (c). Here, the substrate is immersed in the NP solvent at a constant speed, keep it for a while inside the solvent and then pull it up with a constant speed. The NP layer deposits itself on the substrate while it is pulled up and the excess liquid will drain from the surface, during this time the evaporation of the solvent start. The thickness and the uniformity of the NP layer can be controlled by many factors: submer-sion time, withdrawal speed, number of dipping cycles, the composition and the concentration of the solvent.

### 3.2. Electron microscope

Electrons are an elementary ionizing radiations particles with a negative charge, which produces various signals when it interacts with a specimen. Different interactions can occur and various products can be obtained when the electrons hit the material, as summarized in figure 3.3. Depending on the detection methods, the wealth of different information about the specimen such as morphology, topology, topography (secondary electrons), crystal structure (elastically scattered electrons), and composition of a material can be achievable. The ba-

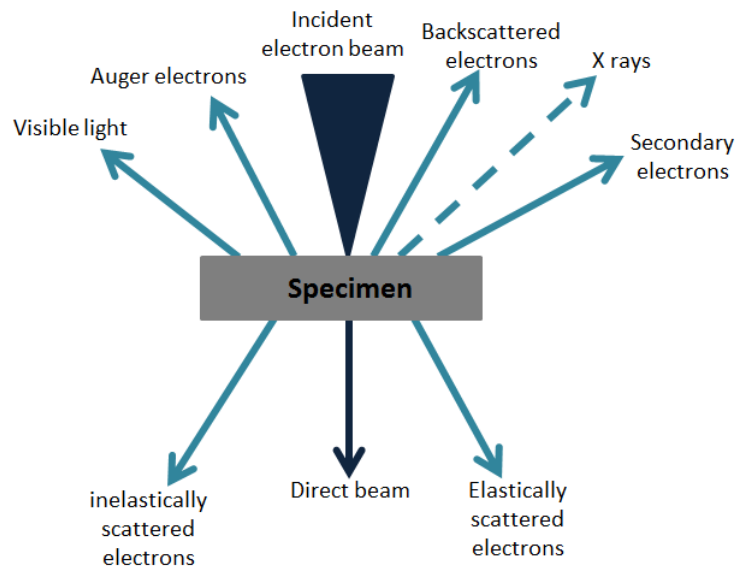


Figure 3.3.: Interaction of electrons with matter leading to several secondary effects.

One of the basic concepts of electron microscopy is that the accelerated electrons act not only as particles but also as waves. In the non-relativistic approximation, the de Broglie wavelength associated with an electron is

$$\lambda = \frac{h}{P} = \frac{h}{\sqrt{2m_e eV}} \quad (3.2)$$

Where,  $h$  is the Planck constant,  $P = \sqrt{2m_e eV}$  is the momentum,  $e$  is the electron charge and  $V$  is the accelerating voltage.

Electron microscopy usually operates in two different modes. The first mode is called scanning electron microscopy (SEM), which probes a bulk sample with smaller energies of the order of 20 keV and wavelength of the order of 0.00863 nm which is much smaller than the optical and x-ray wavelength. The other

mode is called transmission electron microscopy (TEM), which probes very thin specimen and operates at energies of the order of few hundred keV, in this case, the relativistic effect has to be taken into account and added to the wavelength expression as

$$\lambda = \frac{h}{\sqrt{2m_e eV \left(1 + \frac{eV}{2m_e c^2}\right)}} \quad (3.3)$$

### 3.2.1. Scanning Electron Microscopy (SEM)

One of the most common techniques for sample characterization, particularly to study the morphology of nanoparticles and thin films is Scanning Electron Microscopy (SEM). Using a focused beam of high energy electrons it produces direct space images of the sample with a resolution in the nanometer range. In SEM, a beam of electrons is produced at the top of the microscope by an electron gun. The electron beam is accelerated through high voltage (0.5-30 kV) and passes vertically through a system of apertures and electromagnetic lenses to produce a focused beam of electrons onto the sample. The beam scans the sample surface by scanning coils which direct the beam across the sample in a grid fashion manner. Once the beam hits the sample, which needs to be conducive to avoid charging effects, and it has to be dry and vacuum stable, secondary electrons are ejected from it via inelastic scattering and collected by a detector to provide information about the topography of the sample [62].

The schematic setup of the SEM device which consists of an electron gun, condenser lens, scanning coils and the objective lens is shown in figure 3.4. SEM consists of two separate regions, the electron column region and the sample chamber region which maintained at a lower vacuum and it is separated from the electron coulomb by a small valve and it contains the detector. While the electron region contains the source of the electrons and the lens system, and it is maintained at a higher vacuum to avoid any loss of electrons.

The SEM images shown in this thesis were obtained using the SU8000 Hitachi instrument at the PGI-7 institute (Peter Grünberg Institute for electronic materials). Its electron gun is designed for Cold Field Emission (CFE), where the electric field is applied to a very fine tungsten tip. This enables the electrons to overcome the work function and escape from the material. An alternative is a thermal emission, where the filament is heated to extract electrons. In addition, field emission can be thermally assisted, which is referred to as Schottky emission [63].

The electrons are generated at the top of the microscope by the electron gun. These are emitted when their thermal energy overcome the work function of the gun material. They are accelerated and attracted by the positively-charged

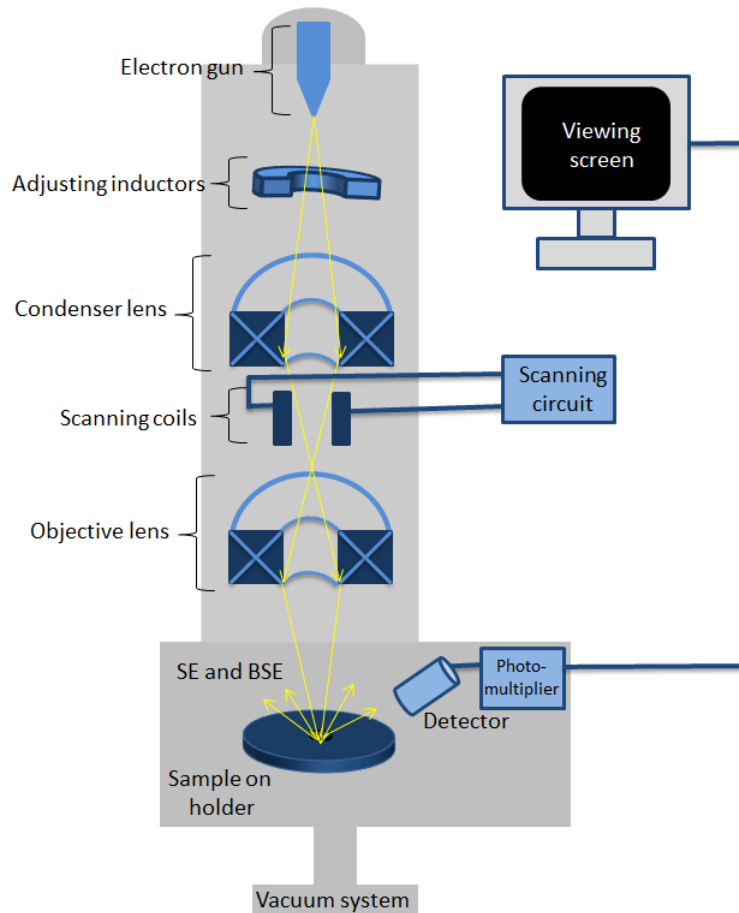


Figure 3.4.: Schematical setup for a scanning electron microscope.

anode. The electromagnetic lenses used to control the path of the electrons when current passes through the coils. The electromagnetic lenses consist of two types of lenses: the condenser lens which converges the beam before the electron beam cone opens again and it defines the resolution. The objective lens which converges the beam once more before hitting the sample and it focuses the beam onto the sample.

When the electrons interact with the sample, this can result in the generation of many different types of electrons or photons. In the SEM, two types of electrons used for imaging are the backscattered electron (BSE) mode and the secondary electron (SE) mode. The BSE's belongs to the primary electron beam and are reflected after elastic interaction between the beam and the sample. On the other hand, SE originates from the atoms of the sample due to the inelastic interaction between the electron beam and the sample. BSEs emerge from deeper regions of the sample while SE originates from surface regions (figure

3.5). Therefore, BSE and SE both carry different types of information. The BSE can probe the specimen composition due to the sensitivity to differences in atomic number. While the SE show very good surface details (topological contrast).

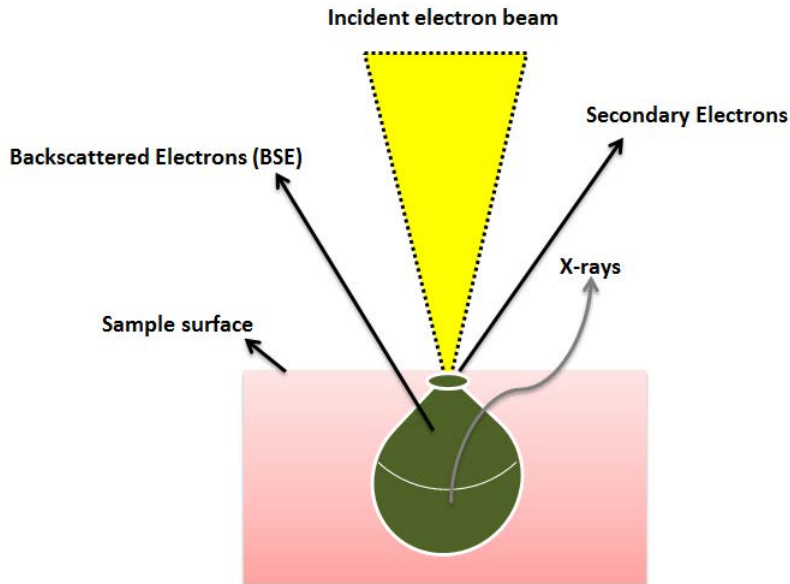


Figure 3.5.: Diagram explaining different types of signals emitted by the interaction between the incident electron beam and the sample surface and the area from which they originate.

### 3.2.1.1. Imaging

The resolution of the image depends on the magnification, i.e the area on the specimen scanned by the electron beam which is smaller than the display and the number of pixels of the detector. The resolution in the SEM is controlled by the size of the interaction volume and it is limited by spherical and chromatic aberrations in magnetic lenses. Also, at higher magnification, astigmatism play an important role. For a high magnification image, the alignment of the electron beam is important to get a better-focused beam at the sample. The alignment of the beam is carried out in different steps as explained in the following.

Firstly, at low magnification, the sample stage height from the end of the electron column is varied to get an optimum height and best focus. Then, the mechanical aperture is adjusted manually to have a circular and maximum exposure of the beam. Second, at high magnification an alignment of the lens

to ensure that the electron beam passes through the optical axis of the lenses. After all these adjustments, if an astigmatism is observed i.e. an inhomogeneous field in the deflection coil lead to an elliptical beam instead of a circular one, an eight pole electromagnet is housed in the objective lens to avoid this. The shape of the beam can be tuned, by adjusting the current in the electromagnet [64].

When the incoming electron beam interacts with the sample, different products are generating as shown in figure 3.3. The secondary electrons which are inelastically scattered from the sample are the only products that contribute to imaging. The penetration of the incoming electron beam depends on the electron energy, atomic mass and the density of the sample. As mentioned before, the resolution of the image depends on the interaction volume. In addition, it depends on the conductivity of the sample. The sample has to be conducive to prevent the accumulation of the electrostatic charge at the surface. These charges create a negative potential over the sample surface and this negative potential deflects the incoming electron beam and also changes the path of the secondary electrons. This produces artifacts in the imaging. The secondary electrons are accelerated towards the detector, then the generated photons are guided by light pipe and then hit a photomultiplier to generate photoelectrons which are then amplified and converted into an image by a CRT or CCD camera.

## 3.3. Magnetometry

### 3.3.1. Superconducting Quantum Interference Device (SQUID)

SQUID magnetometer is a very sensitive magnetometer ( $10^{-8}$  emu ( $10^{-11}$  Am<sup>-2</sup>) due to the special design of the detection coil and the Josephson junction, which is used for high-precision measurements of magnetic properties of tiny samples with tiny magnetic moments. Here, a vertical magnetic field from -7 to 7 T is available which is produced by a superconducting magnet. It also provides a high-precision temperature ranging from 1.9 - 400 K. SQUID uses the properties of electron-pair wave coherence and Josephson junctions to detect very small magnetic signals. The central elements of SQUID is a superconducting ring incorporated with a Josephson junction (figure 3.6).

In this study, a commercial SQUID magnetometer (Quantum Design, model MPMS XL) was used to study the macroscopic magnetization of our systems. The SQUID device is shielded by a magnetic shield from the external magnetic field and the sample space. SQUID is connected to the detection coil (pickup coil) around the sample space by superconducting wires. The detection coil used in our SQUID magnetometer is a second-order (second derivative) gradiometer as shown in figure 3.7 to avoid any background signal from a homogeneous field and it is surrounded by a superconducting magnet (type II) in order to get a

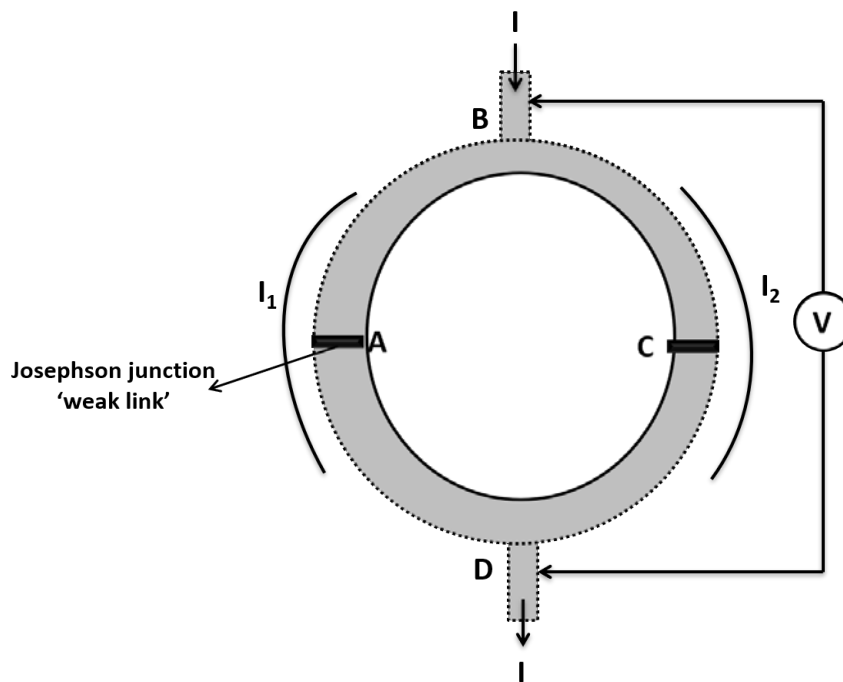


Figure 3.6.: Superconducting Quantum Interference Device (SQUID) as simple magnetometer.

uniform magnetic field over the sample. The upper and lower coils are rotating clockwise, while the two coils in the middle are rotating counter-clockwise. Due to this unique geometry, only the stray field is detected from the sample and any change in the field outside the coil is not detected. The sample is moved through the pickup coil where it is mounted in a drinking straw of diameter 9 mm and attached to the end of a sample rod. Then the sample rod is inserted into the sample space which is maintained at low pressure and filled with He gas in order to cool the sample.

### 3.3.1.1. Josephson junction

Josephson junction made of two superconductors connected through a small insulating layer (figure 3.8). It is inductively coupled to an rf circuit and it forms the foundation of the SQUID.

The magnetic flux quantization in a superconducting ring and the Josephson effect are the two fundamental physical properties that determine the SQUID function.

The magnetic flux inside a superconducting ring (figure 3.6) is quantized [64]

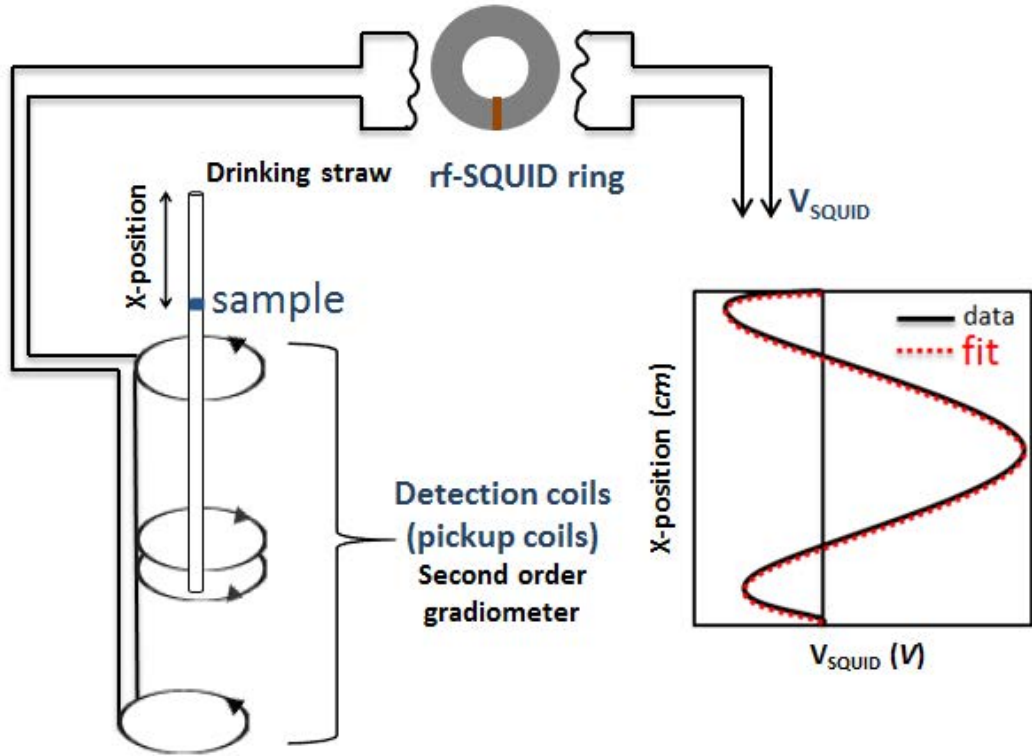


Figure 3.7.: Schematic setup of the detection system with second-order gradiometer for an rf-SQUID, the inset shows the response curve versus sample position fitted with a point dipole approximation. Inspired from [65]

and the total magnetic flux inside it is given by [66]:

$$\phi_T = \oint \vec{B} \cdot d\vec{s} = n\phi_0 \quad (3.4)$$

Where  $\vec{B}$  is the vector potential,  $n$  is an integer and  $\phi_0$  is the flux quanta given by:

$$\phi_0 = \frac{h}{2e} \approx 2.07 \times 10^{-15} Tm^2 \quad (3.5)$$

The interesting physics arises from the tunneling of Cooper pairs (electron-electron pair) across the insulating barrier. The phenomenological superconductors wave functions can be written as [66]:

$$\psi(\vec{r}) = \sqrt{n_s} \cdot \exp(i\phi(\vec{r})) \quad (3.6)$$

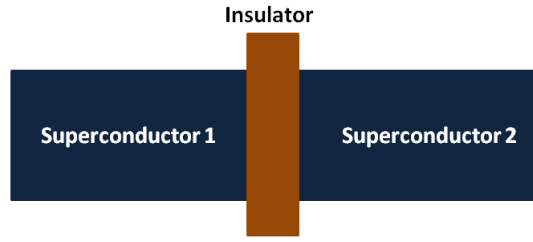


Figure 3.8.: A Josephson junction: It is made of two superconductors connected through a small insulating layer.

where  $\phi(\vec{r})$  is the phase factor and  $n_s = \psi \cdot \psi^*$  is the Cooper pair density. The current density through the barrier (insulator) separated the two superconductors can be written as:

$$I = I_0 \sin(\delta) \quad (3.7)$$

Where  $I_0$  is the critical current density and  $\delta = \phi_2 - \phi_1$  is the phase difference between the two superconductors.

The above equation is known as the first Josephson equation and describes how the tunneling current depends on the phase difference between the two superconductors.

If a voltage  $V$  is applied across the Josephson junction, then the current density can be written as:

$$I = I_0 \sin(\phi_2 - \phi_1 - \omega t) \quad (3.8)$$

Where  $\omega$  is given by:

$$\omega = \frac{2eV}{\hbar} \quad (3.9)$$

The above equation is known as the second Josephson equation which tells that the current oscillates with a frequency  $\omega$ .

### 3.3.1.2. Modes of measurements

Quantum design provides two different transport options to be used for measurements with the MPMS. One is transported DC option and the other is Reciprocating Sample Option (RSO) transport option. The DC option is the

default mode in MPMS and is a part of the base system and performs the stepped DC scan. The RSO transport option is primarily used for samples with a small magnetic moment which offers a relatively fast type of measurement and allows more averaging and better noise rejection than the DC option. The RSO option is more preferred for routine magnetic measurements because it can perform both the stepped DC scan and the RSO scan. Furthermore, the RSO is cheaper in construction but less sensitive than DC. In the DC technique, the sample starts at the lowest point of the scan length and sequentially it moves upward through the superconducting pickup coils and it is returned to the starting point at the end of each scan. While in the RSO technique, the sample starts in the middle of the scan length and it moves down, up then back down to stop in the center. The DC SQUID contains two parallel Josephson junction (figure 3.9a), while the RSO SQUID contains one Josephson junction (figure 3.9b). In

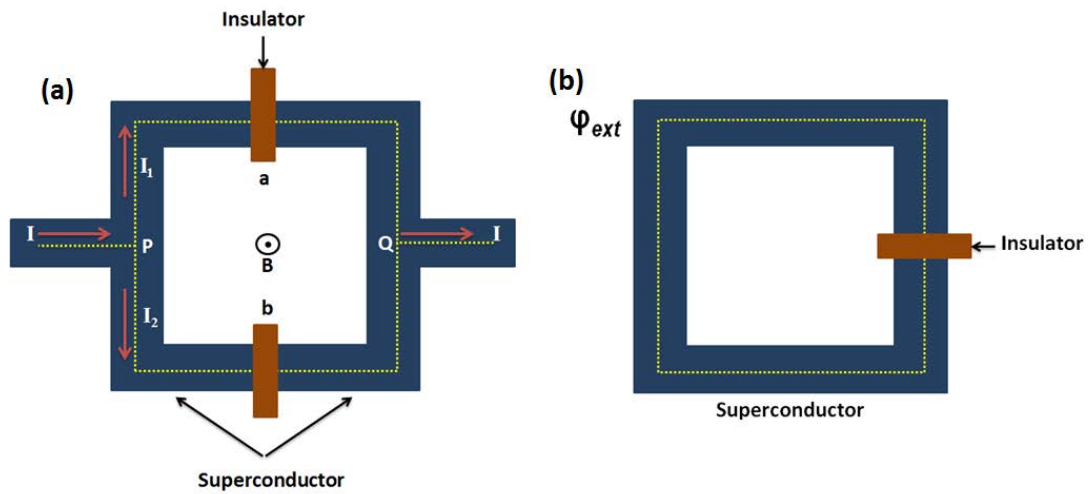


Figure 3.9.: (a) A DC SQUID is made up of two Josephson junctions a and b connected in parallel, (b) RSO SQUID is made of one Josephson junction superconducting loop in an external magnetic field.

the DC SQUID the direct current  $I$  is the sum of currents  $I_1$  and  $I_2$  along two branches, which is given by

$$I_1 = \frac{I_0}{2} \sin \delta_a \quad (3.10)$$

$$I_2 = \frac{I_0}{2} \sin \delta_b \quad (3.11)$$

Where  $\delta_a = \delta_0 + \frac{q_e}{\hbar}\phi$  and  $\delta_b = \delta_0 - \frac{q_e}{\hbar}\phi$ .

In the presence of a magnetic field  $\vec{B}$ , a magnetic flux  $\phi$  is created and results in a phase difference in the current of the superconductors. The difference is given by:

$$\delta_a - \delta_b = \frac{2q_e}{\hbar}\phi \quad (3.12)$$

Then the total current can be written according to equation 3.7 as:

$$I = I_0 \sin \delta \cos\left(\pi \frac{\phi}{\phi_0}\right) \quad (3.13)$$

Where  $\phi_0 = \frac{h}{2q_e} \approx 2.07 \times 10^{-15} \text{ Tm}^2$ .

An oscillation in the current is produced due to change in applied magnetic flux. The internal flux inside the SQUID  $\phi_i$  jumps in steps by factors of  $\phi_0$  if the applied magnetic flux more than  $\frac{1}{2\phi_0}$  because the internal flux  $\phi_i$  which is quantized, is related to the applied magnetic flux. These steps determine how sensitive a DC SQUID can be.

For RSO SQUID, the total flux quantization is given by [66]:

$$\phi = \phi_e - LI \quad (3.14)$$

Where  $\phi_e$  is the external flux due to the rf oscillating circuit, L is the inductance and I is the current flowing in the loop.

The phase change around the loop is given as

$$\delta + \frac{2q_e}{\hbar} \oint \vec{B} \cdot d\vec{s} = \delta + \frac{2q_e}{\hbar}\phi \quad (3.15)$$

Where  $\delta$  is the phase difference across the junction.

The phase change around the loop in equation 3.12 must be equal  $2\pi n$ , then  $\delta$  is given by

$$\delta = 2\pi n - \frac{2q_e}{\hbar}\phi = 2\pi n - 2\pi \frac{\phi}{\phi_0} \quad (3.16)$$

Then the current in the loop becomes

$$I = I_0 \sin \delta = I_0 \sin\left(2\pi \frac{\phi}{\phi_0}\right) \quad (3.17)$$

From equation 3.14 the current is given by

$$I = \frac{\phi - \phi_e}{L} \quad (3.18)$$

A stable flux state will be obtained when equation 3.14 and 3.15 are satisfied simultaneously.

The flux  $\phi$  through the loop can be written as [66]:

$$\phi = \phi_e - LI_0 \sin\left(2\pi \frac{\phi}{\phi_0}\right) \quad (3.19)$$

The magnetic flux jumps from one quantum level to another, only when the current equal the critical current. To use SQUID as a detector for magnetization, it is coupled inductively to an external LC rf oscillating circuit (figure 3.10), where the resonance frequency of this circuit is given as  $\omega_0 = \frac{1}{\sqrt{LC}}$ . The inductance L and the capacity C comes from the superconducting loop and the Josephson junction of the SQUID ring. The SQUID ring is coupled to the signal that transferred from the pickup coil. The current that transferred from the pick-up coil creates an additional magnetic flux which penetrates the SQUID ring, due to this, a current is generated inside the superconducting ring which reduces the total flux inside it. In this thesis an rf SQUID based on the above principle was used for the magnetization measurement.

### 3.3.1.3. Theory of operation

The magnetic signal of the sample is obtained via a second-order gradiometer superconducting pick-up coil with four windings (figure 3.7). This coils with a SQUID antenna (orange in figure 3.10) forms a part of the whole superconducting circuit transferring the magnetic flux from the sample to an rf SQUID device, which is located away from the sample in liquid helium path. The rf SQUID device acts as a magnetic flux-to-voltage converter (black in figure 3.10). The output voltage amplified and read out by the magnetometer's electronics (green in figure 3.10). When the sample is moved up and down through the pickup coils, it produces an alternating magnetic flux in the pick-up coils which

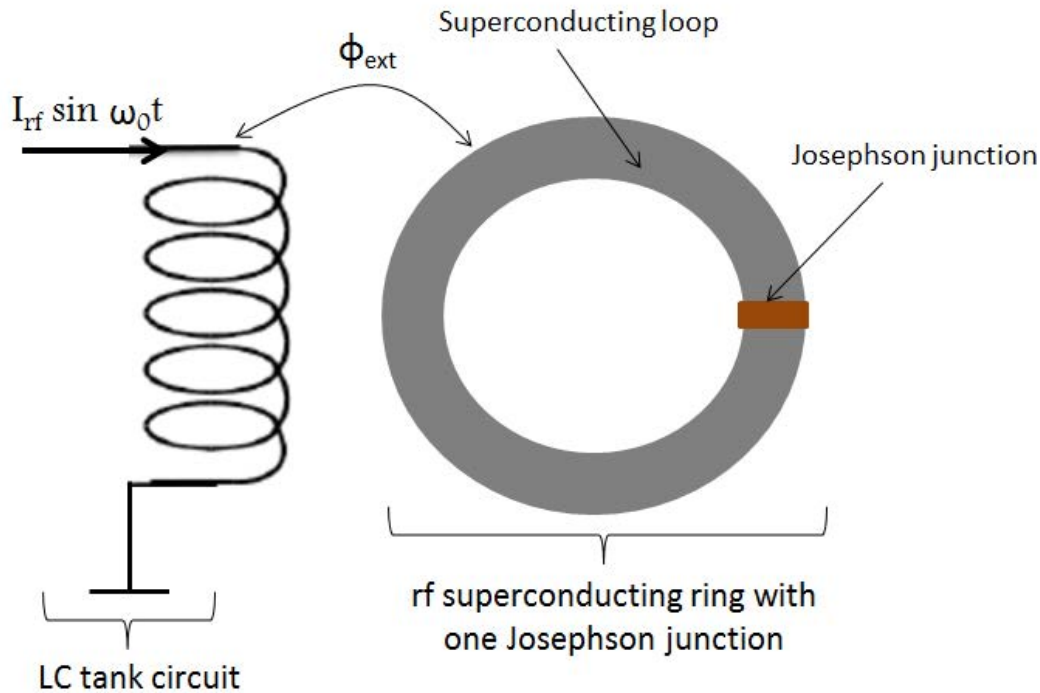


Figure 3.10.: Schematic diagram of an rf SQUID with one Josephson junction.

leads to an alternating output voltage of the SQUID device. The flux changes and the SQUID sensors provide a response curve for voltage versus distances as shown in figure 3.7. "MPMS MultiVu" software used to measure the response curve. Then the response curve is fitted with a theoretical curve of a single point dipole, the sample position can be specified. Then the "MPMS MultiVu" software calculates the magnetic moment of the sample using a measurement algorithm. This method works for both options of the SQUID magnetometer.

#### 3.3.1.4. Measurement Procedures

To get information about the magnetic ordering of the magnetic nanoparticles and other properties (e.g. the blocking temperature  $T_B$ ), temperature-dependent magnetization has been measured via Zero Field Cooled (ZFC)- Field Cooled (FC) measurement procedure (figure 3.12). ZFC magnetization curves are measured after the sample is cooled from high temperatures (here 400 K) to a low temperature (here 5K) in the absence of a magnetic field. After that small magnetic field is switched on and the magnetization of the sample is recorded during heating up to the maximum temperature. For an FC magnetization curve, the magnetization of the sample is measured during cooling the sample from high temperature to low temperature in the presence of a magnetic field.

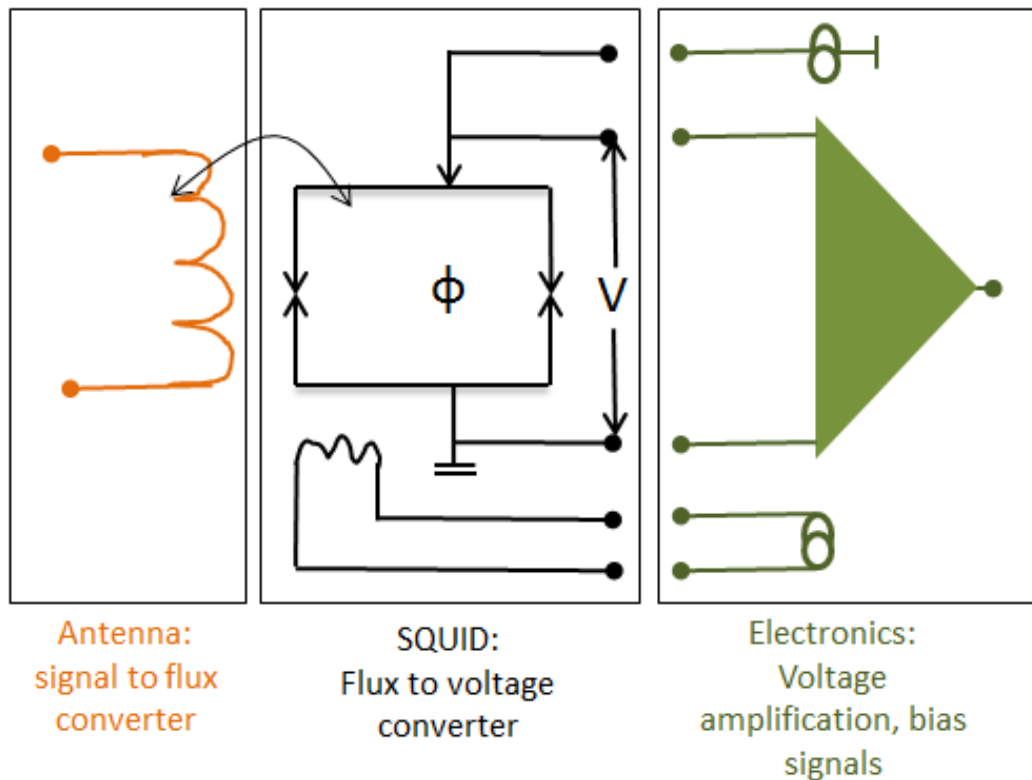


Figure 3.11.: SQUID = flux to voltage converter

Furthermore, field dependent magnetization curves,  $M(H)$ , were measured via changing the magnetic field at a constant temperature.

### 3.4. X-ray instruments

Generally, X-rays are conventionally generated by x-ray tubes in laboratories when the matter is irradiated by a beam of high-energy charged particles such as electrons. In an x-ray tube, a filament is heated to produce electrons which are then accelerated towards the anode which is positive. Then the electrons knock out core electrons from the anode, which gives rise to x-ray radiation. X-rays are guided up to the sample, where it pass through a monochromator and slits to obtain a monochromatic and well-collimated beam. The size of the beam can be defined by slits before the sample depending on the experimental requirements.

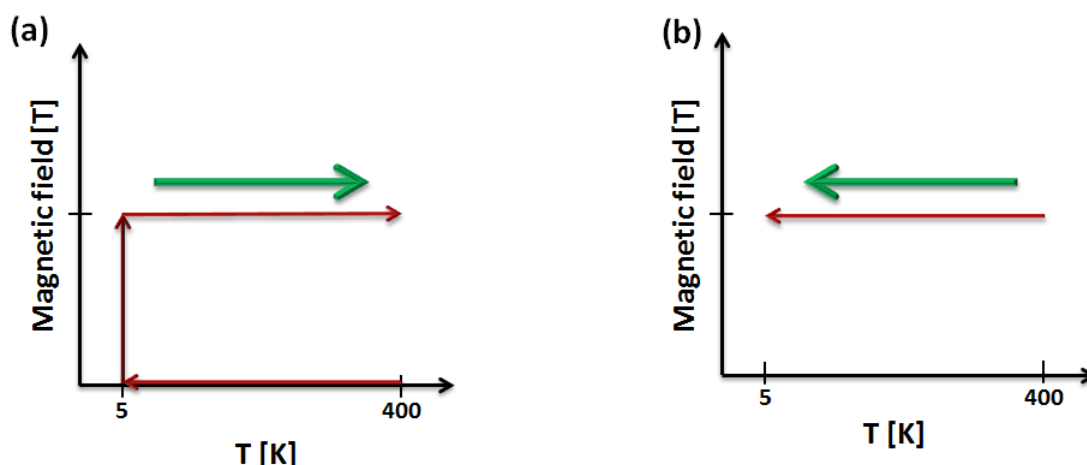


Figure 3.12.: Measurement procedures for (a) zero field cooling and (b) field cooling, where green arrows mark the paths along which the magnetization is recorded.

### 3.4.1. Gallium Anode Low-Angle X-ray Instrument (GALAXI)

The JCMS GALAXI (Gallium Anode Low-Angle X-ray Instrument) diffractometer at Forschungszentrum Jülich, is a high brilliance laboratory small-angle X-ray scattering instrument [67]. Figure 3.13 shows the main components of GALAXI. Chemical correlation at nanometer and mesoscopic length scales in bulk materials and structures deposited on a surface can be investigated by using this instrument.

Here, a Metaljet source built by Bruker AXS is used to produce X-rays with a wavelength of 0.13414 nm. An electrons beam at 70 keV energy and 200 W power hits the liquid metal jet composed of GaInSn alloy, and then x-rays are produced. After Parabolic Montel optics, monochromatic  $\text{GaK}_\alpha$  radiation with an energy of 9243 eV is achieved. Afterward, the beam size can be defined and collimated with an inclination of  $0.4^\circ$  by using two slits S1 and S2 separated by 4 m distance. After that, a third slit S3 is used to reduce the background. At the sample position, a beam with a flux of  $10^9$  photons/ $\text{mm}^2$  hits the sample and the scattered photons are detected by a Pilatus 1M 2D position-sensitive detector with  $169 \times 179 \text{ mm}^2$  active area. The X-ray flight path between the X-ray source and the detector is fully evacuated. Different Q-ranges can be detected by changing the sample to detector distance between 835 mm to 3535 mm in 5 steps, and thus structure with different correlation sizes up to 200 nm can be studied. GALAXI has different applications in the hard matter field as well as in soft matter field. Hard matter applications include determination of the size and size distribution of nanoparticles in solutions or deposited on surfaces as well as the ordering between those nanoparticles, also reflectometry measurement

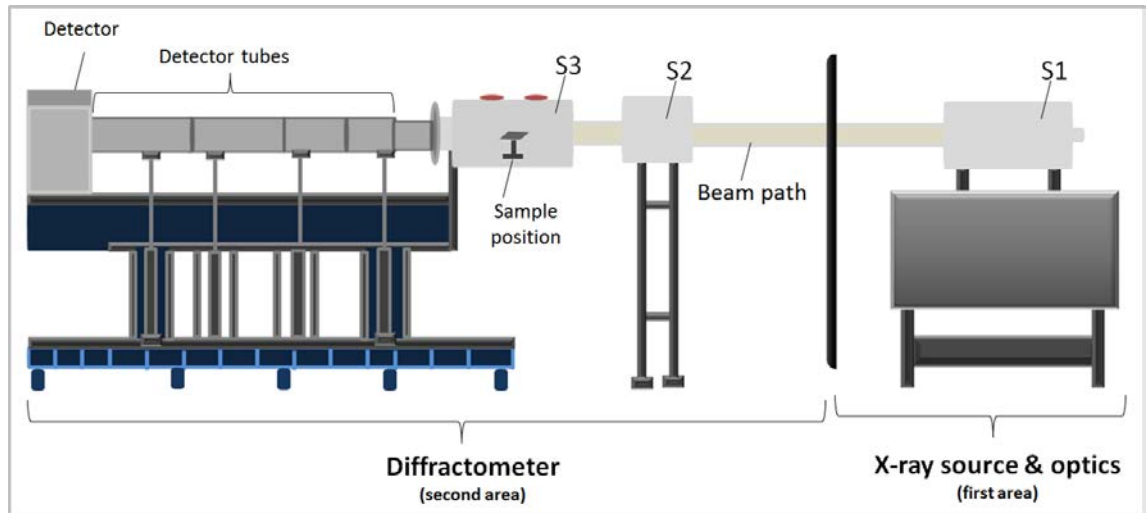


Figure 3.13.: Schematic drawing of GALAXI showing its main components.

for layered thin films, in order to determine the thickness of the layers and the interfacial profiles. Soft matter applications include nanocomposite materials and polymers with different topology.

#### 3.4.1.1. Small Angle X-ray Scattering (SAXS)

In SAXS experiments as presented in this work, the X-ray beam with a small spot size is directed towards the nanoparticles dispersion, which is filled in quartz glass capillaries (Hilgenberg GmbH) with 1.5 mm outside diameter to reduce multiple scattering events in the dispersion and 0.01 mm wall thickness, which is closed by a silicone ball was added by using a silicone gun to allow the measurement of the dispersions in a vacuum. The scattered intensity is recorded on a position-sensitive detector at a sample-to-detector distance  $L_{SDD}$  behind the sample. All SAXS measurements in this thesis are performed in transmission geometry with two different detector distances, short detector distance of 835 mm and long detector distance of 3535 mm were measured. By GALAXI, multiple samples can be measured automatically under the same set up over a day, the capillaries are placed in a sample holder that can hold up to 11 capillaries as shown in figure 3.14. To bring the respective capillary of the dispersion of interest into the beam path, the sample holder can be shifted vertically. The capillaries filled with the solvent and the nanoparticle dispersions as well as an empty capillary is measured under the same conditions as a reference sample for the subtraction of the background.

In order to determine the beam center and the sample-to-detector distance, silver behenate (AgBH) is measured for a short time 120s. AgBH generates



Figure 3.14.: Samples of SAXS experiments filled in a samples holder that can move vertically for automatic measurement of multiple samples over a day.

sharp rings at multiples of a scattering vector with magnitude  $Q_{AgBH} = 1.076 \text{ nm}^{-1}$ . Thus, by doing the azimuthal integration of the detector data, as shown in figure 3.15, both the beam center and the sample-to-detector distance can be determined quickly. The distance  $L_{SDD}$  is obtained by determining whether the peak center positions are truly at multiples of  $Q_{AgBH}$ . To load the raw tif file obtained from the detector and for the coordinate transformation, Fit2D software is used [68].

Furthermore, in order to put the count rate of the detector into absolute units of  $\text{cm}^{-1}$ , a pre-characterized calibration sample needs to be measured to determine the conversion factor. For this purpose, a fluorinated ethylene propylene (FEP) (Dupont, USA) is measured at the largest sample-to-detector distance, which produces a broad ring on the detector where the peak value  $I_{FEP}^{peak}$  in figure 3.16 (left) is compared to the numeric value obtained from ESRF beam line,  $\left(\frac{d\Sigma}{d\Omega}\right)_{peak}^{ESRF} = 6.6577 \pm 0.0019 \text{ mm}^{-1}$ . The transmission of FEP at the wavelength of GALAXI is  $T_{FEP} = 0.52$  and its thickness is  $d_{FEP} = 0.035 \text{ cm}$ . The absolute unit calibration of SAXS data is performed according to the procedure in appendix D.

The thickness and the transmission for each sample, are determined by a vertical scan ( $P_z$ ) of the samples and measuring the intensity of the beam on a single-pixel detector as shown in figure 3.16 (right). The vertical scan provides the intensity of the direct beam, the blocked beam and the profile of the sam-

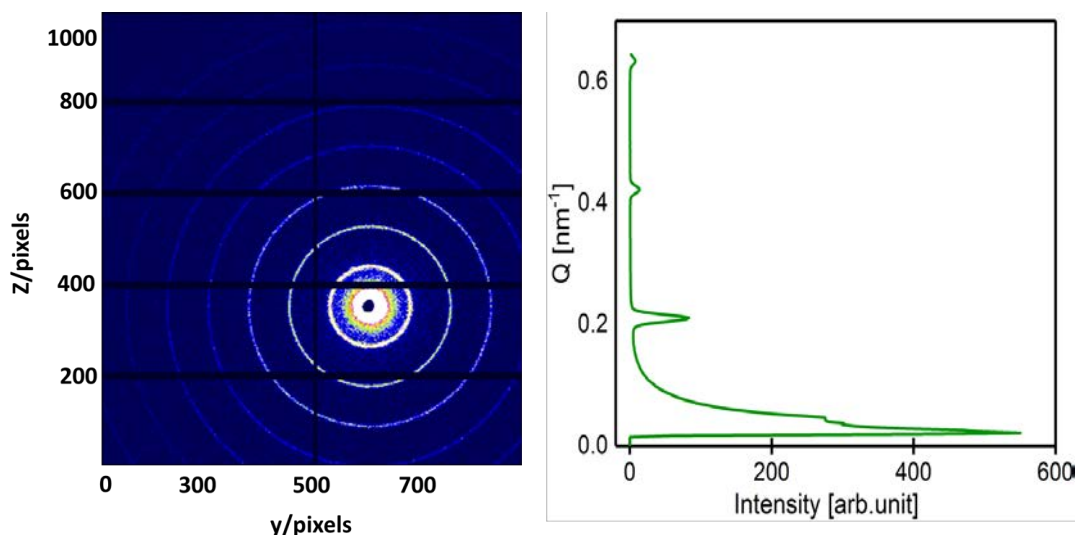


Figure 3.15.: AgBH calibration to determine the beam center and the sample-to-detector distance. In the left, the measured intensity recorded on the detector. on the right, the transferred measured intensity to polar coordinates, where from the projection on  $Q$ , the optimal parameters for beam center and sample-to-detector distance are determined.

ples. The scan value at the position where the sample is measured provides the transmission value of the sample by butting the transmission of the direct beam ( $T_{D,beam}$ ) to one and the transmission of the blocked beam ( $T_{B,beam}$ ) to zero. While the width of the sample ( $D_{sample}$ ) is determined from the obtained width value from the sample profile at the half transmission value between the maximum sample profile transmission ( $T_{sample}$ ) and the determined transmission value at the center.

To obtain the scattering from the nanoparticles, the scattering from the solvent and the capillary need to be subtracted from the sample as shown in appendix D. Each sample is measured at two sample-to-detector distance: short sample-to-detector distance to increase the measured range of the magnitude of scattering vector  $Q$  and large sample-to-detector distance to study the low  $Q$  range. The data from both distances are merged into a single data set for modeling a form factor to determine the sample structure.

A typical SAXS setup used in GALAXI (Sec.3.4.1) is shown below in figure 3.17: a Metaljet source emits a beam of X-rays which is focused and monochromatized by Parabolic Montel optics. The size of the beam is adjusted by a system of slits ( S1 & S2), then the beam hits the sample and enters the flight path, which has to be under vacuum because air scatters the beam. The symmetric pattern on Pilatus 1M 2D position-sensitive detector produced, which is radially averaged to give the typical plots of diffracted intensity versus scattering vector

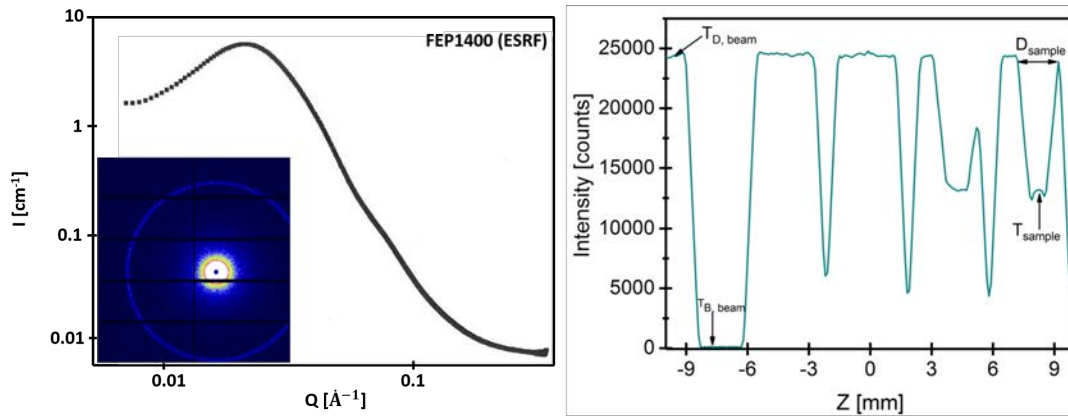


Figure 3.16.: Scattering curve of FEP measured by the ESRF (left) and the vertical scan of the sample holder (right) from which the sample transmission and the width can be determined to scale the data to absolute unit.

$Q = \frac{4\pi}{\lambda} \sin \theta$ . The  $Q$  dependent intensity curves were fitted using the "SasView" software to find a suitable form factor. From SAXS data, information about the shape, mean size and size distribution of the nanoparticle can be obtained.

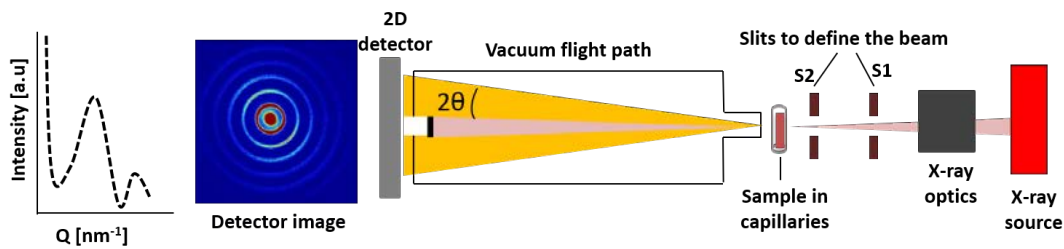


Figure 3.17.: Illustration of SAXS measurement principle, where the beam comes from right to left.

### 3.4.1.2. Grazing Incidence Small Angle X-ray Scattering (GISAXS)

In this work, small-angle x-ray scattering under grazing incident (GISAXS) measurements have been performed for multiple samples presented in this work. The measurement has been performed in reflection geometry. For the experiment, the sample is placed on a flat holder as shown in figure 3.18, that can be adjusted with two translational (along  $y$ -axes and  $z$ -axes) and two rotational ( $\alpha$  and  $\beta$ ) degrees of freedom as shown in the geometry of the GISAXS experiment (figure 3.19). The sample holder can be moved in a vertical direction to center the sample and in the plane to set the beam at the center of the sample. Fur-

thermore, to set the desired incident angle, the sample stage is tilted and while moving the stage, multiple scans of the beam transmission are performed to center the sample first and to be sure that the zero angle corresponds to the flat sample orientation. Usually, the incident angle is set close around the critical angle of the total reflection of the studied material.

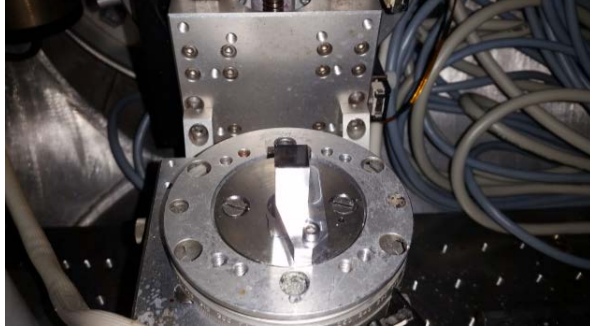


Figure 3.18.: The sample holder for the GISAXS experiment that can be tilted and moved in three dimensions.

During the measurement, a monochromatic X-ray beam with an incident wave vector  $\vec{k}_i$ , which lies in the XZ, plane is directed on a sample surface with a very small incident angle  $\alpha_i$  with respect to the surface. The X-ray is reflected off the substrate surface, scattered from the particles along  $\vec{k}_f$  in the direction  $(\alpha_f, \theta)$ . The Z-axis defines the out-of-plane component of the scattering vector while Y-axis defines the in-plane component of the scattering vector. The condition  $\alpha_i = \alpha_f$  satisfies the specular reflection condition. The scattered intensities lie on the YZ plane are detected by a 2D detector. The samples were measured for a few hours at one fixed angle until sufficient counting statistics are obtained. To remove the horizontal stripes in the scattering data, the detector is shifted five times vertically during the measurement. The data obtained from GISAXS measurement as an image file where the scale is defined by the pixels. However, to obtain information about the nanoparticle size, shape and crystallite size one has to convert the images on the reciprocal scale. At first, one has to convert pixels to angles by knowing information about the position of the direct beam  $(y_c, z_c)$ , sample to detector distance ( $L_{SDD}$ ) which can be determined from AgBH as described before in Sec. 3.4.1.1. By knowing the beam center and  $L_{SDD}$ , the scattering angles are determined from the geometry in figure 3.19 for each pixel on the detector with  $(y, z)$  coordinate

$$\theta = \arctan\left(\frac{(y - y_c)d_{pix}}{L_{SDD}}\right) \quad (3.20)$$

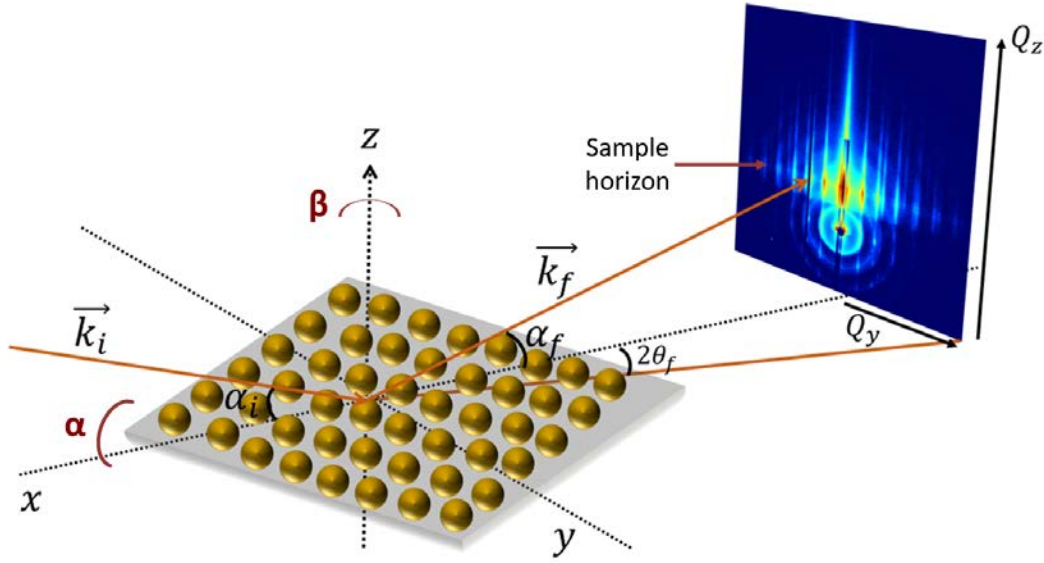


Figure 3.19.: Three dimensional view of the geometry of the GISAXS measurements along the x-axis on the yz plane with the scattering angles.

$$\alpha_f = \arctan\left(\frac{(z - z_c)d_{pix}}{L_{SDD}}\right) \quad (3.21)$$

where  $d_{pix} = 0.172$  mm is the pixel size of the detector. From the scattering angles, the scattering vector coordinates can be given as:

$$Q = \frac{2\pi}{\lambda} \left\{ \begin{array}{l} (\cos(\alpha_f) \cos(2\theta_f) - \cos(\alpha_i)) \\ \cos(\alpha_f) \sin(2\theta_f) \\ (\sin(\alpha_i) + \sin(\alpha_f)) \end{array} \right\}$$

Only small angles are involved in GISAXS, therefore the trigonometric functions in the previous equations can be approximated by  $\cos(x) \approx 1$  and  $\sin(x) \approx x$ , which yields to first approximation"

$$Q = \left\{ \begin{array}{l} 0 \\ \frac{2\pi}{\lambda} \left( \frac{(y - y_c)d_{pix}}{L_{SDD}} \right) \\ \frac{2\pi}{\lambda} \left( \frac{(z - z_c)d_{pix}}{L_{SDD}} \right) \end{array} \right\}$$

From the GISAXS data, different characteristic length scales from the peaks periodicity and peak widths can be determined. As well as, GISAXS data is studied by comparison with a calculated model for the diffuse scattering in the framework of the distorted-wave Born approximation. Therefore, the software package BornAgain [60] is used to formulate and calculate specific nanostructure models. The experimental data can be compared with the simulated data in order to obtain the desired information.

#### 3.4.1.3. X-ray Reflectometry (XRR)

XRR measurements described in this thesis have been performed at GALAXI instrument. It is an analytical non-destructive technique used to analyze X-ray reflection intensity curves from grazing incident X-ray beam to determine the parameters of a single nanoparticle layer or multi-layer including thickness, density, and surface or interface roughness using the effect of total external reflection of X-rays.

In XRR experiments, the X-ray reflection of a sample is measured around the critical angle. The X-ray beam reflected by a sample at grazing incidence angles, where below the critical angle of total external reflection, it penetrates only a few nanometers into the sample and above this angle, the penetration depth increases rapidly. In XRR, the electron density changes at every interface, where a part of the X-ray beam is reflected. The interference of these partially reflected X-ray beams creates an oscillation observed in the reflectivity curve.

When the X-rays incident on a flat surface of a material at a grazing angle is smaller than the critical angle for the total reflection of the material, it undergoes total reflection. Thus, XRR is related to the values of the refractive index and X-ray wavelength.

Figure 3.20 shows a simple geometry of XRR measurement for a simple system consisting of a single homogeneous film on top of a homogeneous substrate, the incoming X-ray beam has to pass through two interfaces: first the air/film interface and second the film/substrate interface. At each interface, one part of the beam is reflected while the remaining part is continuing its original path (transmitted). The reflected beam at the lower interface have to travel a longer distance than the beam reflected at the upper interface. Since X-rays can be considered as electromagnetic waves, this path difference results in a phase shift between X-rays reflected at the upper and at the lower interface. This path difference however changes when changing the incident angles. Therefore, oscillation can be observed. The distance between two maxima or two minima ( $D = \frac{2\pi}{Q}$ ) directly proportional to the film thickness.

In a typical X-ray reflectometry experiment on GALAXI, a sample is placed

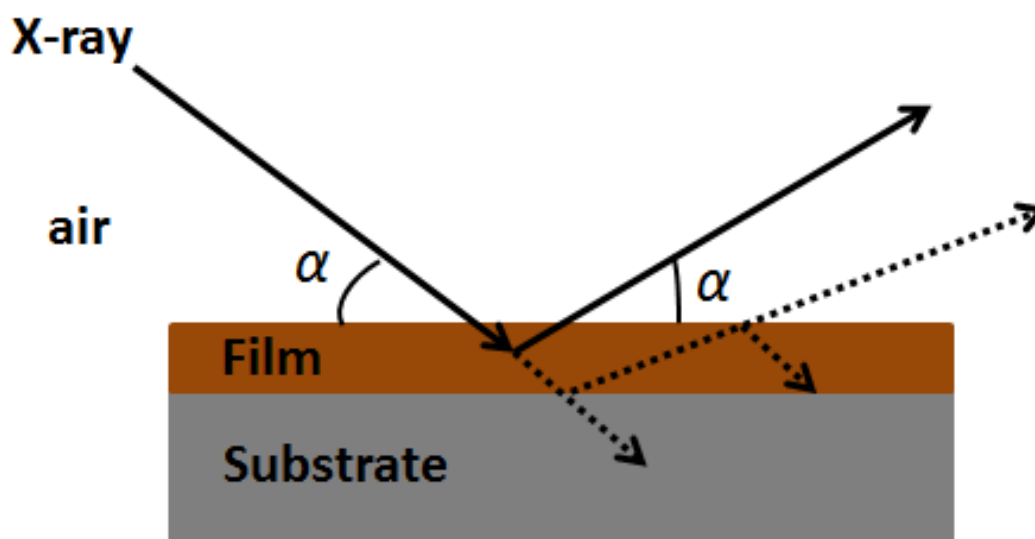


Figure 3.20.: Schematic of X-ray reflectometry measurement.

on a flat holder that can be moved in the vertical direction to center the sample and in the plane to set the beam at the center of the sample. Furthermore, it can be tilted to set the desired incident angle. To center the sample, three alignment procedures are performed. The sample holder at the beginning is moving in the vertical direction to center the sample, then followed by a horizontal scan to set the beam at the center of the sample. The measurement usually performed at a short sample detector distance for observing a wide  $q$ -range and under specular condition. In an experiment, the XRR profile is then obtained by mutually moving and counting the scattered X-rays under a specular condition with respect to the incident angle.

The investigation of the reflectivity curve has been performed by determination models of vertical scattering length density profiles, which reproduce the characteristics and the required information from the data. The phase of the reflectivity can't be recorded from the XRR measurement, thereby, it is not possible to uniquely deduce from the measured intensity the scattering length density profile. Therefore, a reasonable profile must be determined that is consistent with the measured intensity.

Typically, the measurements have been performed with two periods, first period with low counting time ( $t \approx 5$  s / step) which produce the low  $Q$ -range data and second period with high statistics ( $t \approx 121$  s / step) which reproduce the high  $Q$  data. Usually, a range of  $\theta = 0^\circ - 2^\circ$  is measured in this thesis in a step size of  $0.002^\circ$ , which corresponds to a  $Q$  range of  $0 - 3$   $\text{nm}^{-1}$ .

### 3.5. Neutron techniques

Neutrons are electrically neutral, have a diameter of  $\approx 1.7 \times 10^{-15}$  m and usually penetrate matter easily. Neutrons are produced by nuclear fission or by spallation. In this study, the neutron measurements were performed by using neutrons produced by fission of uranium produced from the fuel elements "nuclear reactor, FRM II" which is located in Garching, Germany.

Nuclear fission includes splitting of the nucleus of heavy atoms into two or more smaller, lighter nuclei. Neutrons and gamma photons and huge amounts of energy are released due to the fission process.

Neutrons are guided up to the sample via neutron guide through bundled reflection. Monochromators and slits are used to obtain a monochromatic and well-collimated beam. The size of the beam can be defined by slits before the sample, depending on the experimental requirements.

#### 3.5.1. Magnetic reflectometer MARIA

The magnetic reflectometer MARIA with a high incident angle, is a neutron reflectometer with polarization analysis, which is operated by the Jülich Center for Neutron Science (JCNS) at Heinz Maier-Leibnitz Zentrum (MLZ) in Garching, Germany [69]. It is designed to study samples with a layer thickness of 0.3 – 30 nm and can be used in GISANS mode to study lateral structures in the range from nm to  $\mu\text{m}$ . Furthermore, the structures of a thin magnetic layer up to monolayer can be investigated by using this instrument. The sample sizes are typically in the order of  $10 \times 10 \text{ mm}^2$  and using a monochromator (Velocity selector), the wavelength of the neutrons can be chosen in a range of  $\lambda = 4.5 \text{ \AA}$  to  $10 \text{ \AA}$  for polarized neutrons, with the highest intensity at  $4.5 \text{ \AA}$  and in the range from  $4.5 \text{ \AA}$  to  $40 \text{ \AA}$  for unpolarized neutrons which provides a  $Q_z$  range from  $0.002 \text{ \AA}^{-1}$  to  $3.2 \text{ \AA}^{-1}$ . To study the magnetic structure of a sample, an electromagnet with up to 1.3 T is available, as well as a cryostat to cool the sample down to 4 K.

The schematic representation of MARIA is given in figure 3.21. The incoming neutrons beam which is produced by the reactor is guided to the instrument through the neutron guide (vertically focusing elliptic guide). The Fermi chopper can be used to define the start time of the neutrons. Polarized neutrons are generated by a double reflection polarizer placed after the velocity selector, and spin reversal is performed by an RF-flipper. A pair of slits S1 and S2 separated by 4 m distance is used to define the beam size before the neutron beam hits the sample. The sample is mounted in a hexapod for the sample movement (figure 3.22). MARIA provides temperature from 4 K up to room temperature by using a cryostat around the sample position. Magnetic field up to 1.3 T can be provided in the standard configuration. Behind the sample, a

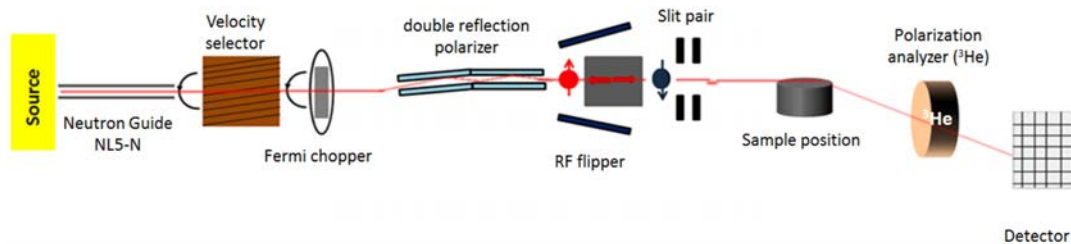


Figure 3.21.: The MARIA instrument at Heinz Maier-Leibnitz Zentrum used for (polarized) neutron reflectometry.

$^3\text{He}$  cell analyzer is placed in order to analyze the neutron state. At the sample position, a polarized neutron beam with flux  $5 \cdot 10^7 \text{ n cm}^{-2}\text{s}^{-1}$  hits the sample and the scattered intensity is recorded by a position-sensitive  $^3\text{He}$  2D detector, which has  $1024 \times 1024$  pixels with a quadratic dimension of 0.576 mm. The sample-to-detector distance in the standard setup is 1.91 m. The sample and collimation apertures for reflectometry experiments are typically set to 2 mm along the scattering geometry, and the distance in between is 4.1 m. This gives an instrumental resolution of approximately  $0.01 \text{ nm}^{-1}$ . Additionally, the neutrons have a wavelength spread of  $\frac{\Delta\lambda}{\lambda} = 0.1$  (FWHM).

Similar to GALAXI, the neutron reflectometer is controlled onsite by the NICOS software and the data is provided as compressed text files for each detector image and each angle.

The typical applications of MARIA is to investigate depth-resolved the laterally averaged magnetization (reflectivity), and the correlations between their lateral fluctuations (GISANS). Moreover, MARIA can be used to investigate the magnetic roughness and the formation of magnetic domains in the layered structures.



Figure 3.22.: Hexapod sample table.

#### 3.5.1.1. Polarized Neutron Reflectometry (PNR)

The fundamentals of the neutron reflectometry can be discussed in the same framework of the x-ray reflectometry. In neutron reflectometry, the average nuclear structure of the layers can be studied instead of probing the vertical electron density as in the X-ray reflectometry. Moreover, by using polarized neutron reflectometry (PNR), the magnetic spin density of the layers can be determined and the depth dependence of the in-plane magnetization profile [59, 70]. The PNR experiment presented in this thesis was performed at MLZ beamline MARIA, where the reflected neutron beam is collected on a position-sensitive detector. The scattered reflectivity of the polarized neutrons at MARIA is measured by varying the angle from sample to source and detector. Monochromatic neutrons are measured on a detector at specular condition ( $\alpha_i = \alpha_r$ ).

The alignment procedure for the sample differs from the XRR. In the beginning, a laser pointer is used to prealign the sample because the used silicon substrate is transparent for neutrons. The final alignment of the sample is performed by moving it until observing the intensity of the reflected beam on the position-sensitive detector.

During the experiment, the reflectivity curve is measured by rotating the sample and the detector simultaneously, then the neutrons are integrated until reaching a counting statistic above the noise level. From the neutron reflectivity experiment, for each measured angle, a two-dimensional image is obtained, where one dimension is the pixel coordinates  $z$  along the scattering angle and the other

dimension is the incident angle for the respective line.

Figure 3.23 shows the typical configuration of the specular PNR experiment, where neutron reflectivity is measured as a function of the wave vector transfer  $Q_z$ . The polarization of the neutron either parallel or antiparallel to the applied field direction. Typically, four cross-sections ( $R^{++}$ ,  $R^{+-}$ ,  $R^{-+}$ ,  $R^{--}$ ) are measured to determine the depth profile of the averaged in-plane magnetization vector. The symbols of + and - label the spin polarization of the neutron beam being parallel (spin-up) and antiparallel (spin down) to the magnetic field  $H$ , respectively. Where ( $R^{++}$ ,  $R^{--}$ ) called non spin-flip (NSF) cross-sections, which yield  $M_{\parallel}$  as a function of  $Q$ , while ( $R^{+-}$ ,  $R^{-+}$ ), called spin-flip (SF) cross-sections, which yield  $M_{\perp}$  as a function of  $Q$ . In addition to the in-plane magnetization vector, in-plane correlated roughness and magnetic stripe domains can be determined from off-specular PNR experiment where  $\alpha_i \neq \alpha_r$  which is not illustrated here.

In this thesis, PNR measurements of a monolayer of cobalt ferrite nanoparticles film were performed in order to get information about the magnetization depth profile of the COF NP monolayer. More details about the results will be explained later in chapter 6.

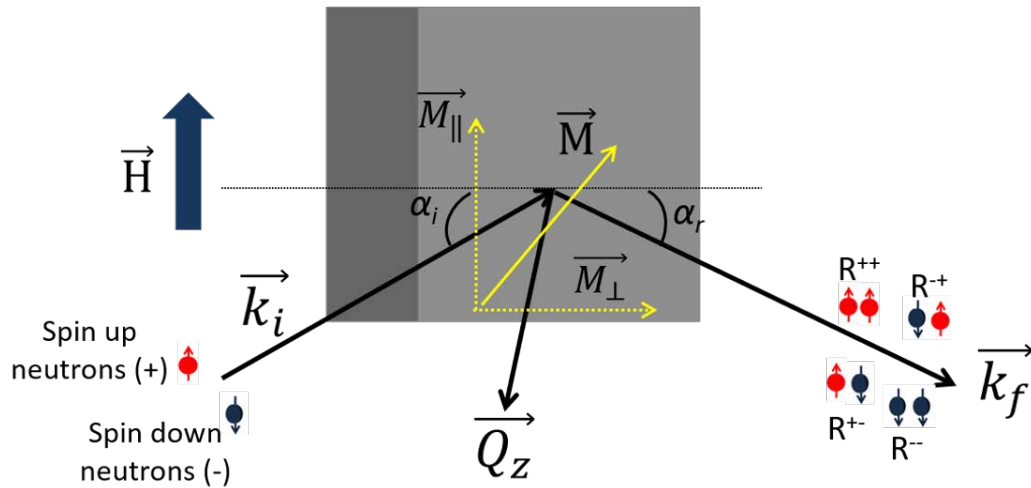


Figure 3.23.: Typical configuration of specular PNR experiment. Neutrons are polarized, either parallel or antiparallel to the external magnetic field  $\vec{H}$ . The  $\vec{M}_{\parallel}$  and  $\vec{M}_{\perp}$  are the two projections of  $\vec{M}$  with respect to  $\vec{H}$ .

## 4. Structural characterization of line gratings by grazing incidence small angle x-ray scattering (GISAXS)

Periodic structures on silicon surface with sub- $\mu m$  and nm dimensions are becoming more interesting due to the wide range of technological applications such as anti-reflective surfaces, grating couplers for biosensors, masks for semiconductor photolithography and diffraction gratings for spectrometers and monochromators in synchrotron radiation beamlines and free-electron lasers. Furthermore, gratings are considered as very precisely fabricated model systems for methodological studies of tools in dimensional nanometrology. Gratings are a highly ordered system because they can be produced with a high accuracy using different technologies such as electron beam lithography (EBL). In this chapter, the fundamentals of the GISAXS experiment on grating lines that performed at GALAXI instrument in Forschungszentrum Jülich will be described first. Then the mathematical principles of the data analysis and numerical simulation will be given. Later on, the structural characterization of two different grating structures with different dimensions, from large structures up to almost 300 nm down to structure smaller than 300 nm by GISAXS and XRR will be presented.

### 4.1. GISAXS on grating structures

GISAXS is a well know X-ray scattering technique, which permits access to nanostructured surfaces, buried structures and depth-resolved profile in layer systems. Furthermore, information on structural roughness and on long-range periodic perturbations can be obtained by GISXAS.

The cross-sectional view of the surface gratings shown schematically in figure 4.1(a) with grating height  $H$  and period  $P$ , which is equal to the sum of the groove width  $W$  and the mesa width  $D$ . The structure factor  $S(\vec{q})$  in equation 4.1 dominate in the scattering intensity distribution of the gratings because gratings considered as a highly ordered system of scatterers.

$$I(\vec{Q}) \propto NF(\vec{Q})S(\vec{Q}) \quad (4.1)$$

Where  $F(\vec{Q})$  is the form factor characterizes the shape of the scatterers (i.e. line shape) and  $N$  is the number of the scatterers. The geometry of GISAXS measurement [71] at the trench-patterned substrate is shown schematically in figure 4.1(c). A monochromatic X-ray beam with an incident wave vector  $\vec{k}_i$  is directed on a sample surface with a small incident angle  $\alpha_i$ . The resulting reflected and scattered radiation with wave vector  $\vec{k}_f$  is collected with a detector at exit angles  $\alpha_f$  and  $2\theta_f$ . Where the X-Y plane is the sample plane, the X-axis lies in the scattering plane and Z-axis perpendicular to the sample plane. With this coordinate system, the scattering vector  $\vec{Q} = \vec{k}_f - \vec{k}_i$  takes the form:

$$\begin{aligned} Q_x &= k(\cos 2\theta_f \cos \alpha_f - \cos \alpha_i) \\ Q_y &= k(\sin 2\theta_f \cos \alpha_f) \\ Q_z &= k(\sin \alpha_i + \sin \alpha_f) \end{aligned} \tag{4.2}$$

GISAXS measurement for trench-patterned substrates has already been described by several groups [72] and [73]. The GISAXS measurement as the incoming beam along the grating lines is called non-coplanar geometry, conical mounting, or sagittal diffraction geometry. It is called coplanar geometry when the incoming beam is perpendicular to the grating lines [74]. The scattered pattern obtained from gratings can be understood by reciprocal space representation [74, 75]. The grating lines periodically extending in the y-direction with vanishing height represented in reciprocal space as a series of grating truncation planes (GTP) as shown in figure 4.1(b) that are perpendicular to the grating surface and parallel to the grating lines. The GTP is parallel to the  $Q_z$  and  $Q_x$  and separated by  $\delta Q_y = \frac{2\pi}{P}$ , where  $P$  is the gratings period as shown in figure 4.1(b).

The scattered pattern of the grating lines (figure 4.1(c)) was recorded by the detector, arises from the intersection of the Ewald sphere with radius  $\frac{2\pi}{\lambda}$  and the grating truncation planes which is the reciprocal space representation of the grating lines as shown in figure 4.2(b). Depending on the azimuthal angle  $\phi$  between the grating line and the direction of the incident beam, two special cases can be identified: the first case, as the incoming beam directed along the lines (figure 4.2(a))(i.e.  $\phi = 0^\circ$ ) and the second case, as the incoming beam perpendicular to the lines (figure 4.2 (b))(i.e.  $\phi = 90^\circ$ ).

In case of the incoming beam parallel to the lines, the Ewald sphere intersects the grating truncation planes as drawn in figure 4.2 (c). This gives periodically grating truncation rods repeated along  $Q_y$  (orange lines in figure 4.2(c)). The intersection between the Ewald sphere and the grating truncation rods arises semi-circular spots (red spots in figure 4.2 (c)) while the blue spot indicates the specular reflection spot on the detector. The GISAXS pattern of grating lines is strongly dependent on the misalignment of the lines with respect to the

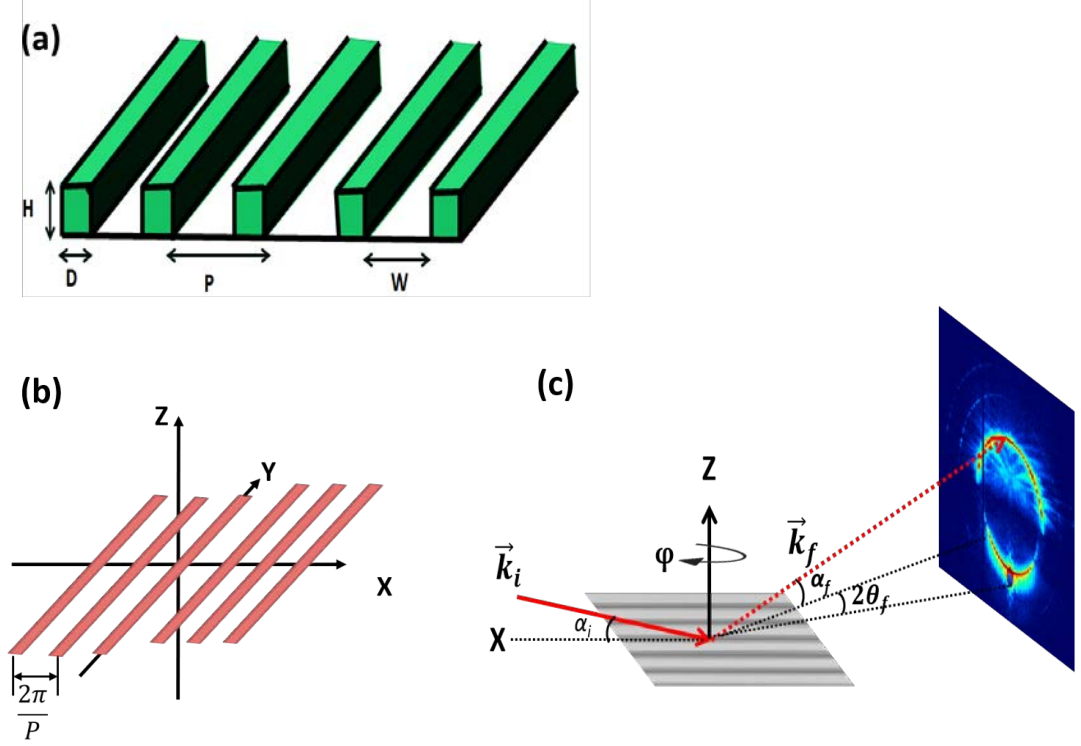


Figure 4.1.: Schematic representation of grating lines with period  $P$ , mesa width  $D$ , groove width  $W$  and height  $H$ . (a) Cross-sectional view in real space. (b) Reciprocal space representation of grating lines. (c) Scattering of a collimated X-ray beam from grating lines oriented parallel with respect to the incident beam (i.e.  $\phi = 0^\circ$ )

direction of the direct beam (i.e. the azimuthal angle  $\phi$  between the lines and the direct beam).

While in the case of the incoming beam perpendicular to the lines, i.e.  $\phi = 90^\circ$ , the lines are aligned in the usual orientation of a diffractive optical element. In this case, due to the constructive interference between the waves reflected from the top and the bottom of the grating lines, the dominant features are the grating diffraction orders along  $Q_z$  direction. The reflection grating formula or grating equation for the distance between interference maxima of the orders  $n$  and  $n+\Delta n$  along  $Q_z$ , obtained from the optical path difference formula  $\Delta s = P(\cos(\alpha_f) - \cos(\alpha_i))$  can be written as:

$$\Delta n\lambda = P\left(\cos(\alpha_{f,(n+\Delta n)}) - \cos(\alpha_{f,(n)})\right) \quad (4.3)$$

In case  $\phi = 90^\circ$  the grating truncation planes shown in figure 4.1(b) are paral-

lel to the detector plane. Therefore, no grating truncation rods are visible and the detector plane only contains the specular axis.

Furthermore, if the grating is rotated by the angle  $\phi$  in the sample plane, the grating lines become no longer parallel to the x-axis and the grating truncation planes rotated around the z-axis by  $\phi$ , therefore the scattering pattern of the grating becomes asymmetric.

The positions of the grating diffraction orders can be determined from the following relations [76]:

$$\alpha_f = \arcsin \left\{ \left[ \sin^2 \alpha_i - \left( \frac{n\lambda}{P} \right)^2 - \frac{2n\lambda \sin \phi \cos \alpha_i}{P} \right]^{\frac{1}{2}} \right\} \quad (4.4)$$

$$\theta_f = \arcsin \left( \frac{\cos \phi n\lambda}{\sin \phi n\lambda + P \cos \alpha_i} \right) \quad (4.5)$$

Or, in  $Q_y$ - $Q_z$  coordinates as follows:

$$Q_z = \frac{2\pi}{\lambda} \cos \alpha \sin \alpha \left\{ 1 + \left[ 1 - \left( \frac{n\lambda}{P \sin \alpha} \right)^2 \right] \right\} \quad (4.6)$$

$$Q_y = \frac{2\pi}{P} \quad (4.7)$$

With  $n$  is the diffraction orders number and  $P$  is the gratings period.

## 4.2. Direct data analysis and numerical simulation

The phase problem of scattering results from the fact that only the absolute square of magnitude  $|\psi_f((\vec{k}_i, \vec{k}_f))|^2$  of any scattered wave  $\psi_f$  is measured by the detector because it is not possible to separate the structure factor  $S(\vec{q})$  and the form factor  $F(\vec{q})$  in equation 4.1. Therefore, in this case, only information about the wave amplitude is observable and missing the phase information. As a result, the form factor in equation 4.1 can't be obtained directly from the inverse Fourier transform of the measured scattering pattern.

In order to get real-space structural information from reciprocal space scattering patterns, simulation, and data analysis are required to solve the phase problem. In scattering under grazing incidence, the popular methods used to analyze the data are:

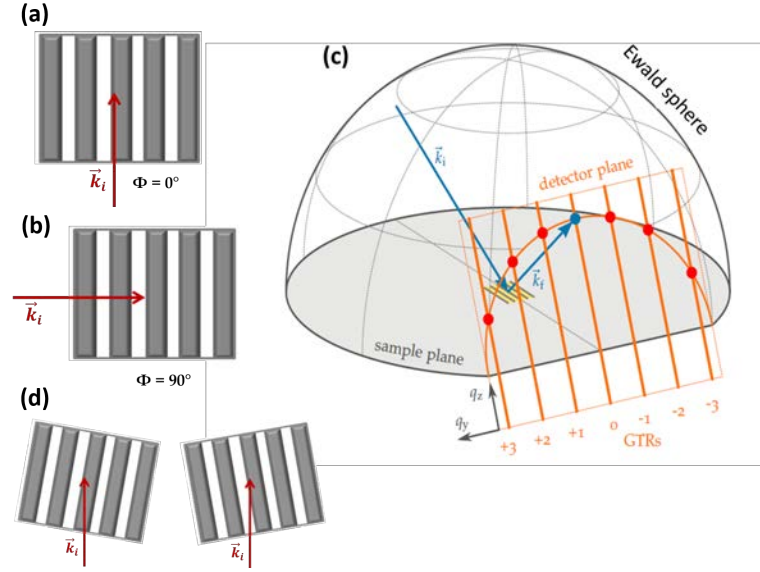


Figure 4.2.: (a) The parallel orientation between incident beam and grating lines i.e.  $\phi = 0^\circ$ . (b) The perpendicular orientation between incident beam and grating lines i.e.  $\phi = 90^\circ$ . (c) The intersection of grating truncation rods (orange lines) which are the reciprocal space representation of grating lines and the Ewald sphere (grey mesh) in reciprocal space reconstruction in case of parallel orientation. The intersection leads to semi-circular sharp spots (red spots) on the detector. (d) Misalignment between the incident beam and the grating lines (i.e. the direct beam almost parallel to the grating lines).

(I) In order to find a closest and similar model of the measured scattering data (two-dimensional pattern), numerical modeling of the  $F(\vec{q})$  and  $S(\vec{q})$  is required. This method requires careful selection and physically meaningful models for the form factor and for the structure factor and the validation of the chosen model. Several software packages are available for the calculation, simulation and fitting of the GISAXS scattering patterns in the framework of Born approximation (BA) and Distorted Wave Born Approximation (DWBA) [77–80].

(II) Fourier transform of the scattered intensities, known as the Patterson function [81], which yields the power spectral density (PSD) or what is known as an autocorrelation function. The PSD provides information about the lateral and the vertical correlation lengths which allow access to the oscillatory part of the scattering pattern.

In order to obtain qualitative insights into the morphology and into the evo-

lution of the nanostructural dimensional parameters, a numerical simulation of the measured GISAXS pattern by careful selection of suitable models with suitable parameters for the  $F(\vec{q})$  and  $S(\vec{q})$  was performed.

Also, it is possible to get the structural parameters directly from the scattering data without requiring numerical simulation of the form factor and the structure factor. By this method, access to the uncertainties of the dimensional parameters obtained by scattering measurements is possible, which includes GISAXS and XRR in the framework of this thesis. The dimensional parameters obtained in this way could be considered as starting or reference values for more advanced and complex data analysis. Furthermore, the parameters obtained by direct data analysis help to reduce the parameters for simulation and increase the accuracy of the optimized model parameters by giving them strong variation ranges of the starting parameters.

Direct data analysis of the GISAXS and XRR data allows traceability of the scattering measurements and it gives a general understanding of the model used and its uncertainty.

The direct analysis of the GISAXS and XRR data in this thesis is based on the Fourier transform of the scattered intensity and determining separation distances directly from the scattering image or from the reflectance profile.

### Fourier transform

The Fourier transform of the intensity carried out of the one-dimensional data profile, i.e. horizontal line cuts along  $Q_y$  or vertical line cut along  $Q_z$  in GISAXS and reflectance curves in XRR. The Fourier transform can be defined as the integrable function  $f(x)$  as:

$$F(\xi) = \int_{-\infty}^{\infty} f(x) \exp(-i2\pi\xi x) dx \quad (4.8)$$

The PSD can be obtained from the absolute square of the Fourier transform in equation 4.8:

$$PSD(\xi) = |F(\xi)|^2 \quad (4.9)$$

## 4.3. Dimensional nanometrology of surface gratings

Several techniques were reported on the fabrication of surface structures with great accuracy and dimensions down to several manometers such as photolithography tools in the Extreme Ultra-Violet regime (UV) (EUV lithography) and

directed self-assembly of block copolymer (BCP) thin films. Suitable metrology techniques are required in order to measure the surface structural parameters with sufficient accuracy. Different analytical techniques are available for direct analysis, such as atomic force microscopy (AFM), scanning electron microscopy (SEM) as well as for indirect analysis, such as GISAXS and XRR.

### Microscopy methods

Microscopy methods, such as scanning electron microscopy (SEM), belong to the real space or direct methods of nanometrology. The images obtained by these methods represent the real space of the sample on the field of measurement, which typically covers an area in the range of  $\mu m^2$ . Real space methods do not require abstract models for the shape of the investigated nanostructures like indirect scattering methods. Furthermore, they yield only local information about the structure surface.

### Scattering methods

On the opposite of the microscopy techniques, X-ray scattering techniques do not provide a direct topography of the surface but the information in reciprocal space can be brought back to real space by fitting procedure of the measured X-ray data. The patterns produced by these methods represent the reciprocal space of the sample, which covers a large area. The reciprocal space or indirect method requires an abstract model, which yields the structural parameters, i.e. gratings period  $P$  and groove width  $W$ . Also, scattering methods yield global information and also they yield statistically significant average feature sizes, which sometimes are more relevant than the very localized size information of the real space methods. Furthermore, GISAXS techniques provide surface sensitivity and a variation of the probed scattering depth.

It is easy to detect any periodic structure along a specific direction of the reciprocal lattice by performing a scan of the wave vector along this direction. Statistical information integrated over a large area covered by a footprint of the incident beam on the surface of the material can be obtained by this scan. Therefore, the scattering pattern averaged over a large area and it is not localized information like the information obtained from microscopy techniques.

## 4.4. Large pitches close to 300 nm

This section focuses on characterizing grating lines with large pitches on a silicon substrate. The characterization was done locally by SEM to obtain real-space information and globally by GISAXS to obtain reciprocal space information. Furthermore, XRR measurements on the grating lines were carried out to determine the height of the grating lines and the thickness of the capping layer. The gratings presented in this section have been fabricated on  $10 \times 10 \times 0.5 \text{ mm}^3$  silicon substrate and co-designed with the Eulitha company, Switzerland. These grat-

ings have been created by the displacement talbot lithography method, which will be explained briefly in Sec. 4.4.1. Furthermore, discrete Fourier transform (DFT) of extracted and pre-processed GISAXS intensity profiles were done for this gratings, for the determination of the grating parameters such as D, W, H, and P.

#### 4.4.1. Materials and methods

The sample is  $10 \times 10 \times 0.5 \text{ mm}^3$  silicon substrate with a periodic rectangular-shaped grooves. The grating lines have period P of 300 nm, a groove width W of 150 nm and a line-height H of 100 nm. The structure was produced by the displacement talbot lithography method [82].

Displacement talbot lithography (DTL) is a very active lithographic method for patterning periodic structure with features ranging from a few micrometers down to sub nanometers. A high-resolution photolithography periodic structure like diffraction gratings could be obtained by DTL without need projection of complex and expensive optics. Furthermore, DTL is able to obtain sub-micron resolution periodic patterns over large areas with low cost and it enables to print gratings with absolute control of period and grating phase. DTL is a contactless method (i.e. do not require contact between the mask and the substrate) in contrast to the photolithography methods which require perfect contact between the mask and the substrate. Talbot effect considered as an interference based on self-imaging phenomena of a periodic structure illuminated by a monochromatic and collimated light beam. In the case of grating lines, the Talbot self-images appear and repeat in the light propagation direction with a Talbot period of  $\frac{2P^2}{\lambda}$ , where P is the grating period and  $\lambda$  is the wavelength of the light. In DTL, during the exposure, the distance between the mask and the substrate is changed by one or multiple Talbot periods as shown in figure 4.3(a). More details about the principle of DTL published in [82] [83].

Figure 4.3(b) shows a schematic representation of the gratings fabrication process. Briefly, after the DTL exposure (figure 4.3 (a)) by commercially available PhableR 100 system from Eulitha (Switzerland) by using Cr mask, the pattern is transferred from photoresist into an antireflective coating (ARC) by reactive ion etching (RIE) in an oxygen plasma. Then, the pattern is further transferred into a Cr hard etching mask by RIE. The residuals of ARC and photoresist are removed by RIE in oxygen plasma after Cr etching. Finally, the patterns transferred into the silicon substrate using  $SF_6/C_4F_8$  by deep reactive ion etching (DRIE). The details of the parameters used in the fabrication of the grating lines presented in this section are attached in Appendix B, where all of these parameters are taken from the sample preparation report of Eulitha company.

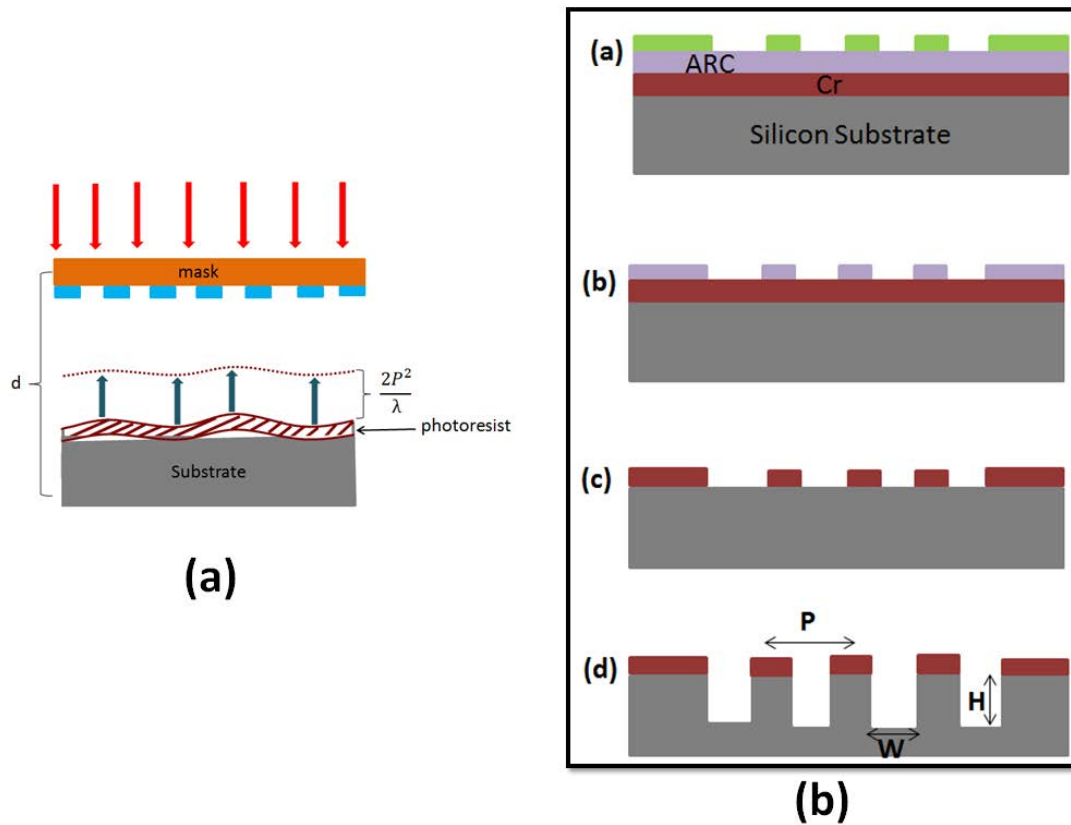


Figure 4.3.: (a) Schematic diagram showing the DTL method. The photoresist coated substrate is moved towards the mask by approximately one Talbot period during the exposure. (b) Schematic representation of the fabrication process of the grating lines by DTL method: (a) exposure and development of photoresist; (b) dry etching into anti-reflective coating (ARC); (c) dry etching into Cr layer; (d) etching of Si substrate.

#### 4.4.2. Scanning Electron Microscopy (SEM)

The easiest and direct way to investigate the morphology of the gratings formed on the silicon substrate is to carry out direct imaging of the surface by SEM as shown in figure 4.4. The SEM yields real space information about the substrate surface, the uniformity of the gratings pattern, the sharpness of the structure and the quantitative characterization of the grating parameters (groove width and gratings period). SEM image in figure 4.4(a) confirms a periodic array of parallel stripes with a groove width of 150 nm and a period of 300 nm. Figure 4.4(b) shows a cross-section SEM image of the gratings, which confirm rectangular-shaped concave trenches and the 3-D view of the gratings (figure 4.4(d)) confirms rectangular-shaped concave trenches and the surface quality of the gratings. The line profile of the SEM image (figure 4.4(a)) is shown in fig-

ure 4.4(c). Here we probe a lateral periodicity of the grooves  $P$  nearly  $\approx 300$  nm which is in a perfect agreement with the nominal value from the company. SEM does not provide any information about the silicon oxide layer which covered the silicon motifs.

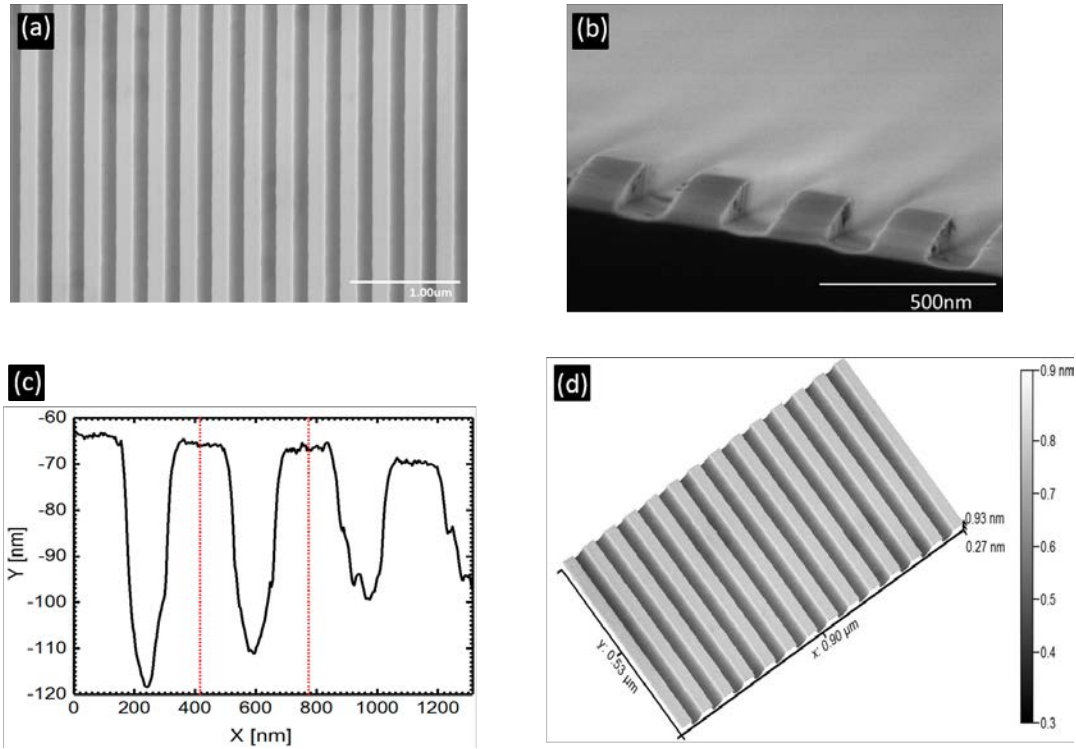


Figure 4.4.: (a) SEM image of the grating lines on Si substrate. (b) A cross-section SEM image of the grating lines. (c) Line profile of the pattern, where the distance between the two red dotted lines represents the gratings period. (d) 3D-SEM image of the pattern.

Layer	Thickness (nm)	Roughness (nm)	SLD( $10^{-6} \text{ \AA}^{-2}$ )
Grooves	100.2 $\pm$ 6.3	3(1)	10.9
SiO <sub>2</sub>	14.8 $\pm$ 10.2	1.3(2)	10.5
substrate (Si)	-	0.5(2)	20

Table 4.1.: Parameters obtained from fitting of the XRR data.

#### 4.4.3. Determination the capping layer thickness and the line height by XRR

XRR measurement was carried out at GALAXI (Sec. 3.4.1) for the characterization of the sample layers structure and to probe the depth profile of the gratings. Furthermore, via XRR, information about the depth profile of the electron density of the material can be obtained. In our study, XRR measurement was performed in order to obtain the depth of the grooves and the thickness of the silicon oxide layer covering the lines. Figure 4.5(a) shows the X-ray reflectivity profile (red symbols) of the grating lines patterned on a silicon substrate with a simulation of the data (black solid line). The measurement performed around the specular spot as the incoming beam perpendicular to the lines. The XRR curve shows Kiessig fringes with a period length that corresponds to a real space correlation length  $\approx$ 100 nm, which can be identified as the line-height. Referring to the origin of the Kiessig fringes, in case of the grating, the top surface of it has an average electron density lower than the substrate density due to the lack of material inside the grooves. The contrast of electron density gives the Kiessig fringes related to the depth of the grooves.

The XRR data were fitted to a model structure shown in figure 4.5(c) by Genx software. In order to fit the data, a thin silicon dioxide layer covering the lines was assumed with an SLD value smaller than the bulk value. The SLD profile obtained from the gratings shown in figure 4.5. A grooves depth  $\approx$  100 nm and SiO<sub>2</sub> layer thickness  $\approx$  15 nm is determined, the other fit parameters are shown in table 4.1.

#### 4.4.4. GISAXS

GISAXS measurements were performed in two different geometries, as the incoming beam perpendicular to the grating lines (Sec. 4.4.4.1) and parallel to it (Sec. 4.4.4.2). The scattered GISAXS patterns measured when the incident beam almost parallel to the grating lines are very sensitive to any change in the azimuthal angle  $\phi$  as shown in Sec. 4.4.4.3. The grating lines can be easily aligned to better than  $\phi = 0.01^\circ$  just by looking at the changes of the GISAXS

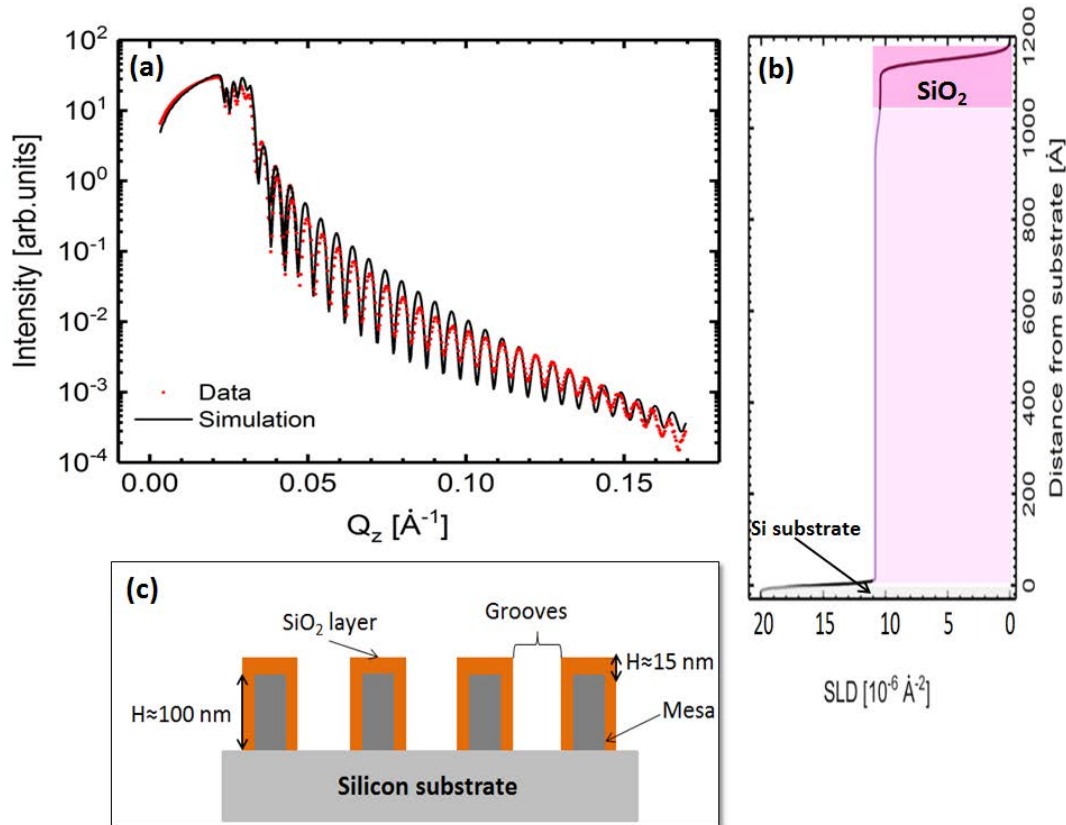


Figure 4.5.: (a) X-ray reflectivity as a function of momentum transfer ( $Q$ ) of grating lines. Data shown as red symbols and fits shown as the black solid line. Parameters of the fit are displayed in table 4.1. (b) Modeled scattering length density (SLD) as a function of distance from air interface. (c) Sketch of the model used for fitting XRR data with the relevant parameters that are used to describe it.

patterns on the detector. If the grating lines are not well aligned with respect to the incident beam, the resulting scattering GISAXS pattern will be asymmetric, i.e. the semi-circle Bragg spots only appear on one side. Fourier transformation was performed for the scattering GISAXS patterns in parallel orientation (Sec.4.4.4.2). The measured scattered GISAXS data has been validated by simulation using BornAgain software in the framework of DWBA (Sec.4.4.5). Furthermore, the grating periodicity as calculated from the GISAXS pattern will be shown.

#### 4.4.4.1. Perpendicular orientation

The geometry of the GISAXS measurement as the direct beam perpendicular to the grating lines shown in figure 4.2(b) with an azimuthal angle  $\phi = 90^\circ$  between the direct beam and the lines. Figure 4.6 (a) shows the GISAXS pattern recorded at an incident angle  $\alpha_i = 0.06^\circ$  with respect to the substrate surface. Intense maxima are observed along the specular axis at  $Q_y = 0 \text{ nm}^{-1}$ . Figure 4.6(b) shows the vertical intensity profile obtained at  $Q_y = 0 \text{ nm}^{-1}$ . From figure 4.6 (b), peaks at  $Q_z = 0.1 \text{ nm}^{-1}$  and  $Q_z = 0.148 \text{ nm}^{-1}$  were observed, which corresponds to  $\alpha_f = 0.06^\circ$  and  $\alpha_f = 0.09^\circ$ , respectively. The peak observed at  $Q_z = 0.1 \text{ nm}^{-1}$  represents the specular peak and the other peak observed at  $Q_z = 0.148 \text{ nm}^{-1}$  represents the grating diffraction order.

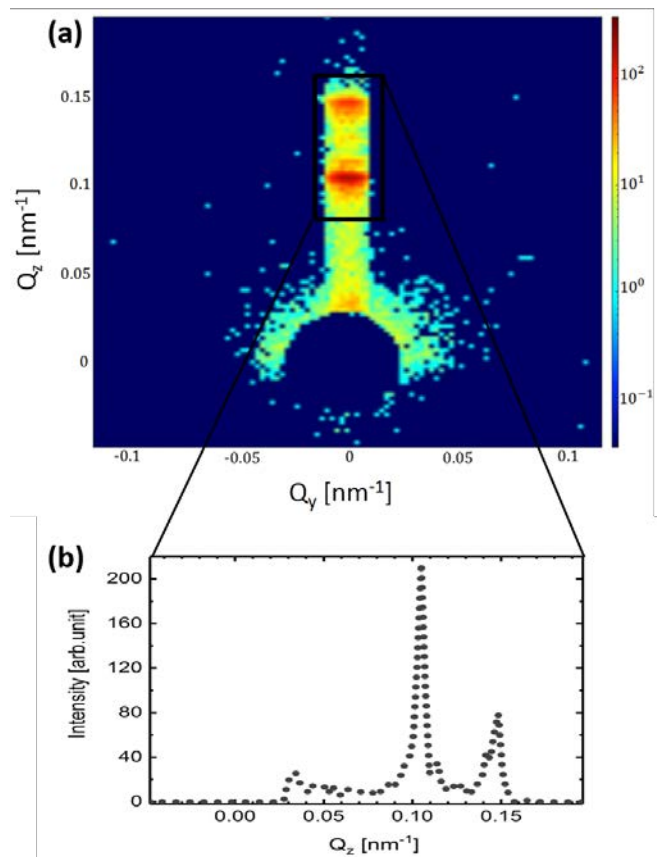


Figure 4.6.: (a) GISAXS scattering image of grating lines at  $\alpha_i = 0.06^\circ$  as the incoming beam perpendicular to the lines. (b) Intensity profile along the vertical specular axis as a function of  $Q_z$ . The peak position at  $0.1 \text{ nm}^{-1}$  represents the specular peak.

#### 4.4.4.2. Parallel orientation, Fourier Transform analysis

The scattering pattern as the incoming beam parallel to the lines ( $\phi = 0^\circ$ , figure 4.2 (a)) has a different appearance than other geometries. Figure 4.8(a) shows the GISAXS pattern of grating lines in the parallel orientation where the GISAXS measurement is carried out at an incident angle  $\alpha_i = 0.38^\circ$ , photon energy  $E_{ph}=9243$  eV and sample to detector distance  $SDD = 3528$  mm. In this geometry different features were observed in the GISAXS pattern. The main prominent feature observed is the intersection of the GTRs and the Ewald sphere along  $Q_z$  with a periodicity of  $\Delta Q_y = \frac{2\pi}{P}$  as shown in figure 4.2 (c). A series of diffraction orders on a semicircle is observed as a result of the intersection between GTRs and Ewald sphere, which is very sensitive to the perfect alignment between the incident beam and the lines. The positions of the diffraction spots in  $Q_z, Q_y$  coordinates are calculated by using equations 4.6 and 4.7 and compared with the experimentally observed spots as shown in figure 4.7. A slight difference is observed between the calculated peak positions and the measured ones. This difference might be due to the refraction effects, which were not properly accounted for in equations 4.6 and 4.7.

The obtained semicircle contains the specular reflection in the uppermost position and it has a radius of  $SDD \times \tan \alpha_i$  with center around the intersection of the sample horizon and the specular axis.

Figure 4.8(a) shows other additional features in the GISAXS pattern, such as the satellite rings, which indicate a high periodicity of the structure, and diffuse Bragg sheet. These features arise most probably as explained in [84–87] from different structure features such as roughness and imperfections of the grating, the shape of the gratings, and sidewall angle or due to the stitching pattern of the electron beam lithography machine. But these additional features have no effect on the calculation of the groove width as well as on the gratings periodicity. The grating GISAXS pattern shows a constant diffraction efficiency for all orders observed means the gratings are with low roughness.

Figure 4.8(b) shows the averaging extracted intensity profile  $I(Q_y)$  from  $Q_z = 0.3 \text{ nm}^{-1} - 0.7 \text{ nm}^{-1}$ . A Fourier transform is applied to the intensity profile  $I(Q_y)$  in order to determine the PSD from the absolute square of the Fourier amplitude (equation 4.9).

The resulted PSD profile is shown in figure 4.8 (c) as a function of the correlation length  $d_{corr}$ . PSD profile is expressed in terms of the signal frequency  $\zeta$  in reciprocal space, which is related to the real space correlation length via the following relation:

$$d_{corr} = 2\pi\zeta \quad (4.10)$$

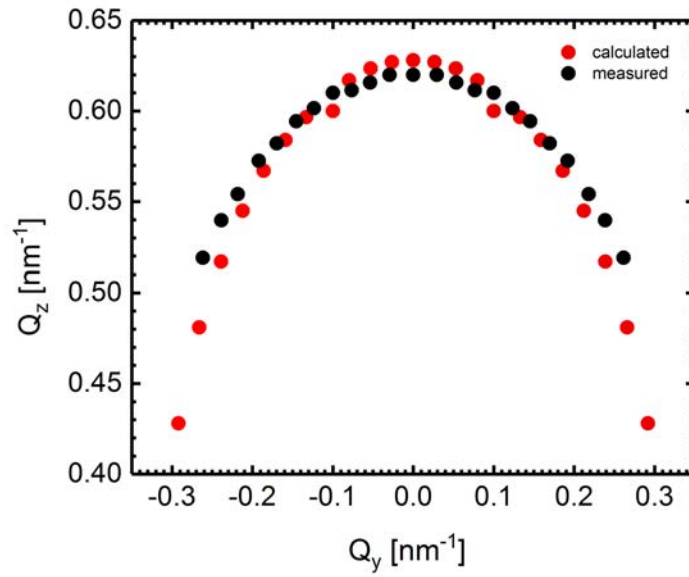


Figure 4.7.: Comparison between calculated and measured peak positions in the GISAXS scattering pattern of grating lines. The red and black circles represent the calculated and the measured positions, respectively. The calculated peak positions match the measured one, quite well.

Prominent peak are observed in the PSD spectrum in figure 4.8 (c), this peak corresponds to the grating periodicity and it is fitted by a Gaussian function in order to determine the center position and the peak width. The peak is located at a center position of  $d_{corr}=299.6(3)$  nm with a width of  $\sigma=5(1)$  nm . The value of the mean peak position obtained from PSD are in a good agreement with the nominal value of the gratings period which represented by the dashed vertical lines in figure 4.8 (c).

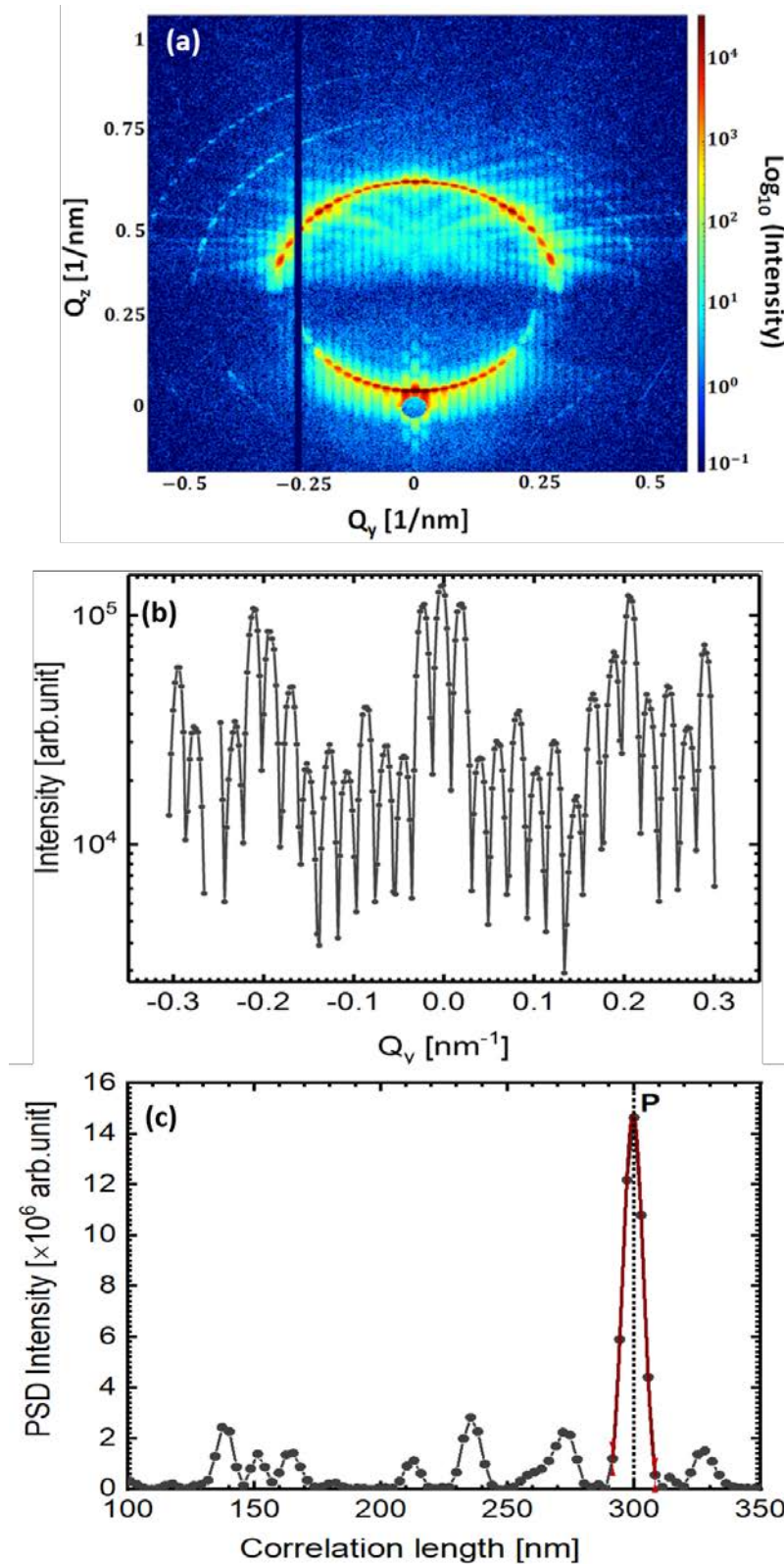


Figure 4.8.: (a) GISAXS pattern of grating lines at  $\alpha_i = 0.38^\circ$  as the incoming beam parallel to the lines. (b) Intensity profile  $I(Q_y)$  along the intersection of the Ewald sphere and GTRs in (a) as a function of  $Q_y$ . The peak positions along the semicircle correspond to the diffraction orders of the gratings. (c) PSD of the  $I(Q_y)$  profile in (b), the dotted vertical line indicates the nominal values of grating period  $P$  and the red solid line represent the fit of the peak using Gaussian function.

#### 4.4.4.3. Rotation around the surface normal vector

The grating must be rotated carefully in the sample plane by the angle  $\phi$  around the normal to the surface plane, in order to get a perfect alignment of the gratings with respect to the incident beam (i.e. the direct beam exactly parallel to the grating lines) as shown in figure 4.2(a). Otherwise, if the grating is not perfectly aligned with respect to the direct beam (figure 4.2(d)), the diffraction order spots no longer appear in the semicircle pattern as shown in figure 4.8(a). In case the grating lines are no longer parallel to X-axis, the GTRs in figure 4.1(c) are rotated around the Z-axis by  $\phi$ , therefore the scattering GISAXS pattern from grating lines becomes asymmetric as shown in figure 4.9(a). Even for a small deviation in  $\phi$  (i.e. small deviation from parallel alignment), large changes in the scattering GISAXS pattern of the grating are observed, because at a small incident angle  $\alpha_i$ , the curvature of the Ewald sphere is very steep at the intersection with the GTRs [74].

Figure 4.9(a) shows the GISAXS pattern of grating lines obtained by the rotation of the gratings around the normal to the surface (Z-axis). The rotation of the gratings performed in both directions, right and left directions as shown schematically in figure 4.2(d). The scattered GISAXS pattern obtained by rotating the grating in the right direction is shown in the right side of the figure 4.9(a), where the grating in this case rotated by  $\phi = 6.3^\circ$  to the right direction, while the left side of the figure 4.9(a) shows the GISAXS pattern obtained by rotating the grating to the left direction by  $\phi = 9.5^\circ$ . The misalignment between the direct beam and the grating lines leads to geometric distortion, and due to this geometric distortion, the diffraction order spots are aligned along a hyperbola. The positions of these orders can be calculated in a similar way as for perfect parallel alignment by using these relations (equations 4.6 and 4.7) [75]. The distance between the diffraction orders represents the grating period  $P$ . The averaged and extracted  $I(Q_y)$  profile in both orientation directions are displayed in figure 4.9(b), where the violet solid line represents the right orientation and the pink solid line represents the left orientation. The intensity profile along  $Q_y$  is averaged horizontally from  $Q_z = 0.015 - 0.15 \text{ \AA}^{-1}$ .

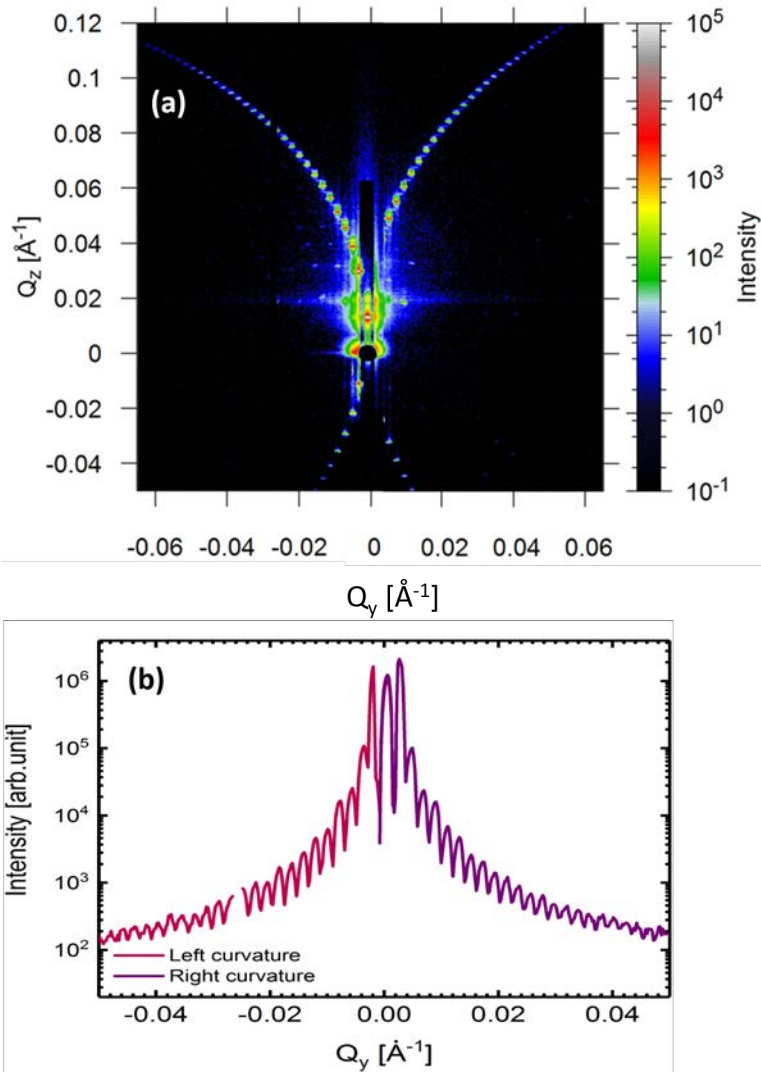


Figure 4.9.: (a) GISAXS pattern of grating lines for different azimuthal rotation close to the parallel orientation  $\phi = 0^\circ$  recorded at  $\alpha_i = 0.085^\circ$ . GISAXS pattern at right recorded at  $\phi = 6.3^\circ$  while at left recorded at  $\phi = 9.5^\circ$ . (b) The extracted average intensity profile  $I(Q_y)$  as a function of  $Q_y$ , where the violate line represents the right curvature and the pink line represents the left curvature.

#### 4.4.5. Validation by simulation using BornAgain

Simulation of the scattering GISAXS pattern of the grating structure was performed for the validation of the analysis process as described in section 4.4.4.2. The BornAgain software is a well-known tool for the simulation of the GISAXS patterns, interference functions, and form factors of structure models to solve equation 4.1 using distorted-wave Born approximation (DWBA). The software provides a comprehensive framework for modeling correlated and uncorrelated particles on a substrate and for modeling monolayer or multilayer samples with a smooth or rough surface and interfaces.

Using BornAgain software, only the main feature in the GISAXS pattern (i.e. semicircular spots) in parallel geometry has been simulated. By BornAgain the higher orders semicircles and the diffuse scattering can't be simulated at this stage, because at present, the DWBA is not adapted to describe diffuse scattering from surface gratings because their structures can't be treated as a small perturbation of a smooth surface [88].

The construction of the semicircular diffraction spots of the grating lines structure by BornAgain has been performed by considering a long-box-Lorentz-shaped particles silicon on a silicon substrate (9.243 keV, refractive index components  $\delta = 5.78164736e \times 10^{-6}$ ,  $\beta = 1.02294578 \times 10^{-7}$ , values from the x-ray database [89]), by assuming the width of the box  $W = 120$  nm, a height of  $H = 106$  nm, and a length of  $48.2 \mu\text{m}$ . Furthermore, certain degrees of disorder in the gratings periods were introduced, because as shown in figure 4.10, when the line profile of the grating lines (black solid line) fitted with a square wave function with different periods (green and yellow dotted lines), each period value fits a certain set of grooves, but not all grooves, such as the green dotted line represents a grating with a period of 319 nm, while the yellow dotted line represents 335 nm as a grating period. Therefore, four degrees of disorder were considered in order to obtain the simulated pattern in figure 4.11(b).

Figure 4.11 (b) is showing the simulated pattern of the experimental GISAXS pattern in figure 4.11(a). The simulation was carried out only for the main feature observed in the GISAXS pattern (figure 4.8 (a)), the semicircular spots. Horizontal slice at  $Q_z = 0.617 \text{nm}^{-1}$  for the experimental and the simulated data are shown in figure 4.11 (c). The simulated intensity as a function of  $y$  and  $z$  shows a good agreement with the experimental data. The grating parameters obtained from the simulation are in good agreement with the nominal values and the values obtained by Fourier transform and PSD in section 4.4.4.2.

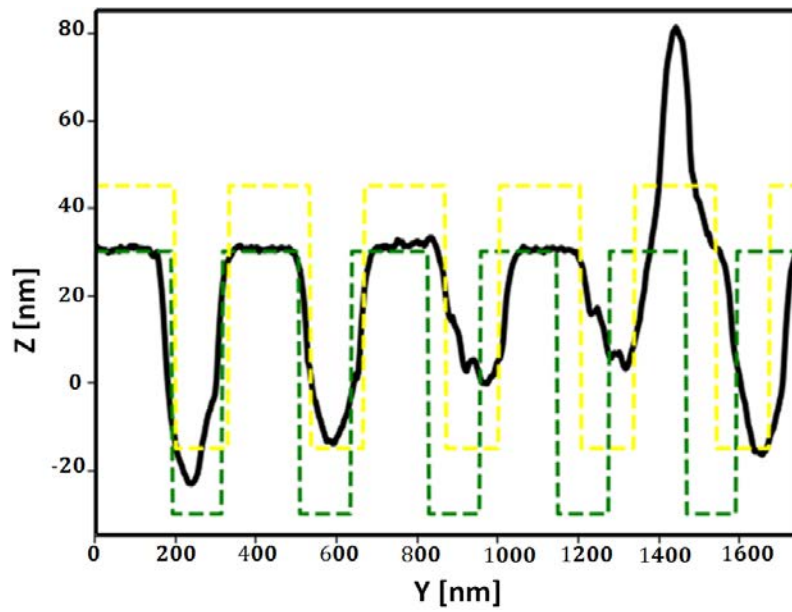


Figure 4.10.: Line profile of the gratings (black solid line) fitted with a square wave, where the green and the yellow dotted lines represent 319 nm, 335 nm as a gratings periods, respectively.

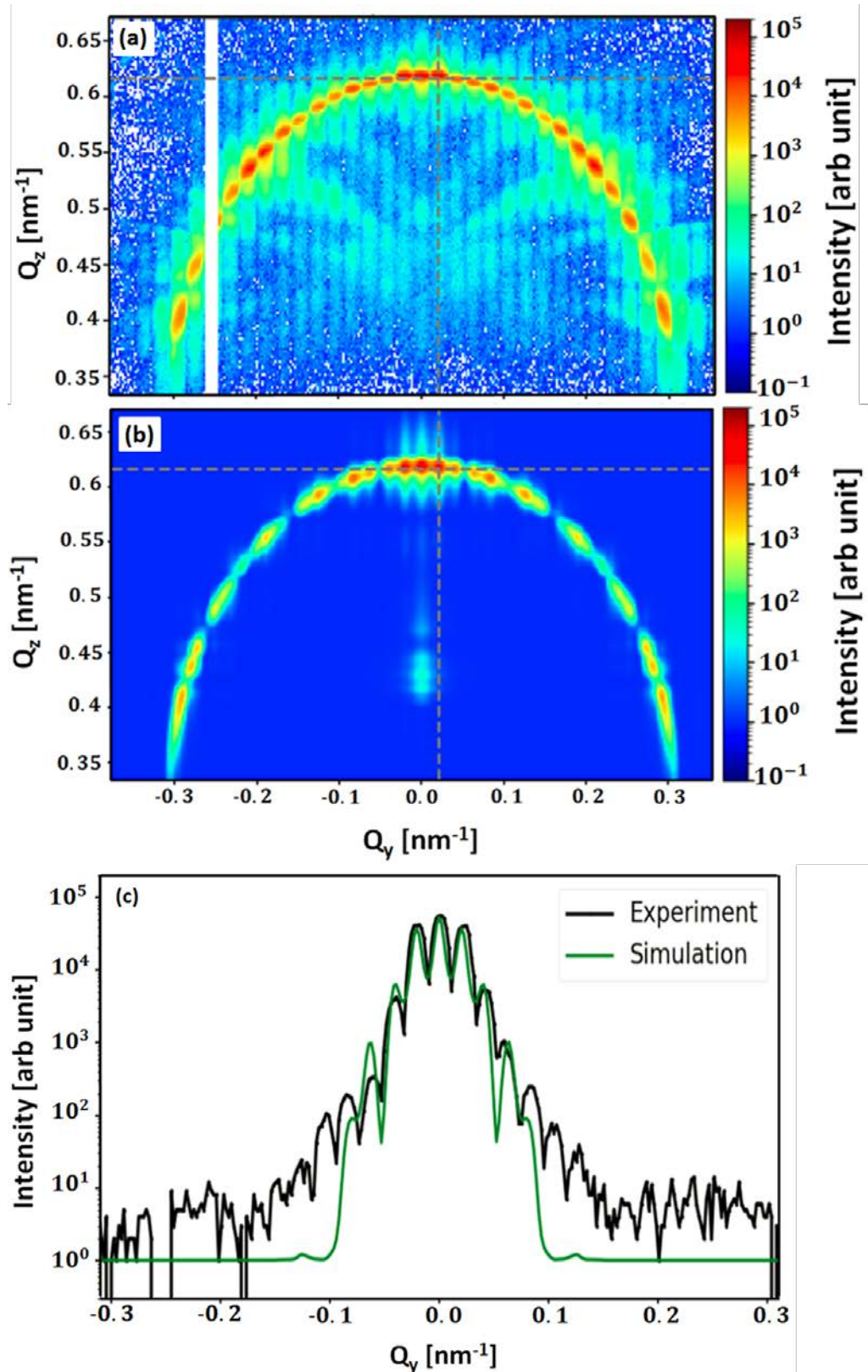


Figure 4.11.: (a) GISAXS pattern of grating lines at  $\alpha_i = 0.377^\circ$  as the incoming beam parallel to the lines. (b) Simulation of GISAXS scattering pattern from grating using BornAgain software with a long Lorentz box model. (c) Intensity profile at a constant  $Q_z = 0.617 \text{ nm}^{-1}$  of experimental (black solid line) and the simulation (green solid line) data as a function of  $Q_y$ .

## 4.5. Small pitches below 300 nm

In the previous section 4.4, large structure sizes with  $\approx 300$  nm as a grating period were characterized, while the focus in this section is on the characterization of nanostructures with groove width below 100 nm. The gratings presented in this section have been created by the electron beam lithography (EBL) method as explained later in 4.5.1.

In this section, different etching processes (potassium hydroxide (KOH) and tetramethyl ammonium hydroxide (TMAH) with different etching time (30s, 60s, 90s) were used for fabrication the gratings. Therefore, three different groups of gratings will be explained in this section. The first group (S1) consists of two samples (S1\_01, S1\_02) were fabricated without silicon dioxide layer above the gratings, second group S2 (S2\_01, S2\_02) consists of samples similar to S1 samples but with a silicon dioxide layer above the gratings. Last group S3 (S3\_01, S3\_02, S3\_03) were fabricated only by using TMAH etching but with different etching time. More details about these samples will be given later.

The main goal of the work presented in this section is the determination of the structural grating parameters such as D, P and W in figure 4.1 (a) by microscopic and x-ray methods for all different gratings. Furthermore, direct GISAXS data analysis will be presented.

The differences between the GISAXS patterns for the gratings presented in this section and the one presented in section 4.4 will be obvious because as the structure size decrease, the number of the GTRs that intersect the Ewald sphere will decrease. Therefore, the GISAXS pattern of the gratings will be affected.

### 4.5.1. Sample preparation

The samples are  $10 \times 10 \times 0.5$  mm<sup>3</sup> silicon substrate with periodic grooves over the whole surface area. The nanostructure parameters are different for different samples depending on the etching types and time. The structure was produced by the electron beam lithography method (EBL). The samples were prepared at the Institute Helmholtz nanoelectronic facility (HNF) at Forschungszentrum Jülich.

The EBL equipment installed at HNF-FZJ Jülich is electron-beam writer Vistec EBPG 5000plus. It is a high-resolution electron-beam lithography system, which is capable to write structures below 20 nm size reproducibly. It is equipped with a thermionic field-emitter cathode which delivers beam currents between 100pA and 150nA at 50kV. Smaller sample, 5-inch masks and wafers up to 150 mm can be handled by this system. The system consists of a high-precision laser-interferometric x-y table and a height measurement device for dynamic write-field and focuses correction. In addition, the system consists of two deflection systems, a slower one with a resolution of 16 bits and a fast one with a resolution

of 14 bits due to the deflection of the electron beam within a write field to the individual figures and only the area has to be written is filled. The maximum write field at a resolution of 12.5 nm is  $800 \times 800 \mu m$ , while at higher resolution, the writing field becomes smaller. The minimum feature size achievable by this system is smaller than 30 nm.

The standard process for the fabrication of the grating lines investigated in this section by the EBL method is sketched in figure 4.12. Usually, the substrate made of silicon and covered with a 20-50 nm silicon dioxide layer (see figure 4.12(I)), on top of which a protective resist layer is coated (see figure 4.12 (II)) for protection during dicing into smaller pieces. After dicing, the protective resist is removed (see figure 4.12 (III)) by different solvents (Ac+IPA+DI). Then, an e-beam resist layer is coated by spin coating (see figure 4.12 (IV)). The structure geometry is transferred to the e-beam resist layer by electron beam exposure and successive development of the exposed areas (see Figure 4.12(V)). In the next step, the structured e-beam resist layer is used as a mask to transfer the pattern into the silicon dioxide layer by means of reactive ion etching (RIE) process (see figure 4.12(VI)). After removing the e-beam resist layer by using the same solvents (Ac+IPA+DI) used to remove the protective resist in step (VII), the silicon dioxide layer serves as a hard mask for the final deep etching into the substrate (see figure 4.12(VIII)). The details of the parameters used in the fabrication of the grating lines presented in this section are attached in App. C, where all of these parameters taken from the sample preparation report of the HNF institute.

For the final step (step VIII) in the EBL method, wet chemical etching was used to transfer the structure geometry to the silicon substrate. The idea behind wet etching is to use different chemical solutions such as potassium hydroxide (KOH) or tetramethyl ammonium hydroxide (TMAH). The etching rate for N-Si (110) by using KOH faster than TMAH, where the KOH etching rate is 1.292 m/min while the TMAH etching rate is 1.114 m/min.

First gratings group S1 was fabricated without silicon dioxide layer above the gratings, where S1\_01 produced by using KOH etching while S1\_02 produced by TMAHA etching. For the second group S2 samples, KOH etching was used to produce S2\_01 and TMAH etching for S2\_02. Third group S3 was produced with a silicon dioxide layer above the gratings and only TMAH etching was used to transfer the structures to the silicon substrate. Samples in S3 produced with different etching time, 30s, 60s and 90s, were used to produce S3\_01, S3\_02, S3\_03, respectively.

In next sections, structural characterization by SEM (Sec.4.5.2), GISAXS (Sec.4.5.3) and XRR (Sec.4.5.4) with a direct data analysis for gratings produced by KOH and TMAH etching will be presented.

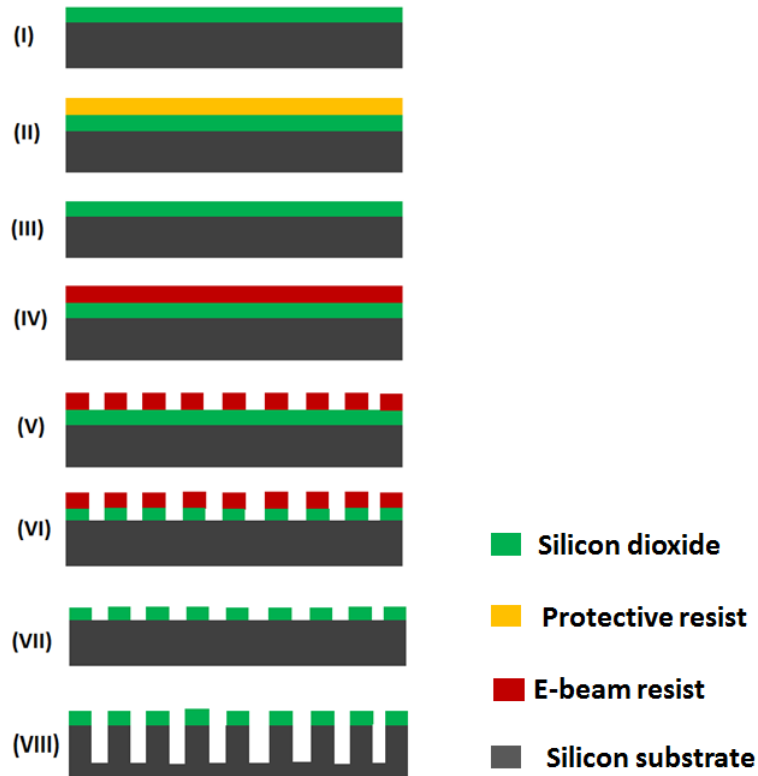


Figure 4.12.: Grating lines fabrication by e-beam lithography (EBL) method.

#### 4.5.2. Scanning Electron Microscopy (SEM)

In this section, SEM images for each grating group (S1, S2, S3) will be shown. From SEM, real space information about the substrate surface, the uniformity of the gratings pattern, sidewall geometry, and quantitative characterization of the grating parameters (groove width and gratings period) can be obtained.

Figure 4.13 shows SEM images with the line profiles for the first gratings group S1, where figure 4.13(a) represents S1\_01 and figure 4.13(b) represents S1\_02. SEM images for S1\_01 and S1\_02 confirms a very smooth and regular pattern of parallel stripes. Furthermore, as can be seen from the SEM image for S1\_02 (figure 4.13(b)) there are some areas in the grooves where the etching doesn't work, particularly when the grooves get wider. Maybe by increasing the exposure during e-beam writing helps to solve this problem, but then the lateral dimensions become too large. Line profiles of the SEM images shown in figure 4.13(a) and (b) are shown in figure 4.13 (c) and (d), respectively, which confirms a periodic pattern for both samples. The grating parameters of S1 samples as obtained from SEM images are summarized in table 4.2. The gratings periodicity  $P$  was calculated by measuring the distance between two peaks (i.e. dotted red lines) in figure 4.13 (c) and (d), which gives  $\approx 200$  nm and  $\approx 230$  nm.

Parameter	S1_01	S1_02
Gratings periodicity (P) [nm]	230.4(2)	212.1(1)
Groove width (W) [nm]	93.5(1)	67.5(6)
Mesa width (D) [nm]	140.5(1)	143.3(3)

Table 4.2.: Grating parameters of S1 samples obtained from SEM.

Parameter	S2_01	S2_02
Gratings periodicity (P) [nm]	239.5(7)	239.8(5)
Groove width (W) [nm]	101.01(3)	74.7(4)
Mesa width (D) [nm]	157.2(2)	161.6(3)

Table 4.3.: Grating parameters of S2 samples obtained from SEM.

nm for S1\_01 and S1\_02, respectively.

Figure 4.14 shows the SEM images with the line profile of S2 samples, where figure 4.14 (a) and (b) represents SEM images of S2\_01 and S2\_02, respectively and figure 4.14 (c) and (d) shows the line profile of S2\_01 and S2\_02, respectively. KOH etching was used to produce S2\_01 sample, while TMAH etching was used to produce S2\_02 sample. Furthermore, there's a silicon dioxide layer covered the gratings of both samples, which can't be seen by the SEM technique. SEM images for both samples confirm a regular and periodic pattern. The S2\_01 shows only one depth profile as shown in figure 4.14(a) and 4.14(c), while S2\_02 sample shows two different depth profile as shown in figure 4.14 (b) 4.14(d). The grating parameters of S2 samples as obtained from SEM images are summarized in table 4.3. The gratings periodicity P was calculated by measuring the distance between two peaks (i.e. dotted red lines) in figure 4.14 (c) and (d), which gives  $\approx 230$  nm and  $\approx 250$  nm for S2\_01 and S2\_02, respectively.

SEM images and line profiles of the last samples group S3 presented in this section are depicted in figure 4.15. Where figure 4.15 (a)-(c) shows the SEM images of S3\_01, S3\_02 and S3\_03 respectively, while figure 4.15 (d)-(f) shows the line profiles of S3\_01, S3\_02 and S3\_03 respectively. TMAH etching was used to produce all S3 samples with a silicon dioxide layer above the gratings. The only difference between all S3 samples just in the time used to transfer the structure to the silicon substrate (i.e. etching time). The time for etching used to produce S3\_01 is 30s, 60s for S3\_02 and 90s for S3\_03. SEM images were

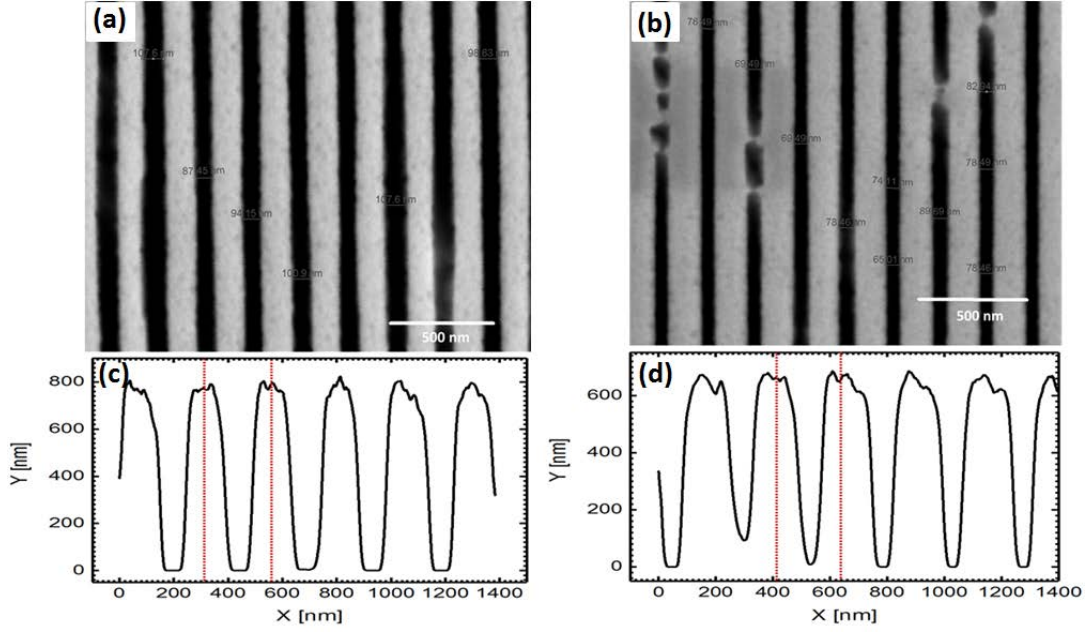


Figure 4.13.: (a) SEM image for S1\_01, (b) SEM image for S1\_02, (c) Line profile for S1\_01 and (d) Line profile for S1\_02.

Parameter	S3_01	S3_02	S3_03
Gratings periodicity (P) [nm]	248.6(3)	235.1(7)	81.1(3)
Groove width (W) [nm]	50.5(1)	50.4(7)	19.1(1)
Mesa width (D) [nm]	194.2(9)	183.5(7)	65.8(2)

Table 4.4.: Grating parameters of S3 samples obtained from SEM.

shown in figure 4.15(a)-(c) confirms periodic and regular gratings. Furthermore, as can be seen from the SEM images that the gratings show some roughness, where it can be reduced by increasing the etching time. As can be seen in the SEM images (figure 4.15(a)), the gratings produced with short etching time are highly rough, while the gratings produced with longer etching (figure 4.15(b) and (c)) time are less rough. The gratings parameters of all S3 samples as obtained from SEM images are summarized in table 4.4. This sample group shows only one depth profile as shown in SEM images (figure 4.15 (a)-(c)) and in the line profiles (figure 4.15 (d)-(f)). The gratings periodicity P obtained from the line profiles were calculated by measuring the distance between two peaks (i.e. dotted red lines) in figure 4.15 (d)-(f), which gives  $\approx 200$  nm,  $\approx 150$  nm and  $\approx 170$  nm for S3\_01, S3\_02 and S3\_03, respectively. The gratings periodicity and the groove width are inversely dependant on the etching time, i.e. P and W values decrease as the etching time increase.

4. Structural characterization of line gratings by grazing incidence small angle x-ray scattering (GISAXS)

---

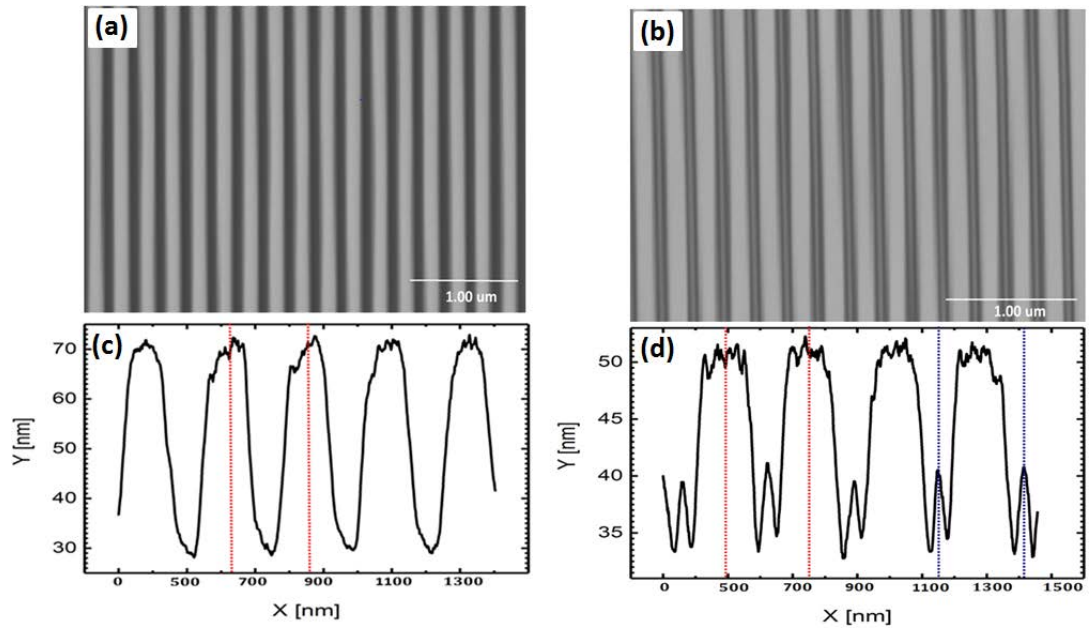


Figure 4.14.: (a) SEM image for S2\_01, (b) SEM image for S2\_02, (c) Line profile for S2\_01 and (d) Line profile for S2\_02.

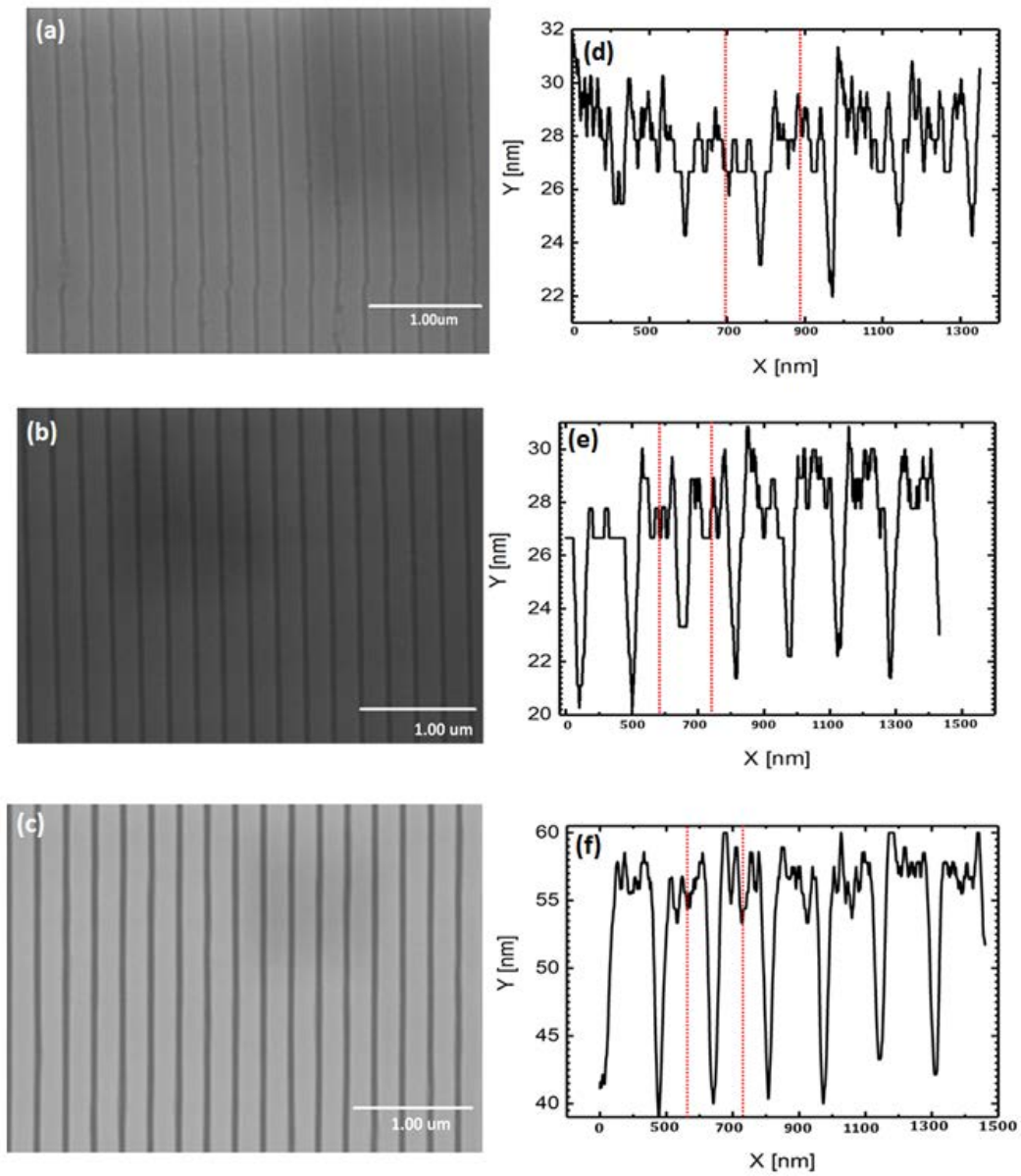


Figure 4.15.: (a) SEM image for S3\_01, (b) SEM image for S3\_02, (c) SEM image for S3\_03, (d) Line profile for S3\_01, (e) Line profile for S3\_02 and (f) Line profile for S3\_03 .

### 4.5.3. GISAXS

GISAXS measurements were carried out in order to obtain information about uniformity, regularity, roughness, periodicity and line shape. Furthermore, to get information about the full three-dimensional characteristic features of the sample probed. The measurements were performed into two different orientations, as the incoming beam perpendicular to the grating lines (Sec. 4.4.4.1) and parallel to it (Sec. 4.4.4.2), but only the GISAXS results of parallel geometry will be shown in this section. The scattered GISAXS pattern of the samples presented in this section shows a few differences compared to the pattern obtained from the sample with large pitches presented in Sec. 4.4, due to the different parameters of the grating. Generally, as the structure size change, the number of GTRs that intersect the EWALD sphere will be changed, and this will affect the GISAXS scattering pattern.

In this section, the GISAXS scattering pattern of all samples group (S1, S2, S3) will be shown and the intensity profile as a function of  $Q_y$  will be shown for each sample in section 4.5.3.1. Furthermore, Fourier transforms analysis and power spectral density (PSD) of extracted and pre-processed GISAXS intensity profile will be shown in section 4.5.3.2, in order to determine gratings parameters and compare it with its nominal values.

#### 4.5.3.1. Parallel orientation, grating parameters determination

The scattered GISAXS patterns in the parallel orientation of incident beam and grating lines for all samples group S1, S2 and S3 in addition to the intensity profile  $I(Q_y)$  for each sample are displayed in figures 4.18, 4.19, and 4.20, respectively. Several features have been reported previously in Sec. 4.4 for gratings with large groove width are observed also for the gratings with smaller groove width, in addition to other observed features which will be explained in detail for each sample.

The main features that are directly observable on the detector image for all samples: first, a series of high intensity spots, are periodically placed on a semi-circle (dotted black semi-circle in figure 4.16), due to the intersection of the EWALD sphere with the reciprocal space representation of the gratings (i.e. GTR) as explained earlier, and it has its highest point at  $\alpha_i = \alpha_f$ . Moreover, the intensity of the Bragg spots along the semi-circle depends on the beam and the grating structure as will be shown later for different grating with different dimensions and structures. The grating periodicity can be calculated from the distance between the Bragg spots by using equation 4.7.

The high-intensity periodic spots on the semi-circle originate due to the regular, periodic structure of the grating lines with a lateral regular repeated displacement at every pitch distance  $P$ . Therefore, a Bragg peak (i.e. high-intensity spots/orders) was produced every  $Q_y = \frac{2\pi n}{P}$ . Where  $n$  is an integer, represents

the order number and  $P$  is the periodicity of the line.

A second main feature is observed, the low-intensity diffuse scattering (i.e. the white extended dotted tilted lines in the GISAXS image in figure 4.16) which is a highly complex feature. In addition to the main features, extinction of some Bragg spots is observed for some gratings, which will be shown later. The origin of the diffuse scattering features mainly comes from the gratings morphology, such as, sidewall angle, capping layer, grating dimensions, bottom corner rounding, line shape, etc. Analysis of the diffuse scattering features is not an easy process and can't be done by direct simple Fourier analysis or via DWBA as explained earlier for grating with a large pitch (Sec. 4.4). It requires to find a specific two dimensional model using a qualitative form factor for the line cross-section, as explained briefly in the outlook (Sec. 4.6) of this chapter. The diffuse scattering features observed are independent of change in the momentum transfer (i.e. change of the incident angle). The broad extended tilted lines in the GISAXS images are a signal of a sloped sidewall with respect to the substrate normal direction [90] which can be calculated in an easy way for each grating structure.

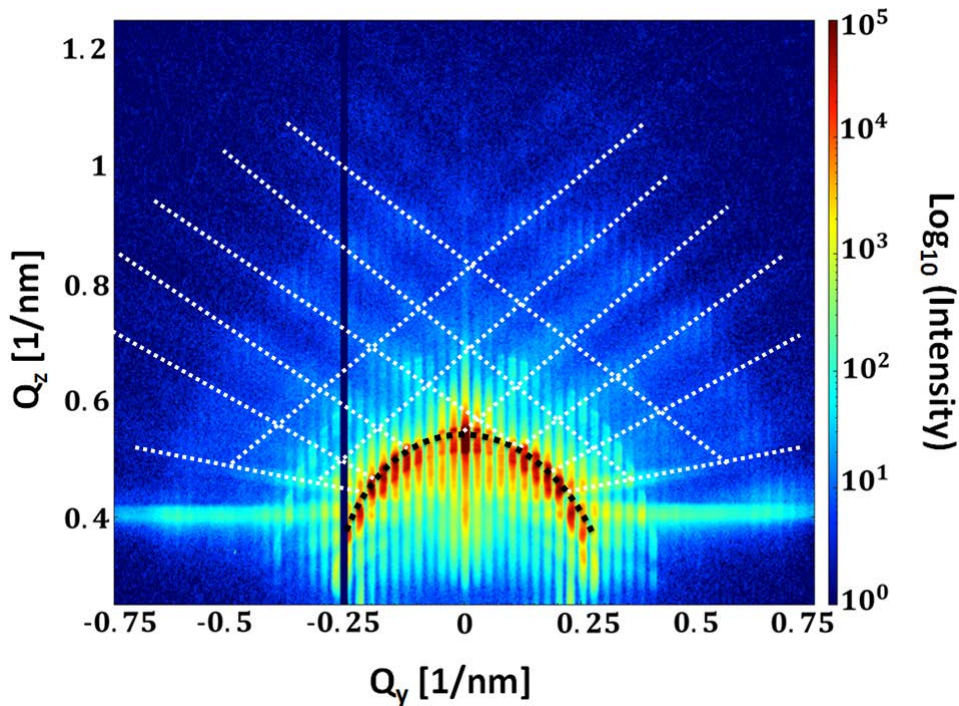


Figure 4.16.: GISAXS image of gratings. The arc drawn in black indicates the high-intensity Bragg spots (i.e. first main features). The tilted lines drawn in white indicate the diffuse scattering (i.e. second main features).

Furthermore, for all line gratings investigated in this section, there are some

issues that can't be observed by SEM, but are confirmed by GISAXS scattering data. The bottom of the etched grooves is not plane (i.e. not defined), it is rather curved with a certain sidewall angle, but the top corners of the lines are much better defined as shown schematically in figure 4.17. This can be understood easily by the fabrication process. The top area of the lines covered by the e-beam resists acting as the etch mask, which protects and leads to more defined top corners of the lines. After etching, the resist removed by an oxygen plasma treatment, which leads to oxidizing the surface and causes an oxide layer. The oxide layer formed is not a stoichiometric  $\text{SiO}_2$  and perhaps not homogeneous from the silicon interface to the surface. The thickness of the formed oxide layer on top of each grating (S1, S2, S3) will be determined by X-ray reflectometry in Sec. 4.5.4.

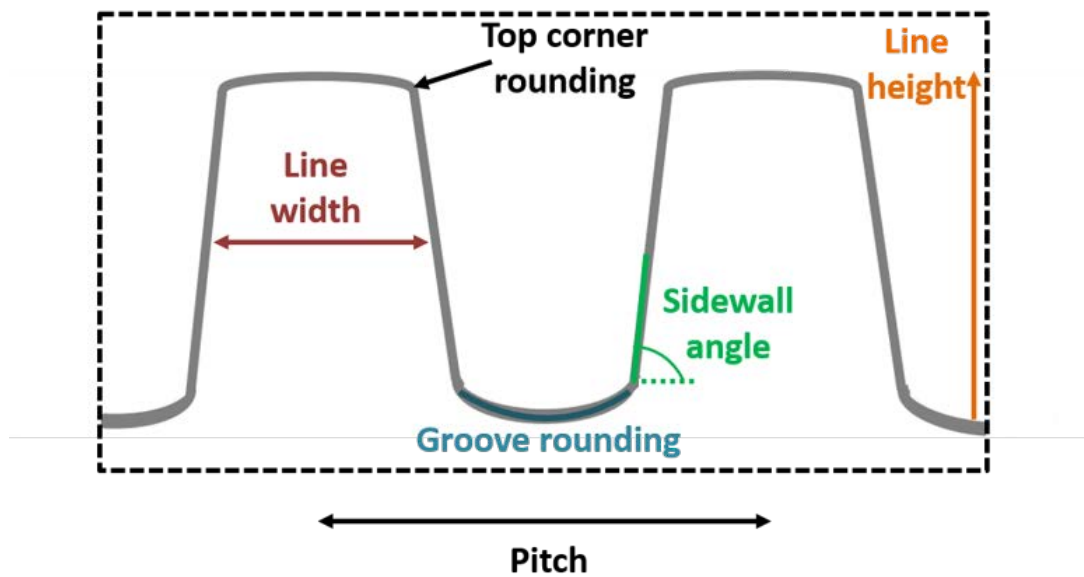


Figure 4.17.: A sketch of the grating model which explains and confirms the GISAXS data.

Figure 4.18 presents the GISAXS patterns with the average intensity profile as a function of  $Q_y$  for S1 samples, where figure 4.18 (a) and (b) shows the GISAXS maps for S1\_01 and S1\_02, respectively. While, figure 4.18 (c) and (d) shows the average intensity profile for S1\_01 and S1\_02, respectively. The GISAXS measurement was carried out at an incident angle of  $\alpha_i \approx 0.4^\circ$ . The main features (semi-circle spots, diffuse scattering lines) that have been reported previously are directly observed for both S1 samples. The sidewall angle of the lines as determined easily from the tilted diffuse lines  $\approx 10^\circ$ , using the protractor. Furthermore, the intensity of the Bragg spots along the semicircle drops

sharply with departing from  $Q_y=0$  as shown in the average intensity profile in figure 4.18 (c) and (d). The sharp drop of the Bragg spots intensity might come due to the line roughness or due to the smaller structure depth. Features symmetric around  $Q_y = 0$  are indicative of a good alignment of the lines with respect to the beam. The grating periodicity as defined from the Bragg spots  $P \approx 243$  nm for S1\_01 and  $P \approx 241$  nm for S1\_02, which is in a good agreement with the value obtained from SEM. The diffuse scattering lines for S1\_02 sample (figure 4.18 (b)) which produced by TMAH etching less than the S1\_01 sample which produced by KOH etching (figure 4.18 (a)), which means that the S1\_02 grooves more plane than S1\_01 (i.e. smaller sidewall angle).

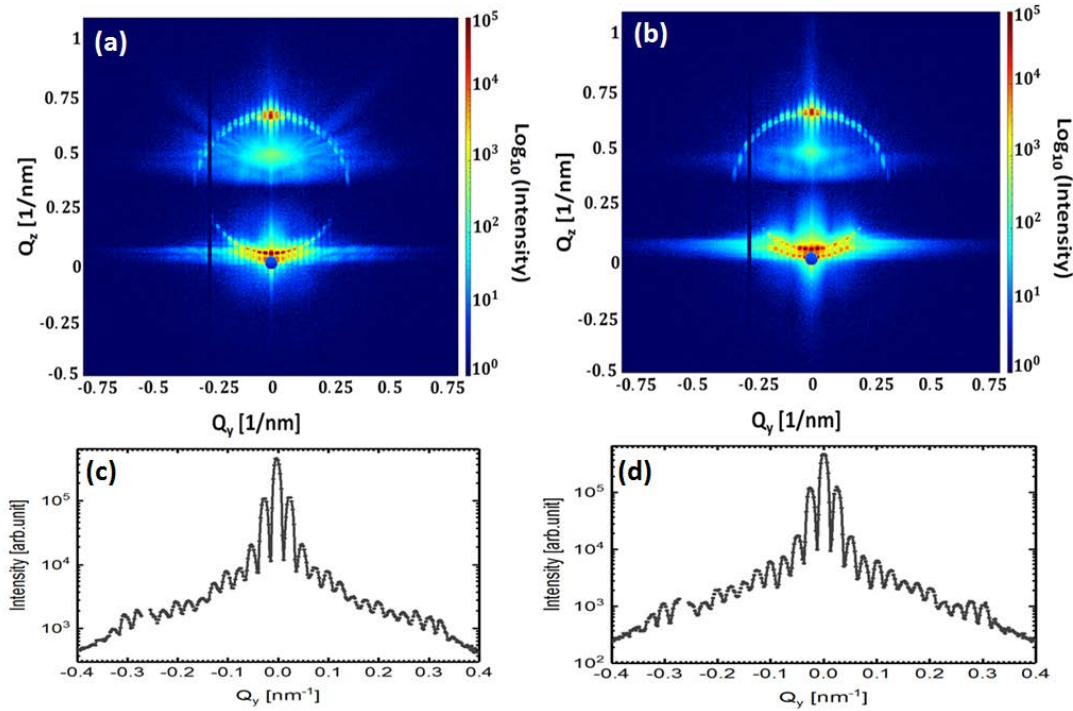


Figure 4.18.: GISAXS patterns at an incident angle  $\alpha_i=0.4^\circ$  for (a) S1\_01 and (b) S1\_02. The bottom right and left-hand images display the intensity as a function of  $Q_y$  along the semicircle for (d) S1\_01 and (e) S1\_02.

The GISAXS patterns together with the average intensity profile as a function of  $Q_y$  for S2 samples are shown in figure 4.19. GISAXS maps for S2\_01 and S2\_02 are shown in figure 4.19 (a) and (b) respectively. While, figure 4.19 (c) and (d) shows the average intensity profile for S2\_01 and S2\_02, respectively. The GISAXS measurement was carried out at an incident angle of  $\alpha_i \approx 0.3^\circ$ . The main features (semi-circle spots, diffuse scattering lines) that have been reported previously are directly observed again for S2 samples. The distance between these two semi-circles is  $\approx 104$  nm for S1\_01 and  $\approx 85$  nm for S1\_02.

Moreover, in sample S2\_02, a higher-order satellite ring is observed, indicating a high periodicity of the structure. Furthermore, a second semi-circle below the main semi-circle was observed for S2\_02 sample as shown in the GISAXS image (figure 4.19 (b)), which can be explained as the grating fabricated with two different depth profiles as shown previously in the SEM and in the line profile (figure 4.3 (b) and (d)) and will be confirmed by XRR later in Sec. 4.5.4. The distance between these two semi-circles defines the periodicity between the two depth profiles, which is  $\approx 100$  nm, which is in good agreement with the value obtained from the SEM-line profile. The sidewall angle of the lines as determined easily from the tilted diffuse lines  $\approx 15^\circ$ . The grating periodicity as defined from the Bragg spots  $P \approx 241$  nm for S2\_01 and  $P \approx 240$  nm for S2\_02, which is in a good agreement with the value obtained from SEM.

The average intensity as a function of  $Q_y$  ( $I(Q_y)$ ) along the semi-circle is extracted for each GISAXS image as shown in figure 4.19 (c) and (d). Features symmetric around  $Q_y=0$  are indicative of a good alignment of the lines with respect to the beam.

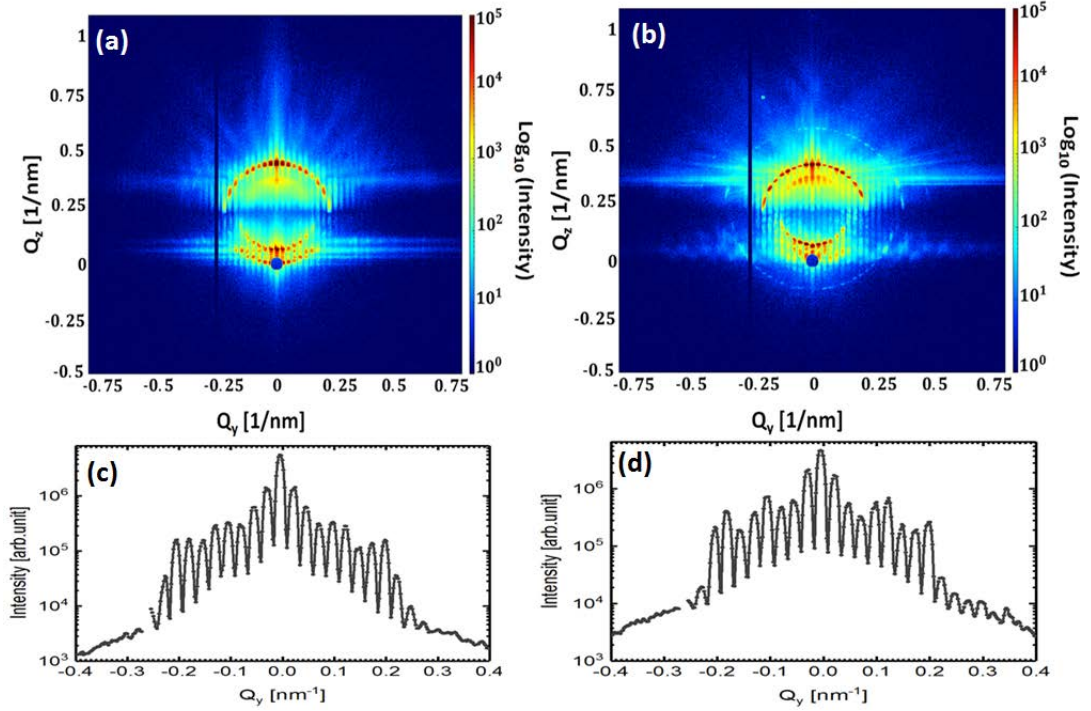


Figure 4.19.: GISAXS data at an incident angle  $\alpha_i=0.3^\circ$  for (a) S2\_01 and (b) S2\_02. The bottom right and left-hand images display the intensity as a function of  $Q_y$  along the semicircle for (d) S2\_01 and (e) S2\_02.

The GISAXS patterns together with the average intensity profile as a function of  $Q_y$  for S3 samples are shown in figure 4.20, where figure 4.20 (a), (b) and (c)

shows the GISAXS maps for S3\_01, S3\_02, and S3\_03, respectively. While the average intensity profile for S3\_01, S3\_02, and S3\_03 as a function of  $Q_y$  are shown in figure 4.20 (d), (e) and (f), respectively. The GISAXS measurement was carried out for all three samples at an incident angle  $\alpha_i \approx 0.35^\circ$ . The main features (semi-circle spots, diffuse scattering lines) that have been reported previously are directly observed again for all S3 samples. Moreover, a high order satellite ring is observed in all GISAXS images, indicating a high periodicity of the structure. Furthermore, a second semi-circle below the main semi-circle was observed for all S3 samples. The distance between these two semi-circles is found  $\approx 270$  nm,  $\approx 200$  nm and  $\approx 220$  nm for S3\_01, S3\_02, and S3\_03 respectively. The sidewall angle of the lines as determined easily from the tilted diffuse lines  $\approx 20^\circ$  for all samples. The grating periodicity as defined from the Bragg spots  $P \approx 268$  nm,  $P \approx 249$  nm and  $P \approx 230$  nm for S3\_01, S3\_02, and S3\_03, which is in a good agreement with the value obtained from the SEM.

The average intensity as a function of  $Q_y$  ( $I(Q_y)$ ) along the semi-circle is extracted for each GISAXS image as shown in figure 4.20 (d)-(f). Features symmetric around  $Q_y = 0$  are indicative of a good alignment of the lines with respect to the beam.

So far, we presented the GISAXS results for different gratings fabricated by using different etching type (i.e. KOH and TMAH) and with different etching time. All samples have shown the main features that can be obtain in the GISAXS patterns of grating lines, in addition to other minor features observed for a certain grating as explained before. By GISAXS, information on structure roughness and long-range periodic perturbation can be achievable. Furthermore, gratings periodicity calculated from GISAXS is in a good agreement with the values obtained from the SEM.

4. Structural characterization of line gratings by grazing incidence small angle x-ray scattering (GISAXS)

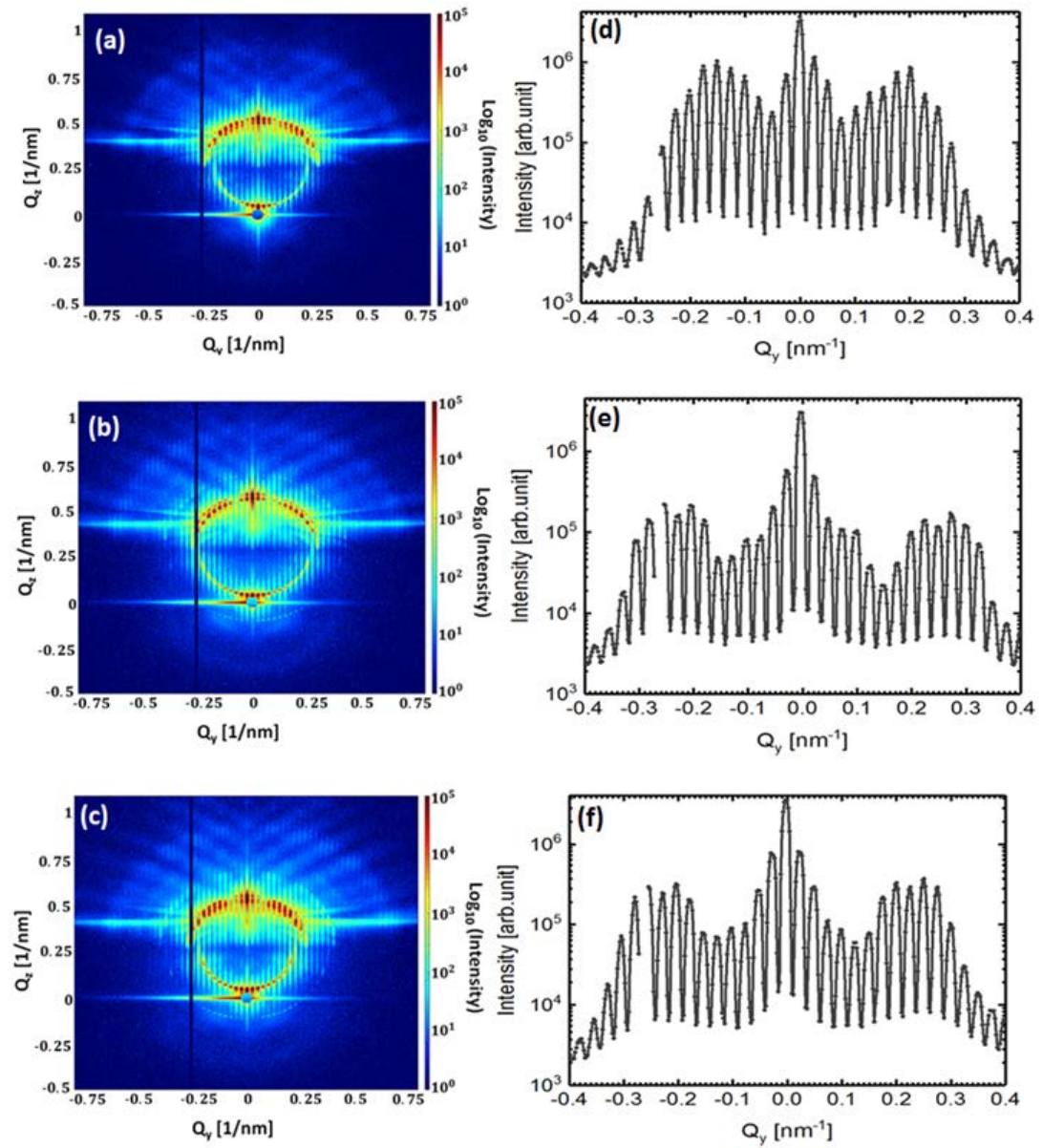


Figure 4.20.: GISAXS data at an incident angle  $\alpha_i=0.35^\circ$  for (a) S3\_01, (b) S3\_02 and (c) S3\_03. The bottom images displays the intensity as a function of  $Q_y$  along the semicircle for (d) S3\_01, (e) S3\_02 and (f) S3\_03.

#### 4.5.3.2. Fourier Transform analysis of GISAXS in parallel orientation

The main aim of this section is to determine gratings periodicity by direct GISAXS data analysis by performing a Fourier transform analysis of the extracted intensity profiles  $I(Q_y)$  shown in figure 4.18 (a) and (b), figure 4.19 (a) and (b) and figure 4.20 (a), (b) and (c) along the semi-circle and then find the PSD profile from the absolute square of the Fourier amplitude (equation 4.9) and later on, compare the periodicity obtained from PSD profile with the periodicity value obtained from GISAXS maps and SEM.

The direct data analysis of the  $I(Q_y)$  profile of some gratings (S1\_01 and S1\_02) investigated in this section becomes unstable and not accurate because as the structural dimensions decrease, the number of the gratings truncation rods that intersect the Ewald sphere also decreased. This leads to increase in the spacing between the diffraction orders (i.e. the high-intensity Bragg spots along the semi-circle), therefore, the detector images detected contains signal with fewer periods, which leads to less obvious peaks in the Fourier transform profile and in the PSD as shown later in the resulted PSD profile for S1 gratings (figure 4.21). Otherwise, the PSD profile for S2 gratings (figure 4.22) and S3 gratings (figure 4.23) shows a pronounced peak that corresponds to the grating periodicity  $P$ .

The resulted PSD profiles is expressed in terms of the signal frequency  $\zeta$  in reciprocal space, which is related to the real space correlation length via equation 4.10. Figure 4.21 (a) and (b) shows the PSD profiles as a function of the correlation length for S1\_01 and S1\_02, respectively. The sharp peak observed for the two samples corresponds to the grating periodicity. For S2\_01 and S2\_02 samples, the PSD profile, figure 4.22 (a) and (b) shows only one sharp peak which corresponds to the grating periodicity. While, PSD profile, figure 4.23 (a)-(c) for S3\_01, S3\_02, and S3\_03 shows a sharp peak corresponding to the grating periodicity in addition to other peaks observed around it. A Gaussian fit (red line) was carried out for the main peak observed for each sample in order to determine the center position  $d_{corr}$  (i.e. grating periodicity  $P$ ) and the width of each peak  $\sigma$ . The resulted  $d_{corr}$  and  $\sigma$  for each sample are summarized in table 4.5.

The larger peak width obtained for S1 gratings due to the smaller periodicity  $\approx 227$  nm, which leads to increasing the spacing between the diffraction orders, therefore, the signal obtained by the detector contains few periods. As a result, a wide peak will be observed. Therefore, the different Fourier analysis method is required because direct Fourier analysis not accurate in this case.

The grating periodicity obtained from the PSD profile for all samples almost matches the value obtained from SEM and GISAXS maps.

sample name	$d_{corr}$ [nm]	peak width ( $\sigma$ ) [nm]
S1_01	226.76(7)	86(5)
S1_02	227.38(8)	79(7)
S2_01	247.68(9)	20(2)
S2_02	247.8(1)	19(3)
S3_01	249.37(3)	14(1)
S3_02	249.4(3)	12(1)
S3_03	248.99(6)	13(1)

Table 4.5.: Gratings parameters obtained from PSD.

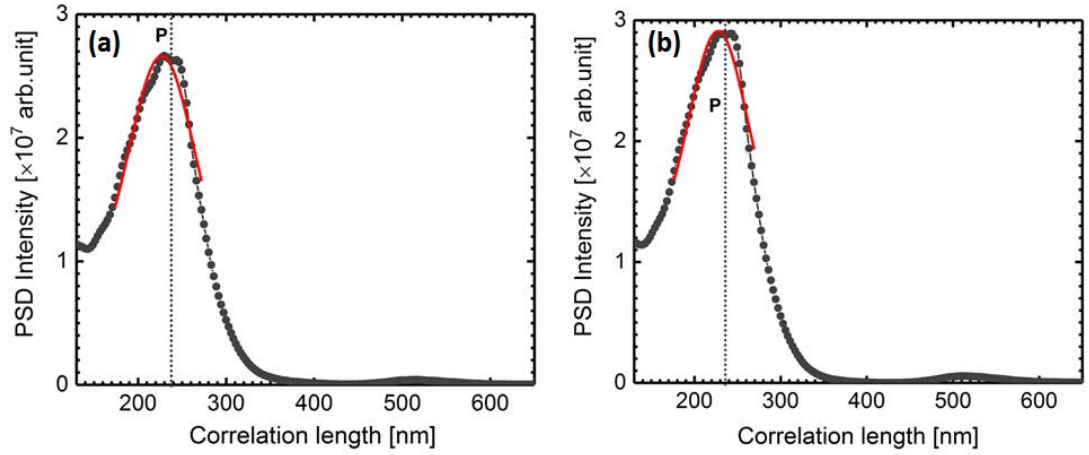


Figure 4.21.: PSD of the  $I(Q_y)$  profiles shown in figure 4.18 (d) and (e), where (a) for S1\_01 and (b) for S1\_02.

#### 4.5.4. XRR results of line height and capping layer thickness

XRR measurements were carried out at GALAXI ( Sec. 3.4.1) for the characterization of all gratings structure investigated in this section (Sec. 4.5) to probe the height of the grating lines  $H$ . Furthermore, it is carried out in order to determine the composition of the structural layers and the thickness of the oxide layer which is not stoichiometrically formed on top of the gratings.

XRR results of S1\_01 and S1\_02 samples with the SLD profile are displayed in figure 4.24 (a) and (b), respectively. Both curves show no Kissing fringe, which can be understood that the grooves fabricated with a large depth ( $>300$  nm), which is higher than the resolution of the GALAXI instrument to observe it. Furthermore, no oscillations observed corresponds to an oxide layer above the gratings. Therefore, both reflectance curves (red points) were simultaneously fitted by assuming a very thick homogeneous groove layer (silicon material) with density smaller than the silicon density, which is calculated from the following

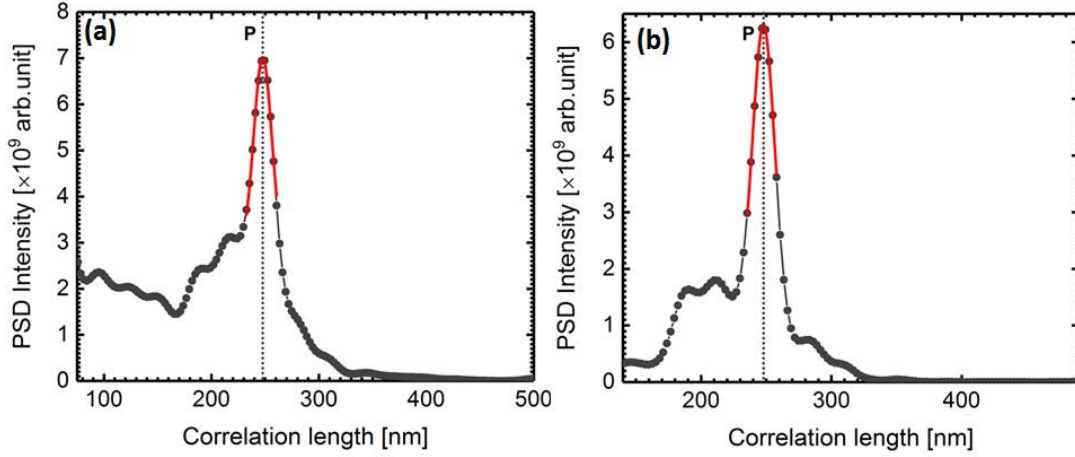


Figure 4.22.: PSD of the  $I(Q_y)$  profiles shown in figure 4.19 (d) and (e), where (a) for S2\_01 and (b) for S2\_02.

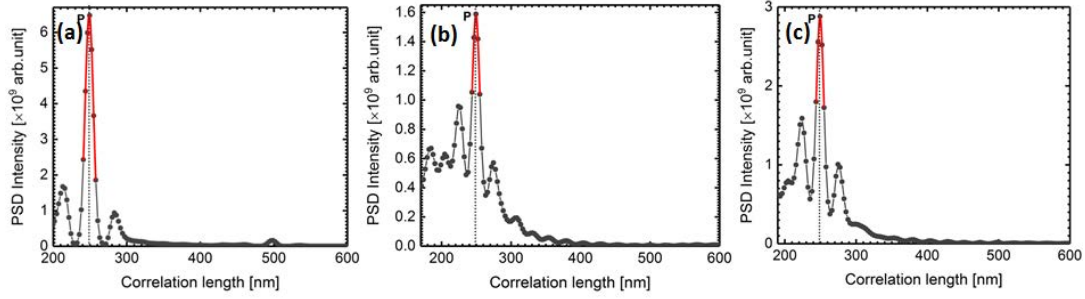


Figure 4.23.: PSD of the  $I(Q_y)$  profiles shown in figure 4.20 (d), (e) and (f), where (a) for S3\_01, (b) for S3\_02 and (c) for S3\_03.

relation:

$$Density_{(groove)} = Density_{(silicon)} \left(1 - \frac{D}{W}\right) \quad (4.11)$$

Where, silicon density  $\approx 2.32 \text{ g/cm}^3$ ,  $D$  is the mesa width and  $W$  is the groove width. In addition to the groove layer, we assumed a very thin oxide layer on top of it. Both layers (the groove layer and the oxide layer) are formed on top of a silicon substrate with the silicon density used in equation 4.11. The oxide layer formed in this case, it is the natural oxidation layer on top of a silicon substrate which is usually has a thickness of  $\approx 1\text{nm}$ . The oxide layer observed thicker than the natural one, due to the removal of the resist by oxygen plasma etching as explained before, which causes increased oxidation of the silicon because of

the large surface area of the lines. The SLD profiles obtained by assuming the two-layer model for both samples are shown as an inset in figure 4.24. XRR data fitting gives that the lines height of S1\_02 gratings which produced by TMAH etching larger than S1\_01 which produced by KOH etching.

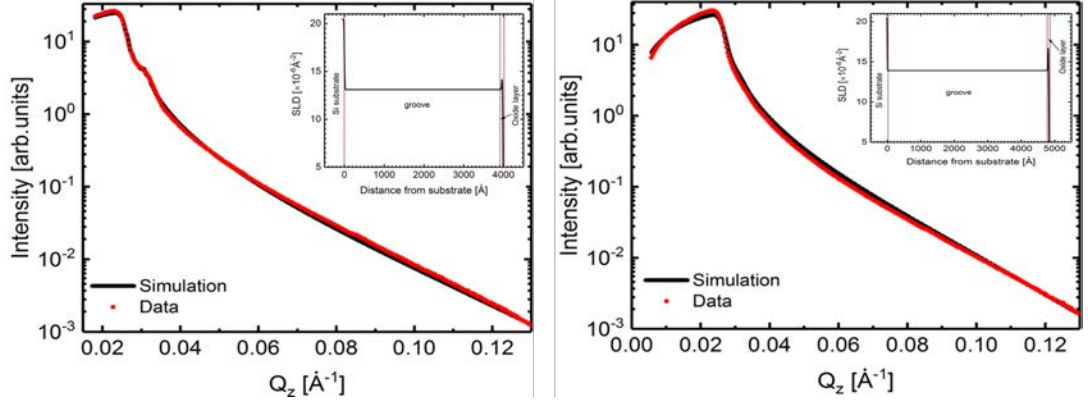


Figure 4.24.: X-ray reflectivity as a function of momentum transfer ( $Q_z$ ) of (a) S1\_01 and (b) S1\_02 grating lines. Data shown as red symbols and fits shown as black solid line. Inset shows the scattering length density (SLD) profile as a function of distance from air interface.

The XRR results of S2\_01 and S2\_02 grating lines with the SLD profiles are shown in figure 4.25 (a) and (b), respectively. The reflectance curve of the S2\_01 sample produced by KOH etching shows an oscillation with only one length scale. The period length of  $\Delta Q_z = 0.44 \text{ nm}^{-1}$  corresponds to a real space correlation length  $2\pi/\Delta Q_z = 14.3 \text{ nm}$ , which can be identified to the oxide layer thickness. The oscillation is due to the constructive and destructive interference of the reflections from the top and the bottom of the oxide layer on top of the gratings. The XRR data for S2\_01 sample (red points in figure 4.25 (a)) were fitted by assuming a two-layer model (silicon oxide layer-groove layer-silicon substrate). The best-fit gives the thickness of the silicon oxide layer  $\approx 13.4(2) \text{ nm}$  and height of the lines  $\approx 596.8(1) \text{ nm}$ . The SLD profile of S2\_01 grating structure is shown as inset in figure 4.25 (a).

The reflectance curve of S2\_02 sample shows oscillations with two different length scales, smaller one corresponds in real space to the large layer thickness, while the larger one corresponds to the small layer thickness in real space. The period length of the large oscillation  $\Delta Q_z = 0.38 \text{ nm}^{-1}$  corresponds to a real space correlation length  $2\pi/\Delta Q_z = 16.5 \text{ nm}$ , while the period length of the small oscillation  $\Delta Q_z = 0.132 \text{ nm}^{-1}$  corresponds to a real space correlation length  $2\pi/\Delta Q_z = 47.6 \text{ nm}$ . The S2\_02 was fabricated by TMAH etching, where during the fabrication process two different depth profiles were formed as shown before in the SEM image and in the line profile (figure 4.14 (b) and (d)). Therefore, the

two different oscillations observed in the XRR curve corresponds to two oxide layers formed on top of the gratings with two different thicknesses. The XRR data were fitted by assuming a three-layer model (oxide layer\_2, oxide layer\_1, groove layer, a silicon substrate). The best-fit values obtained, the first silicon oxide layer thickness is 15.7(1) nm, the second silicon oxide layer thickness is 32.9(3) nm and the height of the lines  $\approx 374.2(1)$  nm. The SLD profile of the S2\_02 grating structure that explains the model used for fitting is shown as an inset in figure 4.25 (b).

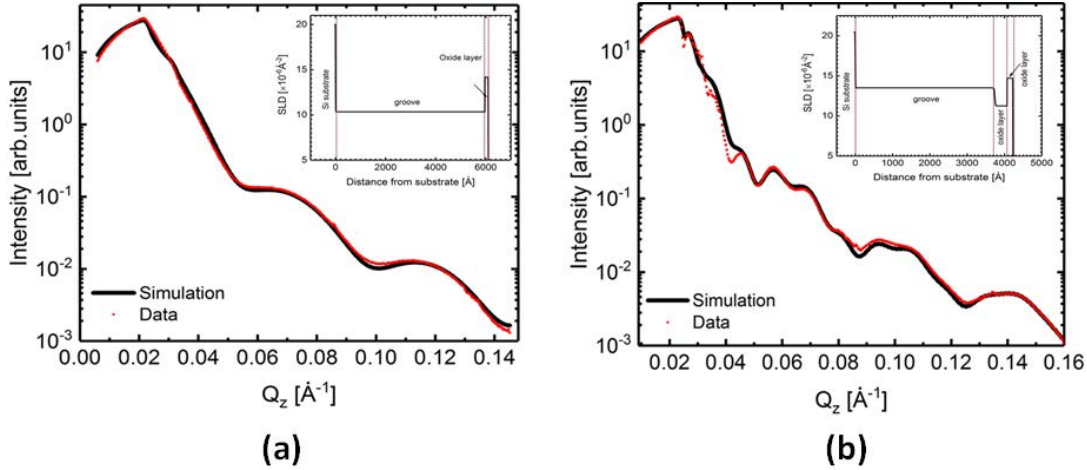


Figure 4.25.: X-ray reflectivity as a function of momentum transfer ( $Q_z$ ) of (a) S2\_01 and (b) S2\_02 grating lines. Data shown as red symbols and fits shown as the black solid line. Inset shows the scattering length density (SLD) profile as a function of distance from air interface.

The reflectivity curves with the SLD profiles of S3 grating lines are shown in figure 4.26. The XRR curves of all S3 samples were produced by TMAH etching with different etching time show an oscillation with only one length scale, which can be identified as the oxide layer thickness. The S3\_01 shows an oscillation with a period length of  $\Delta Q_z = 0.1 \text{ nm}^{-1}$  corresponds to a real space correlation length  $2\pi/\Delta Q_z = 62.8 \text{ nm}$ , the S3\_02 shows an oscillation corresponds to a real space correlation length  $\approx 62.8 \text{ nm}$  and S3\_03 shows an oscillation corresponds to  $\approx 67 \text{ nm}$  as a real space correlation length. The oscillation observed in the XRR curves is due to the constructive and destructive interference of the reflections from the top and the bottom of the oxide layer on top of the gratings. The XRR data in figure 4.26 left side image are shown as symbols, while the fit for each curve is shown as a black solid line. The XRR data for all S3 samples were fitted by assuming a simple three-layer model (silicon oxide layer, groove layer, a silicon substrate). The best-fit values obtained a silicon oxide layer thickness of  $\approx 45.36(6) \text{ nm}$  and the height of the lines  $> 300 \text{ nm}$ . The SLD profiles of S3 grating lines are shown in the right image in figure 4.26.

4. Structural characterization of line gratings by grazing incidence small angle x-ray scattering (GISAXS)

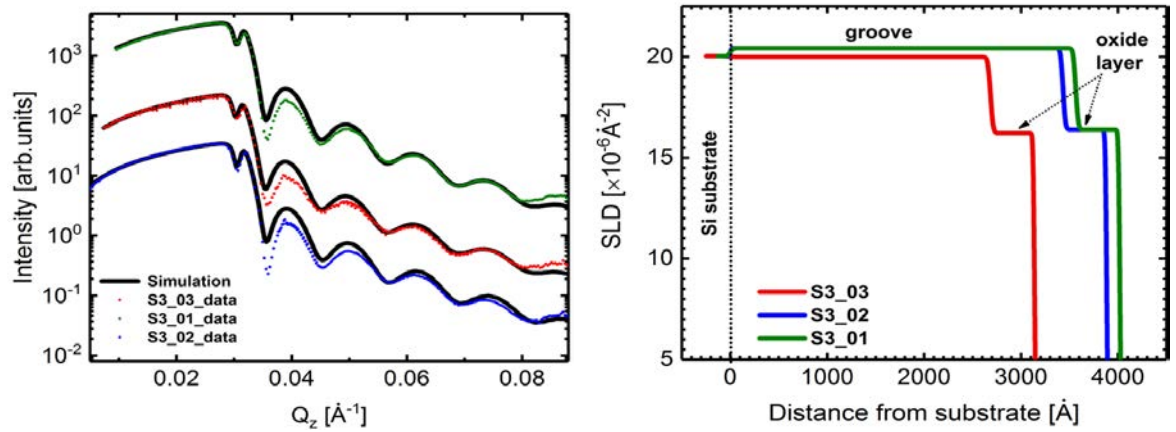


Figure 4.26.: Left side image : X-ray reflectivity as a function of momentum transfer ( $Q_z$ ) of S3 grating lines. The data are shown as symbols and fits shown as a black solid line; red points correspond to S3\_03, blue points for S3\_02 and green points for S3\_01 points. The XRR curves for S3\_03 were multiplied by 10 and S3\_01 multiplied by 100. Right side image: SLD profiles as a function of distance from the air interface obtained by fitting XRR data in left side image.

Even though all S3 samples were fabricated using different etching time, they are shown almost the same behavior. From the XRR curves, no features correspond to the depth of the groove because the depth of the groove higher than the resolution of the instrument to observe it.

## 4.6. Summary and Outlook

In this chapter, for dimensional investigation of grating structures with two different grooves width, ranging from large width close to 150 nm down to small width close to 54 nm, XRR and GISAXS measurement have been applied. In general, the main goal was to evaluate the structural parameter values by GISAXS and XRR, to serve it as a starting point to validate a model-based data analysis. GISAXS technique shows that it is a suitable nanometrological tool for measuring dimensional parameters on nanostructured surfaces and it could be extended as a tool to yield further insight into recent nanotechnological applications such as nanostructured polymer thin films or into industrial applications.

The fundamental principle for the presented PSD analysis method is the same for all gratings investigated in this chapter, but this method is less accurate when the groove size decrease as explained before. The direct analysis of the Bragg spots positional periodicities directly from the GISAXS data, without invert modeling of a form factor and a structure factor helps to avoid the need to assess the correctness of the chosen form factor model and structure factor for numerical simulation and, therefore, makes the data analysis traceability possible. The direct data analysis method limits the analysis mainly to determine the structure factor and thus defines the positions of the scattering features, therefore, only limited dimensional parameters such as grating period, groove width and line-height can be acquired. But it helps in the traceability of GISAXS measurements without requiring chosen models for the form factor and the structure factor.

Standard Fourier transform of GISAXS intensity ( $I(Q_y)$ ) profiles from the gratings with large groove width close to 150 nm proved to be a suitable method to determine the gratings periodicity and the groove width. The results were obtained from PSD are in a good agreement with the nominal values obtained from GISAXS and SEM.

For the smaller groove width, the number of GTRs that intersect the Ewald sphere reduces, therefore, the diffraction orders separated with long distances and, discontinuities observed in the extracted data. For this reason, the standard Fourier transform is not sufficient in this case. A different approach to that of standard Fourier transform that is able to overcome the spaced data, is required.

The direct Fourier analysis of the intensity profiles extracted from the GISAXS data has an advantage in providing information about the structure factor parameters, without requiring to introduce a complex form factor of the grating lines. But for a larger set of grating parameters and for further understanding of the features observed on the GISAXS patterns of gratings (i.e. diffuse scattering lines), a modeling of the 2D scattering GISAXS pattern is required.

Therefore, as an outlook for future activities on this work, full modeling of

the scattering intensities observed in the GISAXS data using the semi-kinematic and dynamic theories could be investigated, mostly by using distorted wave Born approximation (DWBA) and Maxwell equations. Full modeling yields a larger set of the structure parameters such as the sidewall angle, the corner-rounding at bottom of the lines, moreover, the shape of the line cross-section. Furthermore, the form factor and the structure factor parameters can be varied in a suitable way up to evaluate the sensitivities of the scattering features in the GISAXS image. Full modeling of the 2D GISAXS pattern should provide additional details on the origin of the diffuse line scattering.

The semi-kinematic DWBA is the most known approach in GISAXS modeling which takes into account multiple scattering effects. But, DWBA is limited to certain form factors such as a sphere, rectangle, boxes, trapezoids, etc. Therefore, in the case of arbitrary shapes, modeling of the 2D GISAXS data of the gratings has to be done by solving Maxwell's equations and by using the finite element method. The Maxwell solver allows arbitrary form factor of the gratings as shown in figure 4.17, which accounts for line-height, sidewall angle, top radius, bottom radius, rounded bottom edges and thickness of an oxide layer. After modeling the grating lines with suitable form factors, implementation of it into BornAgain software can be done for the comparisons of different methods of analysis and for the validation of the analysis results of the models against the nominal values of direct analysis.

## 5. Self assembly of silica nanoparticles on flat and patterned silicon substrates

The primary goal of this chapter is the successful preparation of highly ordered nanostructures. A simple NPs arrangements that have been discussed extensively in theory, is the hexagonal lattice in a plane. In this part of the thesis, a procedure to fabricate such long-range order nanostructures from nanospheres has been developed. The preparation of such self-assembled lattices with long-range order is presented in detail on the case of the hexagonal lattice from silica nanospheres with  $\approx 50$  nm in diameter, where it self-assembled on flat silicon substrates as a monolayer and multilayers, respectively. Therefore, for this goal, this chapter separates into various parts. First, general introduction about silica NP and why particularly used in this study will be presented. After that, the synthesis and characterization of silica nanoparticles are described in Sec. 5.3.2. This is followed by a quantitative evaluation of self-assembled  $\text{SiO}_2$  NP monolayer and multilayers on flat Si substrate. Thereafter, the structural characterization results of the template-assisted self-assembly of  $\text{SiO}_2$  NP are presented. Part of this work were published in Qdemat, Asma, et al. [91].

### 5.1. Current state of research on nanoparticles monolayer self-assembly

The fabrication of such systems these days is usually performed by a top-down process such as lithography, molecular beam epitaxy, which requires advanced and expensive machines [21]. An alternative method of building materials is a bottom-up process, where nanomaterials sized building blocks are produced from the atomic or molecular level by chemical processes and higher-order nanostructures can be obtained by self-assembly methods [24, 92]. Furthermore, the bottom-up process has the ability to produce structures with low cost than those fabricated by the top-down process. In addition, the origin of the properties of the self-organized systems originates from the properties of their small components and can show collective properties from the long-range order and interacting forces. The self-assembly process is a complicated process that requires a deep understanding of the underlying driving forces and it is still an active field of research.

NP serves as building blocks and once they are self-assembled into a super-

lattice or into an ordered structure, which may possess novel properties and might be considered as an ideal model to study the interparticle interaction on the length scales defined by the nanostructure. Self-organized NPs into an ordered structure has been studied extensively since decades, due to their potential applications in various fields, such as functional materials and biomedicine. The self-assembly of NPs over large areas is determined by various factors. The main factor that plays an important role in the NP self-assembly process is the monodispersity of particles, i.e. NP size distribution. Colloidal particles such as silica NP are easily prepared with a very high degree of monodispersity in large quantities. For this reason, they are often used for self-assembly studies. Monodispersed colloidal particles are usually stabilized by stearyl alcohol or polydimethylsiloxane (PDMS) to avoid agglomeration and to be dispersed in apolar solvents like cyclohexane, chloroform or toluene.

Several methods are known in the literature to prepare large areas of monolayers on substrate starting from NP dispersion. The most notable techniques are the Langmuir-Blodgett/Schaefer method [93–95], spin-coating [45], capillary forces [96], Liquid-air interface [97], doctor blade casting [98], dip coating [99], drop-casting [100], evaporation-driven processes (i.e. slow evaporation of the solvent) and electrophoretic deposition [101], where a dispersion of colloidal spheres is confined between two parallel solid electrodes. Moreover, patterned substrate was also used to improve the ordering between the particles. The resulting order of the NPs usually depends on the preparation techniques used. Some of the preparation techniques are quick to perform with low costs such as drop-casting, dip-coating and spin-coating techniques comparable to other techniques.

The Langmuir-Blodgett/Schaefer technique is a method usually designed for the preparation of organic molecules monolayers, but later on, it has been transferred to the formation of nanoparticle monolayers [102, 103]. The idea behind this technique is that the dispersion is slowly evaporated from an organic solvent on a water surface, where it then is compressed by movable barriers on the surface to monolayer density. By this technique, a high degree in-plane order for 10 nm NPs on the surface is possible as obtained from in-situ XRR and GISAXS results [103]. The main challenge in this technique is to transfer the ordered particles from the surface to the wafer without destroying the order. The study done by Wen et al. [104] shows that micrometer-sized ordered arrays can be obtained by the Langmuir-Schaefer method if the solvent evaporation is well controlled.

Using a liquid-air interface method like the study performed by Kondo et al. [105], colloidal nanospheres tend to organize into 2D ordered structure. In this method, after spreading the nanospheres on the liquid-air interface, it floats on the surface of the liquid. They spontaneously form a 2D hexagonal array due to the attractive interactions between them. After that, the ordered film is transferred to a substrate. The morphology of the ordered structure can

be controlled by various parameters, such as the size of the nanospheres, the concentration and the surface hydrophobicity. From this study, one requirement to achieve ordered colloidal monolayer is that the interparticle interaction should be sufficiently weak.

Furthermore, for 2D NPs self-organization, the capillary forces method was used. The idea behind this method is that, when the NPs are hanging in a thin liquid layer with a thickness smaller or equal to the NP diameter, they tend to order into 2D hexagonal arrays due to attractive capillary force between them [106]. The speed of the particle transport can be controlled by controlling the evaporation rate [106].

Another technique is the drop-casting method, which is a cheap, fast method and does not require advanced instruments. The idea behind this method is, that the NPs transferred to the substrate by spreading a drop of NPs dispersion on a flat surface and then allowing the solvent to evaporate slowly. During the evaporation, the NPs self assemble randomly or into an ordered structure [107]. By using this method, the exact amount of NPs needed for monolayers formation is set. Furthermore, the drop-casting method is a well-known method to prepare multilayered samples. The main challenges of the drop-casting method are: control the self-assembly process by control the environmental conditions during the evaporating of the solvents and choosing the correct solvent for the NPs. Furthermore, choosing the correct NPs concentration and the correct volume of the NPs droplet that spread on the substrate surface. A common phenomenon that is always observed from the drop-casting method is known as the ‘coffee-ring’ effect, where the NPs distribution is inhomogeneous and the particles tend to agglomerate at the edge of the drying droplet [108–110]. The reason for this effect is the evaporation-driven capillary flow of the particles induced by the inhomogeneous evaporation profile of a pinned drop with a finite contact angle [108]. The addition of the surfactants in the NPs dispersion might alter the drying pattern, as they influence the particle-particle, particle-substrate, or particle-free interface interaction [109].

In the drop-casting method, if the solvent to get planed NP distribution on the substrate is recognized, then the only challenge in this method is how to control the self-assembly process toward long-range order. There are some methods reported on how to get long-range NP order, one of these methods is the study carried out by Bigioni et al. [100]. In this study, they showed that by using a mixture of solvent/co-solvent, a large long-range order on the micrometer scale can be possible. Also, they used a combination of toluene as a solvent and dodecanethiol as a co-solvent and they found that the monolayer formation at the liquid-air interface is affected by the evaporation kinetics and the amount of the excess dodecanethiol ligand molecules in the dispersion. Two important parameters are required in the drop-casting method in order to get long-range ordered monolayers and to capture the kinetics and the essential physics of

the drying during the self-assembly process: (i) The flux of the NP to the droplet surface, and (ii) the diffusion length in the liquid-air interface which can be tuned by the particle size, surface tension or osmotic pressure. The NP diffusion to the droplet surface is controlled by the solvent evaporation rate, where the shrinking droplet height catches particles from the dispersion. In order to increase the interfacial diffusion length, the particles have to pins on the interface, therefore, a mechanism is required to be present to control the droplet evaporation.

Figure 5.1 shows a schematic diagram of the self-assembly process during the early stages of the drying. In terms of monolayers of stearyl alcohol grafted NP prepared by drop-casting, no study is found in current literature as to which solvent and conditions have to be used to obtain a single uniform, homogeneous monolayer.

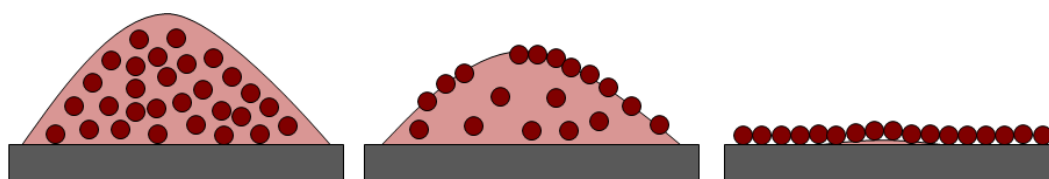


Figure 5.1.: Schematic diagram of the self-assembly process during the first drying stage according to [100]. First, the NP stabilize on top of the droplet surface as the droplet volume shrinks, where they can still move in two dimensions to obtain long-range order. Second, with the remaining slow evaporation rate, the ordered structure remains.

In particular, related to silica NP, there are also several methods that were reported on fabrication of highly ordered monolayer of silica NP on a solid substrate. Such as electron beam lithography [111], dip coating [112], spin coating [113, 114] Langmuir–Blodgett (LB) technique [115] and capillary immersion force [116]. Y. Wang demonstrates highly ordered and closely packed self-assembled monolayers of microsized  $\text{SiO}_2$  spheres on a silicon substrate and on a glass substrate by dip-coating method [112] and Ogi et al. [117] reported the fabrication of a monolayer of  $\text{SiO}_2$  nanoparticles of size 550 and 300 nm on sapphire substrates by using the spin coating method.

The above methods typically result in small monolayer area and non-uniformity of the resulting monolayer. Due to these disadvantages, these methods are not suitable in the industry. Drop-casting is a simple, cheap method and permits the formation of a monolayer over a large area in a short period. Due to these advantages, the drop-casting method has the potential for industrial application since it fulfills the industry requirements.

In this study, a drop-casting method to prepare a monolayer from stearyl alcohol grafted silica NPs is presented. To obtain a uniform, homogeneous dis-

tribution of the NPs on a silicon substrate and to achieve long-range order, the influence of the concentration of NPs and the stearyl alcohol, the volume of the drop on the formation of large-area monolayers were investigated. Information about the particle size, shape and size distribution were obtained from SAXS measurements. To deduce information about the structural order of self-organized particles, SEM, X-ray reflectivity (XRR) and GISAXS measurements have been used. SEM images give a direct view of the particles ordering within a small area in real space. While XRR and GISAXS provide information about the out of the plane and in-plane ordering of the particles in reciprocal space.

## 5.2. Introduction to silica nanoparticles

Silica particles have received in recent years much interest and have been widely used in various applications for centuries due to their extensive existence in nature. Moreover, silica can be purchased at a low cost, which makes the application of silica more communal. Particularly, the silica NPs used in this study have two main important advantages. First of all, they can be prepared with a narrow size distribution which is essential for the self-assembly process. Second, the surface of the particles can be chemically modified resulting in particles, which, if dried carefully, do not immediately aggregate irreversibly, which might increase the time for self-assembly. In addition, also the relatively low Hamaker constant of silica as compared to other inorganic materials might limit the Van der Waals attraction between the cores of the particles, making them more free to move, thereby favoring self-assembly to high-quality monolayers. Generally, the possibilities for chemical modification of the surface of silica particles as well as within the particles lead to use it in various fields such as medicine, biology, engineering and the development of customized materials [118].

## 5.3. Experimental methods

### 5.3.1. Synthesis of stearyl silica nanoparticles

The method used to synthesize silica nanospheres used in this study is known as '*The microemulsion*' and in the following is further elaborated about this method.

The silica NPs used in this study come from a collaboration with Dr. Johan Buitenhuis of the institute of Biomacromolecular Systems and Processes (IBI-4) at Forschungszentrum Jülich. Here, monodisperse silica particles were prepared in two steps. First monodisperse core silica particles were synthesized in a reverse microemulsion system [119–121]. After purification from the microemulsion, the particles were grafted with stearyl alcohol (figure 5.2) following van Helden [122]. In this procedure, the stearyl alcohol forms covalent bonds

to the silica surface, resulting in a stearyl layer of about 2 nm thickness. This gives sterically stabilized colloidal silica nanoparticles, which can be dispersed in nonpolar solvents like cyclohexane, chloroform, or toluene. Here particles with a diameter of about 50 nm were obtained, using toluene as a solvent. Concentrations are expressed as volume fractions, which are calculated using the densities of solvent, silica and stearyl alcohol and assuming additivity of volumes. For the stearyl silica particles, an average density of 1.8 g/mL was used, which is also in agreement with a density measurement on former stearyl silica colloids of similar size. According to the synthesis process described, a colloidal dispersion with 5.4 vol% stearyl silica nanoparticles was prepared as stock and a colloidal dispersion with 0.11 vol% stearyl silica nanoparticles was prepared as dilute dispersion. The particles were stored in a sealed bottle and had a shelf-life time of more than two years after which they start degrading.

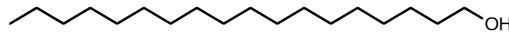


Figure 5.2.: Chemical structure of stearyl alcohol molecule.

### 5.3.2. Nanoparticles characterization

In this section, the experimental methods, conditions and data treatment that were applied to characterize the nanoparticles will be presented.

#### Scanning Electron Microscopy

Scanning electron microscopy is used to provide a direct view of the particles, to study the surface and to obtain information about the particle shape, size and size distribution. For the sample measured by SEM, a 5  $\mu$ L drop of dispersion with a concentration of 5.4 vol% is transferred to a silicon substrate. The SEM used in our measurement is Hitachi SU8000 (Sec.3.2.1). To evaluate the particle size and size distribution, the diameter of over 100 nanospheres is measured manually and the size distribution is evaluated by a simple function, a log-normal distribution function is fitted to the histogram

$$f(d, d_0, \sigma) = \frac{1}{d\sigma\sqrt{2\pi}} \cdot \exp\left(\frac{-(\ln(D/D_0))^2}{2\sigma^2}\right) \quad (5.1)$$

Where the parameters  $D_0$  is the mean particle diameter and  $\sigma$  is the Log-normal slandered deviation.

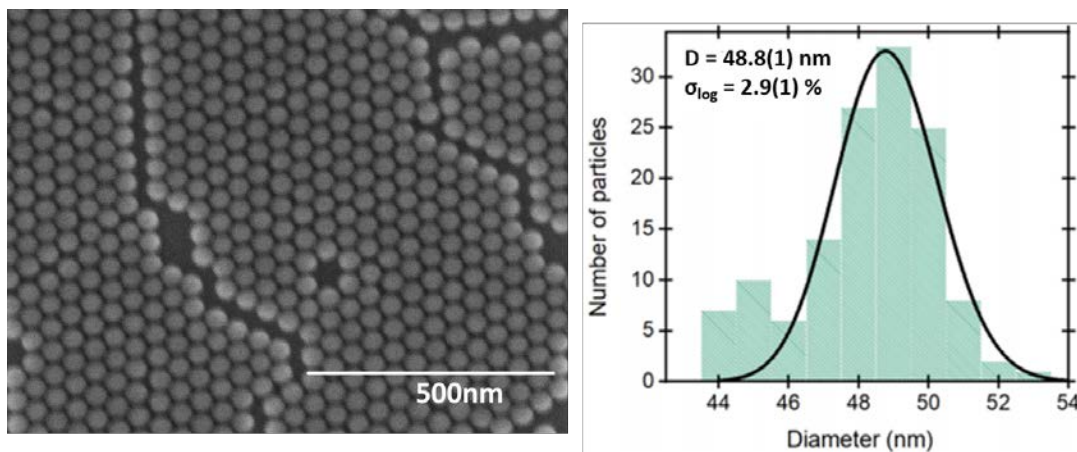


Figure 5.3.: SEM image (left) and evaluated size distribution (right) of the silica nanoparticle

The ideal SEM micrograph in figure 5.3 shows nanoparticles with a spherical shape. Their average diameter is estimated to  $48.8 \pm 1.5 \text{ nm}$  and size distribution ( $\sigma$ ) with 3% by the log-normal distribution fit obtained from a statistical analysis of 100 particles as shown in figure 5.3. SEM clearly revealed that the particles are regular spherical particles and once deposited over a silicon wafer, tend to self-organize in a regular hexagonal layer without agglomeration. Furthermore, the nanospheres tend to be more close to each other. Moreover, they are qualitatively homogeneous in shape.

### Small-Angle Scattering

For the SAXS measurement, the silica nanoparticles dispersions are filled in quartz glass capillaries (Hilgenberg GmbH) with 1.5 mm outside diameter and 0.01 mm wall thickness, which is closed by a silicone ball was added by using a silicone gun to allow the measurement of the dispersions in a vacuum. Two different concentrations, 5.4vol% and 0.11vol% were measured and toluene used as a solvent.

The samples are measured at two sample-to-detector distances of 3.53m and 0.83m using GALAXI instrument (Sec.3.4.1). The capillaries filled with the toluene solvent and the nanoparticle dispersions as well as an empty capillary is measured under the same conditions as a reference sample for the subtraction of the background. The typical exposure time was approximately 3h per sample. The absolute unit calibration of SAXS measurements at GALAXI is performed according to the procedure described in App. D.

Only the SAXS data of the dispersion with a concentration of 0.11 vol% is shown in this section. The data was evaluated using "SasView" software. For a

quantitative evaluation of the data, a shape model was assumed to produce the data. In our case, the spherical model (App.E.1) was used. By using SAXS, information about the average size and shape of the nanoparticles over a large volume of the sample can be accessible.

### Shape model

In figure 5.4 the SAXS data of the silica nanoparticles dispersion with a concentration of 0.11vol% is shown. The data shows the first form factor minimum at a smaller scattering vector ( $Q$ ), which can tell that the average particle size is large. Furthermore, the data shows the minima are qualitatively sharp due to the smaller size distribution of the particles.

To obtain a quantitative evaluation of the SAXS data, the SAXS curve was fitted to the form factor of spherical shape (App.E.1). The obtained parameters from the fit of the data are tabulated in table 5.1.

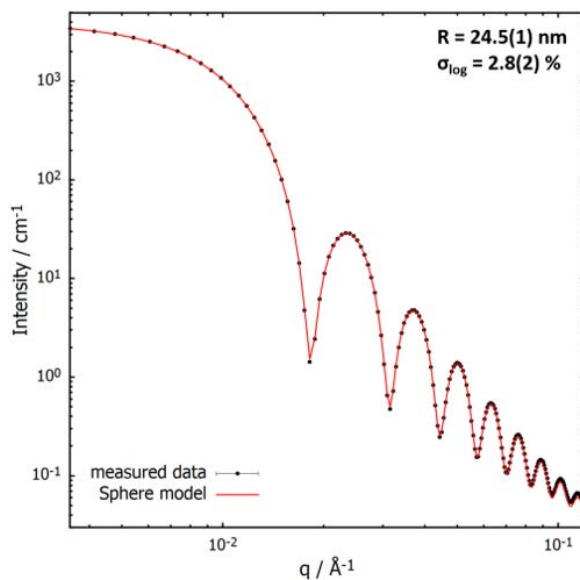


Figure 5.4.: SAXS data of SiO<sub>2</sub> NPs together with the fit (black line) to the data (red points) assuming a spherical form factor.

### Comparison of SAXS and SEM

The size and the size distribution obtained by the best spherical fit of the SAXS data and the values determined from SEM are listed in table 5.2. Within the e.s.d. the values are identical.

Sample name	R[nm]	$\sigma_R$ %	SLD <sub>solvent</sub> [10 <sup>-6</sup> Å <sup>-2</sup> ]	SLD <sub>core</sub> [10 <sup>-6</sup> Å <sup>-2</sup> ]
SiO <sub>2</sub> - 0.11vol%	24.5(1)	2.8(1)	8.5	15.5

Table 5.1.: Parameters obtained from fitted SAXS data with the spherical form factor shown in figure 5.4. The size of the sphere is given in terms of radius R. The respective log-normal size distribution is given as  $\sigma_R$ . The SLD<sub>solvent</sub>, SLD<sub>core</sub> are the scattering length density of the core and the solvent, respectively.

Parameter name	SAXS	SEM
R [nm]	24.5 (1)	24.4 (1)
$\sigma_R$ %	2.8 (1)	2.9 (1)

Table 5.2.: Comparison of nanoparticle length scale as viewed by SAXS and SEM.

### 5.3.3. Deposition process of nanoparticles on wafer surface

In this chapter, the preparation steps for all samples presented are explained. Furthermore, the drop-casting measurement steps used for monolayer formation and the factors that have an influence on the monolayer formation are explained in detail. The general procedure for a drop-casting experiment is easy, simple and well known, but there are multiple crucial points that need to be taken into account before starting the drop-casting experiment, i.e. deposit the nanoparticles on the substrate: first, the nanoparticle dispersions and the substrate need to be prepared. Second, a suitable nanoparticle concentration has to be chosen for the dispersion, as well as a suitable solvent that has to be chosen which influences the evaporation driven self-assembly. Furthermore, the environmental conditions such as the temperature and the kind of the container where the sample put in and dried in during the solvent evaporation, play an important role to control the drop-casting experiment.

Each point mentioned in the previous paragraph is described in detail in the following besides the characterization methods used to show its effects on the samples.

#### Preparation of the Silicon Substrate

The substrates used in our study are single-crystalline N-type silicon substrates with (100) orientation that were purchased from Crystec GmbH with a thickness of 0.5 mm and cut into 10\*10 mm<sup>2</sup> pieces. The wafers are polished on one side, where this side used for nanoparticle deposition using the drop-casting method. To remove dust particles and contamination from the substrate surface, the substrates are cleaned using an Elmasonic P60 ultrasonic bath, where the substrates first are alternately ultra-sonicated in acetone, ethanol, and deion-

ized (DI) water for 5 min, respectively. After that, the wafers were stored in ethanol until use it. N2 gas was used to dry the silicon substrates directly after taking it out from the ethanol just before nanoparticle deposition. After the above treatment of the substrate, the drop-casting method was used to deposit nanoparticles on the substrates.

### Determination the concentration of the solution used for monolayer formation

In order to improve the NPs ordering over the whole sample area, stearyl alcohol was used as an assistant, more details will be explained in section 5.9. Therefore, in the beginning, a solution that contains the silica nanoparticles and the stearyl alcohol was prepared as explained later in this section.

At the beginning, before the preparation of the monolayer solution, the nanoparticles' concentration in the dispersion for a monolayer formation on a substrate surface has to be determined, which can be estimated geometrically from the particle-to-particle distance  $a_{p-p}^2$  on the hexagonal lattice with a lattice constant  $a$ . But for densely packed spheres in two dimensions, one has to take into account the reduced average by including the packing density  $\eta$  in the plane and  $a_{p-p}^2$  has to be replaced by the average maximum cross-section that the particle is taking in the lattice. The packing density for densely packed spheres in two dimensions is  $\eta = \pi\sqrt{3}/6 \approx 0.9069$  and the cross-section is given by  $\pi r^2$ .

The number of nanospheres  $N_{nanospheres}$  expanding over the substrate area  $A_{substrate}$  by assuming a perfect hexagonal lattice of nanospheres is given by:

$$N_{nanospheres} = \frac{A_{substrate}}{\pi R^2} \quad (5.2)$$

Where  $R$  is the particle radius which is in our case  $\approx 25$  nm as determined from SAXS and SEM in Sec. 5.3.2.

The number of the nanoparticles in the dispersion with volume  $V_{disp}$  can be estimated from particle volume concentration  $c_V$  and the volume of a single nanosphere  $V_p$ ,  $V_p = 4/3\pi r^3$ .

$$N_{nanospheres} = \frac{c_V V_{disp}}{V_p} \quad (5.3)$$

The particle volume concentration  $c_V$  can be determined from:

$$c_V = \frac{c_m}{\eta\rho} \quad (5.4)$$

Where  $c_m$  is the particle mass concentration and  $\rho$  is the density of the particle that can be determined from the literature value.

By combining the above equations together, then the particle mass concentration becomes:

$$c_m = \eta\rho \frac{A_{substrate}}{\pi R^2} \frac{V_p}{V_{disp}} \quad (5.5)$$

Typically, for silica nanospheres with a diameter in the order of 25 nm and with stearyl alcohol molecule grafted the nanoparticle in the order of 2 nm, the optimal mass concentration for a drop of volume in the order of  $5\mu\text{L}$  used for a monolayer preparation on  $10 \times 10 \text{ mm}^2$  silicon wafer is in the order of 2.9 mg/mL as obtained from equation 5.5 by considering  $\eta \approx 2.2$ ,  $\rho$  for amorphous silica  $\approx 1.8 \text{ g/mL}$ , the radius of the particle  $R \approx 25 \text{ nm}$  and the  $V_{disp} = 5\mu\text{L}$ . Using the calculated  $c_m$  value, the optimal particle volume concentration  $c_V$  can be determined from equation 5.4 which is in order of  $7.323 \times 10^{-4}$ . Therefore, the number of the nanospheres in the dispersion of  $5\mu\text{L}$  can be calculated from equation 5.3 which is in order of  $4.5 \times 10^{15}$  nanospheres, while the number of the nanospheres that self-assemble in the silicon wafer is in order of  $4.5 \times 10^{10}$  nanospheres, which can be explained that some particles are lost during the drop-casting process.

The nanoparticle dispersion used in the preparation of the solution used in the monolayer formation is the stock solution with volume fraction 5.4%, which is equivalent to a mass concentration  $c_m = 97.2 \text{ mg/mL}$ . The mass concentration estimated from the volume fraction as follows:

$$c_m = \nu\rho \quad (5.6)$$

Where  $\nu$  is the volume fraction and  $\rho$  is the density of the amorphous silica  $\approx 1.8 \text{ g/mL}$  which is lower than the pure silica due to the stearyl alcohol reduces the effective density.

The solution with 0.1 vol% stearyl silica and 0.1 vol% stearyl alcohol where used in the monolayer formation was prepared, by adding  $20 \mu\text{L}$  of 5.4 vol% stearyl silica and  $20 \mu\text{L}$  of 5.4 vol% stearyl alcohol to  $0.96 \text{ mL}$  of toluene. After that, only  $5 \mu\text{L}$  of this solution was taken by a micropipette and dropped onto the silicon substrate to form the monolayer.

### Evaporation and drying process during drop-casting

The cleaned silicon substrates used for the drop-casting experiments are commonly placed in a clean Petri plate. The drop-casting procedure is varied for

the optimization of the long-range order in the monolayer. The following variations have been performed using silica dispersion with a concentration of 5.4 vol%: In the first stage of the monolayer preparation in Sec. 5.8, to study the influence of the speed of the evaporation process for the primary solvent, 5  $\mu\text{L}$  of stearyl silica dispersion was taken by a micropipette and dropped onto the silicon wafer, the primary solvent, toluene in our case is evaporated at ambient conditions of 22 C° in an open clear Polystyrene box within few minutes. After the evaporation of the primary solvent, an addition of 5  $\mu\text{L}$  toluene added to the already self-assemble film then directly the Polystyrene box where the sample placed is covered. By covering the Polystyrene box after additive of the toluene, the evaporation rate will reduce and the particles get more time to order.

In the second stage of the monolayer formation in Sec. 5.9, to study the influence of the speed of the evaporation process for the primary and the minor solvents, 5  $\mu\text{L}$  of the solution contains the stearyl silica and stearyl alcohol was taken by a micropipette and dropped onto the silicon wafer, the primary solvent, toluene in our case is evaporated at ambient conditions of 22 C° in an open clear Polystyrene box within few minutes. While the minor solvent, stearyl alcohol that was added to the silica dispersion is evaporated after toluene because it is evaporation rate lower than toluene. After 30 minutes, the clear Polystyrene box where the sample is placed is closed. Toluene has a boiling point  $\approx 111$  C°, while the stearyl alcohol has a boiling point  $\approx 210$  C° at 15 mmHg.

In the third stage of the monolayer formation in Sec. 5.12, furthermore, we tested the possibility to improve the monolayer quality by adding an additional annealing step. The sample obtained in the second stage of the monolayer formation and after it is placed in the closed clear Polystyrene box, it was placed for various periods in an oven at a temperature above the melting point of the stearyl alcohol without moving the sample. During the heat treatment, the stearyl alcohol is melted and particles become free to move which leads to further self-assemble.

### **Variation of the nanoparticle and stearyl alcohol concentration and local characterization by SEM**

To study the influence of the concentration of the nanoparticle and the stearyl alcohol on the monolayer formation. First, the nanoparticle concentration without stearyl alcohol was varied, to obtain the suitable nanoparticles concentration for mixing with stearyl alcohol. Mainly the concentration of the nanoparticles in the toluene decides the number of the nanoparticle layers formed (monolayer or multilayer). Second, the concentration of the nanoparticle and stearyl alcohol was varied together, to get the optimal concentration value for the solution used to form the monolayer. By using SEM and GISAXS, information about the samples' quality and the lateral order of the samples are quantified.

Figure 5.5 shows SEM images taken at different positions in the wafer sur-

face with the same magnification for two samples that were prepared by the drop-casting method under the same conditions with two different nanoparticle concentrations. In both concentrations, the nanoparticles form close-packed structures with hexagonal arrangements. For the nanoparticles with a low concentration (0.11vol%), left side SEM images in figure 5.5, many structural defects could be observed. Some regions are almost empty with few particles. Some regions also have big holes, which form due to less nanoparticle concentration in the solution (figure 5.5 (a) and (c)). There are some regions where a second complete layer forms on top of the first layer (figure 5.5(b)) with some structural defects especially cracks, which form because of the fast drying of the toluene during the drop-casting process. For the nanoparticles with higher concentration (5.4vo%), figure 5.5 (d-f), a non-continuous multilayer of nanoparticles was formed over some regions in the wafer surface as shown in figure 5.5 (d), while some regions over the entire substrate are covered with large areas of almost perfectly multilayers as shown in figure 5.5 (e) and (f). In addition, the hexagonal ordering is quite long ranged with fewer structural defects. In the case of the multilayer, the close packing is better, because the ordering is taking place in three dimensions, where there is an extra degree of freedom of the ordering.

Summarizing the different concentrations of nanoparticles dispersions discussed above, the largest areas of almost perfectly ordered nanoparticles are obtained from the nanoparticles dispersion with a concentration of 5.4vol%. If the nanoparticles concentration is reduced, such a not homogeneous nice ordering or non-uniform monolayers may be observed over small regions in the substrate surface. The morphology over the substrate surface is more homogeneous observed by using a higher concentration of nanoparticles.

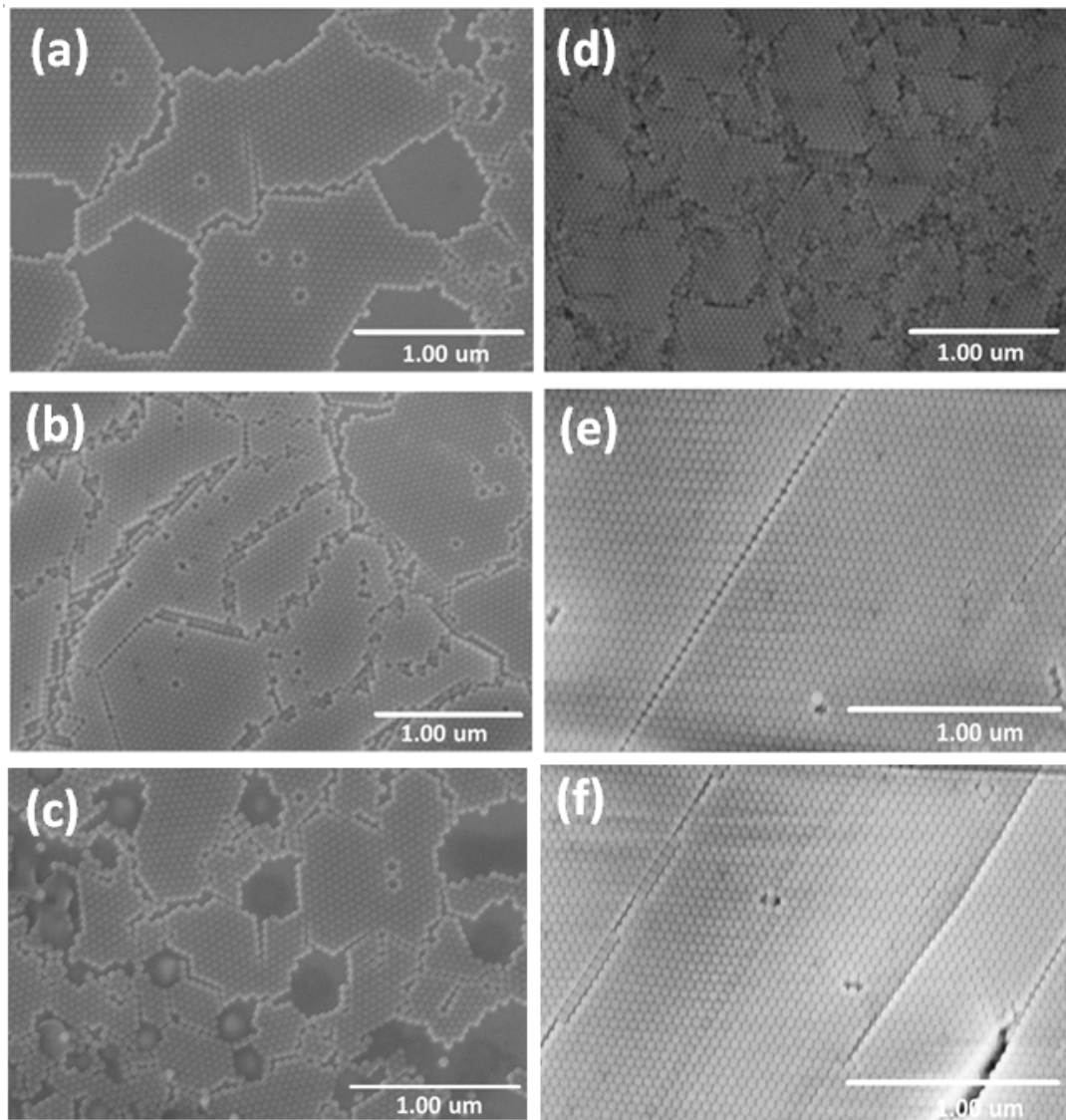


Figure 5.5.: SEM images of SiO<sub>2</sub> NPs with 0.11 vol% concentration (left) and SiO<sub>2</sub> NPs with 5.4vol% concentration (right). Different region of the same samples are shown in (a-c) and (d-f), respectively. For both concentrations, simple drop-casting method was used to deposit the nanoparticles in the wafer surface.

Figure 5.6 shows the SEM images for different samples prepared by the drop-casting method using a solution consisting of stearyl silica and stearyl alcohol with different concentrations. The SEM images for all samples were taken at the same positions in the wafer surface and with the same magnifications. Figure 5.6 (a) shows SEM image of stearyl silica and stearyl alcohol solution with a final concentration of 0.0022 vol%, by dilute particles dispersion and stearyl alcohol together. It is visible that almost there are no nanoparticles in the wafer surface, just a few individual particles or small clusters distributed almost over the whole surface area. In the following two cases (SEM images in figure 5.6 (b) and (c)), in one case, we dilute the nanoparticle dispersion and kept the stearyl alcohol as a stock and in the other case we kept the nanoparticles as a stock and we dilute the stearyl alcohol. Figure 5.6(b) shows SEM image for stearyl silica with a concentration of 0.0022 vol% and stearyl alcohol of a concentration of 0.1 vol%. It is obvious that a self-assembled network structure was formed almost across all the substrate area. The nanoparticles tend to arrange into a two-dimensional short range hexagonal ordering. Furthermore, small areas of monolayer were observed over some regions in the wafer surface. Figure 5.6 (c) shows SEM image for stearyl silica with a concentration of 0.1 vol% and stearyl alcohol of a concentration of 0.0022 vol%. By increasing the concentration of the stearyl silica particles and reducing the stearyl alcohol concentration, inverse to the case of the previous SEM image, a combination of multilayers and monolayers can be observed almost over the whole surface area. Again, the nanoparticles tend to arrange into two-dimensional hexagonal ordering with quite long-range order with some structural defects were observed especially cracks formed during drying in due to the fast evaporation of the toluene. In the last case, we kept both the particle dispersions and the stearyl alcohol as a stock solution with the final concentration of 0.1 vol% where the SEM results are shown in figure 5.6 (d). From this figure, one can observe that there are a good coverage uniformity and a nice homogeneous ordering over the entire substrate. Furthermore, the nanoparticles arrange into two-dimensional long-range hexagonal order with some structural defects (i.e. cracks) formed during drying in process.

Summarizing the above results obtained from the different concentrations of the nanoparticles dispersions and of the stearyl alcohol discussed above, the influence of the silica particles and the stearyl alcohol on the surface coverage and the uniformity of the monolayer on the wafer is obvious as seen from the SEM images. Here, the optimal values of the concentration of silica and stearyl alcohol to improve the monolayer quality and to obtain the largest area of monolayers are in order of 0.1 vol %. Whilst, using a solution consisting of different concentrations of silica and nanoparticles, such a nice ordering and small not homogeneous monolayer areas obtained.

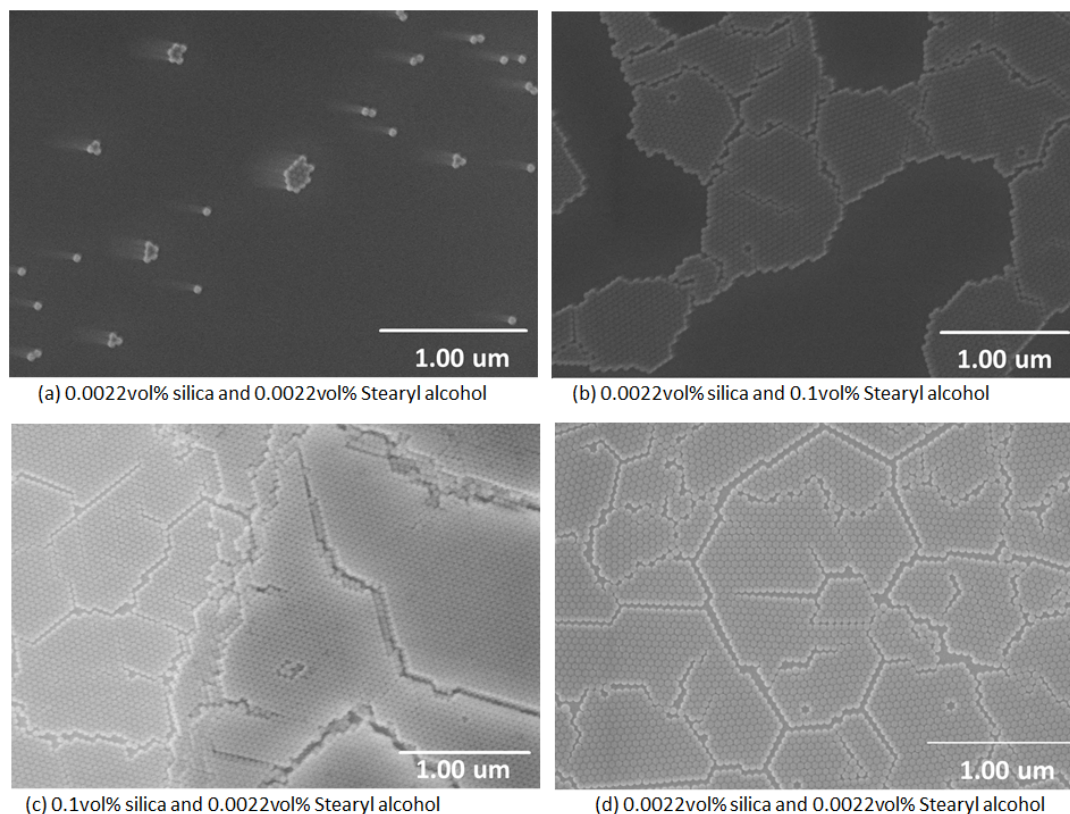


Figure 5.6.: SEM images were taken at different position in the substrate surface of self- assembled nanoparticles using stearyl alcohol as assistance, simple drop-casting method was used to deposit the nanoparticles in the substrate surface. Different nanoparticles and stearyl alcohol concentration were used: (a) The concentration values for NPs and stearyl alcohol, 0.0022 vol% and 0.0022 vol%, respectively, (b) 0.0022 vol% silica and 0.1 vol% stearyl alcohol , (c) 0.1 vol% silica and 0.0022 vol% stearyl alcohol and (d) 0.1 vol% silica and 0.1 vol% stearyl alcohol.

### Variation of nanoparticles deposition methods and local characterization by SEM

In addition to the concentration of the nanoparticles as well as the stearyl alcohol, the method used in depositing the nanoparticles in the wafer surface has an influence on the monolayer formation and its quality. In this part of this section, results obtained from different methods used to deposit the nanoparticle in the substrate surface are presented briefly. Figure 5.7 (a) shows the SEM image of self-assembled nanoparticles by the spin-coating method. As can be seen, the substrate surface is partially covered with distributed nanoparticles which form together small chains or grains separated from each other. By using the drop-casting method as can be seen in figure 5.7 (b), perfect multilayers of hexagonally ordered silica nanoparticles can be observed. Figure 5.7 (c) shows the SEM image of self-assembled silica nanoparticles by the dip-coating method. As can be seen, hexagonally ordered nanoparticles with relatively large correlation lengths can be obtained. Even though a second layer forms on top of the first layer. The second layer is not a complete layer but forms islands forming effective layers. Since perfect multilayers produced by the drop-casting method and almost the morphology is homogeneous over the entire sample, one more chance can be given to the nanoparticles to improve their ordering by adding extra toluene to the already self-assembled film. Figure 5.7 (d) shows the SEM image of the nanoparticle monolayers formed by the drop-casting method, followed after one minute by an addition of extra toluene to the film and reducing its evaporation rate by covering the sample container. As can be seen, the substrate surface is covered by a monolayer of well-ordered nanoparticles but the monolayer fabricated by this method is not homogeneous over large sample areas.

Summarizing the methods discussed above, the largest area monolayers can be produced using the drop-casting method by reducing the evaporating rate. However, such a nice monolayer is not homogeneous over the whole substrate surface.

The samples produced by the drop-casting method with an addition of stearyl alcohol shown in figure 5.6(d) and the drop-casting method with an addition of toluene shown in figure 5.7 (d) have been the main focus on our study for further improvements of nanoparticle monolayers and for scattering experiments because in these samples the long-range order and the large monolayer areas obtained is of interest.

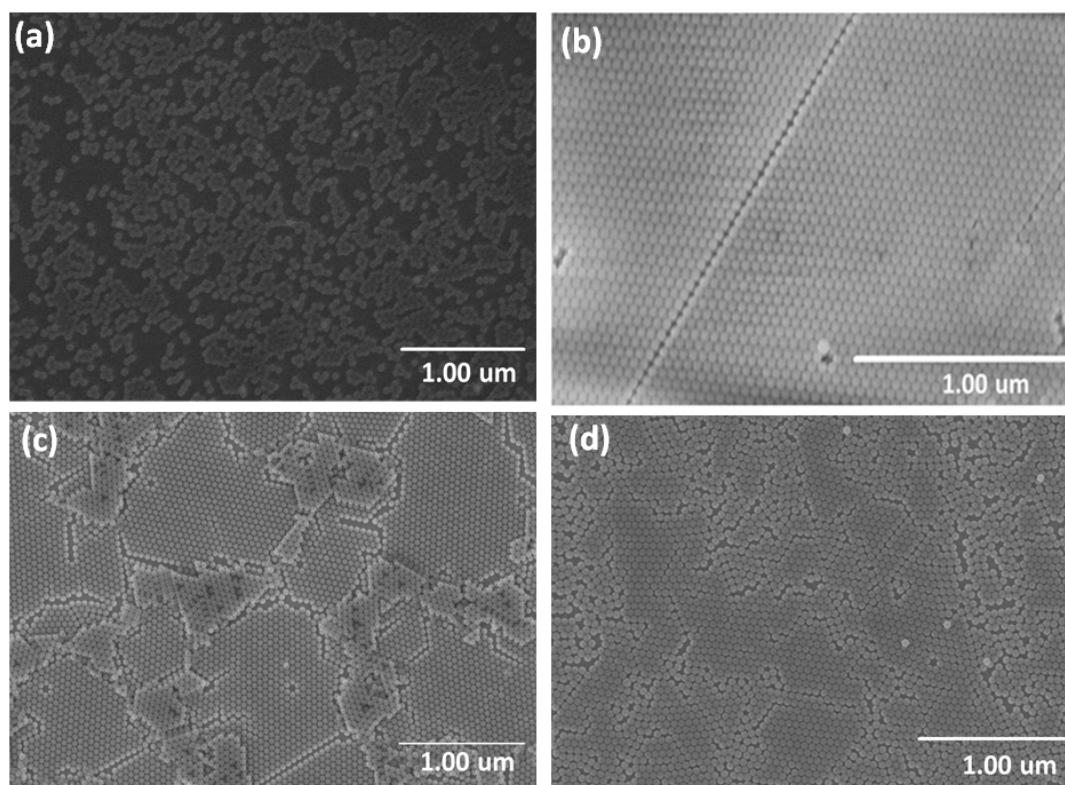


Figure 5.7.: SEM images of self assemble nanoparticles with the same concentration (5.4 vol%) using various preparation methods. (a) spin-coating, (b) drop-casting, (c) dip-coating and (d) slow evaporation method. (without stearyl alcohol)

## 5.4. Formation of nanoparticle monolayers and local characterization by SEM

A colloidal dispersion with 5.4 vol% stearyl silica nanoparticles was prepared as stock. In addition, a stock solution of 5.4 vol% stearyl alcohol in toluene was made. These two stock solutions were used to fabricate a large monolayer area of ordered nanoparticles on a silicon substrate by the drop-casting technique with and without the assistance of stearyl alcohol. The monolayer preparation methods were carried out as follows. In the beginning, prior to the use of stearyl alcohol to assist monolayer formation,  $\approx 5 \mu\text{L}$  of 5.4 vol% NPs stock dispersion was dropped onto a cleaned silicon substrate, followed after one minute by addition of an extra  $\approx 3 \mu\text{L}$  toluene to the film. While doing so, the sample was kept unmoved and the sample container was covered to reduce the evaporation rate. In the next method, in order to improve the NPs ordering over the whole sample area, stearyl alcohol was used as an assistant. Firstly, in this method, a solution with 0.1 vol% stearyl silica and 0.1 vol% stearyl alcohol was prepared, by adding  $20 \mu\text{L}$  of 5.4 vol% stearyl silica and  $20 \mu\text{L}$  of 5.4 vol% stearyl alcohol to 0.96 mL of toluene. After that,  $5 \mu\text{L}$  of this solution was taken by a micropipette and dropped onto the silicon substrate. Then the droplet quickly spread over the substrate surface and the sample was left open for one day to let it dry. A last optional step added in the monolayer fabrication is the heat treatment, which was used in order to reduce the number of cracks in the monolayer still obtained in method two.

Characterization of  $\text{SiO}_2$  NP monolayer has been done by scanning electron microscope (SEM, Hitachi SU8000) to characterize the ordering of the NPs locally in real space. In addition, XRR measurements were performed at the diffractometer Gallium Anode Low-Angle X-ray instrument GALAXI (Sec. 3.4.1) using a monochromatic x-ray beam with a wavelength of  $\lambda = 0.134 \text{ nm}$  and a beam size at the sample of  $0.7 \times 0.7 \text{ mm}^2$  in order to obtain depth resolved profile and to investigate the out of plane ordering of the NPs in reciprocal space. Furthermore, GISAXS measurements were carried out at GALAXI to obtain information about the in-plane ordering of the NPs. In GISAXS, the incident X-ray was irradiated on the sample at a grazing angle of  $\alpha_i$ , and the scattering pattern was recorded by a Pilatus 1M 2D position-sensitive detector with  $169 \times 179 \text{ mm}^2$  active area at a sample-detector distance of 3528 mm.

### First stage: ordered nanoparticles monolayer by simple drop casting method

Figure 5.8 shows SEM images at a different locations and under various magnifications of the  $\text{SiO}_2$  NP monolayers obtained by simple drop casting with adding additional toluene and reducing its evaporation rate by covering the sample as described in section 5.4; the first method of monolayer formation. From the

images, it is seen that the particles do not cover the whole surface area of the substrate. There are some areas covered with only a few NPs and some areas, where particles can be found above the first layer. Also, over some areas, the particles are randomly and irregularly distributed. The monolayer produced by this method is usually not homogeneous over large sample areas, which might be due to the surface tension leading to a contraction of the particles during drying of the sample. Nevertheless, with the present monodisperse particles with a small size distribution of  $< 4\%$  as used, some areas with a reasonable degree of ordering are observed.

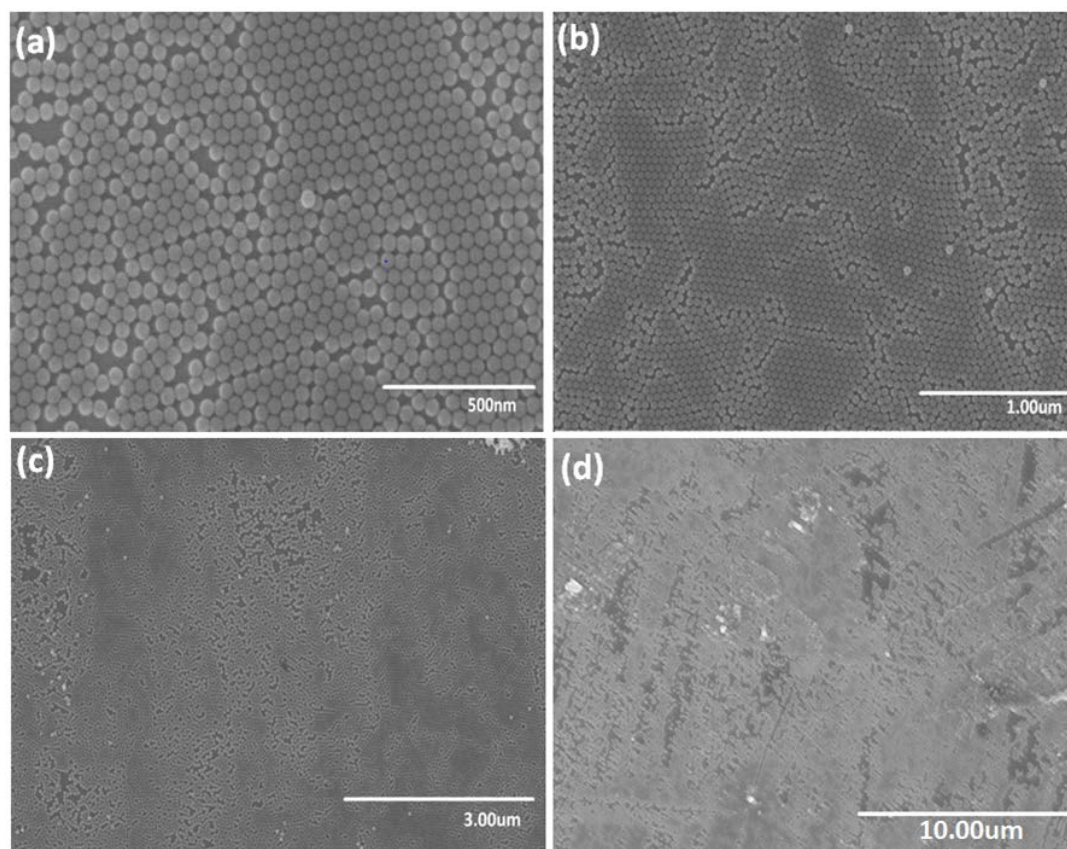


Figure 5.8.: Series of SEM images (a)-(d) with various magnifications, taken at different positions of a monolayer of SiO<sub>2</sub> NPs, assembled on a silicon wafer with extra toluene added after drop casting (without stearyl alcohol).

#### **Second stage: Improve monolayer quality by stearyl alcohol assistance**

The quality of the monolayers obtained by the simple drop-casting method still show several artifacts. The ordered domains are small and separated by cracks and in addition some tendency to multilayer formation is observed. Re-

ferring to the origin of the cracks, we considered the following explanation. After drop-casting, a thin film of colloidal dispersion of NPs is formed, which (partially) might self-assemble and at the same time starts to dry. During this process it might be that monolayers of better quality could form by self-assembly, when the particles are still free to move. Then, on further drying, the coherent contraction of the monolayer dimensions is opposed by pinning of domain edges to substrate surfaces at the late stages of drying, i.e. the NPs become less free to move, which then eventually might lead to cracks. Therefore, it was considered that adding stearyl alcohol might fill the gaps between the particles in the monolayer and thereby might reduce crack formation.

In the experiments as shown before in Sec.5.3.3, the influence of the volume of the droplet, the concentration of silica particles and the stearyl alcohol on the surface coverage and the uniformity of the monolayer on the wafer were investigated. Here, we considered a 5  $\mu\text{L}$  droplet with 0.1 vol. % NPs and 0.1 vol.% stearyl alcohol to be the suitable parameters to improve monolayer quality. If an excessively high concentration and large droplet volume is used, multilayers of silica particles are formed. While, with low concentration and small droplet volume, only separated islands are formed. More details about the preparation of the colloidal dispersion and its mixture with stearyl alcohol is explained before in Section 5.4.

Figure 5.9 shows a series of SEM images at a different location and under various magnifications of the NP monolayer obtained after using stearyl alcohol as assistance. As can be seen from the SEM images, less particles are observed in a second (or third) layer, i.e. less multi-layer formation is observed. However, still a lot of cracks are observed in the resulting monolayers. So unfortunately, our idea to reduce crack formation by the addition of stearyl alcohol does not seem to work. However, the monolayers formed seem to be more long range ordered, i.e. many hexagonal domains which are separated by cracks, still have the same orientation. So the monolayers obtained by the addition of stearyl alcohol are significantly better compared to the monolayers obtained by the simple drop-casting method.

The reason for the resulted large monolayer is not clear as the effect of the stearyl alcohol is complicated. For instance, the precipitation of the stearyl alcohol on evaporation of the toluene, might first take place on the particles and/or on the surface of the wafer. Moreover, the continuous evaporation of the toluene and possible drying from the edge of the droplet, might also play a key role on the monolayer formation. However, this is very speculative and work on the mechanism of this monolayer formation is not easy and outside the scope of the present study.

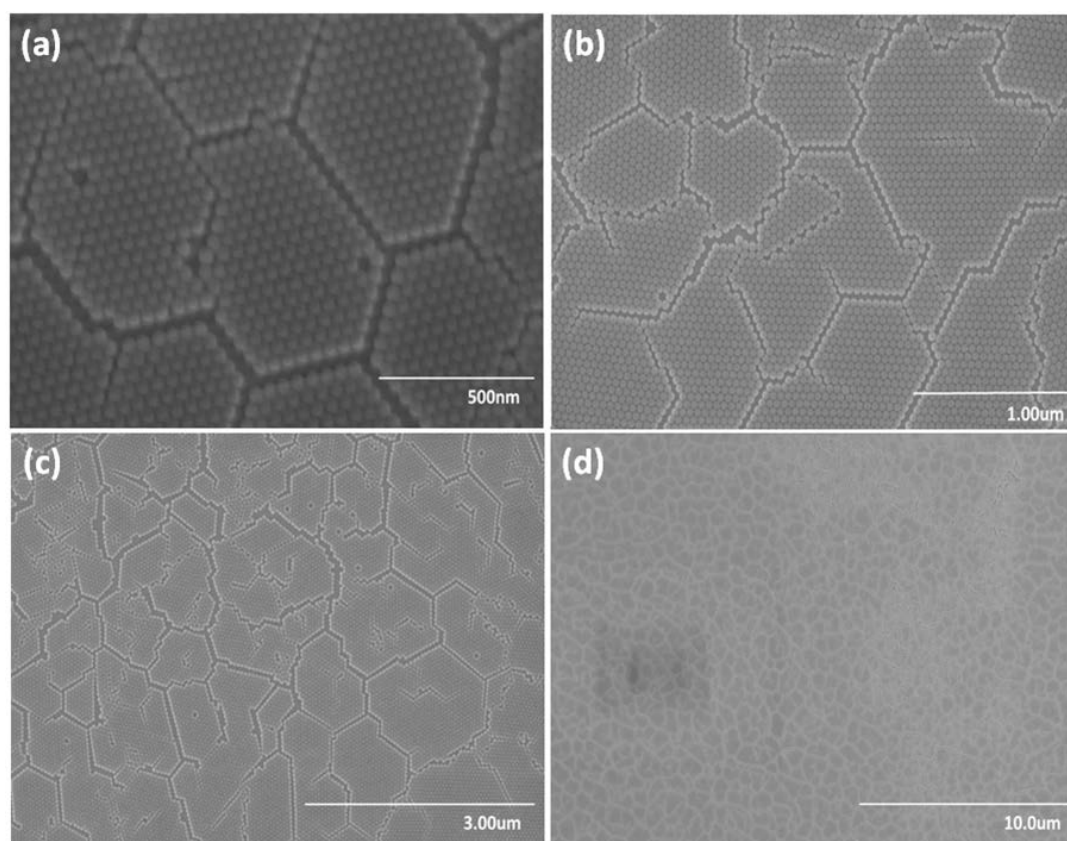


Figure 5.9.: Series of SEM images (a)-(d) with various magnifications, taken at different positions of a monolayer of  $\text{SiO}_2$  NPs, assembled on a silicon wafer after using stearyl alcohol as assistant.

**Third stage: Improve nanoparticles ordering via annealing process**

In order to avoid the cracks and other defects in the monolayers with stearyl alcohol from the previous section, the monolayers were heat treated in an oven. The idea was to melt the stearyl alcohol in the monolayer obtained by the previous method, thereby obtaining free mobile particles again, which are free to move and self-assemble further, to obtain a layer with improved order. The special possibility after further self-assembly is that we can solidify the ordered layer with only a minor change in volume by simply cooling to room temperature. The essential aspect of solidifying the monolayer by freezing the stearyl alcohol as compared to simple evaporation of a solvent, was thought to be the advantage of the annealing step leading to the minor volume change. This might especially reduced the number of cracks, which are thought to originate from the volume change during monolayer formation by evaporation. This process might be comparable to crack formation sometimes observed in dry soil.

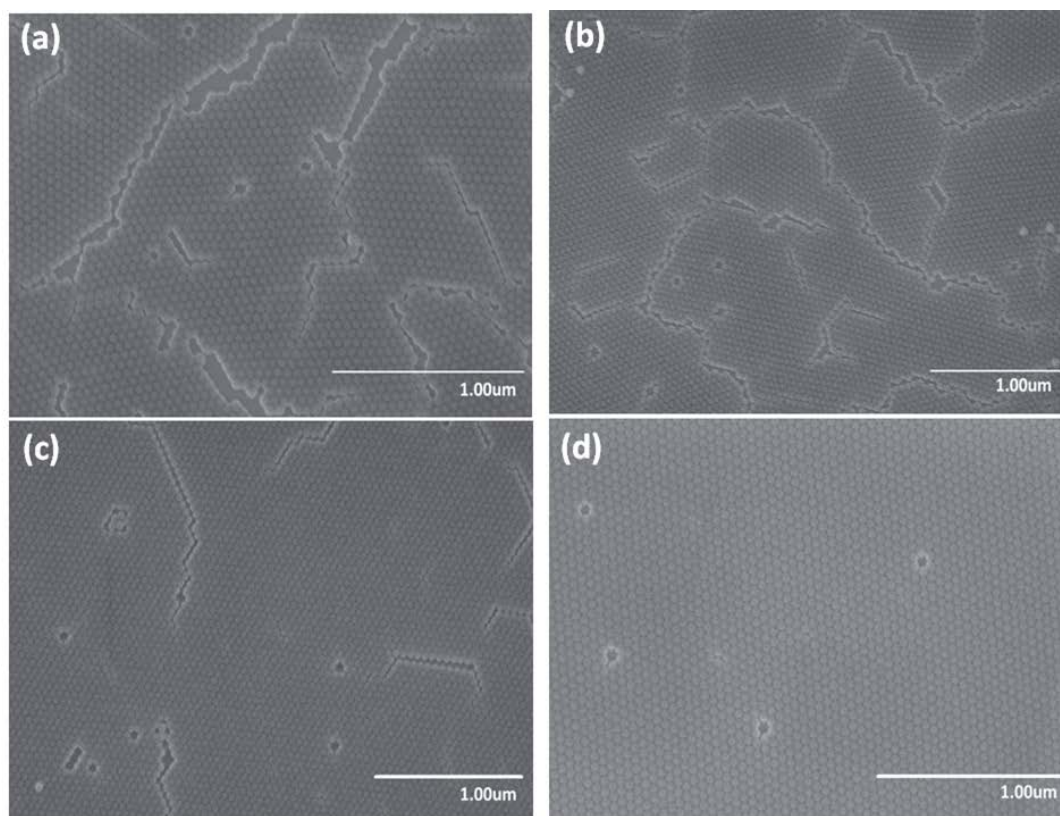


Figure 5.10.: SEM images of stearyl silica monolayer with stearyl alcohol as assistant on silicon substrate heated-treated at 70 C° for various period of time: (a) 15min, (b) 2 hours, (c) 29 hours, (d) 10 days.

In order to test the idea from the previous paragraph, the monolayer obtained

in the previous section was treated at a temperature of about 70 C°, which is about 10 degrees above the melting point of stearyl alcohol. The time of the heat treatment was varied in a broad time range from 15 minutes up to 10 days. To prevent the slow evaporation of the small amount of stearyl alcohol in the monolayer, we put the sample in a small closed polystyrene box together with a small stearyl alcohol grain, to obtain a stearyl alcohol atmosphere. The optimal heat-treatment time was found to be the longest time used of 10 days as shown in figure 5.11 which shows a horizontal line cuts along  $Q_y$  at  $Q_z = 0.34 \text{ nm}^{-1}$  taken from GISAXS data of the same sample after different periods in the oven. It is observable from the figure 5.11 that more lateral peaks along  $Q_y$  after 10 days in oven can be observed and it become more intense and sharp along  $Q_z$ . Which is a signal of long-range periodic order of the nanoparticles.

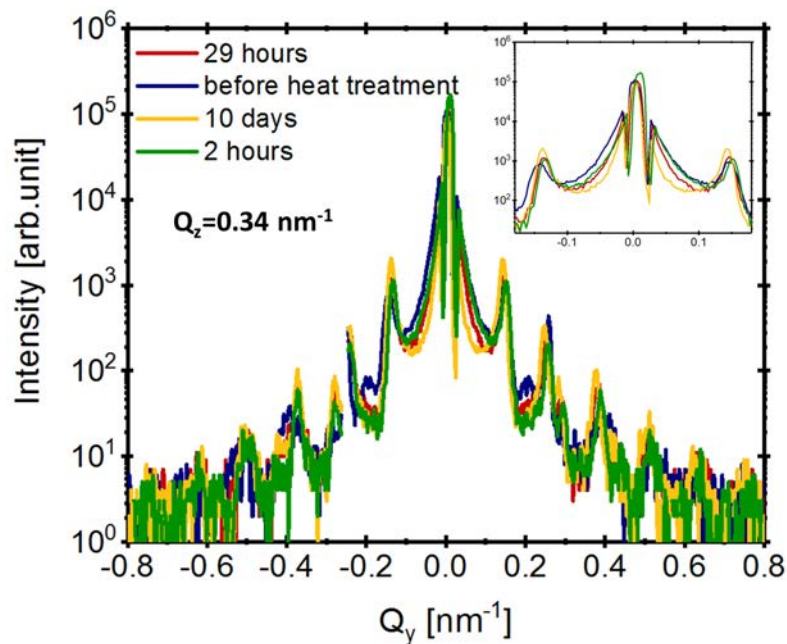


Figure 5.11.: A line-cut along  $Q_y$  at  $Q_z = 0.34 \text{ nm}^{-1}$  taken from GISAXS data of the same sample after different period in the oven.

SEM images taken after different duration in the oven at 70 C° are shown in figure 5.10. As can be seen from the SEM images, the degree of ordering improves with longer time in the oven. Especially for the sample after 10 days a large, uniform, homogeneous monolayer of  $\text{SiO}_2$  NPs with relatively large correlation lengths is obtained, also with a relatively good hexagonal order. The ordering between NPs over the whole sample area is evidently improved and the number of the cracks reduced, compared to the first simple drop-casting method without stearyl alcohol and also compared to the second method using stearyl alcohol, but without heat treatment. This can be illustrated by

a two-dimensional fast Fourier transformation (FFT) shown as inset in figure 5.12. Sharp peaks in the FFT confirm the presence of long range self-assembled monolayer order.

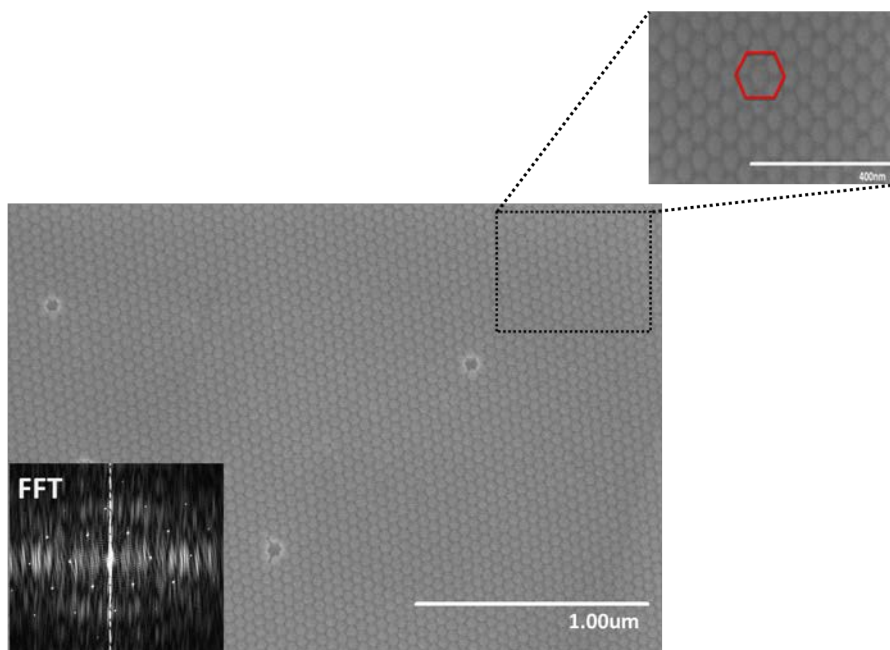


Figure 5.12.: SEM image of self-assembled spherical stearyl silica nanoparticles after drop-casted on a silicon substrate and after 10 days in the oven (with stearyl alcohol). The inset shows the two dimensional Fourier transform pattern of the SEM image.

#### 5.4.1. Global and depth-resolved characterization by XRR and GISAXS

SEM is a local probe, it provides qualitative information about only a few micron size areas and does not provide any information about short and long-range correlations between nanoparticles. Therefore, to confirm the SEM results obtained in the previous section 5.4, GISAXS and XRR measurements were performed to understand the nanoparticle ordering at a large length scale. By XRR experiments, information about out of plane nanoparticle ordering can be obtained and GISAXS measurements probe information about in-plane nanoparticle ordering which can be immediately seen in the in-plane Bragg spots.

The XRR and GISAXS measurements were carried out at GALAXI (Sec.3.4.1) for the three samples produced in the previous section 5.4, in the three stages of monolayer formation. The first sample produced in the first stage, the second sample produced in the second stage and the third sample produced in the third stage after 10 days in the oven (figure 5.10). The GISAXS measurements

were performed for all samples under incident angle  $\alpha_i \approx 0.25^\circ$ . The sample-to-detector distance is set to the largest distance of 3.528 m for all measurements, which is determined by a calibration measurement of silver behenate (AgBH). Furthermore, the beam center is determined by the calibration measurement of AgBH to transfer the detector image from pixel coordinates to momentum transfer coordinates ( $Q_y, Q_z$ ).

The GISXAS data provides information about the lattice structure, a direct measure of the lattice constant and the coherence length. For the studied nanospheres, a two-dimensional hexagonal structure is obtained as long-range ordered structure. To confirm the long-range hexagonal order, the peak positions are determined. For the two dimensional hexagonal lattices, the expected peak positions are given by the equation that relates the lattice constant  $a$  with the interplanar distance  $d$  [123]:

$$d_{hk} = \frac{a}{\sqrt{\frac{4}{3}(h^2 + hk + k^2)}} = \frac{2\pi}{Q_y^{hk}} \quad (5.7)$$

Where  $h$  and  $k$  are the Miller indices and  $Q_y^{hk}$  is the Bragg peak position. The GISAXS peak broadening is described by a Lorentzian function, while the peak broadening due to the instrument resolution is described by a Gaussian function. Therefore, to account for the instrument resolution, the GISAXS peak is fitted by a Voigt function, which is a convolution of a Gaussian  $G$  and Lorentzian  $L$  functions. From the peak fitting, the structural coherence length is determined. The Voigt function  $V$  is given as:

$$V(x; \sigma, \gamma) = \int_{-\infty}^{+\infty} G(x'; \sigma) L(x - x'; \gamma) dx' \quad (5.8)$$

Where  $G(x; \sigma)$  and  $L(x; \gamma)$  are given by the following relations:

$$G(x; \sigma) = \frac{1}{\sigma\sqrt{2\pi}} e^{(-\frac{x^2}{\sigma^2})}$$

$$L(x; \gamma) = \frac{\gamma\pi}{x^2 + \gamma^2}$$

Where  $\gamma$  is the half width at half-maximum (HWHM) of the Lorentzian profile and  $\sigma$  is the standard deviation of the Gaussian profile related to the HWHM

( $\beta$ ), by  $\beta = \sigma\sqrt{2\ln 2}$ .

The Gaussian contribution to the Voigt function (instrument resolution) can be determined from the beamwidth of the direct beam measurement of GALAXI shown in figure 5.13. The direct beamwidth in this case is determined by a Gaussian fit to  $\sigma = 0.01239 \text{ nm}^{-1}$ , which corresponds to a FWHM of  $\beta = 0.01459 \text{ nm}^{-1}$ . By fitting the  $Q_{hk}$  peak in the Yoneda band to the Voigt function,  $\gamma_{hk}$  are determined for each sample. From the HWHM of the Lorentzian ( $\gamma_{hk}$ ), the coherence length can be calculated using the following equation:

$$\zeta = \frac{2\pi}{\gamma_{hk}} \quad (5.9)$$

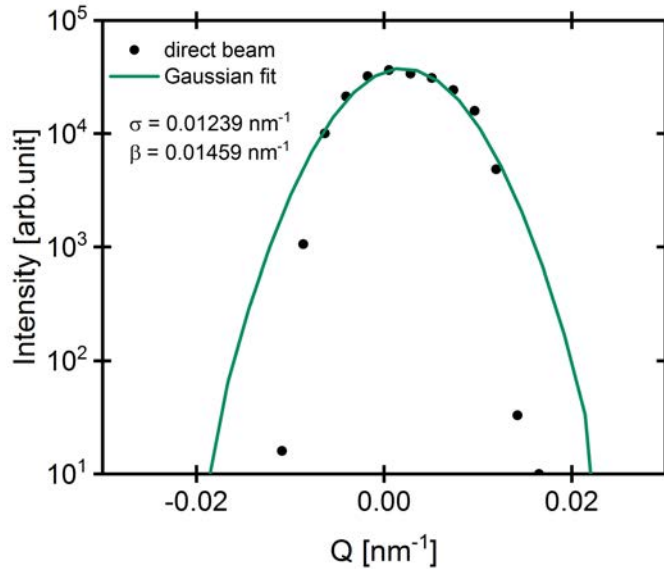


Figure 5.13.: Direct beam width for GALAXI measured with the detector set to a distance of  $L_{SDD} = 3.528 \text{ m}$ .

### X-ray Reflectometry

X-ray reflectometry experiments were performed to provide statistical information on the average electron density distribution with respect to the vertical axis and to determine the layers thicknesses and the interface roughness of the prepared sample. Furthermore, to reveal the out-of-plane ordering of the nanoparticles. Figure 5.14 (a), (b) and (c) show the XRR data of the as-prepared monolayers in the first, second and third stages. The x-ray reflectivity has been measured on GALAXI (Sec.3.4.1). The critical angle ( $\alpha_c$ ) for total reflections

Table 5.3.: The parameters obtained from the fitting of the XRR data shown in figure 4 (c) according to the model in Figure 4 (d).

Layer	Thickness (Å)	Roughness (Å)	$\rho(10^{-6}\text{Å}^{-2})$
Silica layer	478(2)	5.2(5)	see text
Substrate	-	2.1(5)	21.6(1)

at  $Q_z = 0.3nm^{-1}$  does not change for all XRR curves shown in figure 5.14. This value corresponds to the one for the silicon substrate. The critical angle of the silicon substrate is quite sharp confirming a flat substrate. After the critical edges, the Kiessig fringes appear in figure 5.14 (b) and (c) due to the interference of reflected waves from the air-nanoparticle and nanoparticle-substrate interface, respectively. Qualitative differences between the XRR curves are obvious. The reflectivity curve in figure 5.14 (c) shows Kiessig fringes up to high values of the scattering vector magnitude  $Q$  which proves that a highly ordered, homogeneous and uniform monolayer of NPs over a large surface area that can be achieved using the drop-casting method with a compatible additive. In figure 5.14 (b) the Kiessig fringes observed are much less intense than in Figure 5.14 (c), while the Kiessig fringes in figure 5.14 (a) almost vanishes.

Figure 5.14 (c) shows the XRR data (red points) of as-prepared nanoparticles monolayer after 10 days of heat treatment along with the fit (black solid line). The measured reflectivity curve of the monolayers obtained after 10 days of heat treatment is well reproduced by assuming a parabolic scattering length density profile of the NP layer.

To fit the measured XRR curve of the monolayers obtained after 10 days of heat treatment, we assumed the layer model drawn in figure 5.14(d) consisting of the particle layer on top of the silicon substrate (dark gray). The left side shows the cross section of the model and the right side shows the scattering length density (SLD) variation along the perpendicular direction to the film as extracted from the fit.

The average SLD within the nanoparticles layer given as  $\rho(Z) = \rho_1 - \rho_2\left(\frac{Z-R}{R}\right)^2$  has a parabolic line shape with the maximum value  $\rho_1 = 16.7(1)\times 10^{-6}\text{Å}^{-2}$  in the center of the nanoparticle layer set at  $Z = R$ . The average SLD value at  $Z = 0$  and  $Z = 2R$  is  $\rho_1 - \rho_2 = 16.7 - 12.7 = 4(1)\times 10^{-6}\text{Å}^{-2}$  where  $R$  is the spherical radius and  $2R = D$  is the thickness of the nanoparticles layer.

The fitting parameters obtained from the fitting of the x-ray reflectivity data of the monolayer film of nanoparticles after 10 days of heat treatment shown in figure 5.14 (c) are tabulated in table 5.3.

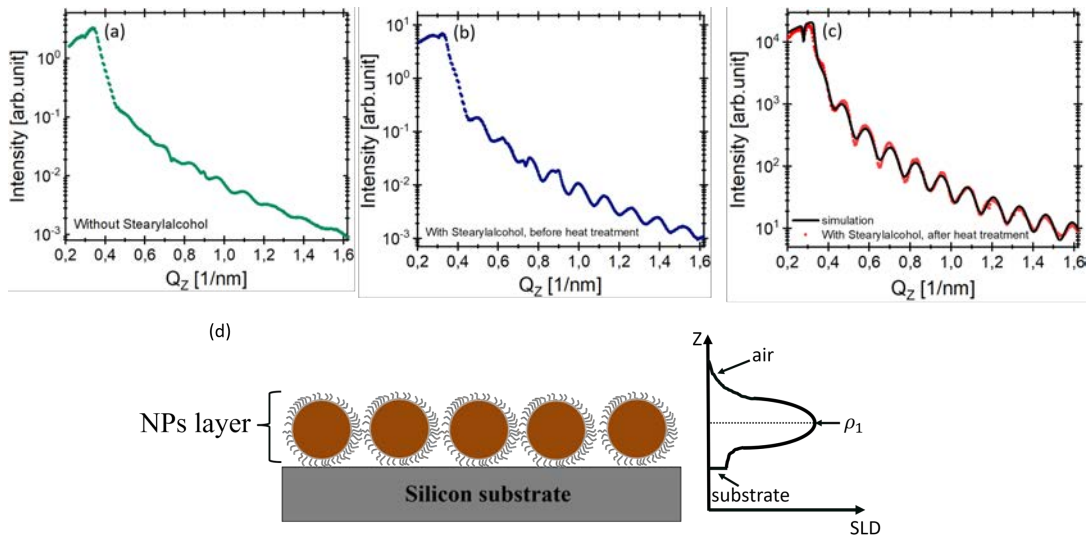


Figure 5.14.: X-ray reflectivity from a monolayer of  $\text{SiO}_2$  NPs (a) without stearyl alcohol. (b) with stearyl alcohol before heat treatment. ((c) with stearyl alcohol after 10 days of heat treatment (red points) along with the fit (black solid line). (d) The model layers structure assumed for fitting the data shown in (c), displaying an ideal in-plane close-packed arrangement of spherical nanoparticles with a parabolic SLD profile of the nanoparticles layer.

### Grazing incidence small angle x-ray scattering

SEM provides qualitative information about only a few micron-sized areas and does not provide any information about short and long-range correlations between NPs. Therefore, GISAXS measurements were carried out to investigate a much larger area of the substrate and to obtain additional information about the range of the in-plane ordering of the NPs in the monolayer.

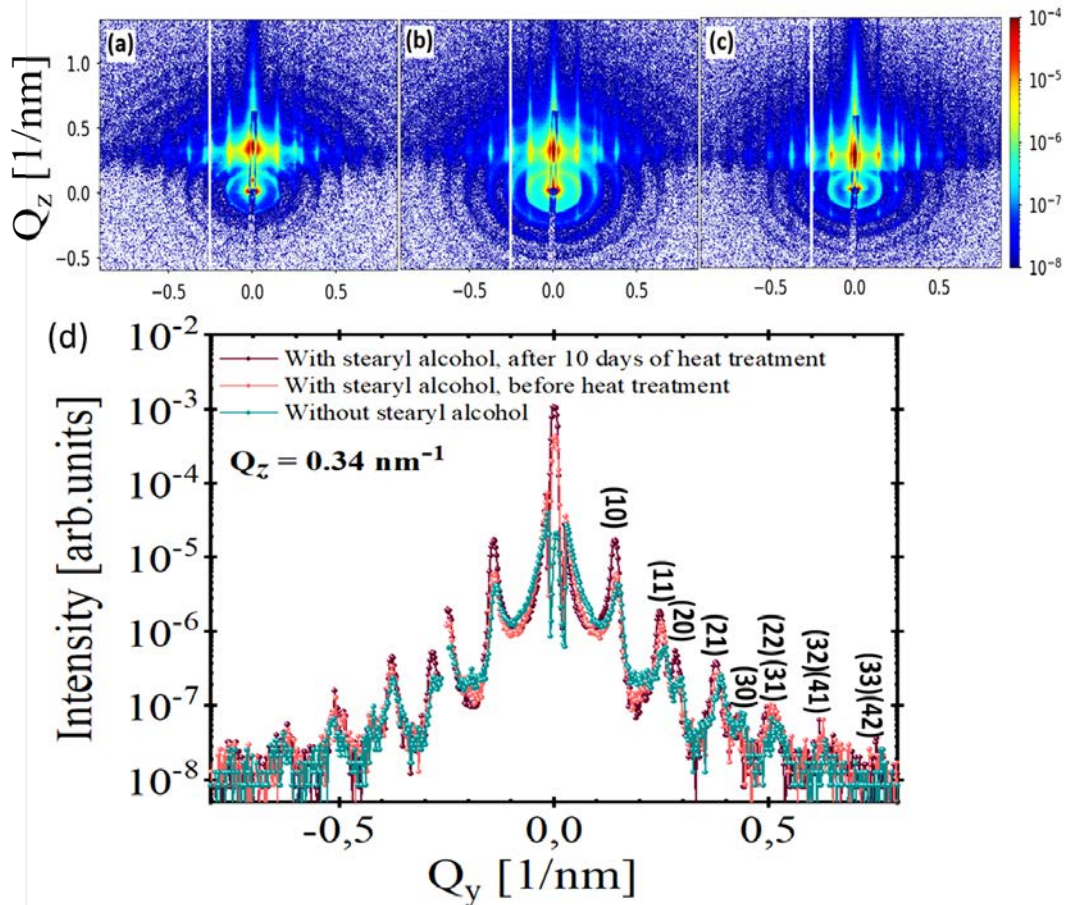


Figure 5.15.: GISAXS pattern of a monolayer of  $\text{SiO}_2$  NPs deposited on silicon substrates (a) before using stearyl alcohol (b) after using stearyl alcohol, before heat treatment and (c) after 10 days heat treatment. (d) Line-cuts from (a), (b) and (c) along  $Q_y$  at a constant  $Q_z = 0.34 \text{ nm}^{-1}$ . The Bragg peaks are indexed by assuming a 2-D hexagonal lattice with a lattice constant  $a = 51.6 \pm 0.4 \text{ nm}$ .

Figure 5.15(a), (b) and (c) show GISAXS scattering patterns of stearyl silica monolayers on silicon substrates. The GISAXS measurements were carried out at an incident angle of  $\alpha_i \approx 0.25^\circ$ . Distinct vertical Bragg rods visible in all GISAXS patterns along the  $Q_y$  direction indicate the long-range periodic order of the NPs. Furthermore, the rods are sharper in  $Q_z$  direction, due to the monolayer nature of the NPs. Moreover, rings of diffuse scattering can also be observed in the GISAXS patterns, which are related to the square of the Fourier transform of the particle shape, i.e. the form factor of the individual NPs. Differences between the GISAXS patterns are obvious. After 10 days of heat treatment (figure 5.15(c)), the Bragg rods become more intense and sharper. Also, more reflections along  $Q_y$  are visible. The appearance of these reflections is due to extended order. Furthermore, after 10 days of heat treatment (figure 5.15(c)) the diffuse rings nearly vanish compared to figure 5.15(a) and (b). This means that nearly all particles are taking part in the long range order as scattering from individual defects is largely suppressed. The intensity ratio in each GISAXS maps in figure 5.15 is quantified by comparing the integrated intensity of the Bragg rods to the integrated intensity of the diffuse rings. The intensity of the Bragg rods is integrated from  $Q_z = 0.17 \text{ nm}^{-1} - 1.4 \text{ nm}^{-1}$ , i.e. the area defined by the dotted orange rectangle in figure 5.16, while the intensity of the diffuse rings is performed from  $Q_z = -0.38 \text{ nm}^{-1} - 0.15 \text{ nm}^{-1}$ , i.e. the area defined by the dashed white rectangle in figure 5.16. The higher intensity ratio is found for the monolayer with stearyl alcohol after 10 days of heat treatment (methods 3).

The integrated intensity values of the Bragg rods and the diffuse rings of all GISAXS maps shown in figure 5.15 are listed in table 5.4. The integrated intensity as a function of  $Q_y$  of the Bragg rods and the diffuse rings of all GISAXS maps shown in figure 5.15 (a-c) is shown in figure 5.17 (a) and (b), respectively. The Bragg rods intensity of the sample after 10 days of heat treatment becomes higher (dark gray in figure 5.17 (b)), while its diffuse rings intensity becomes less (dark gray in figure 5.17 (a)). The high intensity ratio obtained for the sample after 10 days of heat treatment is an indication that most particles are taking part in the long-range order and scattering from individual defects is largely suppressed.

The Bragg peaks observed in the GISAXS pattern are indexed by considering a 2-D hexagonal lattice with a lattice constant  $a = 51.5 \pm 0.4 \text{ nm}$  (value for method 3), which is larger than the particle diameter due to the stearyl alcohol molecule around the nanoparticles. The lattice constant was calculated from the (10) peak position by using the equation linking the interplanar distance  $d$  and the lattice constant  $a$  [124]. The comparison between the intraplaner distances  $d_{hk}$  calculated from the GISAXS scattering pattern for different peaks and the  $d_{hk}$  values calculated by assuming a two-dimensional hexagonal lattice with lattice constant  $a = 51.5 \pm 0.4$  tabulated in table 5.5. The calculated

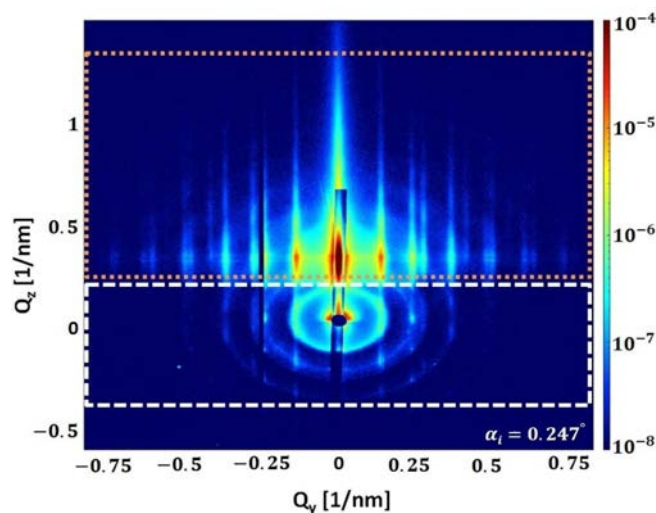


Figure 5.16.: The 2D GISAXS map of the silica monolayer with stearyl alcohol after 10 days of heat treatment. The integrated intensity area of the Bragg rods is presented by a dotted orange rectangle and the integrated intensity area of the diffuse rings is presented by the white dashed rectangle.

values are in good agreement with the observed values, confirming the two dimensional hexagonal arrangement of the nanoparticles. The lattice constant approximately kept the same in all samples produced from the three methods as tabulated in table 5.6, second column. The line cuts from the GISAXS patterns (figure 5.15(a)-(c)) along  $Q_y$  at constant  $Q_z = 0.34 \text{ nm}^{-1}$  are shown in figure 5.15 (d). It is obvious that the Bragg peaks become more intense and sharper after 10 days of heat treatment (violet line, figure 5.15 (d)). This is indicative for a larger coherence length of the crystalline structure and well-ordered NPs monolayer. After taking the instrument resolution into account, a Lorentzian profile is used to fit the first-order peak in each GISAXS pattern, which yields a structural coherence length  $\zeta$  of  $266 \pm 2 \text{ nm}$ ,  $314 \pm 4 \text{ nm}$  and  $> 480 \text{ nm}$ <sup>1</sup> for monolayers without stearyl alcohol, monolayers with stearyl alcohol before heat treatment and for monolayers with stearyl alcohol after 10 days of heat treatment, respectively.

Finally, the GISAXS pattern in figure 5.15(c) is simulated using the BornA-gain software [60] and compared with the obtained experimental result. As one can see, the simulated pattern shown in figure 5.19 (b) closely reproduces the experimental data shown in figure 5.19 (a). The GISAXS data has been simulated assuming a two-layers model, consists of a silicon substrate followed by the particle layer. Nanoparticles have a form factor of a full sphere with  $\text{SiO}_2$  core

<sup>1</sup>About 500 nm is the resolution limit of the instrument. With the present setup only this value can be given as lower bound of the coherence length for method 3

of 23.5 nm radius and a stearyl alcohol shell of 1.7 nm thickness. The 3-D visualization of the model produced by the BornAgain software is shown in figure 5.18. Since nanoparticles are densely packed, the ambient layer, where the NPs are situated, has been described as a graded interface. The Z dependence of SLD for an ideal spherical nanoparticle resulted from the GISAXS simulation. A finite 2D hexagonal lattices of randomly selected sizes have been simulated because the sample is not uniform is shown in figure 5.20. A finite 2D hexagonal lattices of randomly selected sizes have been simulated because the sample is not uniformly covered with the NPs but consists of ordered domains of variable size rotated with respect to each other. To consider the polycrystallinity of the film, an orientational distribution has been applied to the simulated domains. Positions and relative intensities of the Bragg rods (figure 5.19(a)) indicate the absence of preferred domain orientations. Therefore, a uniform orientational distribution, i.e. 120 lattice rotation angles in the range between  $0^\circ$  and  $60^\circ$  with equal weights, has been simulated. To account for the nanoparticles size distribution which contributes to diffuse scattering in the GISAXS pattern and broadens the structural peaks, a Gaussian size distribution with FWHM of 3 nm has been applied in the GISAXS model. The comparison of simulated and measured GISAXS patterns is presented in figure 5.19:

- (a): shows the region of interest of the measured pattern
- (b): shows the simulated pattern in the same  $Q$  range. Poisson noise has been applied to the scattering intensity.
- (c): slice along  $Q_z$  at  $Q_y = 0.14 \text{ nm}^{-1}$  (position of the first Bragg rod, shown with the vertical gray dashed line in the figures (a) and (b))
- (d): slice along  $Q_y$  at  $Q_z = 0.32 \text{ nm}^{-1}$  (position of the Yoneda line, shown with the horizontal gray dashed line in the figures (a) and (b))

As one can see, the model reproduces the scattering from long-range order and even some disorder like particle size distribution or orientational distributions of the domains very well: the peak widths, relative intensities and positions are the same for both, simulated and experimental GISAXS patterns. However, the simulated pattern has a valley in the region of small  $Q_z$  which is not seen in the experimental data. Moreover, simulated intensity decays with increasing  $Q_z$  noticeably faster than the measured one. These observations are signs of additional sample features that are not considered by the present model and require further investigation in the future. Nevertheless, the present model provides a plausible characterization of  $\text{SiO}_2$  NPs arrangements and allows for a determination of the film morphology, as is evident from the good match of experiment and simulation shown in figure.5.19 (d).

Sample name	$I_{BR}$ [arb.units]	IDR[ <i>arb.units</i> ]	$\frac{I_{BR}}{I_{DR}}$
Without stearyl alcohol	$7.2 \times 10^{-3}$	$3 \times 10^{-3}$	2.4
With stearyl alcohol before heat treatment	$1.4 \times 10^{-2}$	$2 \times 10^{-3}$	7.5
With stearyl alcohol after 10 days of heat treatment	$3.4 \times 10^{-2}$	$6.8 \times 10^{-6}$	5130

Table 5.4.: The integrated intensity of the Bragg rods and the diffuse ring as calculated by integration over the areas defined by the dotted orange and white angle drawn in the GISAXS map in figure 5.16. The integrated intensity ratio between the GISAXS peaks and the diffuse rings from single defects are listed in column four.

Miller indices (hk)	$d_{hk} = \frac{2\pi}{Q_y^{hk}}$ [nm]	$d_{hk} = \frac{a}{\sqrt{\frac{4}{3}(h^2+hk+k^2)}}$ [nm]
(10)	43.9(±0.1)	43.7
(11)	25.1 (±0.1)	25.3
(20)	22.4 (±0.1)	22.2
(21)	16.8 (±0.25)	16.3
(30)	14.6 (±0.01)	14.4
(22)	12.7 (±0.05)	12.6
(31)	12.2 (±0.1)	12
(32)	10.1 (±0.05)	10
(41)	9.7 (±0.1)	9.5
(33)	8.8 (±0.25)	8.5

Table 5.5.: Comparison of intraplanar distances measured from GISAXS scattered pattern (2<sup>nd</sup>) column and calculated values by assuming a hexagonal lattice with a=50.5 nm (3<sup>rd</sup>) column .

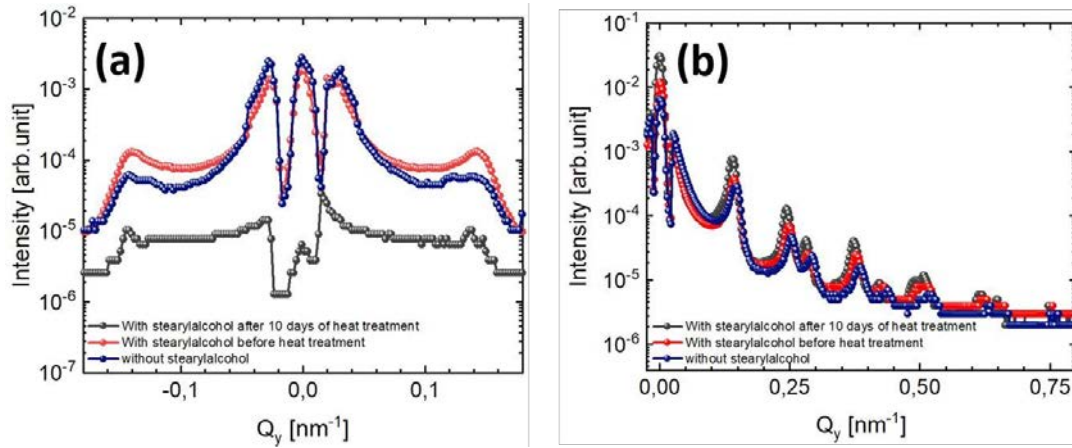


Figure 5.17.: Integrated intensity of the (a) diffuse rings and (b) Bragg rods as a function of  $Q_y$  determined from the GISAXS maps shown in figure 5.15 (a-c). The Bragg rods intensity is integrated from  $Q_z = 0.17 \text{ nm}^{-1} - 1.4 \text{ nm}^{-1}$  and the diffuse rings intensity is integrated from  $Q_z = -0.38 \text{ nm}^{-1} - 0.15 \text{ nm}^{-1}$ .

Method number	a (nm)	$\zeta$ (nm)	Intensity ratio
Method 1	$49 \pm 1$	$266 \pm 2$	2.4
Method 2	$50.3 \pm 0.7$	$314 \pm 4$	7.5
Method 3	$51.6 \pm 0.4$	$> 480$	5130

Table 5.6.: Lattice constant (a), coherence length ( $\zeta$ ) of each GISAXS map and the integrated intensity ratio between the GISAXS peaks and the diffuse rings from single defects.

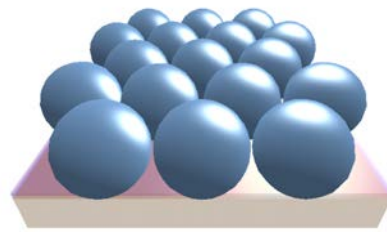


Figure 5.18.: Three dimensional vision of the simulated pattern shown in figure 5.19 (b).

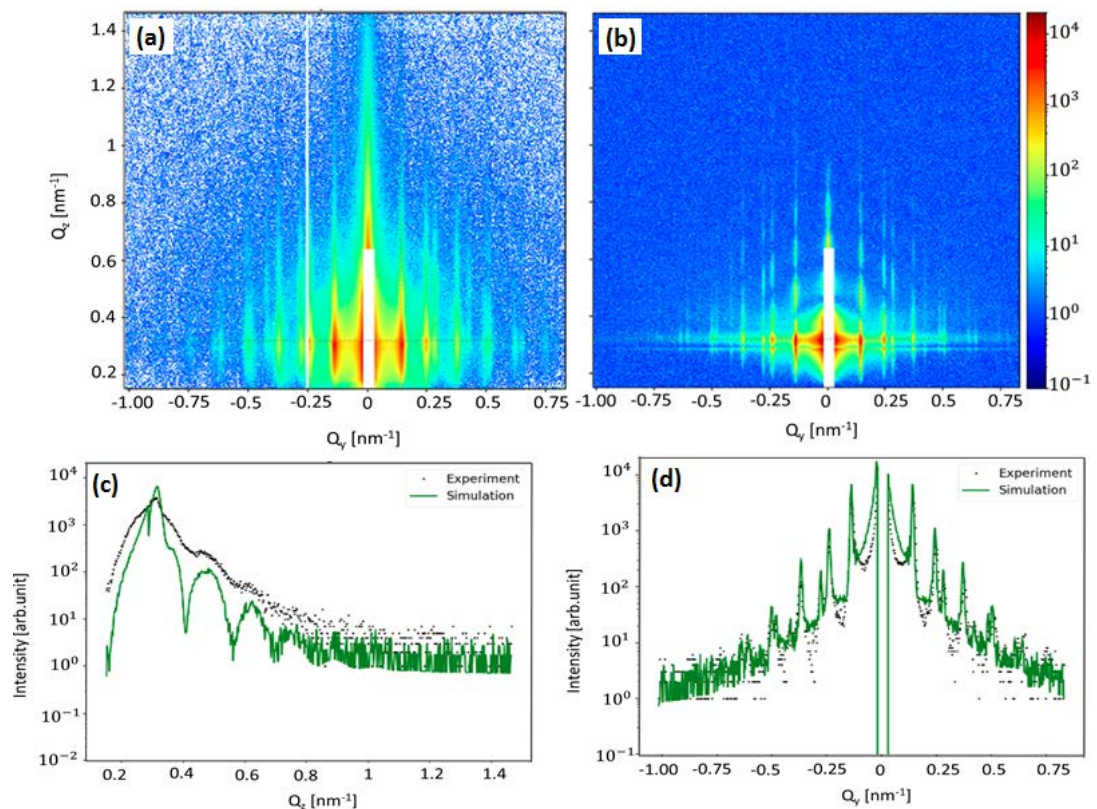


Figure 5.19.: (a) GISAXS pattern of  $\text{SiO}_2$  monolayer drop-casted onto silicon substrate with stearyl alcohol after 10 days of heat treatment. (b) Simulation of the GISAXS data using Born Again software assuming paracrystalline hexagonal lattice interference function with a lattice constant  $a = 52 \text{ nm}$  and a spherical particle with radius of  $25.5 \text{ nm}$ . (c) A vertical slice as a function of  $Q_z$  at  $Q_y = 0.14 \text{ nm}^{-1}$ . (d) A horizontal slice as a function of  $Q_y$  at  $Q_z = 0.32 \text{ nm}^{-1}$ . The experimental data shown as black dots and the simulated data are shown as a green solid line.

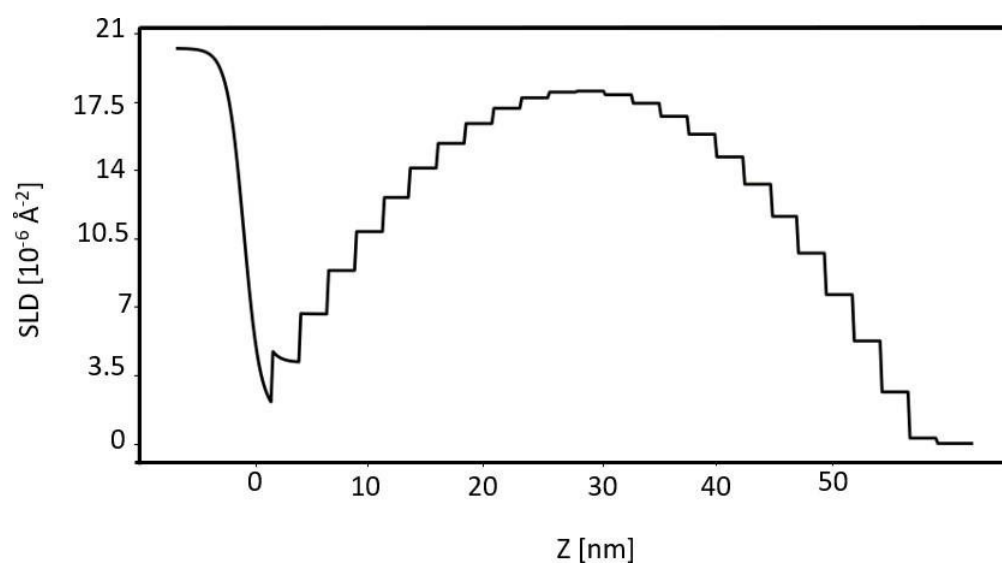


Figure 5.20.: The resulted SLD profile from the simulation of the GISAXS pattern. The particle layer is sliced into 60 slices.

## 5.5. Self-assembly of nanoparticles on two-dimensional nanometer-scale patterned surfaces

The main aim of this section is to show that it is possible to produce highly ordered arrays of particles by using the template assisted self-assembly method. The templates used in our study are trench-patterned silicon substrates that were presented and characterized previously in Sec.4.4. In this section, sample preparation and structural characterization results are discussed.

### Sample preparation and local characterization by SEM

The trench-patterned substrates used in this study are in the shape of nearly a rectangle with sidewall angle at the bottom (i.e. trapezoid), the top width is quite smaller than the bottom width. The line periodicity is of around 300 nm with groove width 150 nm. The nanoparticles placed are in the trench-patterned substrates (i.e. grating lines) using different methods. First, the same method used to produce highly ordered monolayers on the flat silicon substrate (Sec.5.4), i.e. the drop-casting method with stearyl alcohol assistant used to place the particles inside the trenches under the same conditions and the same experimental set-up as explained previously in Sec. 5.4. The first sample (S1) was prepared by the simple drop-casting method with extra addition (Sec. 5.8, first stage), 5  $\mu\text{L}$  of the stock dispersion with concentration 5.4 vol% drop-casted on the substrate surface. The second sample (S2) was prepared by drop-casted 5  $\mu\text{L}$  of a solution with a concentration 0.1 vol% which contains the silica particles and the stearyl alcohol (Sec. 5.4, second stage), then the sample is placed in the oven for 10 days at  $\approx 70^\circ$ .

At the initial stages of directed self-assembly using drop-casting, the silica particle dispersion spreads across the wafer surface without much impact from the patterning. At later stages, the toluene evaporation and the physical confinement at the pattern edge lead to the directed-self assembly of stearyl silica particles into the confined space.

Furthermore, the third sample (S3) was prepared by the dip-coating method. The substrate was immersed in the stock dispersion (5.4 vol%) for 30 seconds and taken out from the dispersion slowly. Eventually, the sample was prepared after 10 cycles of immersing in the dispersion and taken it out of the dispersion. From an experimental perspective, the important factors influencing the particle deposition on structured substrates are: particles concentration, shape, size, stearyl alcohol concentration, groove width, groove profile, roughness, confinement geometry and the preparation method.

The morphology of the samples was checked locally by SEM (figure 5.21). The SEM image for S1 shows a thick deposit of silica particles that fully covers the wafer surface and are formed without any impact of the lithographic patterning, which might be due to the high nanoparticle concentration. This case is almost

similar to the case of drop-casting of nanoparticles over a flat surface. For S2 sample after using stearyl alcohol as an assistant and after heat treatment, as can be seen from figure 5.21 that the nanoparticles are well located at each trench with very few particles on the top of the mesa. Around three columns of particles are observed in each trench. Furthermore, in some trenches, the nanoparticles show a discontinuous column of particles and in some trenches, the particles show a continuous column of particles. Moreover, structural defects are observed i.e. cracks formed during drying. For the S3 sample, it is observed that almost all trenches are filled with nanoparticles with approximately three columns of particles in each trench. As seen from the magnified SEM image that the particles tend to order into a hexagonal lattice. The nanoparticles inside the trenches form multilayers.

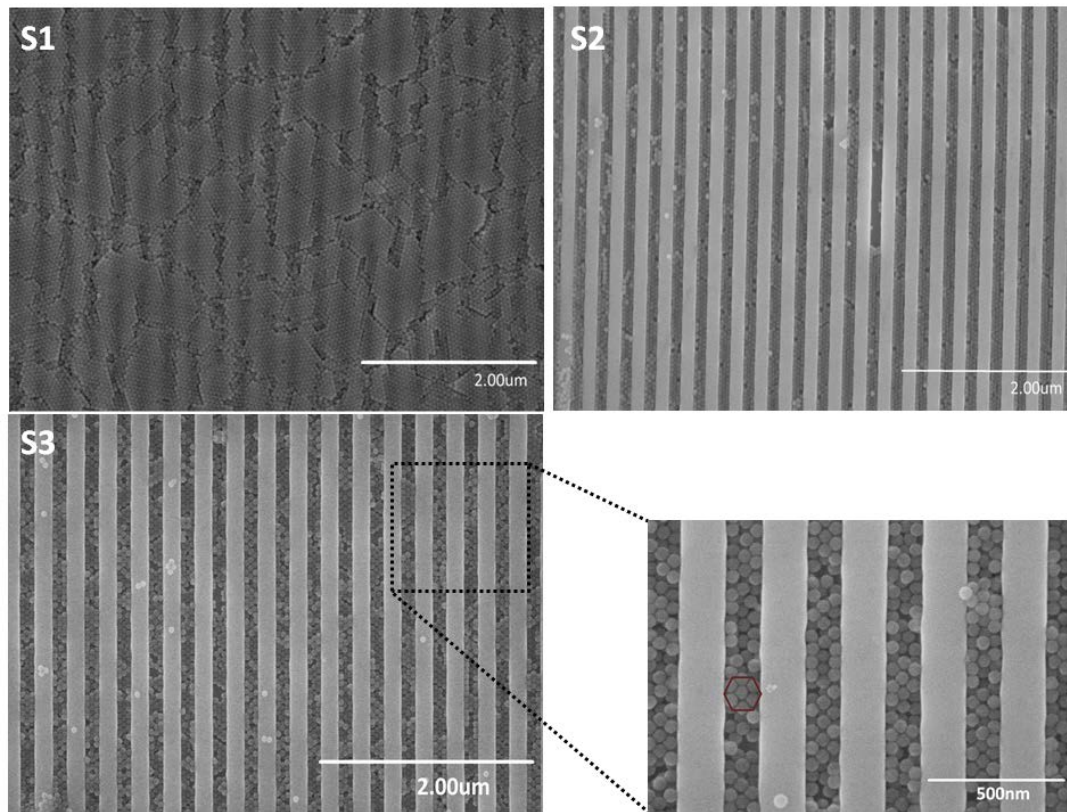


Figure 5.21.: SEM images of self-assembled silica nanoparticles of  $\approx 50$  nm diameter on the trench-patterned silicon substrate. (a) S1-sample, (b) S2-sample and (c) S3-sample, the inset is a magnified SEM image of a close-packed pattern indicated as the black rectangle in (c).

From SEM observations, the dip-coating method is found to be the best approach to place nanoparticles in trench-patterned substrates. Moreover, the

drop-casting method can be used as a method to place the nanoparticles inside trenches if the nanoparticles dispersion is mixed with a suitable chemical assistant, the stearyl alcohol in our case.

### Global characterization by GISAXS

To answer our question, if template-assisted self assembly leads to further improvement in nanoparticle ordering, GISAXS measurements were carried out of the samples shown in figure 5.21 to probe information about large size area not only few micron-size area like SEM, to obtain information about the in-plane ordering of the nanoparticles and furthermore, to probe information about the structural coherence length of the nanoparticles inside the trenches. Then, the GISAXS results for the S2 sample shown in figure 5.21 are compared with the GISAXS results of the sample shown in figure 5.10.

GISAXS patterns for the samples are shown in figure 5.22 and 5.23. The GISAXS experiments for all samples were performed in two geometry, as the incoming beam parallel (right side image) and perpendicular (left side image) to the lines. The direction of the X-ray beam with respect to the trenches is illustrated on the top-right corner of each figure. The GISAXS measurements were performed for all samples almost under the same incident angle  $\alpha_i \approx 0.18^\circ$ . For the parallel case, the lines are tilted with a very small azimuthal angle ( $\Phi$ ) with respect to the normal to the surface plane, to prevent the strong scattering background from the grating lines overwhelming the intensity from the nanoparticles. For S1 and S2 the lines are tilted to the left direction with azimuthal angle  $\Phi = 3^\circ$  for S1 and  $\Phi = 90^\circ$  for S2. For S3 the lines are tilted to the right direction with azimuthal angle  $\Phi = 1.25^\circ$ . The visible semicircle (bent tail) can be observed from the GISAXS pattern in the parallel case for all samples, which comes from the structure factor of the grooves. The powder rings around the beam center are observed, due to the form factor of the nanoparticles. As seen from GISAXS images, 2-D Bragg lines extended along  $Q_y$  are due to the laterally correlated nanoparticles arrangement. The S1 sample shows more intense Bragg peaks along  $Q_y$  than S2 sample, at least eight Bragg peaks can be seen, which might be due to the nanoparticles multilayers covering the whole pattern i.e. scattering from multilayers on a flat surface, in this case, the intensity of the particle is high enough to observe, while for S2 sample six Bragg peaks can be seen, because as seen in the SEM image (figure 5.21) that only few nanoparticles are above the mesa and most of the nanoparticles are placed inside the grooves. Therefore in this case the particles intensity is not high enough and overwhelmed by the scattering from the grating lines. Furthermore, the absence of Bragg peaks along y-direction as the incoming beam is parallel to the direction of the grooves can be explained in this way. The nanoparticles arrangements along that direction can be described by the product of periodic nanoparticles arrangement and periodically stepped

function with a period given by the groove width of the patterned substrates. From the mathematics view, it is known that the Fourier transform of the product of two functions equals the convolution product of the Fourier transform of the individual functions. The  $Q_y$  dependency of the total scattering amplitude is therefore the convolution product of the scattering amplitude due to the non-disrupted periodic nanoparticles arrangement and the scattering amplitude of the lithographic pattern, oscillating around 0. As the groove of the patterned substrates is much bigger than the nanoparticles periodicity along the  $y$ -direction, the total scattering amplitude is 0. So, even if there's a coherent arrangement of the nanoparticles, one can't observe any Bragg peaks.

The GISAXS results of S1 and S2 samples as the incoming beam perpendicular to the lines are shown in Figure 5.22 (left images). For S1, the intensity is distributed in a ring like pattern due to the particles form factor (although not continuous). At least six such rings can be seen. On top of the rings, high-intensity peaks can be observed, which modulate the ring intensity. The two-dimensional Bragg peaks along  $Q_y$  are due to the laterally correlated structures, while the Bragg peaks along  $Q_z$  provide the information on out-of-plane correlations and it is indicative of multilayers nature. For S2, less powder ring are observed, which might be due to the improved ordering between the nanoparticles in the grooves. Like the S1 sample, two-dimensional Bragg peaks along  $Q_y$  are observed, but these peaks are sharper along  $Q_z$  direction, which might be due to the monolayer nature, i.e. the particles assembled inside the groove only in one layer, they didn't form multilayers. Furthermore, less intense Bragg peaks along  $Q_y$  observed for S2 compared to S1, might be due to less particle density. The less appearance of the intense Bragg peaks along  $Q_y$  for S2 sample can be explained as follows: for S1 sample, 5  $\mu\text{L}$  of 5.4 vol% particle dispersion were drop-casted in the substrate surface, while for S2 sample, 5  $\mu\text{L}$  of 0.1vol% solution contains the stearyl silica and the stearyl alcohol, the density of the particle in the solution used to prepare S2 sample is less than the particles density in the dispersion used to prepare the S1 sample.

To translate the GISAXS observations, a line cut (red solid line) along  $Q_y$  at  $Q_z=0.3 \text{ nm}^{-1}$  was taken for S1 and S2 samples on both GISAXS patterns (semi-parallel and perpendicular). In all cases, the lateral peaks are indexed assuming a two-dimensional hexagonal lattice with a lattice constant  $a = 51.7 \text{ nm}$ .

Summarizing the GISAXS observations of S1 and S2 samples, the S2 sample shows better nanoparticle ordering than the S1 sample due to the stearyl alcohol assistant which plays a role in nanoparticles order. Stearyl alcohol has the same influence in improve ordering between nanoparticles in the patterned surface as in the flat surface as discussed in Sec.5.4.

Figure 5.23 shows the GISAXS patterns of the S3 sample. The GISAXS measurement was performed with the incident beam almost parallel (right image) and perpendicular (left) to the lines. For parallel case, the lines are tilted to the

right direction with azimuthal angle  $\Phi = 1.25^\circ$  to prevent the strong scattering background from the lines. From the GISAXS map, no Bragg peaks along  $Q_y$  are seen, only foggy rings around the beam center are observed due to the nanoparticles form factor. The result indicates that the nanoparticles have non-observable coherence in the direction perpendicular to the long axis of the lines. The absence of the lateral Bragg peaks can be explained in the same way as explained previously for the S2 sample. For the perpendicular case, Bragg peaks along  $Q_y$  and  $Q_z$  are observed. The Bragg peaks along  $Q_y$  provide information about in-plane correlation and the Bragg peaks along  $Q_z$  provide information on out of plane correlation. The Bragg peaks along  $Q_y$  are observed due to the laterally correlated structures, while along  $Q_z$  they are due to the particle multilayers inside the groove with a layer thickness of  $\approx 49$  nm.

A line cut along  $Q_y$  at  $Q_z=0.3$  nm<sup>-1</sup> was taken in both GISAXS patterns. There are no-observable Bragg peaks when the beam is almost parallel to the lines. While, when the beam is perpendicular to the lines, Bragg peaks at  $Q_y = 0.12$  nm<sup>-1</sup>,  $Q_y = 0.24$  nm<sup>-1</sup>,  $Q_y = 0.36$  nm<sup>-1</sup> and  $Q_y = 0.48$  nm<sup>-1</sup> can be observed.

The lateral Bragg peaks are indexed assuming a two-dimensional hexagonal lattice with a lattice constant  $a = 52$  nm. While the particles ordered vertically into a hexagonal close-packed (HCP) lattice with  $c = 49$  nm.

Trench-patterned silicon substrates were used as a template to guide nanoparticles self-assembly for further improvements in nanoparticles order. But the GISAXS results of nanoparticles on flat surface and on trench-patterned substrate indicate that the ordering between the particle on flat surface is better than on trench patterned substrate. To confirm this indication, the GISAXS result of the sample produced in the third stage of the monolayer formation (Sec. 5.4) is compared with the GISAXS result of the the S2 sample (Sec. 5.5). Both samples are prepared using the same method and under the same conditions. For a better comparison, the GISAXS data for both sample are normalized. Figure 5.24 (a) and (b) show the GISAXS patterned at  $\alpha_i = 0.18^\circ$  for particles on flat surface and patterned surface as the incoming beam perpendicular to the lines, respectively. Clear differences between the two GISAXS images are observable. More intense and sharper reflections along  $Q_y$  are visible in case of nanoparticles in flat surface, which is an indication to the extended order of nanoparticles over a larger area. In this study, the trench-patterned Silicon substrates did not lead to further improve in the nanoparticles ordering. Figure 5.24 (c) shows a line cut along  $Q_y$  taken from GISAXS images shown in (a) and (b) at the same value of  $Q_z = 0.3355$  nm<sup>-1</sup>.

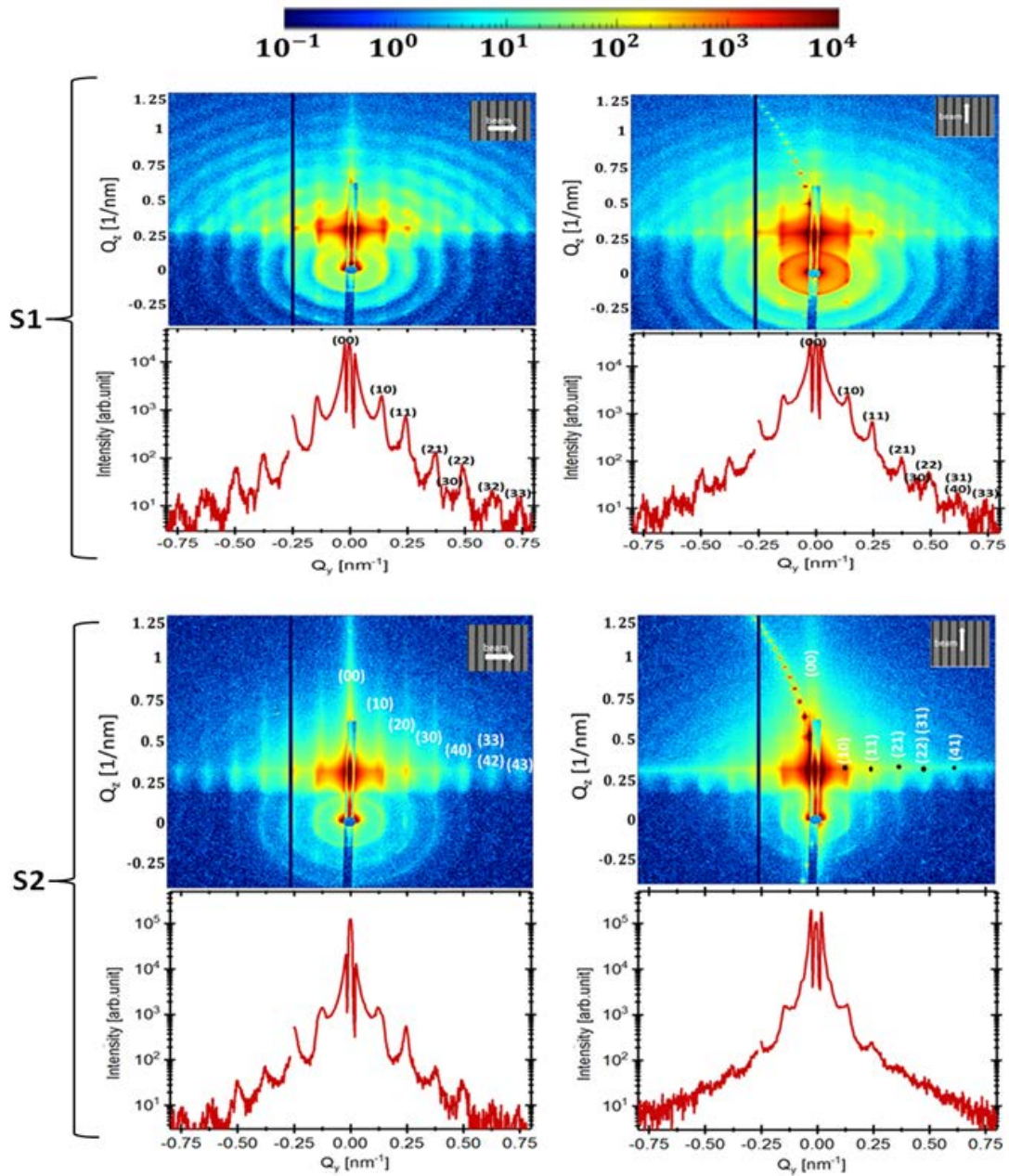


Figure 5.22.: GISAXS patterns of S1 and S2 samples with the direct beam almost parallel to the lines (right side images) and perpendicular to the lines (left side image). The incident angle in both cases for both samples  $\alpha_i \approx 0.18^\circ$ . The direction of the X-ray beam with respect to the trenches is illustrated on the top-right corner of each figure. A line cut (red solid line) from each image along  $Q_y$  at constant  $Q_z = 0.3 \text{ nm}^{-1}$ . The Bragg peaks were indexed according to a hexagonal lattice with  $a = 51.7 \text{ nm}$ .

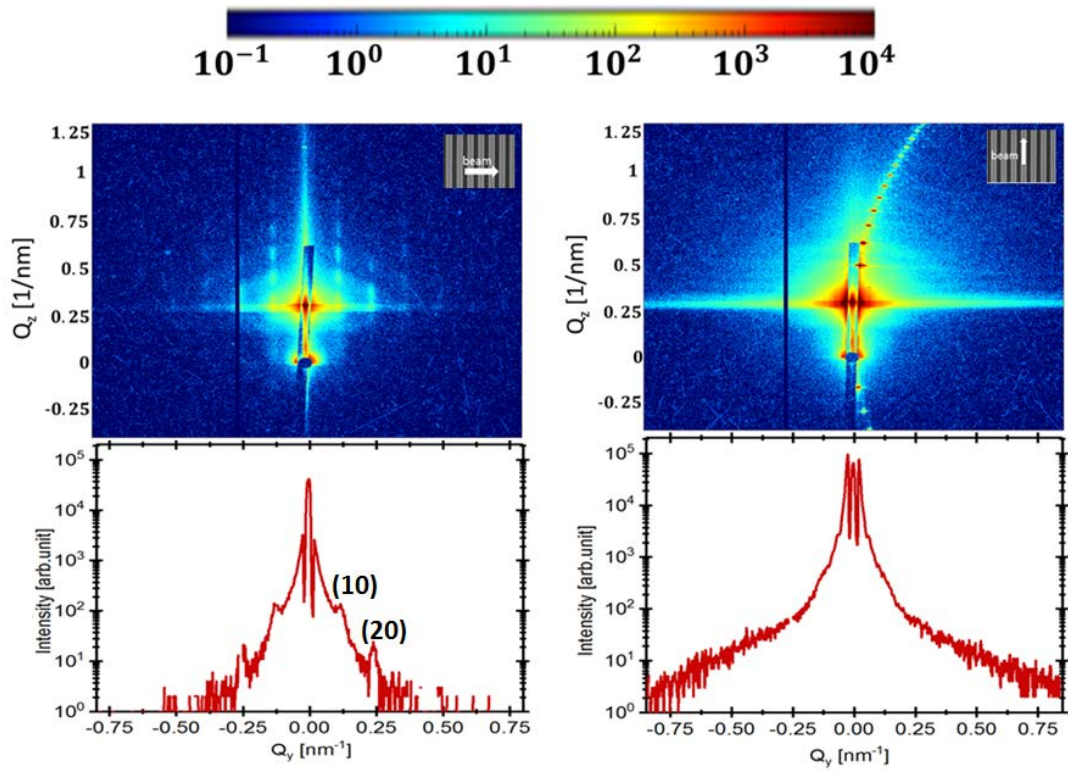


Figure 5.23.: GISAXS patterns of S3 sample with the direct beam almost parallel to the lines (right side images) and perpendicular to the lines (left side image). The incident angle in both cases  $\alpha_i \approx 0.18^\circ$ . The direction of the X-ray beam with respect to the trenches is illustrated on the top-right corner of each figure. A line cut (red solid line) from each image along  $Q_y$  at constant  $Q_z = 0.3 \text{ nm}^{-1}$ . The Bragg peaks were indexed according to a hexagonal lattice with  $a = 52 \text{ nm}$ .

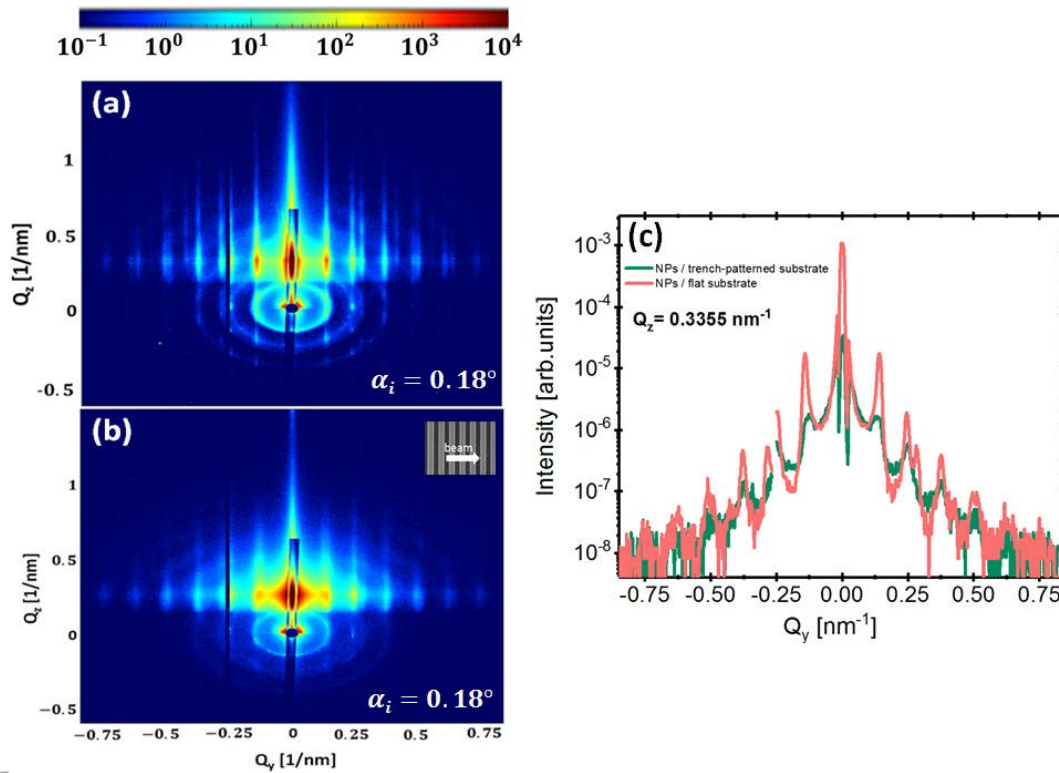


Figure 5.24.: Comparison between self-assembled particles in flat and trench-patterned substrate. (a) GISAXS pattern of self-assembled stearyl silica particles monolayer on flat surface after 10 days in the oven with stearyl alcohol assistant. (b) GISAXS pattern of directed self-assembled stearyl silica particles on trench-patterned silicon substrate after 10 days in the oven with stearyl alcohol assistant. (c) Line-cut from (a) and (b) along  $Q_y$  at a fixed  $Q_z = 0.3355 \text{ nm}^{-1}$ .

## 5.6. Summary

In this chapter, spherical Stearyl grafted silica nanoparticles with a diameter of  $\approx 50$  nm have been investigated. Information about the size as well as the size distribution of the nanoparticle has been obtained using SEM and SAXS techniques. Furthermore, in this chapter the self-assembly of stearyl silica particles on a flat and trench-patterned substrate was of interest, to produce large-area nanoparticles monolayer. The self-assembly of the nanoparticles is significantly influenced by the monodispersity of the nanoparticles and many other factors. Therefore, a full analysis of the preparation and characterization of nanoparticles monolayer with long-range order has been presented. Various methods, such as spin-coating, dip-coating and template-assisted self-assembly, have been used to produce large-areas nanoparticles monolayer. The monolayers with a largest areas were produced using the drop-casting method with a stearyl alcohol assistant. However, the quality of the monolayers obtained still shows several defects. The ordered domains are separated by cracks. Using an additional heat treatment step, the ordering between nanoparticles over the whole sample area is evidently improved and the number of the cracks reduced.

The formation of the monolayer presented in this chapter is significantly influenced by the nanoparticles concentration, the stearyl alcohol concentration, the amount of the droplet, and the annealing time. A special idea behind the formation of the stearyl silica monolayer presented in this chapter is the addition of stearyl alcohol to the nanoparticles dispersion from where the monolayers are formed. The stearyl alcohol results in monolayers with improved order, as confirmed with SEM for the local order and GISAXS for the long-range hexagonal order. A heat treatment melting the stearyl alcohol in the monolayers leads to further improved monolayers. This improved ordering is probably a result of giving the nanoparticles more time to further self-assemble, which is then followed by solidifying the monolayer by simple cooling to room temperature, preventing the large volume change as obtained after evaporation of a solvent. The heat treatment in combination with a compatible additive with a melting point significantly below that of the particles might be a general method to improve the ordering between particles in monolayers as well as multilayers.

Spherical stearyl silica nanoparticle tends to order into a two-dimensional hexagonal lattice. This was confirmed by SEM and GISAXS. The obtained in-plane reflections (Bragg peaks) in the GISAXS patterns can be indexed with a hexagonal structure. Furthermore, the experimental GISAXS data are successfully reproduced/simulated using the Born Again software, assuming a polycrystalline hexagonal lattice of spherical nanoparticle with a size of 50 nm and with a lattice constant  $a = 52$  nm.

The structural characterization of the monolayer by GISAXS is proof that the monolayer is formed not only on small areas of the sample as shown by SEM

but over a macroscopic area of the substrate. Furthermore, it is confirmed by XRR that the sample has a monolayer nature. The stearyl silica nanoparticles were also self-assembled on trench-patterned silicon substrates, which were used as a template to guide/assist nanoparticle self-assembly. GISAXS measurement reveals that the coherent structure of the nanoparticles along and perpendicular to the trench direction can be observed. However, in our study we deduced that the self-assembly on patterned substrates did not improve the ordering of the nanoparticles.

## 6. Investigation of spin structure of Cobalt ferrite nanodots on Silicon substrate

Over the past decades, self-assembly of magnetic nanoparticles on a solid substrate has attracted much interest due to their potential applications in various areas i.e. high-density magnetic storage media [125], nano-scale electronic devices [126–128]. One of the most promising candidates for these applications is the cobalt ferrite [129]. The cobalt ferrite ( $\text{CoFe}_2\text{O}_4$ ) nanoparticles have attracted much interest due to its nanoscale dimensions (i.e. small dimensions) which leads to novel properties as compared to bulk material like superparamagnetism [130]. Moreover,  $\text{CoFe}_2\text{O}_4$  nanoparticles show a novel chemical and physical properties like high coercivity ( $H_c$ ), moderate saturation magnetization ( $M_s$ ), exceptional chemical stability, large magnetocrystalline anisotropy, large magnetostriction and high mechanical hardness. These properties make it a promising material for many other applications i.e. magneto-optical devices [131], contrast agent for MRI [132], drug delivery systems [133], spintronics [134], and magnetohyperthermia [135]. One of the main important factors that play an influence in these applications is the interactions between the magnetic dipoles of the nanoparticles. For this purpose, several studies were reported about the magnetization pattern of an assembly of magnetic nanoparticles, such as the study performed for two-dimensional islands of spherical 21 nm magnetite nanoparticles [136] and also for two-dimensional islands of spherical 21 nm cobalt-ferrite nanoparticles [137].

It is known, when the magnetic nanoparticles assemble into two-dimensional structures, they are generally separated by a few nanometers due to the surfactant layer around the particle. This means that the exchange interaction between the particles is almost negligible and the only interaction dominates in this case, is the long-range dipole-dipole interaction. Thereby, when they order into a regular lattice, they are an interesting system for the study of collective magnetism. A hexagonal lattice of an array of primarily dipolar interacting nanoparticles macrospins is expected to have a super ferromagnetic ground state [137, 138]. The super ferromagnetic ground state is characterized by an equal orientation along one direction for neighboring macrospins in one domain.

In this chapter, the magnetization pattern of an assembly of two-dimensional arrays of hemispherical  $\approx 20$  nm cobalt ferrite nanoparticles will be presented. The magnetocrystalline anisotropy energy, i.e., the energy originating in a misalignment of the magnetic dipole moment with respect to the easy axes of

magnetization of cobalt-ferrite is considerable and introduces energy barriers in the individual nanoparticles, unlike magnetite, where its magnetocrystalline anisotropy energy is known to be low. Therefore, the magnetization pattern of two-dimensional assembly of cobalt ferrite nanoparticles is determined by a competition between dipole-dipole interactions and alignment of the moments along the easy axes of magnetization, unlike magnetite where its magnetization pattern is only determined by collective dipole-dipole interactions [137].

The main goal of this study is the structural and magnetic characterization of 2D arrays of  $\text{CoFe}_2\text{O}_4$  nanoparticles grown on top of a silicon substrate with a hemispherical shape. The closest packing of these nanoparticles is a hexagonal lattice. Moreover, the study of magnetic dipolar interactions between nanoparticles is one of the main focuses of this chapter. For this purpose this chapter split into various parts, a general introduction about cobalt ferrite is given first, then the magnetic properties of cobalt iron nanopowder have been studied to have a better understanding of the magnetic properties of the 2D  $\text{CoFe}_2\text{O}_4$  nanodots monolayer. After that, the quantitative evaluation of the structure of the 2D  $\text{CoFe}_2\text{O}_4$  nanodots monolayer is shown, as well as the characterization of the magnetic properties of the hexagonal arrays of magnetic  $\text{CoFe}_2\text{O}_4$  nanodots are then studied using (MPMS) and polarized neutron reflectometry (PNR) to determine the ground state magnetic behavior of the system.

## 6.1. Introduction to Cobalt Ferrite

Bulk cobalt ferrite ( $\text{CoFe}_2\text{O}_4$ ) is a well-known hard magnetic material with high coercivity and moderate saturation magnetization. Moreover,  $\text{CoFe}_2\text{O}_4$  is a ferrimagnetic material with a high cubic magnetocrystalline anisotropy and high Curie temperature ( $T_c=860\text{K}$ ). These properties, along with their high thermal/chemical stability, its magnetic properties, and its cheap production costs make  $\text{CoFe}_2\text{O}_4$  of much interest for practical use i.e. in magnetic recording applications such as audio and high-density digital recording disks [139, 140], magneto-optics [141] or spintronics [142].

$\text{CoFe}_2\text{O}_4$  crystallizes in inverse spinel structure with space group  $\text{Fd}\bar{3}\text{m}$  similar to magnetite. Here, the divalent cobalt ions  $\text{Co}^{2+}$  occupy half of the octahedral sites, while the trivalent iron ions  $\text{Fe}^{3+}$  are situated at the tetrahedral sites and the other half at the other half of the octahedral sites. The formula unit of the cobalt ferrite can be written as  $(\text{Fe}^{3+})[\text{Co}^{2+}\text{Fe}^{3+}]\text{O}_4$ . A schematic representation of the unit cell of the cobalt ferrite spinel structure is shown in figure 6.1 which contains eight formula units. The lattice constant for cobalt ferrite is in the order of  $a = 8.38 \text{ \AA}$  [143]. The anisotropy constant for bulk cobalt ferrite in order of  $1.8 - 3.0 \times 10^6 \text{ ergs/cm}^3$  [144], which has a room temperature coercivity of  $750 - 980 \text{ Oe}$  [145]. Bulk cobalt ferrite has a saturation magnetization of order  $80.8 \text{ emu/gm}$ . The magnetic moment per cobalt ion in cobalt ferrite is

derived to be approximate  $\mu_{Co} = 3.5 \mu_B$ , where reported experimental values are found in the range from  $3.3 \mu_B - 3.9 \mu_B$  [146]. The calculated magnetic moment corresponds to a saturation magnetization of

$$M_s = \frac{8\mu_{Co}}{a^3} = 450 \text{KA/m}$$

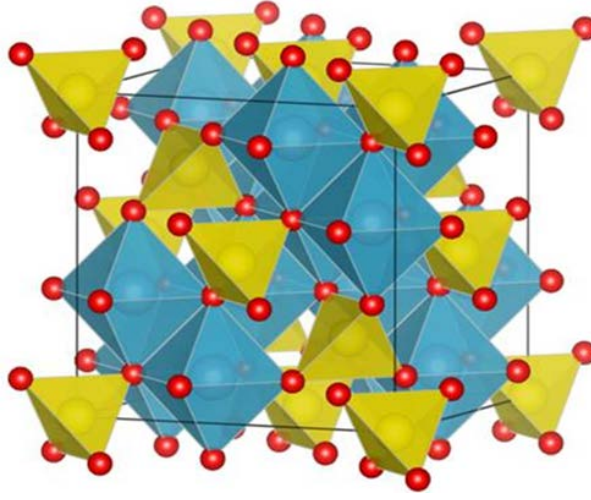


Figure 6.1.: Crystal structure of  $\text{CoFe}_2\text{O}_4$ . The Co atoms sit within the yellow tetrahedral and the Fe atoms sit within the blue octahedral. The red points represents the oxygen ions.

Cobalt ferrite exhibits ferrimagnetism at room temperature. The origin of this ferrimagnetic ordering in cobalt ferrite is due to superexchange (A-O-B, i.e. Co-O-Fe) interaction between tetrahedral (A) and octahedral (B) sublattices which is stronger than both A-O-A and B-O-B intra-sublattice interactions. The tetrahedral-sites have magnetic moments opposite to the magnetic moments of the octahedral-sites. The net magnetic moment of the lattice  $\mu_{total}$  is given by the algebraic sum of the spin magnetic moment as follows

$$\mu_{total} = (\mu_B - \mu_A)$$

where  $\mu_B$  and  $\mu_A$  are the magnetic moment of the octahedral (B) and the tetrahedral (A) sublattices, respectively.

There are studies of the iron atom occupation that were performed using Mossbauer spectroscopy in a magnetic field. They show that in actual bulk cobalt ferrite crystals, the structure is a mixed inverse spinel. The iron ion occupations in the tetrahedral and the octahedral positions are not equal. More iron atoms can shift to the octahedral positions and thus cobalt atoms also occupy the tetrahedral interstices [147, 148], depending on the sample preparation. In the case of nanoparticulate cobalt ferrite, depending on the preparation process and the particle size [149–151], relative content of cobalt and iron in the spinel structure, as well as the relative occupation of the sites varies widely.

## 6.2. Cobalt Iron Oxide nanopowder

The cobalt iron oxide nanopowder  $\text{CoFe}_2\text{O}_4$  used in this study are commercially available (Sigma-Aldrich, 99%) with 30 nm particle size. In order to understand the magnetic properties of  $\text{CoFe}_2\text{O}_4$  Nanodots arrays grown on top of Si substrate, the magnetic properties of the  $\text{CoFe}_2\text{O}_4$  nanopowder have been studied using SQUID (Sec. 3.3.1) (Quantum Design MPMS) magnetometer with 7 T maximum field. The hysteresis loops were measured at 300 K and at 5 K. The magnetization versus temperature measurements were performed in zero-field-cooled (ZFC) and field-cooled (FC) conditions with a 50 Oe and 100 Oe probe field. The resulted magnetic properties of the nanopowder will be described in the following subsection 6.2.

### Nanopowder magnetism

The magnetic properties of the cobalt ferrite nanopowder (CFO) has been studied using SQUID magnetometry. The results are compared with the one obtained for the 2D arrays of  $\text{CoFe}_2\text{O}_4$  nanodots on silicon substrate. Figure 6.2 shows the field dependent magnetization curves at 300 K (left) and at 5 K (right), the inset shows the details of hysteresis curve at small field values. While, the temperature dependent magnetization (ZFC-FC) curves at 50 Oe (left) and 100 Oe (right) is shown in figure 6.3. It is obvious that no loop is observed and the value of Coercivity ( $H_c$ ) measured from the hysteresis curves at 300 K are very small which approach zero. The zero coercivity is the characteristic feature of the superparamagnetic behavior of the magnetic nanoparticles [152]. While, at 5K the sample showed ferromagnetic behavior with a small coercivity ( $H_C$ ) of 300 Oe. Furthermore, in the hysteresis curve at 5 K, an opening is observed at high and low field values. This phenomenon can be described due to the existence of two sublattices of the spinel ferrimagnetic cobalt ferrite. The magnetic moments of the two sublattices are aligned anti-parallel to each other and not equal, thereby result in a net magnetic moment which leads to this opening before reaching the saturation.

The saturation magnetization value of the cobalt iron oxide nanopowder is found  $M_s=0.06$  emu/g to be much lower than the corresponding bulk value of 80.8 emu/g [153]. The reduced saturation magnetization of the nanopowder compared with the bulk value can be explained due to the finite size effects which lead to canting or non-collinearity of spins on their surface, thereby reducing magnetization [154]. Moreover, several crossings are observed around 0 T that indicates other phases present. Moreover, the finite magnetic remanence ( $M_r$ ) indicates that the blocking temperature likely lies above room temperature for the cobalt iron nanopowder.

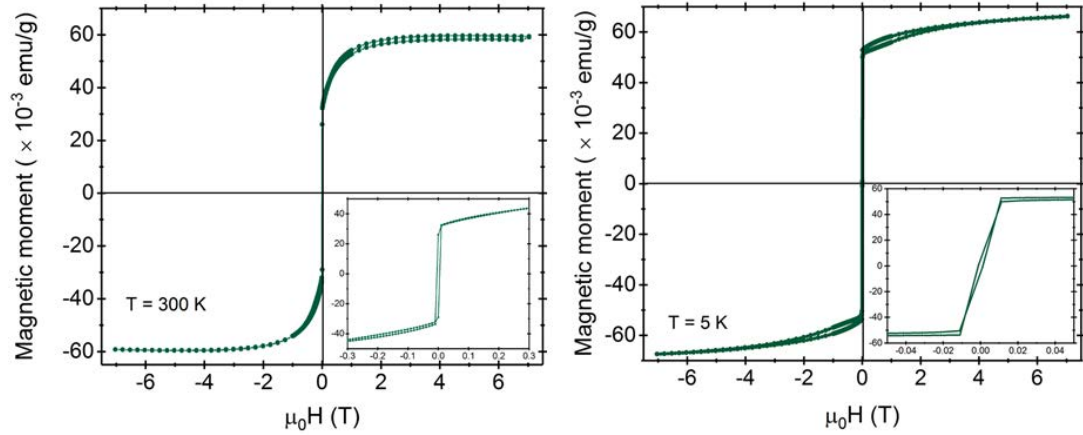


Figure 6.2.: Magnetization hysteresis curves for cobalt iron nanopowder at 300 K (left) and 5K (right).

Zero Field Cooled (ZFC) and Field Cooled (FC) magnetization measurements of the nanopowder at two different magnetic fields are shown in figure 6.3. During the ZFC process, the nanopowder is cooled from 400K down to 5K in the absence of a magnetic field. Then, a magnetic field of 50 Oe and 100 Oe were applied and the magnetization was recorded during the warming cycle. In the FC process, the nanopowder is cooled in the presence of 50 Oe and 100 Oe magnetic field from 400K down to 5K and the magnetization was recorded as a function of rising temperature.

It is obvious from ZFC/FC under two different applied magnetic fields (50 Oe and 100 Oe) shown in figure 6.3 that both, the ZFC and FC magnetization, decrease by decreasing the temperature. Furthermore, a bifurcation between the ZFC and FC is observed, which is a sign of the magnetic relaxation nature of the nanoparticles and confirms their superparamagnetic behavior.

The temperature where the bifurcation between the ZFC and FC curve occurred is known as bifurcation temperature ( $T_b$ ). It is obvious that  $T_b$  remains the same with increasing the applied magnetic field.

By comparing the ZFC-FC data with the hysteresis curves at 300 K and 5K

in figure 6.2 it is clear that below  $T_b$  at  $T=5\text{K}$  the nanopowder shows a small hysteresis and hence acts as a ferromagnetic material. While, above  $T_b$ , no hysteresis is observed and the nanopowder behaves as a superparamagnetic material.

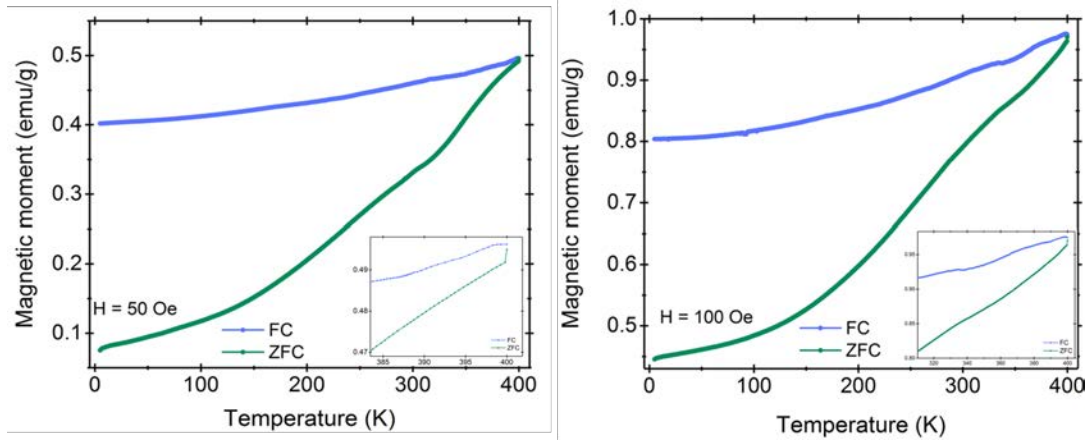


Figure 6.3.: Magnetization-temperature curves recorded in FC and ZFC modes for cobalt ferrite nanopowder in an external magnetic field of 50 Oe (left) and 100 Oe (right).

### 6.3. Experimental methods

This section will focus on the experimental methods used for the structural and the magnetic characterization of the single layer of  $\text{CoFe}_2\text{O}_4$  nanodots grown on top of a silicon substrate. The particle size and their long-range order were studied with scanning electron microscopy (SEM) and grazing incident small-angle X-ray scattering (GISAXS) at GALAXI (Sec. 3.4.1). While the particle's magnetic properties were studied with MPMS at SQUID magnetometry (Sec. 3.3.1) and with PNR at MARIA reflectometer (Sec. 3.5.1).

#### 6.3.1. Sample preparation

Arrays of  $\text{CoFe}_2\text{O}_4$  nanodots with  $\approx 24$  nm in diameter grown on top of a silicon substrate with  $\approx 50$  nm  $\text{SiO}_x$  surface layer were prepared by Jin Xu with the collaboration group of Dr. Giuseppe Portale at the Macromolecular Chemistry and New Polymeric Materials of the University of Groningen. The thickness of the particles layer is  $\approx 10$  nm. The sample was fabricated by a chemical solution deposition method, where a thin film of self-assembled block copolymers was used as templates. The fabrication method of two-dimensional arrays

of CFO nanodots includes thin-film patterning, nanoparticle self-assembly and templated deposition. Further details about the preparation method can be found in Xu. et al. [155].

### 6.3.2. Monolayer structural characterization

#### Atomic Force Microscopy (AFM)

The surface quality and the topography of the sample with a size of  $10 \times 15 \text{ mm}^2$  were probed by an Atomic Force Microscope (AFM, Agilent Technologies 5400). Hereby, the noncontact mode was used. Here, the tip is close enough to detect the sample surface for short-range forces (distance  $< 10 \text{ nm}$ ). Moreover, the tip avoids touching the sample surface. From the topography image, it is possible to estimate both the lateral (XY) and height (z) information from this image; hence, the surface quality can be probed in terms of surface roughness.

#### Scanning Electron Microscopy (SEM)

The two-dimensional monolayer of CFO nanodots grown on  $10.5 \times 15 \text{ mm}^2$  silicon substrate was characterized in top view with SEM micrographs at varied magnifications measured with Hitachi SU8000 (Sec.3.2.1). The micrographs are measured at 5 kV and the shown micrographs in Figure 6.6 are measured by the backscattering electron detector. The sample was characterized first using the SEM to obtain direct information about the particle shape, size and size distribution.

#### X-Ray Reflectometry (XRR)

The sample has been measured with XRR using GALAXI at Forschungszentrum Jülich (Sec. 3.4.1). A Q-range of  $0 - 3.5 \text{ nm}^{-1}$  in 0.002 steps has been measured by using the equipped Ga- $K_\alpha$  source ( $\lambda = 0.13414 \text{ nm}$ ). For footprint correction, the beam width is estimated by the size of the collimation slits, which is 0.5 mm, and the sample width of 10.5 mm.

The obtained XRR data of the sample will be evaluated by fitting the reflectivity curve within the framework of BornAgain software, assuming a model that takes into account the particle shape, which is a hemispherical particle with height  $\approx 10 \text{ nm}$ . Our model will consist of a substrate layer followed by a thick oxide layer and then a thin nanoparticle layer.

#### Grazing-Incidence Small-Angle X-ray Scattering (GISAXS)

GISAXS measurement is performed of the sample at GALAXI instrument (Sec.3.4.1) with a wavelength of  $\lambda = 0.13414 \text{ nm}$ . The measurement was carried out at different incident angles at a sample-to-detector distance of 3532 mm. The first evaluation or estimation of the GISAXS results is the discussion of the

Layer name	SLD( $10^{-6} \text{ \AA}^{-2}$ )
Si	20.984 - 0.4562i
SiO <sub>2</sub>	22.724 - 0.294i
CoFe <sub>2</sub> O <sub>4</sub>	40.3 - 3.83i

Table 6.1.: Scattering length density values used in the simulation of the GISAXS data.

GISAXS detector images obtained for the sample. To get information about coherence length  $\zeta$ , the first order peak along  $Q_y$  in the Yoneda band fitted by a Voigt function. Additionally, the lattice constant  $a$  is determined by using equation 5.7.

The BornAgain software package is used to simulate the two-dimensional detector image on the framework of DWBA for a more precise investigation of the GISAXS data. The data is simulated by assuming a model of hemispherical particles shown in figure 6.4 with a random orientation of a hexagonal lattice interference function. It is assumed that the sample is a multilayer structure with a silicon substrate, silicon dioxide layer and the particles layer. Furthermore, the particle layer sliced into 10 slices with varying SLD. The SLD values of the layers are calculated for each material from literature using the GALAXI wavelength  $\lambda = 0.13414 \text{ nm}$  shown in table 6.1. Moreover, the Gaussian broadening is included to simulate the instrumental resolution of GALAXI. In the simulation, it is assumed that the orientation of the hexagonal lattice is on average random with respect to the beam.

A three-dimensional visualization of the simulated structure obtained using the BornAgain software is shown in figure 6.4.

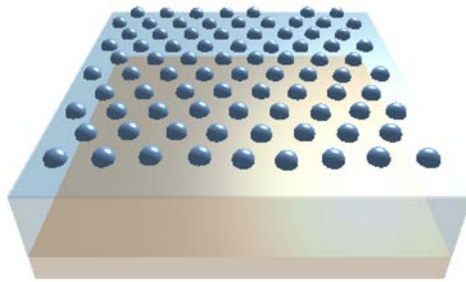


Figure 6.4.: Three dimensional visualization of the simulated structure shown in the right plot of Figure 6.9. The visualization was generated using the BornAgain software package.

### 6.3.3. Monolayer magnetism

#### Macroscopic Magnetization (MPMS)

Using SQUID magnetometry (Sec.3.3.1), the magnetization of the sample as field and temperature-dependent are measured. An approximately  $3 \times 3 \text{ mm}^2$  piece is cut out of the  $10.5 \times 15 \text{ mm}^2$  sample for the measurement using a diamond cutter. The magnetization field-dependence is measured in a range of  $\pm 7 \text{ T}$  at  $300 \text{ K}$  and  $5 \text{ K}$  for in-plan and out-of-plan geometry. Furthermore, the sample magnetization temperature-dependent is measured at  $5, 15, 50, 100, 500 \text{ mT}$  from  $5 \text{ K}$  to  $400 \text{ K}$  for in-plan and out-of-plan geometry.

#### Polarized Neutron Reflectometry (PNR)

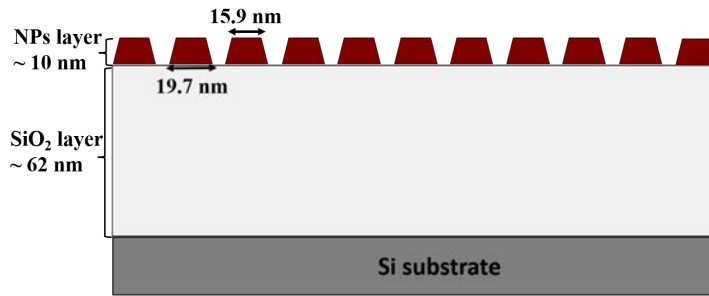


Figure 6.5.: A schematic drawing of the model assumed to fit the neutron reflectivity data. The sample can be modeled by a layered system of a silicon substrate (dark gray), silicon dioxide (light gray) and cobalt ferrite layer (brown). The hexagonal array layer of COF NP is modeled by a single slab of trapezoids.

Polarized neutron reflectivity (PNR) measurements were performed for the 2D  $\text{CoFe}_2\text{O}_4$  nanodots at MARIA instruments (Sec.3.5.1) to probe the depth dependence of the in-plane magnetization profile. Moreover, PNR provides the magnetic ordering of the nanoparticles in the monolayer and it highlights the strength of the dipolar coupling amongst the nanoparticles.

All measurements were carried out at room temperature, in-plane and out-of-plane directions by applying different magnetic fields. The in-plane NR measurements were performed at a remnant field with a full (non spin flip channels  $R^{++}$ ,  $R^{--}$  and spin flip channels  $R^{+-}$  and  $R^{-+}$ ) and half polarization analyses (spin up  $R^+$  and spin down  $R^-$  neutrons), while at  $500 \text{ Oe}$  and at saturation were performed with half polarization analyses. In the out-of-plane direction, the measurements were performed with full and half polarization analyses at  $700 \text{ Oe}$ , remnant and saturation fields as shown in figure F.5.

For analyzing the PNR data, a magnetic profile which mainly represented by

magnetic scattering length density (mSLD) needs to be added besides the structural model i.e. nuclear scattering length density (nSLD). The obtained reflectivities are evaluated assuming the model schematically depicted in figure 6.5. The substrate is set to be silicon with a thick layer of silicon dioxide on top, followed by the  $\text{CoFe}_2\text{O}_4$  particle layer and an ambient environment. The hexagonal array layer is sliced into 50 slices to account for the SLD gradient. For each interface, an interfacial roughness is included.

The particle shape assumed to fit the PNR data is slightly different than particle shape assumed to fit the GISAXS data. Here, particles with a trapezoidal shape where the lateral size at the top is smaller than the lateral size at the bottom as shown in figure 6.5 is assumed. The average lateral density of a hexagonal array layer is modeled by a single slab of trapezoids.

## 6.4. Results and discussion

### 6.4.1. Structural characterization

#### 6.4.1.1. Morphological characterization

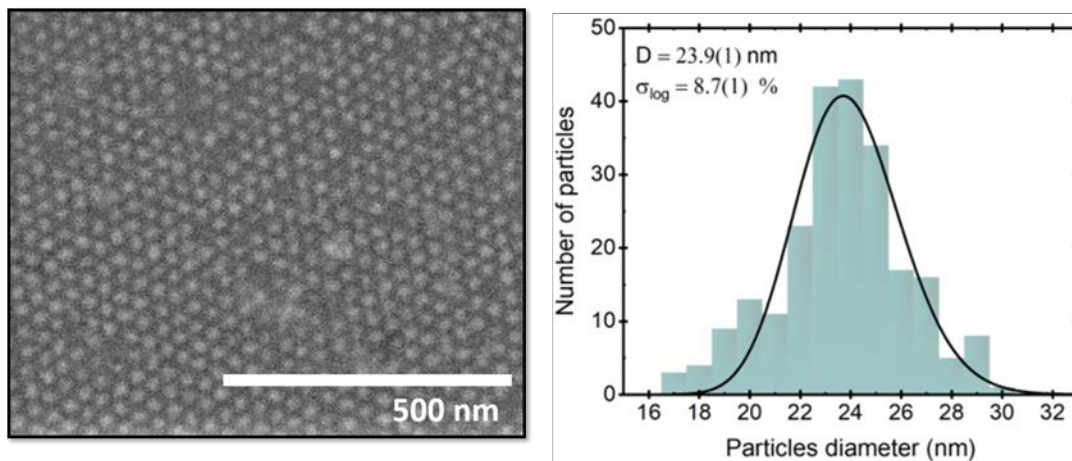


Figure 6.6.: SEM image (left) and the particle size distribution histogram (right) along with a lognormal (black solid line) fit. It yields a size distribution of 8.7%.

The morphology of the sample was investigated using SEM and AFM techniques. Figure 6.6 (left) shows SEM images of the as-prepared monolayer of CFO NPs films at different locations and under various magnifications. SEM clearly reveals that the particles tend to order into two-dimensional hexagonal close-packed ordering, which contains, however, some defects such as vacancies and disclinations. Furthermore, it is qualitatively clear that most of the particles are homogeneous in shape. Figure 6.6 (right) shows the size distribution of

the particles with a lognormal fit. The fitting yields a mean diameter of 24 nm with a size distribution of 8.7%.

The SEM did not reveal the correct shape of the particles, as seen from the images, the particles almost have a spherical shape. The dots arrangement appears regular and distributed uniformly with some dots missing and small bright spots on top of the ordered nanoparticles. These spots might be organic remnants or dust.

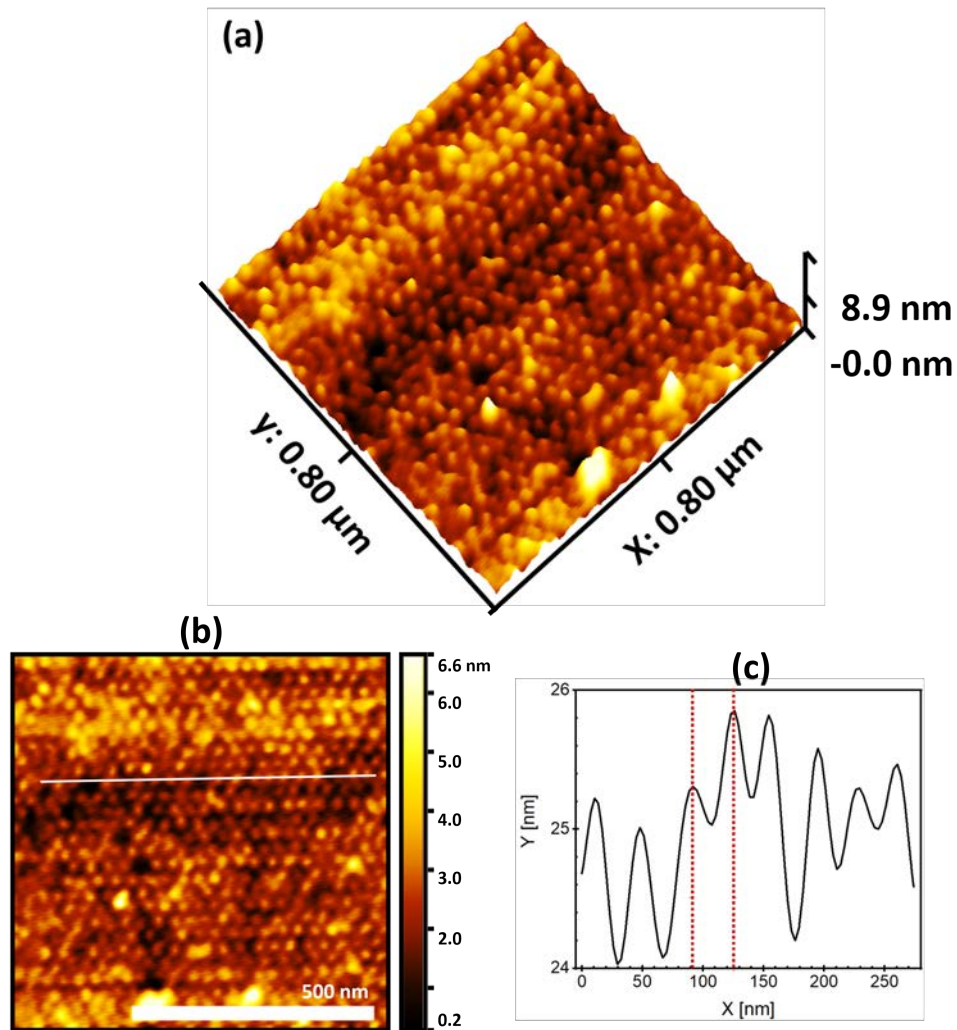


Figure 6.7.: The (a) 3D (b) 2D AFM Topographical images of  $\text{CoFe}_2\text{O}_4$  nanodots and (c) line profile obtained of a selected set of dots.

The topographic atomic force microscopy (AFM) image of the monolayer of  $\text{CoFe}_2\text{O}_4$  grown on oxidized silicon substrate is shown in figure 6.7(a) which is analyzed using the "Gwyddion" software. AFM image is illustrating the uniformity of the dots grown under high-temperature treatment on a silicon substrate with some impurities and imperfections. Line profile (figure 6.7(C)) was employed to estimate the interparticle distance of the NPs. The line profiles confirm that all the dots belonging to an array have almost identical height and width. The interparticle distance as obtained from the line profile (distance between the two dotted red lines) is  $d \approx 34$  nm.

#### 6.4.1.2. Vertical structure

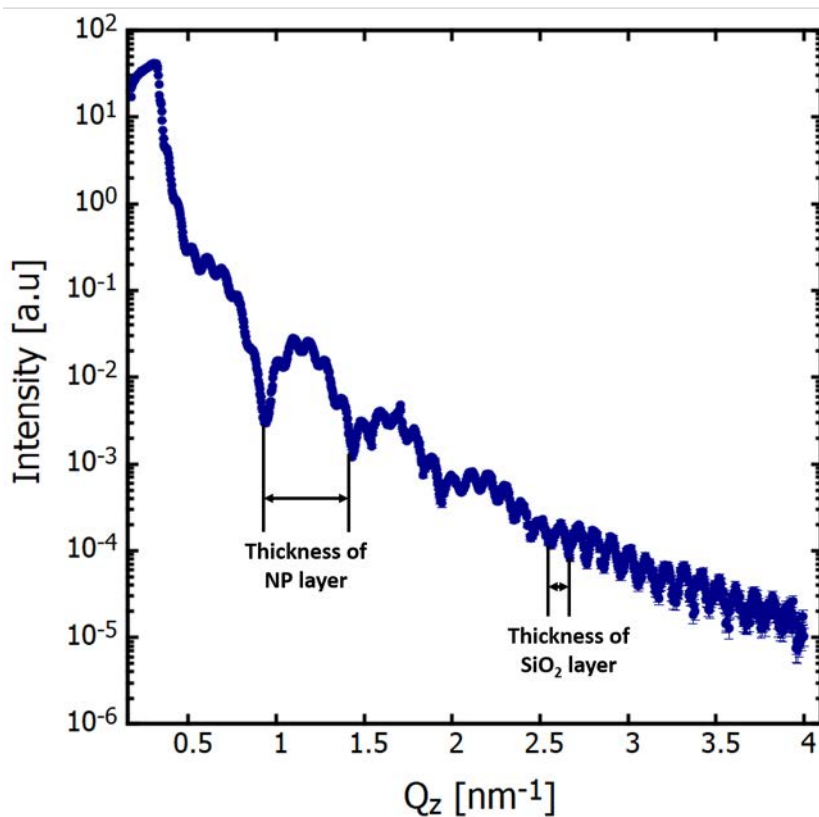


Figure 6.8.: X-ray reflectometry of the  $\text{CoFe}_2\text{O}_4$  monolayer prepared by a high temperature treatment.

X-ray reflectometry measurement is performed to obtain information on the average electron density distribution with respect to the vertical axis and to reveal the out-of-plane ordering of the nanoparticles, whereas neutron reflectome-

try is carried out to access magnetic structure information and to investigate the spin density of the monolayer by polarized neutrons. Figure 6.8 shows the resulted XRR data measured at ambient conditions on GALAXI (Sec. 3.4.1). The reflectivity curve shows two different lengths scales corresponding to two different layer thicknesses. The big oscillation corresponding to a thickness of  $\approx 10$  nm, refers to the thin particle layer grown on top of a thicker SiO<sub>2</sub> layer, which is represented with the Kiessig fringes observed in the reflectivity curve with a thickness of  $\approx 50$  nm.

#### 6.4.1.3. Lateral structure

In this section, the overall morphologies and the superstructure of the self-assembled CFO nanoparticles grown on Si substrate have been characterized using GISAXS shown in figure 6.9. The measurement was performed at an incident angle  $\alpha_i = 0.17^\circ$ . In the GISAXS map, there is a distinct feature observed, which is a vertical sharp line (i.e. Bragg rod) along  $Q_y$ . These lines are broad in the  $Q_z$  direction due to the monolayer nature of the nanoparticles film. The lines extended symmetrically on both sides of the  $Q_y = 0$  which is an indication of a good 2D order of the nanoparticles. The 2D-Bragg rods were successfully indexed assuming a 2-dimensional hexagonal lattice of a lattice constant  $a \approx 34$  nm as calculated from the first Bragg rods position (10). The interplanar distances calculated from Bragg rods positions are tabulated in table 6.2 and compared with the calculated values by assuming a two-dimensional hexagonal lattice using equation 5.7. The calculated interplanar distances from the Bragg rods positions match very well the calculated positions based on a hexagonal lattice, which confirms that the particles arranged in a two-dimensional hexagonal lattice.

In order to reveal more information about the crystalline order of the NP, a line cut at fixed  $Q_z = 0.29 \text{ nm}^{-1}$  was taken as shown in figure 6.9 (b). The 1-dimensional cuts show the in-plane Bragg peaks along  $Q_y$  axis. After taking the instrument resolution into account, a Lorentzian profile is used to fit the first-order peak (10) which yields a structural coherence length of  $\approx 161$  nm, which corresponds to 7 to 8 closed-packed nanoparticles and an indication to a relatively good supercrystalline nanoparticles ordering. Figure 6.9 (c) shows a vertical cut at fixed  $Q_y = 0.21 \text{ nm}^{-1}$ . It is obvious that only one broad peak observed along  $Q_z$  which confirms the 2D nature of the sample. The width of this peak corresponds to the particle height.

Moreover, the GISAXS map has been simulated using the BornAgain software and compared with the obtained experimental results. It is obvious that the simulated pattern (figure 6.10 (b)) closely reproduces the experimental data

Miller indices (hk)	$d_{hk} = \frac{2\pi}{Q_y^{hk}}$ [nm]	$d_{hk} = \frac{a}{\sqrt{\frac{4}{3}(h^2+hk+k^2)}}$ [nm]
(10)	29.9(±0.15)	29.4
(11)	17.1 (±0.05)	17
(20)	14.7 (±0.1)	14.7
(21)	11.3 (±0.1)	11.34

Table 6.2.: Comparison of intraplanar distances measured from GISAXS scattered pattern (2<sup>nd</sup>) column and calculated values by assuming a hexagonal lattice with a=34 nm (3<sup>rd</sup>) column.

(figure 6.10 (a)). The incident angle had to be readjusted to  $\alpha_i = 0.165^\circ$  for the Yoneda line to be at the same height as the detector. In order to obtain the simulated pattern in figure 6.10 (b), a three-layer model has been used. The model consists of a silicon substrate, SiO<sub>2</sub> layer and the particle layer. The 3-D visualization of the model used is shown in figure 6.4. Furthermore, the particle layer has been sliced into 10 slices to account for the SLD gradient as shown in the SLD profile (figure 6.11). Moreover, a two-dimensional hexagonal order of hemispherical particles with height (h)  $\approx 10$  nm and radius (r)  $\approx 8.5$  nm have been found to give the best result. Additionally, various lattice orientations have been taken into account. The lattice parameter of the hexagonal lattice used for the simulated pattern is 34 nm. Slight differences are observable in the intensity, in particular at  $Q_y = 0 \text{ nm}^{-1}$ , where the intensity in the simulated pattern is higher than the experimental pattern. Furthermore, more Bragg peaks are observed in the simulated pattern in the high  $Q_y$ -range, where the experimental intensity drops quicker than simulated, same for the Bragg peaks in the higher  $Q_z$ -range.

The vertical and the horizontal slices of the experimental data and its fitting are shown in figure 6.10 (c) and (d), respectively. The vertical slice was performed at  $Q_y = 0.21 \text{ nm}^{-1}$  and the horizontal slice at  $Q_z = 0.28 \text{ nm}^{-1}$ . The fitted intensity shows a good agreement with the experimental data. The excellent agreement between the experimental and simulated data along the  $Q_z$  direction and the good prediction of the peak positions along the  $Q_y$  direction indicate a reasonable selection of the modeling parameters. The good quality of the GISAXS vertical cut along  $Q_z$  direction gives an accurate derivation of the particle height. The difference between the experimental and the simulated intensity in the regions between Bragg peaks attributed to the orientation of the nonhomogeneous domains. The resulted SLD profile from the simulation is shown in figure 6.11. It is obvious from the SLD profile that the thickness of the silicon dioxide layer  $\approx 60$  nm on top of the silicon substrate. The silicon dioxide formed is amorphous, not quartz as observed from the density. The particles layer thickness  $\approx 10$  nm on top of the oxide layer where it is sliced into 10 slices with different SLD values.

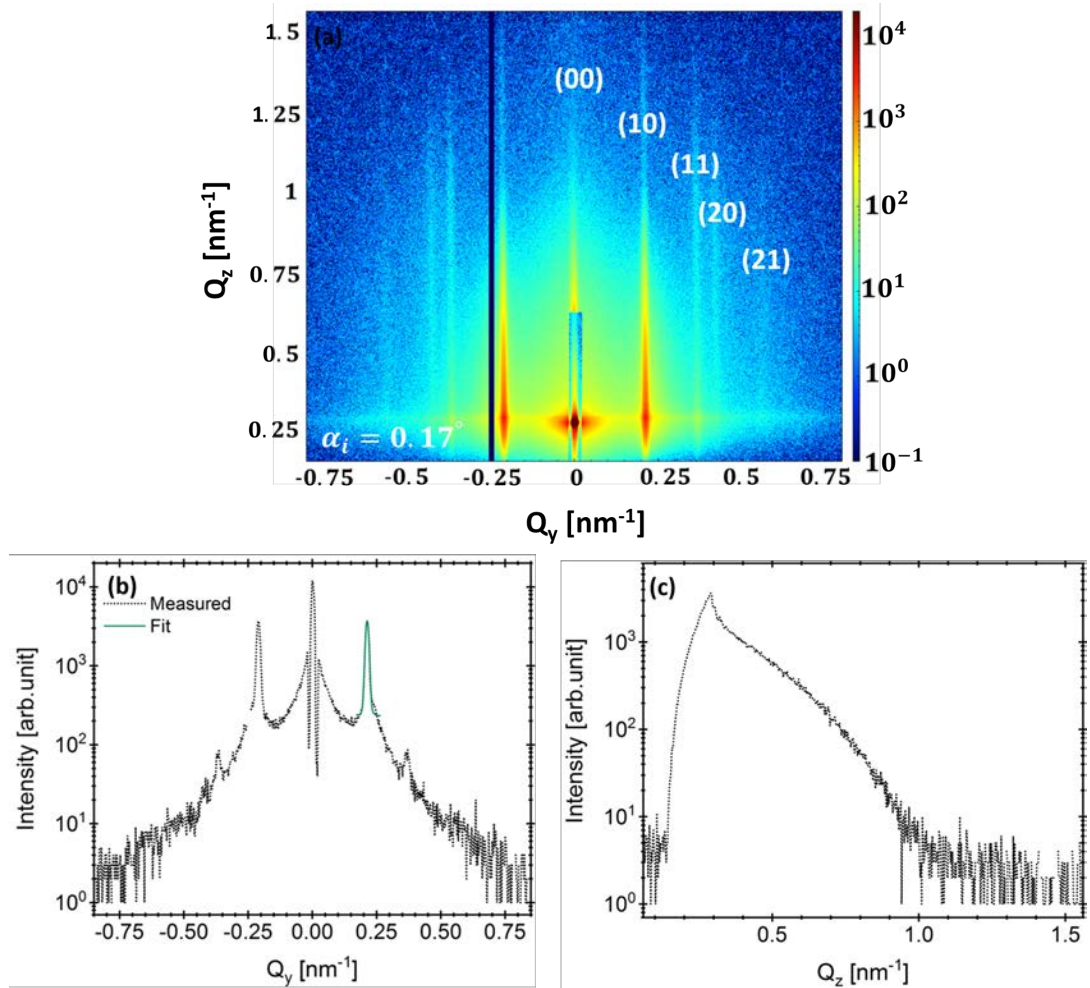


Figure 6.9.: (a) GISAXS pattern of CoFe<sub>2</sub>O<sub>4</sub> NPs grown on top of Si substrate at  $\alpha_i = 0.17^\circ$ . The indexing of the Bragg rods according to a 2D hexagonal lattice with  $a = 34$  nm is also shown. (b) A horizontal line cut of the GISAXS pattern at a fixed  $Q_z = 0.29$  nm<sup>-1</sup> along with Voigt fit (light green line) to (10) Bragg peak. (c) A vertical line cut of the GISAXS pattern at a fixed  $Q_y = 0.21$  nm<sup>-1</sup>.

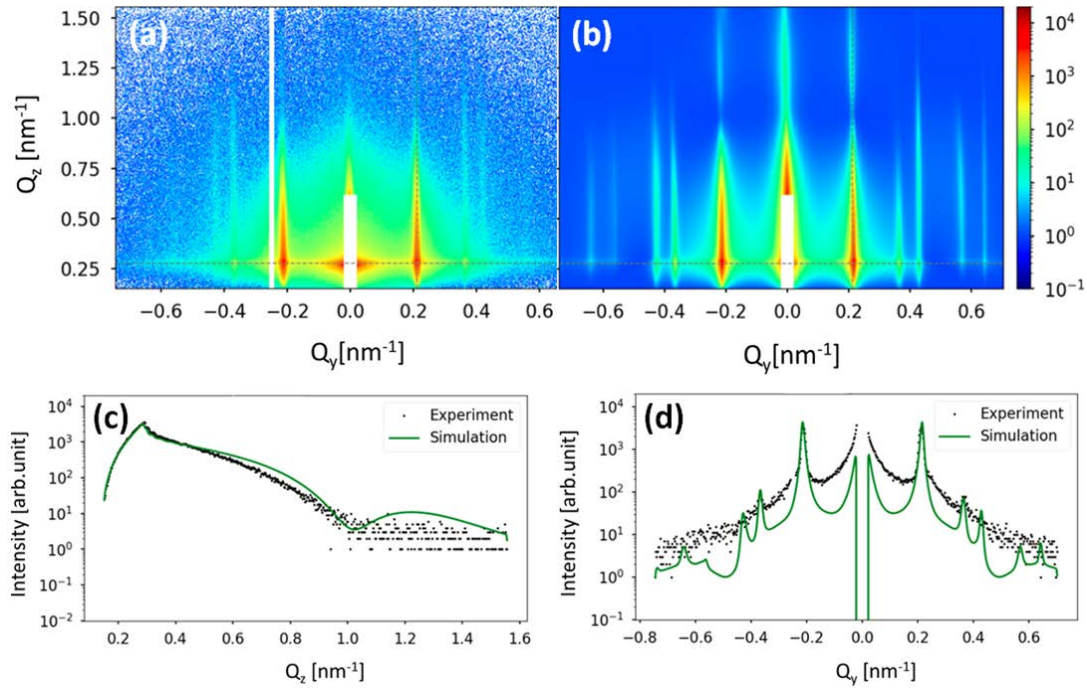


Figure 6.10.: (a) GISAXS pattern of  $\text{CoFe}_2\text{O}_4$  NP monolayer on Si substrate. (b) The simulation of the experimental GISAXS pattern using the BornAgain software assuming hemispherical particles with 10 nm height and 8.5 nm radius. The lattice constant of the hexagonal lattice is 34 nm. (c) A vertical slice as a function of  $Q_z$  at  $Q_y=0.21 \text{ nm}^{-1}$ . (d) A horizontal slice as a function of  $Q_y$  at  $Q_z=0.28 \text{ nm}^{-1}$ . The experimental data are shown as black dots and the simulated data are shown as a green solid line.

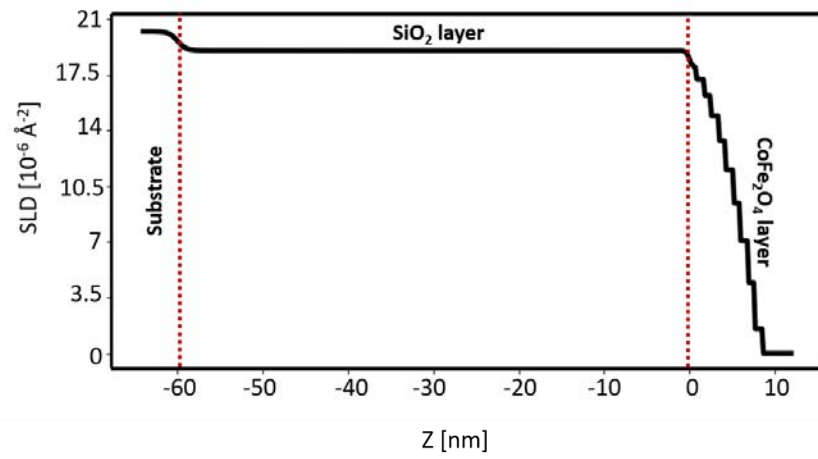


Figure 6.11.: The resulted SLD profile from the simulation of the GISAXS pattern.

## 6.4.2. Magnetism

### 6.4.2.1. Macroscopic magnetization

The field-dependent magnetization of the cobalt ferrite monolayer at room temperature and at 5 K in both directions is shown in figure 6.12. The room temperature measurement at 300 K in both directions exhibit nearly superparamagnetic behavior and additionally includes the Langevin behavior that has been observed for the respective nanopowder for direct comparison (figure 6.2). The magnetic moment with respect to the applied field of the monolayer is smaller in comparison to the particles in the powder. Under the same temperature, the magnetic moment of the particles in the monolayer is larger, if the magnetic field is applied parallel to the sample plane than if the field is applied perpendicular to the sample plane. This is might due to the high shape anisotropy. The nanodots reach saturation faster, when the the magnetic field is applied parallel to the sample plane. This is because the spin alignment is more energetically favorable parallel to the applied field (i.e. in-plane easy axis). In addition to the nearly superparamagnetic behavior in out of the plane direction, a small hysteresis with a coercive field in the order of 7 mT is visible on close inspection as can be seen in the inset. This connects to the temperature-dependent magnetization measurements in figure 6.13, which indicate that the particles are close below the blocking temperature at  $\approx 380\text{K}$  and the system is in a blocked SPM. Furthermore, the center of the loops is slightly shifted towards the negative field direction. This indicates an EB effect.

At a low temperature of 5 K, the NP super spins are in a blocked SPM. In the in-plane direction, no hysteresis is observed and the particles exhibit a superparamagnetic behavior with zero coercivity. While in the out of the plane direction, the particles also show nearly superparamagnetic behavior with a small coercivity of 28 mT. Furthermore, an extra opening is observed at a low and high field in both directions, which is more pronounced in the out of the plane direction. This opening starts to appear around 150 K (see figure F.3). This might come due to the existence of two sublattices of the spinal ferrimagnetic cobalt ferrite. The magnetic moments of the two sublattices are aligned anti-parallel to each other and not equal, therapy, result in a net magnetic moment leading to this opining before reaching saturation.

To study the temperature-dependent magnetization of the cobalt ferrite monolayer, the sample was measured at various fields in both directions under the Fc and ZFC conditions. The ZFC magnetization curves are obtained in two steps. First, in the absence of an external magnetic field, we cool down the sample from 400 K (most particles show paramagnetic or superparamagnetic behavior) down to 5 K. In the second stage we apply a magnetic field of 5 mT, while we increase the temperature from 5 K to 400 K in a stepwise manner. On the other hand, the FC magnetization curves are obtained by measuring the

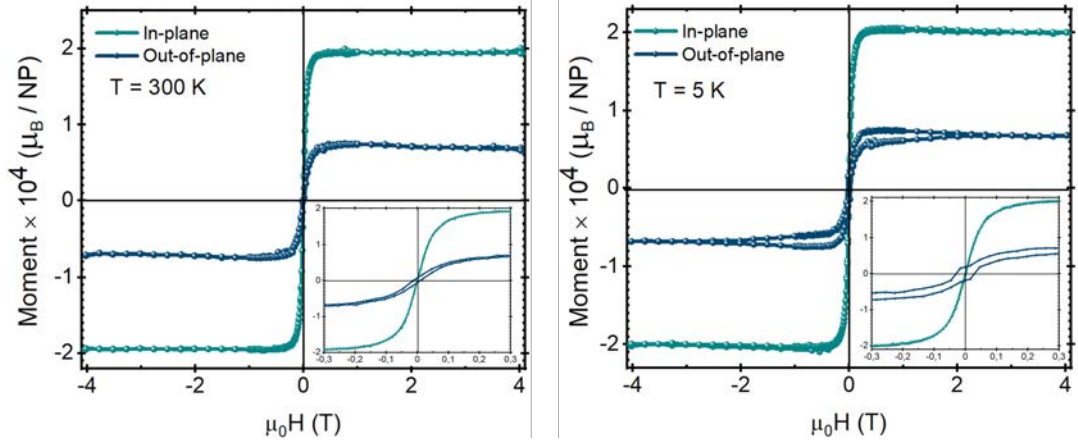


Figure 6.12.: In-plane and out-of-plane magnetization curves of  $\text{CoFe}_2\text{O}_4$  nanodots on Si substrate at 300 K (left) and at 5 K (right).

magnetization ( $M$ ) while decreasing the temperature from 400 K down to 5 K in the presence of a magnetic field. The ZFC/FC magnetization of the monolayer of cobalt ferrite measured at 5 mT in both directions is shown in figure 6.13. The blocking temperature of the monolayer at which maximum magnetization is achieved is found above room temperature in the plane direction while in out-of-plane direction  $T_B \approx 382\text{ K}$ . Below this temperature ( $T < T_B$ ) the particles are in the blocked state, while they are in the superparamagnetic state above it ( $T > T_B$ ). Another interesting feature is the splitting or irreversibility temperature,  $T_{irr}$ , which is qualitatively defined as that temperature where the ZFC and FC curves visibly diverge. The irreversibility temperature will occur near the blocking temperature  $T_{irr} \approx T_B$  for a perfect superparamagnetic system (SPM) with a monodisperse particle size distribution. However, the irreversibility temperature occurs at temperature larger than the blocking temperatures for a superparamagnetic system with a finite size distribution [156], which is an indication for the presence of a maximal turning point on ZFC curve for magnetic spinel ferrites to the blocking of the magnetic moment of individual particles and the mutual magnetic interactions between particles.

As seen in the ZFC curve in the in-plane direction, the magnetization increases rapidly with increasing temperature, while the FC magnetization decreases with decreasing temperature. It decreases rapidly below 200 K. This decreasing might be due to the interparticle interaction. Below the blocking temperature, the ZFC and FC curves split. This is often observed in the SPM system.

The ZFC magnetization in the out-of-plane direction reaches a maximum at about 330 K. Beyond  $T_B$ , the ZFC magnetization decreases and shows a typical paramagnetic behavior. Also, above  $T_B$  the FC magnetization curves follow the same path as ZFC curves, while below  $T_B$ , the FC magnetization increases with

decreasing temperature. Furthermore, the rapid fall off of the ZFC curve peak and the closeness of  $T_B$  and  $T_{irr}$  values illustrate the narrow size distribution for the particles [156]. The splitting of ZFC and FC curves at a certain irreversibility temperature is one of the characteristic features of superparamagnetic state (i.e. above  $T_{irr}$ , the ferromagnetic domain are fully unblocked). The maxima observed at  $T = 330$  K is a normal feature in the ferrite material due to the addition of the two sublattice at a certain temperature known as compensation temperature [157].

On comparing the FC–ZFC data and hysteresis curves data of our sample, we found that below blocking temperature (i.e.  $T = 5$  K), the field-dependent magnetization in the out-of-plane direction shows the formation of small hysteresis loops and hence behaves as ferromagnetic material. Above the blocking temperature, the hysteresis becomes infinitesimal, and the material behaves as a superparamagnetic material.

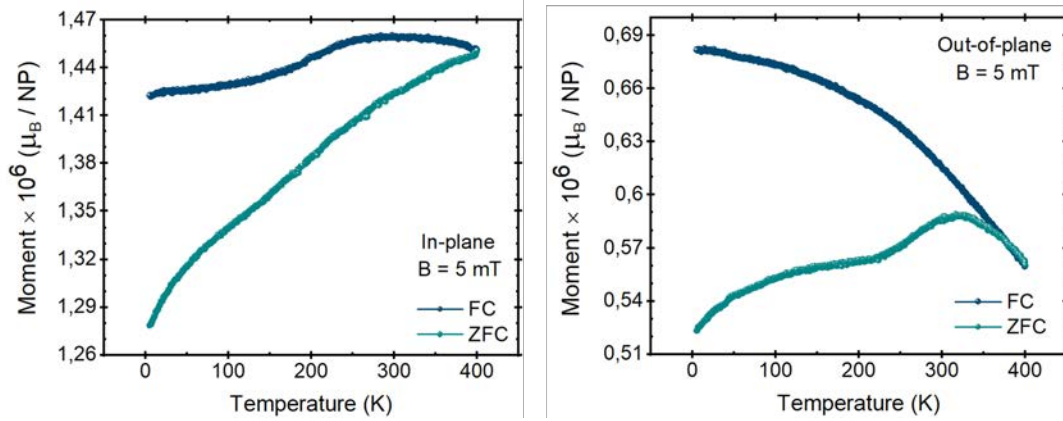


Figure 6.13.: Temperature dependence of the in-plane (left) and out-of-plane (right) magnetization of  $\text{CoFe}_2\text{O}_4$  nanodots on Si substrate at 50 mT. The blue and green curves are the field-cooling and zero-field-cooling curves, respectively.

#### 6.4.2.2. Depth-resolved magnetization

The half-polarized neutron reflectivity data measured at saturation with an applied in-plane field is shown in figure 6.14 (left). A small splitting between the spin-up and the spin-down channels is clearly visible. Also, it is visible that  $R^+ > R^-$ , which corresponds to a small in-plane magnetization component parallel to the applied magnetic field.

Figure 6.14 (right) shows all four reflectivities along with fits to the data points (solid lines) were recorded at remanence with an applied in-plane field: two non spin-flip  $R^{++}$ ,  $R^{--}$  (NSF) and two spin-flip  $R^{+-}$ ,  $R^{-+}$ (SF). No SF scattering was

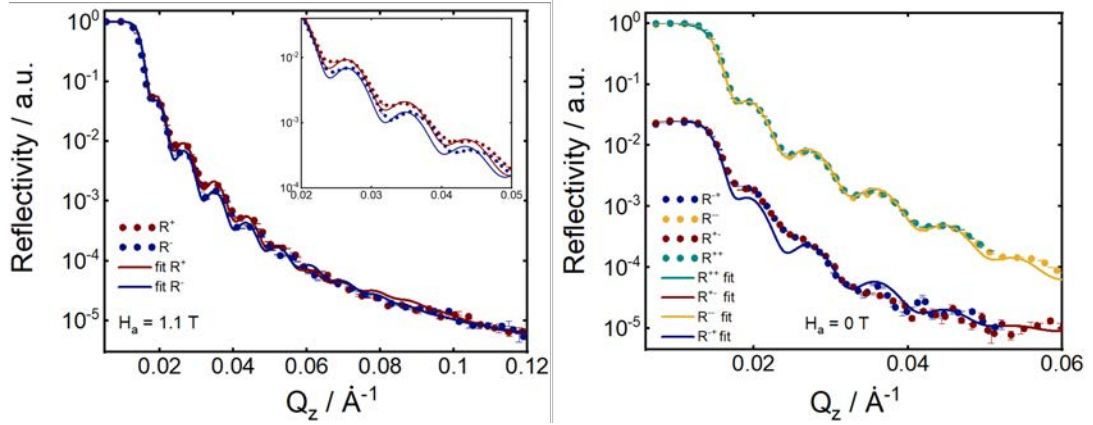


Figure 6.14.: Neutron reflectivity of cobalt ferrite monolayer deposited directly onto a silicon wafer measured at 300 K. The NR measured first at saturation field (left) with half polarization analysis and at remnant field (right) with full polarization analysis. At saturation,  $R^+$  and  $R^-$  are displayed, together with the fits shown by solid lines. The  $R^+$  and  $R^-$  correspond to the states of the RF flipper turned off and on, respectively. At saturation, All four reflectivities: two NSF ( $R^{++}, R^{--}$ ) and two SF ( $R^{+-}, R^{-+}$ ) are displayed, together with the fits shown by solid lines.

observed. From this we conclude that the mean magnetization averaged over the coherence volume is either parallel to the field, or equal to zero. Moreover, no splitting between the two NSF curves, indicating that the sample at remnant approaches a demagnetized state. The difference between the SF and the NSF channels is due to the efficiency of the polarizer and the analyzer.

More details about the microscopic arrangements of the magnetic state become more clear after fitting the data assuming the model shown schematically in figure 6.5. All four reflectivities, SF and NSF (figure 6.14 (right)) were fitted simultaneously by varying the nuclear scattering length density (nSLD), the magnetic scattering length density (mSLD), the layer thickness and the interfacial roughnesses. Here, from PNR one can get the structural, as well as the magnetic depth profile. The NP layer is sliced into 50 slices during the fitting and we consider a variation of the mSLD, which provides information about the magnetic correlation in a monolayer system at the microscopic level. The magnetic moment per formula unit as calculated from the resulted fitting parameters is  $\mu = 1.4 \mu_B/\text{formula unit}$ . It is more than a factor of two smaller than the value of the bulk cobalt ferrite  $\mu = 3.7 \mu_B/\text{formula unit}$ . This is because of the volume fraction of the NP in the monolayer. This can be described due to the frustration effect caused by competing dipole interaction between different pairs of NP in the two-dimensional lattice [124]. The zero mSLD at remanence is not surprising because the hysteresis curve at room temperature (figure 6.12)

does not show a remnant magnetization at zero fields. The zero value of mSLD at remanence might be due to complete randomness in directions of the NP magnetic moments or due to the superspins being aligned parallel to the field in each domain, but are random over the coherence volume. In both cases the net magnetization will be zero and the NSF reflectivities will be unsplit, i.e.  $R^{++} = R^{--}$ . In fact, as is clear in figure 6.14 (right) there is no splitting of reflectivities for up and down polarizations at remanence, clearly showing a demagnetized state over the macroscopic area.

## 6.5. Summary

The preceding chapter provides a full characterization of structural and magnetic properties of a magnetic nanoparticles monolayer. The structural characterization started from local characterization by SEM and AFM, towards the global characterization using x-ray scattering techniques (XRR and GISAXS). The magnetic structure of the monolayer is resolved macroscopically using a SQUID magnetometer and microscopically using reflectometry with polarized neutrons. From the SEM, the nanoparticles were ordered in hexagonal close packed-structures. From GISAXS, a lateral hexagonal ordering of the NP is observed over a macroscopic area of the substrate.

It is confirmed by X-ray and neutron reflectometry that the sample has a monolayer structure. By GISAXS the hexagonal array structure that is observed by SEM is resolved and successfully reproduced using the BornAgain software based in DWBA. Assuming a hemispherical particle with a height of 10 nm, radius of 8.5 nm and a hexagonal arrangement with a lattice constant of 34 nm, the measured GISAXS data match well with the simulated pattern.

Using the knowledge of the structural properties of the sample, the monolayer magnetism is studied using magnetometry and polarized neutron reflectometry. Temperature and field dependent magnetization curves in both directions (in-plane and out-of-plane) have been compared. From the hysteresis, it is confirmed that the easy direction of the magnetization is in the plane. From the ZFC/FC magnetization curves, the blocking temperature of the nanoparticles is found above the room temperature.

The PNR reveals the depth dependence of the magnetization profile. The PNR curves measured for up and down neutrons at saturation show a small magnetization state, while at remanence show a demagnetized state with zero net magnetization.

## 7. Directed self-assembly of iron oxides nanoparticles on patterned substrates

Magnetic nanoparticles especially iron oxide nanoparticles (Maghemite  $\gamma\text{-Fe}_2\text{O}_3$ ) have attracted extensive interest due to their superparamagnetic properties, their ferrimagnetic behavior at room temperature and due to their higher Curie temperature ( $\approx 970$  K). They have been the focus of many types of research because they exhibit attractive properties for potential use in different fields such as high-density magnetic memory systems, or for spintronic devices [158, 159]. In particular, highly ordered arrangements of these nanoparticles are required for these applications [160].

There are various methods for fabricating long-range ordered magnetic nanoparticle arrangements in two and three-dimensions. These include assisted self-assembly using trench-patterned substrates with a feature size of the same order of magnitude as the diameter of the nanoparticles. Then the particles go into the trenches using a suitable deposition method.

Therefore, the main aim of this chapter is to direct or assist the self-assembly of cubic iron oxide nanoparticles within desired structures to produce ordered arrays of these particles over large areas and as a trying to get a single crystalline arrangement of these nanoparticles. Trench-patterned silicon substrate created by E-beam lithography presented in Sec. 4.5 was used as a template to direct the self-assembly of the nanoparticles inside the trenches. In this chapter, a general introduction about iron oxide as well as the current state of research on directed self-assembly of magnetic nanoparticles will be introduced. Then the method used for sample preparation will be presented. After that, the structural characterization and the magnetometry results of nanoparticles inside the trenches will be discussed.

### 7.1. Introduction to Iron Oxides

Iron is the fourth most common element in the Earth's crust and ferromagnetic in its elemental state at room temperature. Iron oxide forms naturally through the reaction of the iron with the water and with the most common element in the Earth's crust, oxygen. Due to the great presence of iron oxides in nature, they have been widely used for centuries. Furthermore, iron oxides can be produced

at low cost, which makes the application from it more popular. In the iron oxides, oxygen anions  $O^{2-}$  form a close-packed lattice with the tetrahedral and octahedral interstices. Iron oxides existing in various crystalline phases. Iron oxide can be ferrimagnetic or antiferrimagnetic depending on the crystalline order. The iron oxide phase and its structural and magnetic properties depend on the oxidation state and abundance of the iron cation in the interstices. In nature and laboratory, there are in total sixteen different iron oxides existing. Despite a wide range of existence of all oxides, there are only four oxides widely used, which are Magnetite, Maghemite, Hematite and Wüstite. They will be introduced briefly in this section.

### Magnetite ( $Fe_3O_4$ )

Magnetite is the most abundant mineral of all iron oxides with the chemical formula  $Fe_3O_4$  or sometimes represented as  $FeO \cdot Fe_2O_3$ . It is a black ferrimagnetic mineral known as a loadstone or natural magnet [161, 162]. Magnetite has an inverse spinel structure in the space group  $Fd\bar{3}m$  containing both divalent  $Fe^{2+}$  and trivalent  $Fe^{3+}$  iron ions. The unit cell with lattice constant  $a = 0.839$  nm consists of 32  $O^{2-}$  ions.

The spinel structure has the formula  $A [B_2] O_4$ , where A represents the tetrahedral sites with the divalent ion and B represents the octahedral sites with the trivalent ions. But in case of the inverse spinel structure, the divalent ions sit on the octahedral sites (B) and the trivalent ions are distributed equally between the octahedral (B) and the tetrahedral site (A) ( $B[AB]O_4$ ). For magnetite, the tetrahedral and the octahedral interstices are filled with trivalent iron ions ( $Fe^{3+}$ ) and half of the octahedral sites are filled with the divalent iron ion ( $Fe^{2+}$ ). That means in total there are eight  $Fe^{2+}$  at octahedral sites, eight  $Fe^{3+}$  at tetrahedral sites and eight  $Fe^{3+}$  at octahedral sites. The formula unit of the magnetite can be written according to the normal spinel structure formula as  $Fe_8^{3+}[Fe_8^{2+}Fe_8^{3+}]O_{32}^{2-}$ . Figure 7.1 (a) shows the crystal structure of the magnetite with a unit cell consisting of 32  $O^{2-}$ , 16 $Fe^{3+}$  and 8  $Fe^{2+}$ .

Magnetite below the Curie temperature  $T_c \approx 850$  K is ferrimagnetic. In magnetite, the magnetic lattice consists of two sublattices, the first one due to the trivalent iron ions at the tetrahedral sites and the other one due to the trivalent and the divalent iron ions at the octahedral sites. The spins of the two sublattices below  $T_c$  are oriented antiparallel to each other with different magnitude. Only the spins of  $Fe^{2+}$  in the octahedral sites contribute to the total magnetic moment because the spins of  $Fe^{3+}$  cancel out on tetrahedral and octahedral sites. The total spin due to  $Fe^{2+}$  is  $S=2$ , which gives a magnetic moment of  $4\mu_B$ .

The  $Fe^{2+}$  and  $Fe^{3+}$  ions on the octahedral sites interact ferromagnetically via double exchange interaction. While  $Fe^{3+}$  ions interact antiferromagnetically via superexchange interaction between the tetrahedral and the octahedral sites

where the strength of the interaction depends on the bond angles. The saturation magnetization of bulk magnetite is in the order of 475 – 517 kA/m [161, 163]. Bulk magnetite at room temperature has a cubic magnetocrystalline anisotropy with [111] and [100] being the easy and hard axis respectively, with a first-order magnetocrystalline constant of  $K_1 = 1.35 \times 10^4 \text{ J/m}^3$  [164]. Magnetite has a conductivity in the order of  $10^2 - 10^3 \Omega^{-1} \text{ m}^{-1}$ , which is very close to the metal. Furthermore, the Verwey transition (metal to insulator phase transition) at  $T_v = 120 \text{ K}$  [165] has been observed for magnetite. Moreover, at a temperature below  $T_v$ , the cubic structure transitions to a triclinic structure, which yields a change to uniaxial anisotropy with near [001] as easy axis [166].

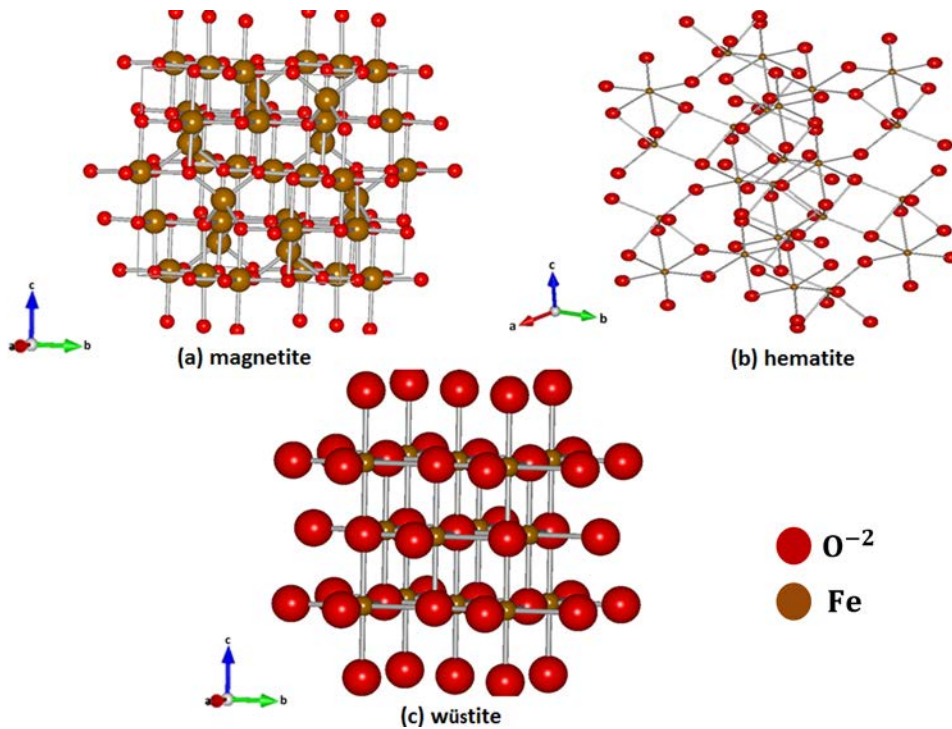


Figure 7.1.: Representation of iron oxide structure of (a) magnetite, (b) hematite and (c) wüstite. The red spheres represent the close-packed  $O^{2-}$  ion and the brown spheres indicate the position of the iron cations occupy either the tetrahedral or octahedral interstices. The visualization was produced using VESTA software [167] where the data used here are obtained from the Inorganic Crystal Structure Database (ICSD).

### Maghemite ( $\gamma - Fe_2O_3$ )

When magnetite is oxidized at low temperatures, maghemite ( $\gamma - Fe_2O_3$ ) forms. Maghemite is a reddish-brown mineral at room temperature. It has a defective inverse spinel structure only composed of  $Fe^{3+}$  ions and additional va-

cancies in the octahedral sites to ensure charge neutrality. The unit cell consists of 32  $O^{2-}$  ions similar to the magnetite structure, the eight tetrahedral sites are occupied by  $Fe^{3+}$  ions and only twelve sites of the sixteen octahedral sites are occupied by  $Fe^{3+}$ , the rest four sites consist of  $2\frac{2}{3}$  vacancy and  $1\frac{1}{3}$   $Fe^{3+}$ . The unit cell formula can be given as  $Fe_8^{3+}[Fe_{12}^{3+} \otimes_{2\frac{2}{3}}^{3+} Fe_{1\frac{1}{3}}^{+3}]O_{32}^{2-}$ , where  $\otimes$  represents a vacancy. The lattice constant of bulk maghemite is found in the literature to be  $a = 0.834$  nm [161].

Maghemite is ferrimagnetic below  $T_c \approx 948$  K, but it is difficult to observe the transition because it is converted to hematite ( $\alpha - Fe_2O_3$ ) above 700 K. The ferrimagnetism arises due to  $Fe^{3+}$  ions at the octahedral sites. The magnetic structure of Maghemite consists of two sublattices similar to magnetite. The magnetic moments are oriented antiparallel to each other in the two sublattices but it oriented parallel to each other in the same sublattice. That means the spins of 8  $Fe^{3+}$  ions at the octahedral sites are canceled out by 8 of  $Fe^{3+}$  ions at the tetrahedral sites due to the antiparallel alignment of the spins in both sites. As a result, the excess of  $Fe^{3+}$  ions at the octahedral sites leads to a net magnetic moment of the order of  $2.5\mu_B$ , which is quite close to the experimental value of  $2.36\mu_B$ . The bulk saturation magnetization at 300 K is found in the literature to be in the range of 290 – 390 kA/m which is smaller than magnetite and the cubic magnetocrystalline anisotropy constant is reported in the literature in the range of  $K_1 = -(1.7 \dots 10) \times 10^4$  J/m<sup>3</sup> [161]. Moreover, maghemite is an insulator.

### **Hematite ( $\alpha - Fe_2O_3$ )**

Hematite ( $\alpha - Fe_2O_3$ ) is the most abundant mineral in rocks. It has a red color and it shows antiferromagnetism behavior. Hematite has a hexagonal unit cell with a lattice constant  $a=0.5034$  nm and  $c=1.375$  nm [161]. The model of the unit cell is shown in figure 7.1 (b). It can be assumed as a hexagonal close-packed (HCP) arrays of  $O^{2-}$  ions stacked along [100] direction while the two-thirds of the sites are filled with  $Fe^{3+}$  ions.

At room temperature hematite is a weakly ferromagnetic and it is paramagnetic above 956 K. Below  $T=260$  K, hematite becomes antiferromagnetic [161]. Hematite is an insulator.

### **Wüstite ( $Fe_xO$ )**

Wüstite ( $Fe_xO$ ) is a black, antiferromagnetic material and metastable at room temperature in the bulk form. It contains only divalent ions  $Fe^{2+}$ . Stoichiometric FeO does not exist at atmospheric pressure, only non-stoichiometric  $Fe_xO$ , where  $x=0.83 - 0.95$  is stable above  $567^\circ$  at atmospheric pressure. When wüstite is cooled down to room temperature,  $Fe_xO$  disproportionates to Fe and  $Fe_3O_4$ .  $Fe_xO$  can be quenched to room temperature, leading to a metastable phase [161].

Wüstite has a crystal structure similar to rock salt structure. It consists of two face-centered cubics (FCC) lattice of  $Fe^{2+}$  and  $O^{2-}$ . The cations and anions are arranged in a cubic close-packed (CCP) structure along the [111] direction. The oxygen ions occupy the main face-centered cubic (FCC) sites and the  $Fe^{2+}$  cations fill the octahedral interstitial sites. The unit cell of wüstite is shown in figure 7.1 (c). The lattice constant varies from 0.428 nm to 0.431 nm, depending on the stoichiometry [161].

Wüstite at room temperature is paramagnetic and antiferromagnetic below Néel temperature  $T_N$  which ranges from 190 K to 211 K, depending on the stoichiometry [161].

From the above-mentioned oxides, only maghemite will be discussed in this chapter.

## 7.2. Nanoparticles characterization

The nanoparticles studied in this chapter are Iron oxide nanocubes with size in the order of  $\approx 13 - 14.6$  nm. They were obtained through collaboration with the group of Dr. Sabrina Dish from the physical chemistry department of the University of Köln. They prepared the particles using an iron oleate route [168] where at the beginning iron oleate is prepared, and the nanoparticles are subsequently obtained by controlling the thermal decomposition of the oleate in high-boiling solvents. The nanoparticles are dispersed in toluene and coated with oleic acid shell in order of  $\approx 1.5 - 1.8$  nm as obtained from small-angle neutron scattering SANS measurements performed by the group of Dr. Sabrina Dish. The main composition of the particles is ferromagnetic maghemite ( $\gamma - Fe_2O_3$ ) as determined from x-ray diffraction measurements that were performed also by the group of Dr. Sabrina Dish.

In the following, the experimental methods used for the characterization of the nanoparticles dispersion are presented.

### Scanning Electron Microscope (SEM)

The micrographs of the drop-casting iron oxide nanocubes on silicon substrate are qualitatively viewed by SEM Hitachi SU8000 (Sec.3.2.1). The micrographs are measured at 5 kV and only the image taken from the backscattering electrons are shown in figure 7.2 (a) to obtain a strong contrast. As seen, the SEM image of the particles is not so clear due to the resolution limit of the SEM, which is not sufficient to observe particles with small size. SEM revealed that the particles are close to the cubic shape and once deposited on a silicon substrate, tend to self-organize into a square lattice. Furthermore, the particles tend to be more close to each other due to the monodispersity of the particles. The collaboration provided transmission electron microscopy TEM image shown

in figure 7.2 (b). The TEM micrographs of individual nanoparticles were obtained using a Zeiss Leo 902 microscope operating at 120 kV with a LaB6 cathode in bright field mode to obtain high-magnification micrographs of individual nanoparticles. The particle size and size distribution of over 100 nanoparticles were measured manually using the GIMP 2 software and evaluated by fitting the size distribution histogram shown in figure 7.2 (c) by a log-normal distribution function (black solid line) as described in Sec. 5.3.2. The particles have a cube edge of  $14.2 \pm 0.1$  nm and a size distribution of 6.6% as obtained from the log-normal fit.

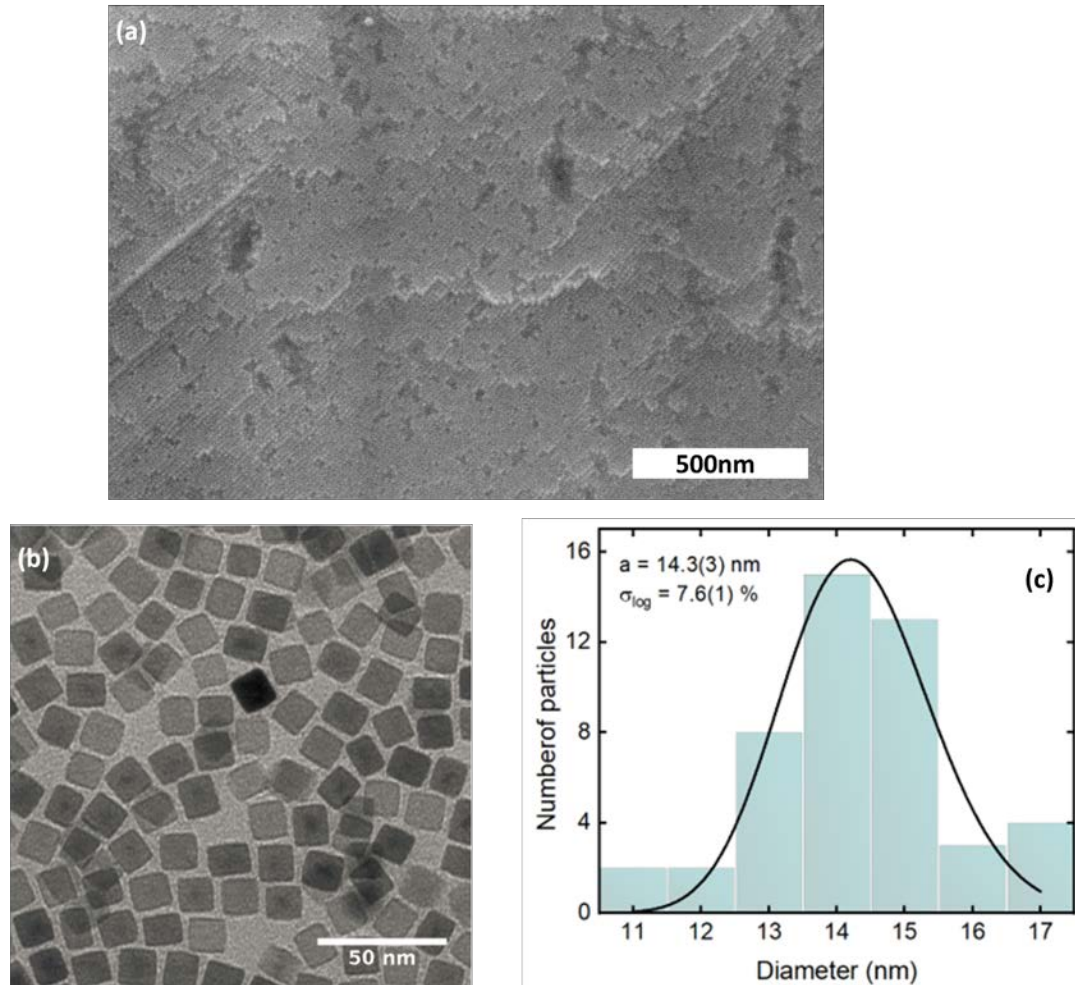


Figure 7.2.: (a) SEM image of cubic iron oxide nanoparticles drop-casted on the silicon substrate. (b) TEM micrographs of the same particles. (c) The particle size distribution histogram.

### Small Angle X-ray Scattering (SAXS)

SAXS measurements of the nanoparticle dispersion were carried out at GALAXI (Sec. 3.4.1) to determine the average size and the shape of the nanoparticles.

The nanoparticles are filled in quartz glass capillaries (Hilgenberg GmbH) with 1.5 mm outside diameter and 0.01 mm wall thickness, which is closed by a silicone ball, which was added by using a silicone gun to allow the measurement of the dispersions in a vacuum. The particle mass concentration in the order of 0.0039 is dispersed in toluene for the measurement. The SAXS measurements were performed for the samples at two different detector distances, the longest detector distance (3.53 m) and the shortest detector distance (0.83 m). In addition to the dispersion of the particles, a capillary filled with toluene as well as an empty capillary are measured under the same conditions as a reference sample for the subtraction of the background. The typical exposure time was approximately 2:30 h per sample. The SAXS data is calibrated to absolute units according to the procedure described in appendix D. The evaluation of the SAXS data was done using the "SasView" software.

In figure 7.3 the SAXS data of the iron oxide nanoparticles is shown. The data shows the first form factor minimum at a smaller scattering vector ( $Q$ ) and the maxima are qualitatively sharp due to the smaller size distribution of the particles.

The SAXS data of the nanoparticles are evaluated quantitatively using various shape models, i.e. various form factors: spherical (Appen.E.1), cubic (Appen.E.3) and spherical core-shell (Appen.E.2) form factors. Moreover, for a further detailed evaluation of the nanoparticle's structure, the SAXS data fitted using a superball form factor (i.e. cubic shape with rounded edges). The fitting is done by Dr. Dominique Dresen from the group of Sabrina Dish. The superball form factor is used to fit the SAXS data of cubic particles to account for the deviation from a perfect cube shape. More details about the superball form factor and its derivatives are described in Dresen's doctoral thesis [169]. The spherical form factors neglect the actual morphology of the nanoparticles and assumes that the particles have a perfect sphere shape. The cubic form factor assumes a perfect cubic shape with defined edges corners. The spherical core-shell form factor assumes a perfectly spherical particle with a core-shell structure, where the shell thickness obtained  $\approx 1.7(1)$  nm. While Dresen's assumed in his superball model that the particles have a cubic shape with a rounded corner (i.e. between a perfect sphere and perfect cube) defined by the shape parameter  $p$ . The obtained shape parameter ( $p$ ) for the superball model is equal  $p = 2.2(1)$ , which means that the particles shape more close to a cube. From figure 7.3 it is clear that the superball form factor gives the best description of the data. The spherical form factor underestimates the first form factor maxima, while the spherical core-shell form factor overestimates the second form factor maxima. The cubic form factor overestimates the first and the second form factor

maxima.

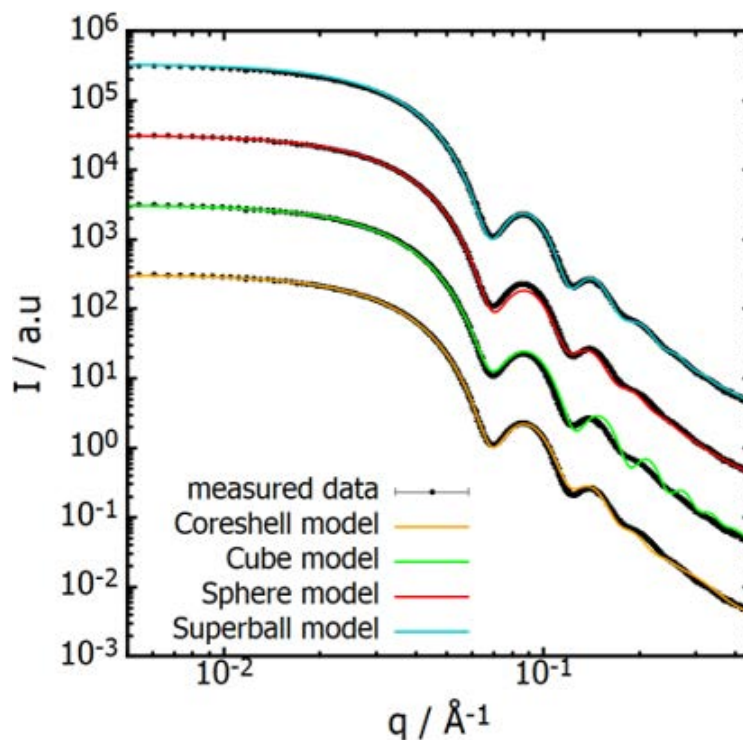


Figure 7.3.: The SAXS data of the iron oxide nanoparticles dispersed in toluene. Spherical (red), core-shell (yellow), cubic (violate) and superball (light blue) form factors were used to fit the data.

The particle size obtained from the four fits are tabulated in table 7.1. The scattering length density of the core and the solvent are fixed ( $SLD_{core}=38.5 \times 10^{-6} \text{ \AA}^{-2}$  and  $SLD_{solvent}=8 \times 10^{-6} \text{ \AA}^{-2}$ ). The size of the sphere and core-shell and the superball are given in terms of the radius  $R$  while the size of the cube is given in terms of the edge length  $a$ .

### Macroscopic magnetization

In this chapter, the macroscopic magnetization of the iron oxide dispersion is measured with respect to the magnetic field using a Quantum Design MPMS XL SQUID magnetometer described in Sec. 3.3.1. For measurements of liquid nanoparticle dispersions, evacuated glass tubes shown in figure 7.4 were used. In the beginning,  $60 \mu\text{L}$  of the nanoparticle dispersion with a concentration of 0.39 vol% was put in a glass tube that was sealed using a hydrogen burner. Then the tube is fixed in a colorless drinking straw with an additional straw

Model shape	R, a (nm)	$\sigma_{R,a}$ %	r (nm)	p
Sphere	6.33(1)	9(2)	-	1
Core-shell	6.3(3)	9.2(1)	1.7(1)	-
Cube	10.22(1)	11(1)	-	$\infty$
Superball	5.4(1)	12.3(1)	-	2.2(1)

Table 7.1.: Particle size and size distribution of iron oxide nanocubes as obtained from the spherical, the core-shell, the cubic and the superball form factors.  $\sigma_{R,L}$  is the log-normal size distribution.

to prevent moving of the tube during the measurement. The magnetization of the sample is then measured while sweeping the magnetic field between  $\pm 7$  T. The magnetic moment  $\mu$  measured from SQUID has a unit [emu], to convert it to magnetization  $M$  [A/m], it is divided by the liquid volume according to this relation

$$M[A/m] = \frac{\mu[Am^2]}{V[m^3]} = \frac{\mu[emu] \times 10^{-3}}{V[m^3]} \quad (7.1)$$

To get the magnetic moment per single particle, the magnetic moment in [emu] is divided by the approximate number of the nanoparticles inside the dispersion of the particle measured (i.e inside  $60 \mu$  L). The number of particles  $N$  was calculated using equation 5.3 by considering the particle volume concentration  $c_V \approx 0.00382$  and the particle mass concentration  $c_m \approx 0.02 \text{ g cm}^{-3}$ . The approximate number of the particles inside  $60 \mu$  L nanoparticle dispersion  $N \approx 8.4 \times 10^{13}$ . Therefore, the magnetic moment/single-particle  $\approx 3.8 \times 10^4 \mu_B$ .



Figure 7.4.: The glass tube inside drinking straw used for measurements of liquid nanoparticles using MPMS.

The measured magnetization of the nanoparticle dispersion at 300 K and 5 K are shown in figure 7.5. The particles were found to be predominately superparamagnetic at room temperature (300 K) (left figure). The sample rapidly magnetizes in relatively small fields so it achieves the saturation magnetization in a field of 2 T, while at 5 K (right figure), it shows a ferromagnetic hysteretic behavior with a coercivity of 300 Oe as shown in the inset.

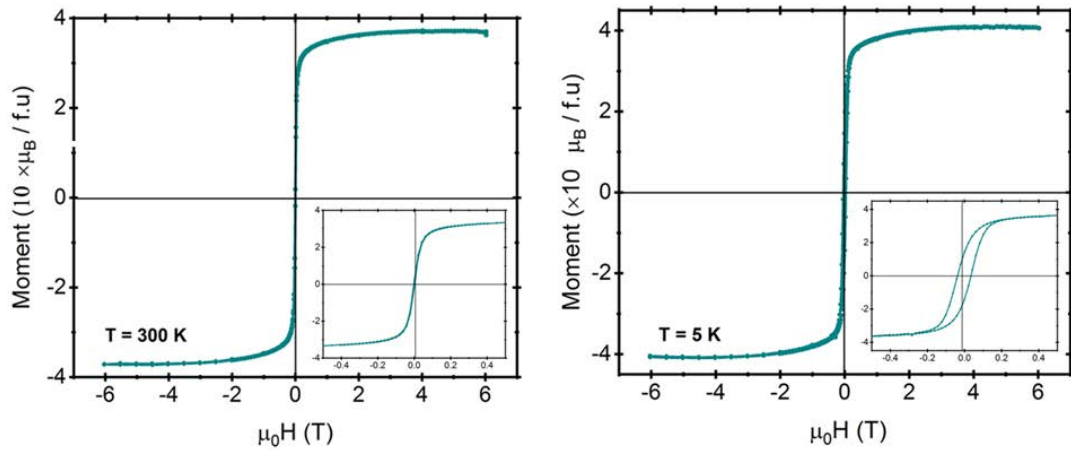


Figure 7.5.: Field dependent magnetization of cubic iron oxide dispersion measured at 300 K (left) and at 5 K (right).

### 7.3. Nanoparticles / pre-structured Silicon substrate

As mentioned before, to improve nanoparticle ordering and to achieve a regular nanoparticle pattern over larger areas, structured silicon substrates of the size of  $10 \times 10 \times 0.5 \text{ mm}^3$  with rectangular grooves were used as a template to guide the assembly of the nanoparticles. More details about the trench patterned substrates used in this study were presented in Sec. 4.5. In particular, sample S2\_02 shown in figure 4.14 (b) is used to deposit the particle above it. The grooves have a width of  $\approx 86 \text{ nm}$  and a period of  $\approx 247 \text{ nm}$ . Furthermore, the samples show two different depth profile as seen in the SEM-line profile (figure 4.14 (d)), in the GISAXS pattern (4.19 (b)) and from the x-ray reflectivity curve (figure 4.25 (b)) which shows oscillations with two different length scales. The particles deposited in these trenches are explained in Sec. 7.2 having size of  $\approx 14.2 \text{ nm}$  and with a superball shape.

With this groove width ( $\approx 86 \text{ nm}$ ) and this particle size ( $\approx 14.2 \text{ nm}$ ), one expects to get six particles per trench as shown schematically in figure 7.6. The actual results obtained from this study are presented in detail in the following sections after explaining the method used for sample preparation (Sec. 7.3.1). The prepared sample is characterized by scanning electron microscopy (SEM). But, SEM is restricted to the image of the surface and does not provide sufficient depth sensitivity to record short and long-range correlations in three-dimensions, particularly, if the particles form layered or crystal-like three-dimensional structure. Therefore, grazing-incidence small-angle x-ray scattering (GISAXS) is performed for structural analyses of nanoparticle arrays and to get insight

into the in-plane and out-of-plane ordering of magnetic nanoparticles on pre-structured silicon substrates (Sec. 7.3.2). Moreover, the magnetic moment as a function of magnetic field and temperature is measured used SQUID magnetometry (Sec. 7.3.3).

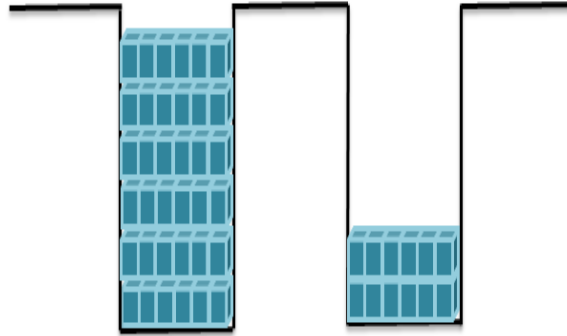


Figure 7.6.: Schematic drawing of the cubic nanoparticles inside trenches.

### 7.3.1. Sample preparation

For the sample preparation, at the beginning, the stock nanoparticles dispersion used to prepare the sample in toluene have an initial concentration of 20 mg/mL were diluted with toluene with a volume ratio of 1:10. Then, the dispersion was put into an ultra-sonic bath for 15 minutes to get a homogeneous dispersion of nanoparticles. Afterward, the naked substrate was immersed in the diluted dispersion for 30 seconds and take it out from the dispersion slowly. Eventually, the sample was prepared after three cycles of immersing in the dispersion and take it out of the dispersion. The last step, after 30 minutes from the last time take out the sample from the solution, an additional 5  $\mu\text{L}$  of the diluted solvent was drop-casted on the sample surface and a plastic ruler was used to remove the excess of the dispersion directly after drop-casting the particles. Furthermore, after each time of sample immersion and take it out, the sample was shaken by hand for a few seconds to force the nanoparticles to move inside the trenches. The SEM image of the self-assembled cubic iron oxide nanoparticles on the trench-patterned silicon substrate obtained as explained earlier in the previous paragraph is shown in figure 7.7. As seen from the images, only a few particles above the mesa are observed. The SEM could not resolve the particles inside the trenches due to its resolution limit which is not sufficient to observe small particles in very deep trenches (i.e. the depth of the trenches  $> 300$  nm). Furthermore, the SEM images reveal two mesas where the particles distributed above it with different width and with two different depths. Furthermore, it is

obvious that the trenches so rough.

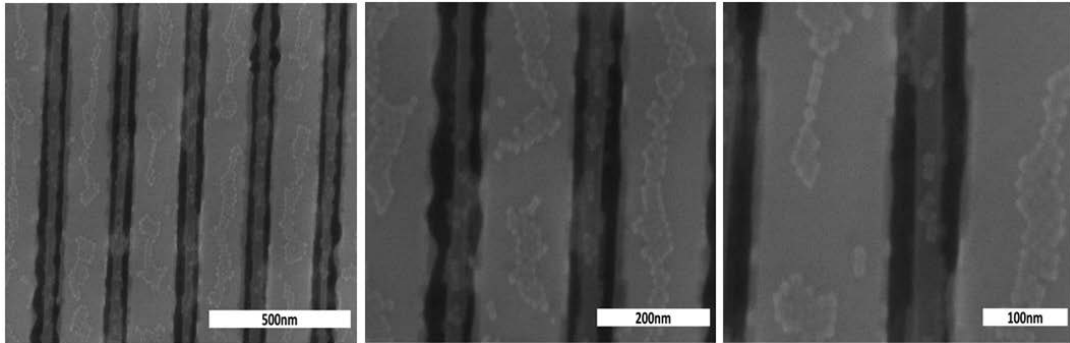


Figure 7.7.: SEM images from high to low magnification of self-assembled cubic iron oxide nanoparticles on the trench-patterned silicon substrate.

### 7.3.2. Structural characterization

In order to characterize the nanoparticle arrangement in the 3D multilayer and to get access to the in-plane ordering, we have monitored the multilayer interfaces by the grazing-incidence small-angle x-ray scattering (GISAXS). Furthermore, X-ray reflectivity (XRR) was carried out to reveal information about layers thickness, roughness and the out-of-plane ordering of the nanoparticles.

#### 7.3.2.1. Vertical Structure from X-Ray Reflectometry

Using GALAXI (Sec. 3.4.1), XRR measurement of the sample produced in Sec.7.3.1 is measured. The XRR data from nanoparticle multilayers formed inside the trenches is shown in figure 7.9. Most probably, the nanoparticle are arranged in the trenches as shown schematically in figure 7.8. As seen from the schematic drawing of the sample, the trench-patterned silicon substrate consists of two different depths with two different mesas. There are two oxide layers, one above the first mesa and the others above the second one. The XRR data obtained from the sample shows three kinks at  $Q_z=0.32 \text{ nm}^{-1}$ ,  $0.38 \text{ nm}^{-1}$  and  $0.48 \text{ nm}^{-1}$  corresponding to the critical angle of silicon, silicon dioxide and iron oxide respectively. The critical angle of the substrate is not sharp confirming non-flat substrate, i.e. pre-structured surface. There is almost one oscillation after the critical angle of the iron oxide, which arises from the oxide layer that covered the structure. Furthermore, Kiessig fringes appear after the oxide oscillation up to  $Q_z=3.5 \text{ nm}^{-1}$ , which corresponds to the nanoparticle layers and confirm the existence of out-of-plane nanoparticle multilayers. The broad oscillation at  $Q_z=0.5 \text{ nm}^{-1}$ , might be a Bragg peak due to nanoparticle multilayer.

The Bragg peaks sit on the maximum of Kiessig fringes and appear due to constructive interference of the reflected x-ray from a periodic electron density variation. The appearance of the Kiessig fringes up to high  $Q_z$  value indicating a good nanoparticle layers with almost identical thickness. The oscillations periodicity corresponds to the layer thickness of  $D \approx 14.5$  nm which is calculated using the following relation

$$D = \frac{2\pi}{\Delta Q_z} \quad (7.2)$$

Where  $\Delta Q_z$  is the difference between two maxima or two minima.

These observations from XRR led us to conclude that the growth of nanoparticle multilayers via template-assisted self-assembly is a feasible process to obtain highly ordered nanoparticle films.

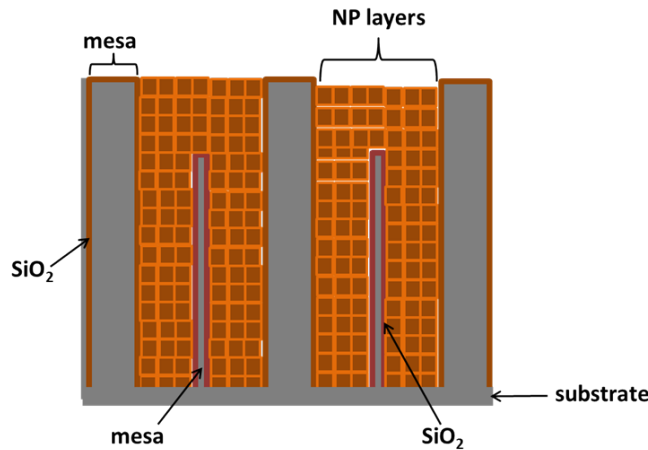


Figure 7.8.: Schematic drawing of the expected arrangement of the cubic nanoparticles inside the trenches.

### 7.3.2.2. GISAXS

To detect the depth-resolved lateral coherent structure of the nanoparticles, GISAXS measurements at GALAXI 3.4.1 were carried out. The measurements were performed in different geometries (i.e. different azimuthal angle  $\Phi$  between the incident beam and the lines). It performed as the incoming beam almost parallel (figure 4.2 (d)), perpendicular (figure 4.2 (b)) and  $45^\circ$  to the trenches, as shown in figure 7.10 (a), (b) and (c) respectively. For the beam almost parallel to the lines, the azimuthal angle  $\Phi$  between the incident beam and the

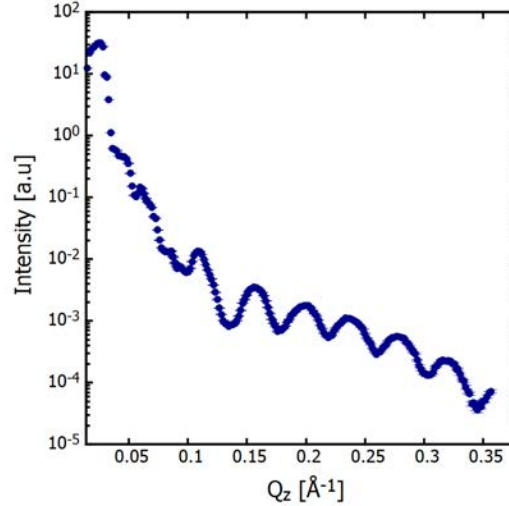


Figure 7.9.: X-ray reflectivity data from nanoparticle multilayers inside trenches.

lines is  $\approx 1.7^\circ$  while for the perpendicular geometry the sample was rotated with an azimuthal angle of  $\Phi=90^\circ$  from the perfect parallel geometry. The lines are tilted from the perfect parallel alignment with a very small angle with respect to the film normal direction to prevent the strong scattering background from the trenches which overwhelms the intensity from the nanoparticles [170]. The measurement was performed with three different geometries to check if the particles form a single crystalline arrangement from the lateral positions of the Bragg peaks. The GISAXS measurements in all cases were performed almost under the same incident angle  $\alpha_i=0.2^\circ$ . As the incoming beam almost parallel to the trenches, a bent tail is observed in the GISAXS pattern (figure 7.10 (a)), which originated from the structure factor of the trenches. The GISAXS intensity maps show strong modulations in both  $Q_y$  and  $Q_z$  directions, which is an indication of long coherence in both of the in-plane and out of plane arrangement of the nanoparticles. The two-dimensional Bragg peaks along  $Q_y$  are due to the arrangement of the laterally correlated nanoparticles while the Bragg peaks observed along  $Q_z$  reveals information about the out of plane coherence structure. The in-plane distance between the nanoparticles is  $d \approx 14.4$  nm.

The GISAXS maps show the same peak positions as the incoming beam perpendicular and  $45^\circ$  to the trenches. Therefore, no correlation between the structural arrangement of nanoparticles and the geometry of the trench-patterned substrates.

A horizontal line cuts along  $Q_y$  at  $Q_z = 0.2071 \text{ nm}^{-1}$  (figure 7.10 (d)) and vertical line cuts along  $Q_z$  at  $Q_y=0.4996 \text{ nm}^{-1}$  (figure 7.10 (e)) were taken for all GISAXS maps. It is obvious from the line cuts that the lateral and the vertical

Bragg peaks are observed in all cases. Three lateral Bragg peaks at  $Q_y = 0.5 \text{ nm}^{-1}$ ,  $0.97 \text{ nm}^{-1}$  and  $1.5 \text{ nm}^{-1}$  and three vertical Bragg peaks at  $Q_z=0.9 \text{ nm}^{-1}$ ,  $1.5 \text{ nm}^{-1}$  and  $2.1 \text{ nm}^{-1}$  are observed.

The lateral Bragg peaks are indexed assuming a hexagonal lattice with a lattice parameter  $a \approx 14.4 \text{ nm}$ . If the particles in-plane are arranged into a hexagonal structure, then in 3-D it forms an FCC structure of stacking of hexagonal layers, i.e. face-centered cubic arrangement oriented in its (111) direction. The inter-layer distance  $c \approx 9.5 \text{ nm}$  corresponds to the third of the space diagonal of a face-centered cubic arrangement of nanocubes. Only (10), (20) and (30) reflections observed, the (11) and the (21) peaks might be hidden as a shoulder of the (20) and the (30) reflections, respectively. After taking the instrument resolution into account, a Lorentzian profile is used to fit the first lateral Bragg peak at  $Q_y=0.5 \text{ nm}^{-1}$  which yields a structural coherence length of  $\zeta \approx 188 \pm 0.05 \text{ nm}$ .

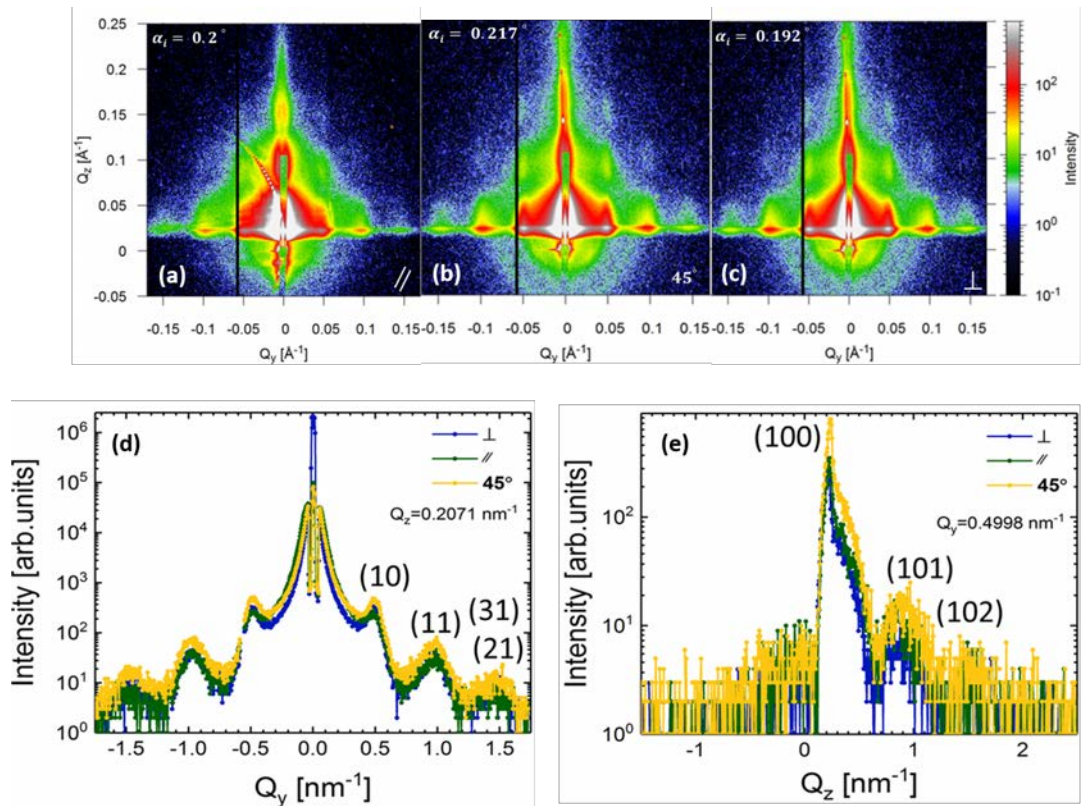


Figure 7.10.: The GISAXS patterns of the cubic iron oxide nanoparticle were deposited on a trench-patterned silicon substrate with different directions of the beam with respect to the lines. (a) as the beam almost parallel to the lines, (b) The azimuthal angle between the direct beam and the line is  $\Phi=45^\circ$  and (c) as the incoming beam perpendicular to the lines where the azimuthal angle  $\Phi=90^\circ$ . In the parallel case, the azimuthal angle  $\Phi$  of the sample was tilted by  $1.7^\circ$  to reduce the scattering intensity from the lines. The angle of the incident beam in all cases  $\alpha_i \approx 0.2^\circ$ . (d) A line cut from (a), (b) and (c) along  $Q_y$  at  $Q_z=0.2071 \text{ nm}^{-1}$ . (e) A line cut from (a), (b) and (c) along  $Q_z$  at  $Q_y=0.4998 \text{ nm}^{-1}$ . The lateral Bragg peaks were indexed according to a hexagonal lattice with  $a = 11.2 \text{ nm}$  while the vertical peaks were indexed according to FCC structure with  $c = 9.2 \text{ nm}$ .

### 7.3.3. Magnetic characterization

The atomic crystalline structure of magnetic materials defines its magnetic properties. But in nanoparticles case, the situation is different due to the finite sizes of the nanoparticles, its properties differ from the bulk. The nanoparticle becomes a single domain with reducing its size. The bulk form of iron oxides shows different phases with different crystal structures and different magnetic behavior as presented earlier in Sec. 7.1.

Iron oxide nanoparticles expected to be superparamagnetic (SPM) at room temperature, and might show other magnetic behavior if it forms a dense assembly of nanoparticles or long-range order arrays extending over large areas depending on the strength of magnetic dipolar interaction between the nanoparticles. Therefore, the template-assisted self-assembly of iron oxide nanoparticles was characterized by a superconducting quantum interference device (SQUID) magnetometry (3.3.1) to study the influence of the confinement in the magnetic properties of the nanoparticles.

#### 7.3.3.1. Macroscopic magnetization

The sample produced in Sec. 7.3.1 are cut into  $3 \times 3 \text{ mm}^2$  pieces using a diamond cutter, then it is fixed on a colorless drinking straw with an addition of another straw to prevent the sample moving during the measurement. The magnetic behavior of the sample i.e. the nanoparticle arrays inside the trenches studied from the temperature dependence magnetization curves under zero-field cooling (ZFC) and field cooling (FC) protocols. The ZFC-FC measurements were performed as the applied field parallel and perpendicular to the long axis of the trenches. Moreover, the measurements were performed at different magnetic fields (50 Oe and 100 Oe). During ZFC measurements the sample is cooled from  $T = 400 \text{ K}$  in a zero field to  $T = 5 \text{ K}$ . Then a small field of the order of  $\approx 50 \text{ Oe}$  and  $\approx 100 \text{ Oe}$  is applied and the magnetization of the sample is measured while sweeping the temperature to  $T = 400 \text{ K}$ . While during the FC measurements the magnetization is measured by sweeping the temperature from  $T = 400 \text{ K}$  to  $T = 5 \text{ K}$  in the same applied field. The magnetic behaviors of nanoparticle arrays inside the trenches obtained from the ZFC and FC curves with different field magnitudes and directions are shown in figure 7.11. Furthermore, the magnetic behavior of the iron oxide nanoparticles self-assembled in trenches studied from the field dependence magnetization curves (hysteresis curves (M-H)) at various temperatures. The hysteresis measurements were performed with an external magnetic field applied parallel as well as perpendicular to the long axis of the trenches. The results compared for different field directions at  $T = 300 \text{ K}$  and  $T = 5 \text{ K}$  are shown in figure 7.12.

Figure 7.11 shows the ZFC and FC curves measured at 50 Oe (left figures) and at 100 Oe (right figures) along and perpendicular to the trenches. The ZFC

curves are shown in green color while the FC curves shown in blue colors. In all cases under the same applied field, the magnetization value as the field parallel to the lines larger than the perpendicular case. This is because the alignment of the spins is more energetically favorable along the trenches than perpendicular. In all figures, the peak temperature ( $T_P$ ) determined by an arrow in the figures. Moreover, we observed that a larger magnetic field will increase the splitting temperature  $T_S$ , where the ZFC and FC curves splitting in both parallel and perpendicular measurements. While at the same magnetic field strength, the  $T_B$  is slightly smaller when field direction is perpendicular to the trenches compare to the situation when the direction is parallel to the trenches. This might be due to the fact that in the easy axis direction the effective relaxation time is smaller due to the favored superspin alignment.

Figure 7.11(a) shows M vs. T curves after ZFC and FC measured at 50 Oe where the magnetic field was applied perpendicular to the long axis of the trenches. The maximum of the ZFC magnetization curve at about  $T_P = 142$  K and the splitting between the ZFC and FC curves occurs at this temperature. The distinct bifurcation of the ZFC and FC plot around  $T_P = 142$  K clearly indicates that the  $T_P$  is the blocking temperature ( $T_B$ ). The ZFC magnetization increases as a function of temperature for a temperature range  $5 \text{ K} < T < 142 \text{ K}$ , indicating that there are blocked moments which start to contribute to the magnetization when the temperature is increased, while the FC magnetization in the same temperature region decreases as the temperature increases since the field induced aligned moments to start randomizing due to thermal energy. Beyond the blocking temperature, both the ZFC and FC curve coincide and the magnetization decreases as the temperature increases due to temperature-induced randomization of the moments. This behavior is typical of superparamagnetic nanoparticles.

Figure 7.11 (b) shows M vs. T curves after ZFC and FC measured at 100 Oe where the magnetic field was applied perpendicular to the long axis of the trenches. The maximum of the ZFC magnetization curve at about  $T_P = 145$  K and the splitting between the ZFC and FC curves occurs approximately at  $T = 185$  higher than the ZFC maximum temperature, which is a typical of the blocking process of an assembly of superparamagnetic nanoparticles and due to a broad distribution of peak temperatures for different sizes of nanoparticles. It is obvious that for the same field direction the ZFC and FC magnetization increased with increasing field. Almost the same features observed in figure 7.11 (a) are also seen here with an additional features in the FC curve. An obvious feature (black circle) at  $T \approx 122$  K can be found indicating the Verwey transition of the magnetite which is very close to the characteristic  $T_v$  of 120 K for magnetite as reported extensively [171, 172]. This is an indication that the sample contains a small amount of magnetite in addition to the ferrimagnetic maghemite.

Figure 7.11 (c) and (d) show  $M$  vs.  $T$  curves measured as the magnetic field was applied parallel to the long axis of the trenches at 50 Oe and at 100 Oe respectively. The maximum of the ZFC magnetization curves at about  $T_P = 151$  K. The splitting between the ZFC and FC curves occurs at  $T = 151$  K and at  $T = 285$  K for (c) and (d) respectively. The distinct bifurcation of the ZFC and FC plot in (c) around  $T_P = 151$  K clearly indicates that the  $T_P$  is the blocking temperature ( $T_B$ ). In both figures the ZFC magnetization increases as a function of temperature for a temperature range  $5 \text{ K} < T < 151$  K, while the FC magnetization in the same temperature region decreases as the temperature increases. Beyond the blocking temperature, both the ZFC and FC curve coincide and the magnetization decreases as the temperature increases due to temperature-induced randomization of the moments. This behavior is typical of superparamagnetic nanoparticles. Below  $T = 140$  K, the magnetization of the FC curve decreases which is possibly due to the dipolar interaction between nanoparticles.

Figure 7.12 shows the hysteresis curves measured as the field parallel and perpendicular to the long axis of the trenches at 300 K (left figure) and 5 K (right figure). We observed “no hysteresis” at 300 K for both directions and the M-H curve shows S-shaped behavior with saturation similar to a superparamagnetic behavior. Whereas at 5 K, an open loop can be observed for both orientation. This can be explained as the nanoparticle superspins are in a blocked superparamagnetic state. It is clear that the easy axis of magnetization is along the trenches as the saturation occurs at around 0.14 T for parallel orientation, whereas for perpendicular case the saturation observed around 0.35 T. Furthermore, the loops center at 5 K for both orientations is slightly shifted towards the negative field direction as shown in figure 7.12 (right), which is an indication of an exchange bias (EB) effect, which can be expected at the interface between antiferromagnetic wüstite and ferrimagnetic magnetite or maghemite. Moreover, the EB effect might occur due to the antiferromagnetic wüstite inside the nanoparticles below its Neél temperature at 198 K [173].

In the perpendicular case, the magnetization is slower to reach saturation than in the parallel case. The difference in magnetization can be calculated from the magnetic squareness, which is defined as the ratio of the remanent magnetization ( $M_r$ ) to the saturation magnetization ( $M_s$ ). The magnetic squareness is widely used for the evaluation of the magnetization reversal mode and of the magnetic anisotropy [174]. The magnetic squareness value will give only information about the change of anisotropy if we consider here no change in the reversal mode inside the nanoparticles.

At both temperatures, the remanent magnetization is significantly higher in the parallel direction than perpendicular direction. The saturation magnetization is almost the same for both directions. The magnetic squareness value in the parallel case is larger than perpendicular case due to the nanoparticles chain

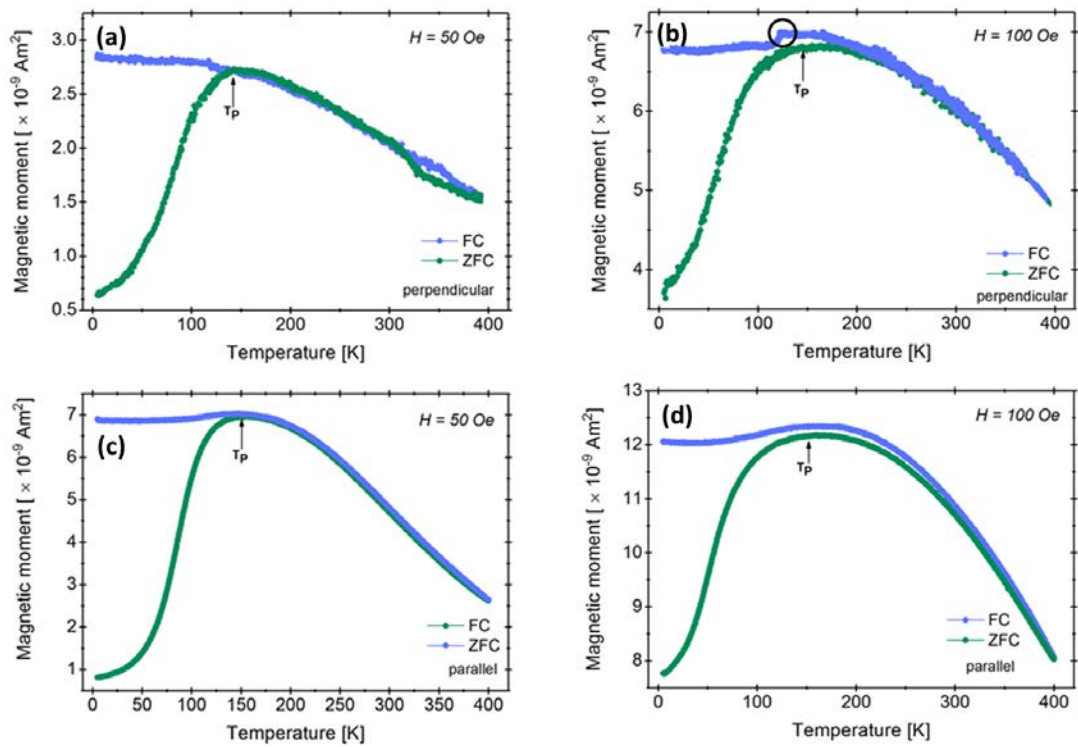


Figure 7.11.: M vs. T curves of the magnetic moment of nanoparticles self-assembled in trench-patterned silicon substrates after ZFC (green) and FC (blue) at two applied fields, i.e. 50 Oe (left) and 100 Oe (right). The magnetic field was applied perpendicular (a), (b) and parallel (c), (d) to the long axis of the trenches. The arrows indicate the peak temperature  $T_P$ , which was defined as the first zero value of the derivative of the ZFC curve.

induced shape anisotropy [170]. The shape anisotropy leads to an energy barrier in the spin reversal process as shown in figure 7.12 (top and bottom figures), a larger coercive field is needed to reverse the spins in the measurement when the magnetic field is parallel to the trenches.

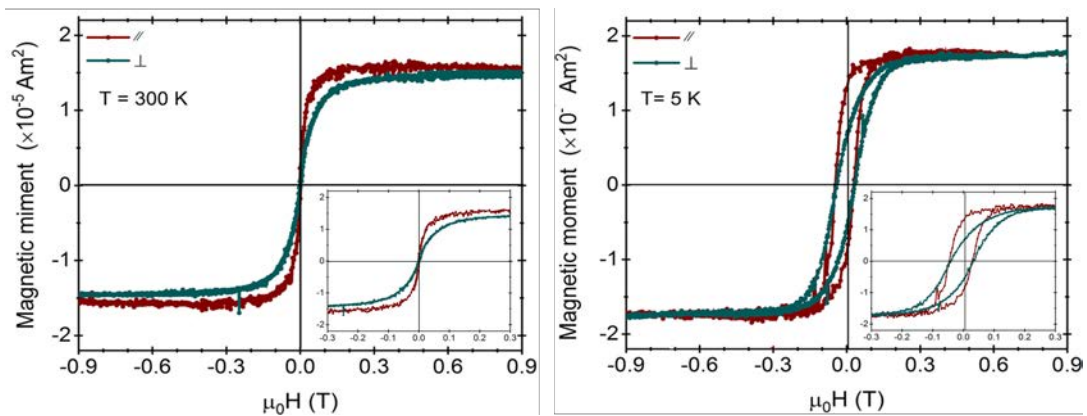


Figure 7.12.: Hysteresis loops for the cubic iron oxide nanoparticles on trench-patterned silicon substrate measured at 300 K (left) and at 5 K (right). The brown hysteresis loops in both figures were measured as the field parallel to the long axis of the trenches, the green ones were measured with the field perpendicular to the trenches.

## 7.4. Summary and outlook

The preceding chapter provides a full analysis of the preparation and characterization of self-assembled superball/cubic iron oxide nanoparticles with a size of  $\approx 14$  nm on trench-patterned silicon substrates, starting from single nanoparticle properties in dispersion, over the study on how to obtain long-range order using assisted self-assembly method.

Using TEM and SAXS, information about the size as well as the size distribution of the nanoparticles have been obtained. Furthermore, using SQUID magnetometry, the magnetic properties of the nanoparticles dispersion in addition to the magnetic moment per single-particle have been studied.

Moreover in this chapter, the iron oxide nanoparticles were also self-assembled on trench patterned silicon substrates, which is used as a template to guide or assists nanoparticle self-assembly. GISAXS measurements on cubic maghemite nanoparticles in grooves show a long coherence in both of the in-plane and out of the plane arrangement of the nanoparticles. Further, we observed from GISAXS there is no correlation between the structural arrangement of nanoparticles and the geometry of trench-patterned substrates. However, we find anisotropy in magnetic properties. Hysteresis loops on this system were measured with an external magnetic field applied parallel and perpendicular to the direction of the trenches. They show a large magnetic preferential direction along the trench, which is induced by magnetic shape anisotropy. Moreover, an EB effect is observed in the hysteresis loops at low temperatures. The magnetization of the FC curves at various fields decreases slightly at low temperatures possibly due to the existence of a small amount of wüstite or dipolar interaction between nanoparticles.

We have demonstrated that spatial confinement can be employed to induce nanoparticle assembly in the trenches. We have further shown that the cubic nanoparticles arrange on FCC structure oriented in its (111) direction. The confinement-induced assembly of anisotropic nanoparticles as shown in this chapter, might provide a promising route toward nanoscale devices with tunable anisotropic properties.

The nanoparticles did not form a single crystalline arrangement due to the structured silicon substrates geometry. The trench patterned substrates show two different depth profiles as shown in figure 4.14 (b). Furthermore, we note that the groove width  $W$  becomes wider with a sidewall angle in the bottom part of the confining channels.

Future improvements of this work: First, it could thus be to manufacture such grooves of sufficient depth and with a groove separation of  $W \approx 86$  nm and with a flat bottom. Second, we have focused on only one type of nanoparticles and patterned substrates, and it is probable that the degree of nanoparticle order could be improved by modifying the particle-wall interactions. Addition-

ally, understanding how particleparticle and particlewall attractions affect the nanoparticle order. Furthermore, the main focus will be on producing a single crystalline arrangement of cubic iron oxide nanoparticles using directed self-assembly method. Then the magnetic correlations between the superspins in the 3D order can be studied using grazing-incidence small-angle neutron scattering (GISANS). Followed by BornAgain simulation of the GISAXS and GISANS data of nanoparticle assembly in confinement.

## 8. Conclusion and Outlook

### 8.1. Summary

In summary, the thesis provides a complete determination of the structural and magnetic ordering of various nanostructures formed using different nanoparticles.

Several controlled self-assembly methods were developed to fabricate various nanoparticle-assembled structures with desired morphology and geometry. In each case, the individual nanoparticle structural and magnetic properties are determined from measurements of the particles in dispersion by means of small-angle scattering. It is then proceeded to study nanostructures where the discussed nanoparticles are used as building blocks to form nanostructures. Concretely studied are surface grating structures with different structure sizes, which were used as a template for assisted self-assembly of magnetic nanoparticles, long-range ordered monolayers of spherical silica nanoparticles in a two-dimensional hexagonal lattice, two-dimensional ordered arrays of cobalt ferrite nanodots and three-dimensional ordered layers of iron oxide nanocubes. The method for the preparation of the second and the fourth structures has been developed within the scope of this thesis.

The structure of the assembled nanoparticles is determined in each case using grazing-incidence scattering and reflectometry to quantify the in-plane and out-of-plane ordering of nanoparticle films, as well as by scanning electron microscopy. In the case of magnetic systems, the magnetic properties of the nanostructures from iron oxide and cobalt ferrite nanoparticles are studied by macroscopic magnetization measurements. Also, PNR measurements along with the fitting are successfully implemented to understand and highlight the magnetic depth profile of the two-dimensional arrays of cobalt ferrite nanoparticles.

The pre-patterned silicon substrates were investigated using GISAXS and analyzed by the direct analysis method. Using this method, the structural parameters can be obtained directly from the measurement data, without the selection of suitable form factors and structure factors for numerical simulations. However, this method restricts the analysis mainly to an evaluation of the structure factor and thus of the positions of scattering features. Therefore, only a limited set of dimensional parameters, namely, the grating periodicity, the groove width, the capping layer thickness, and the line-height can be accessed. The implementations of the direct analysis are based on the evaluation of scattering

features that are present in GISAXS intensity patterns along the semi-circular intersection of the Ewald sphere and the grating truncation rods (GTRs) of the grating. For large pitches, this is achieved by computing the discrete Fourier transform (DFT) of the profile and evaluating the power spectral density (PSD). But the non-uniformly spaced data and the reduced number of GTRs along the intersection required a different approach to that of DFT.

The second nanostructure system is produced using silica nanoparticles of mean diameter  $\approx 50$  nm and dispersed in toluene were self-assembled on silicon substrates. Here, we fabricate a simple, inexpensive approach to obtain highly ordered self- assembled monolayers of stearyl alcohol grafted silica over a large area on a Si substrate using an improved variant of the drop-casting method. The novelty behind our idea is the addition of stearyl alcohol to the NP dispersion from where the monolayers are formed. The stearyl alcohol results in monolayers with improved order, as confirmed with SEM for the local order and GISAXS for the long-range hexagonal order, where the data was reproduced by simulation within the Distorted Wave Born Approximation (DWBA). Additionally, a heat treatment step is added, to melt the stearyl alcohol in the monolayer. This leads to nearly perfectly ordered monolayers. This improved ordering is a result of giving the NPs more time to further self-assemble, which is then followed by solidifying the monolayer by simple cooling to room temperature, preventing the large volume change as obtained after evaporation of a solvent. The formation of the monolayer is significantly influenced by the concentration of the NPs and the stearyl alcohol, the volume of the drop as well as the time of the heat treatment. The optimal heat-treatment temperature to achieve large area SiO<sub>2</sub> monolayer was found to be 70 C° for 10 days.

The stearyl silica nanoparticles were also self-assembled on trench-patterned silicon substrates. GISAXS measurement reveals that the coherent structure of the nanoparticles along and perpendicular to the trench direction can be observed. However, in our study we deduced that the self-assembly on patterned substrates did not improve the ordering of the nanoparticles.

Characterization of two-dimensional arrays of ferromagnetic cobalt ferrite (COF) nanodots was also of interest in this thesis. The dot sizes and their local arrangement were studied with scanning electron microscopy (SEM) and atomic force microscopy (AFM). The long-range in-plane and out-of-plane ordering are revealed by x-ray reflectometry (XRR) and grazing incident small-angle X-ray scattering (GISAXS). The nanodots order into a hexagonal structure as proven by the previous techniques. The GISAXS image shows Bragg rods along  $Q_y$  which correspond to the in-plane hexagonal ordering. The peak positions match with a two-dimensional hexagonal lattice. Moreover, the measured pattern matches well with the simulated pattern using a hemispherical particle

with a height of  $\approx 10$  nm arranged in a two-dimensional hexagonal lattice with a lattice constant of 34 nm.

Macroscopic magnetic properties of cobalt ferrite nanoparticles have been studied using magnetometry. In-plane and out-of-plane field-dependent magnetization measurements confirm that the easy direction of the magnetization is in the plane. According to the behavior of ZFC/FC magnetization curves, in-plane direction, a blocking temperature higher than 400 K is observed, possibly due to the higher magnetocrystalline anisotropy energy. Also, a slight decrease in the FC magnetization at low temperatures obvious which is an indication of the magnetic interaction between nanoparticles.

The microscopic magnetic properties have been studied by polarized neutron reflectivity (PNR) to reveal the depth dependence of the magnetization profile. The in-plane PNR curves measured for up and down neutrons at saturation show a state with small magnetization, while at remanence they show a demagnetized state with zero net magnetization.

Part of this thesis focus on iron oxide nanocubes, self-assembled on pre-structured silicon substrate in order to reach high coherence of the lateral order. GISAXS measurements show a two-dimensional in-plane ordering of nanoparticles. Further, we observe from GISAXS there is no correlation between the structural arrangement of nanoparticles and the geometry of trench-patterned substrates. XRR measurement shows an oscillation which possibly comes from nanoparticle layers inside the grooves. The in-plane Bragg reflections can be indexed to a two-dimensional hexagonal lattice while the out-of-plane reflections are indexed to FCC structure oriented in its (111) direction.

An anisotropy in magnetic properties is observed. Hysteresis loops as the grooves are aligned along and perpendicular to the field direction show a large magnetic preferential direction along the trench, which is induced by magnetic shape anisotropy. Moreover, an EB effect is observed in the hysteresis loops at low temperatures. The magnetization of the FC curves at various fields decreases slightly at low temperatures possibly due to the dipolar interaction between nanoparticles.

Work on this project will be continued in the near future to get a three-dimensional single-crystalline arrangement of nanoparticle and then study the magnetostatic interaction between nanoparticles using polarized grazing incidence small angle neutron scattering (PGISANS).

### 8.2. Conclusion

Based on the results of nanoparticle assemblies presented in this thesis, several, general and specific concluding remarks are drawn:

### General Remarks

*First*, the nanoparticle self-assembly strategy shows its importance and impact, as it allows the fabrication of novel magnetic nanostructures using functional magnetic nanoparticles in a cost-effective and bottom-up manner.

*Second*, a variety of nanoparticle self-assembly methods can be developed either by applying external stimuli, by using guiding templates, or by combining with other advanced nanofabrication techniques. Therefore, the controllability of nanoparticle self-assembly can be greatly improved.

*Third*, nanoparticle-assembled structures with different geometry and morphology, ranging from monolayer to multilayer can be produced using self-assembly methods. Also, the nanoparticle arrangements can be further adjusted by changing a variety of parameters such as the nanoparticle shape, size, interparticle interaction, the topography of the substrate, or the external directing field.

*Fourth*, by fabricating highly ordered superstructures magnetic nanoparticles with well-defined configurations, high-density magnetic data storage media can be produced.

### Specific remarks

*First*, the dimensional parameters determined for the gratings by direct GISAXS data analysis can serve as reference values that must be reproduced by any other analysis methods such as numerical modeling. Thereby, the direct analysis provides a means to validate and compare other analysis methods in a general context, not just for grating structures.

*Second*, heat treatment in combination with a compatible additive with a melting point significantly below that of the particles can be a general method to improve the ordering between particles in monolayers as well as multilayers.

*Third*, by increasing the cobalt ferrite nanodots height, the magnetocrystalline anisotropy energy (KV) will be increased. This leads to a higher blocking temperature, which makes them a prominent candidate for memory storage applications. This might be general for other ferrimagnetic material.

*Fourth*, Spatial confinement (template-assisted self-assembly) is an appealing and promising approach for controlling the assembly of nanoparticles and for approaching highly ordered three-dimensional nanoparticles single-crystalline arrangements. The resulting structure can be controlled by the template (con-

finement) geometry, nanoparticles shape and size; better ordering is expected when the confining wall separation is commensurate with the particle size.

### **8.3. Future prospects**

#### **Grating lines**

Full modeling of the scattering intensities observed in the GISAXS data using the semi-kinematic and dynamic theories, mostly by using distorted wave Born approximation (DWBA) and Maxwell equations. This model will yield a larger set of structural parameters such as the sidewall angle, the corner-rounding at bottom of the lines, as well as the shape of the line cross-section. Furthermore, the modeling of the 2D GISAXS pattern might provide additional details on the origin of the diffuse line scattering.

After modeling the grating lines with suitable form factors, implementation of it into BornAgain software should be done for the comparisons of different methods of analysis and for the validation of the analysis results of the models against the nominal values of direct analysis.

#### **Long range order monolayer of silica nanoparticles**

The development of the monolayer preparation method for silica nanoparticles by the drop-casting method can be considered as a starting point. In the future, our developed method will be employed for various types of magnetic nanoparticles then the magnetic properties of the monolayers will be studied. Also, in the future, the obtained particle monolayer can be used as a template or a two-dimensional deposition mask for nanostructure fabrication as shown schematically in figure 8.1. In this case, the monolayer itself acts as a topographic pattern. Mainly, magnetic multilayers will be sputtered on these nanospheres then magnetic properties of the new system will be studied macroscopically using SQUID and microscopically using neutrons.

#### **Directed self-assembly of Iron Oxides nanoparticles on patterned substrates**

Produce three-dimensional single-crystalline arrangements of magnetic nanoparticles using a template-assisted self-assembly method. Then, the obtained structure will be characterized locally by atomic force and scanning electron microscopies and within the depth by small-angle x-ray scattering under grazing incidence. GISAXS measurements will be performed for structural analysis of nanoparticle arrays and to get insight into the in-plane and out-of-plane order-

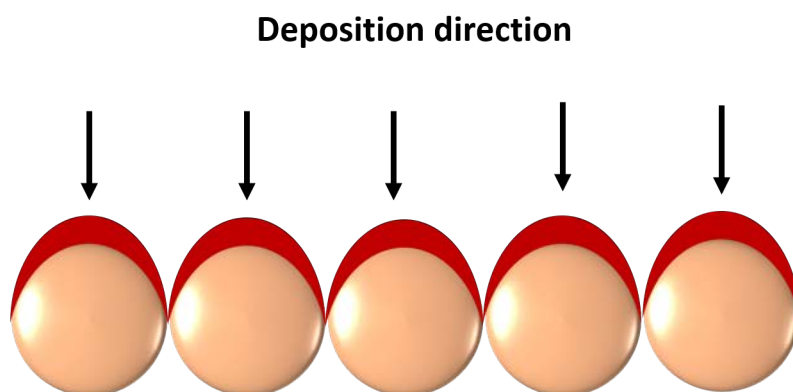


Figure 8.1.: Schematic picture of the film deposited onto nanospheres monolayer.

ing of magnetic nanoparticles on pre-structured silicon substrates. Macroscopic magnetization measurements on a SQUID magnetometer will be performed in order to get first insights on the collective magnetic behavior. The laterally- and depth-resolved investigation of the magnetic behavior will be performed by small-angle scattering of polarized neutrons under grazing incidence. Furthermore, simulation of GISAXS and POLGISANS data using Born Again software will be done.

# Appendices

# A. Derivations

## A.1. Green's function of free Schrödinger equation

let's assume the Green's operator of the full Hamiltonian ( $H$ ) is defined as

$$G = (E \pm i\epsilon - H)^{-1} \quad (\text{A.1})$$

Now, the Green's function of the free Hamiltonian ( $H_0$ ) is given as

$$G_0 = (E \pm i\epsilon - H_0)^{-1} \quad (\text{A.2})$$

The above Green's function operator fulfill the following equation in the position space

$$\left(\frac{\hbar^2}{2m}\Delta + E\right)G_0(\vec{r}, \vec{r}'|E) = \delta(\vec{r} - \vec{r}') \quad (\text{A.3})$$

Equ.A.3 can be represented straightforward in position space as in the following equation

$$G_0(\vec{r}, \vec{r}'|E) = \langle \vec{r} | \frac{1}{E \pm i\epsilon - H_0} | \vec{r}' \rangle \quad (\text{A.4})$$

The green function  $G_0(\vec{r}, \vec{r}'|E)$  describes the stationary radiation of a particle with energy  $E$ , that is generated at  $\vec{r}'$ , by a spherical wave outgoing from the target, i.e.  $G_0(\vec{r}, \vec{r}'|E)$  gives the amplitude of this wave at location  $r$  due to its generation by the source at  $\vec{r}'$ , under the condition that the wave is not further scattered during its propagation from  $\vec{r}'$  to  $r$ .

In the following derivation, the origin of the received spherical wave, either radiating from a source (retarded) or irradiating towards a source (advanced) will be shown, which depends on the sign of the small imaginary factor ( $\epsilon$ ) assumed in Eq.A.1.

The eigenfunctions of the momentum operator in position space will be used in order to obtain the representation of the Green function in Eq.A.3 in position space

$$\langle \vec{r} | \vec{k} \rangle = \frac{1}{\sqrt{2\pi^3}} e^{i\vec{k} \cdot \vec{r}} \quad (\text{A.5})$$

also, the free Hamiltonian is diagonal in momentum space. Inserting both into the matrix element (Equ.A.4) one obtains

$$G_0(\vec{r}, \vec{r}' | E) = \int d\vec{k} \int d\vec{k}' \langle \vec{r} | \vec{k} \rangle \langle \vec{k} | \frac{1}{E \pm i\epsilon - H_0} | \vec{k}' \rangle \langle \vec{k}' | \vec{r}' \rangle \quad (\text{A.6})$$

$$G_0(\vec{r}, \vec{r}' | E) = \frac{1}{2\pi^3} \int d\vec{k} e^{i\vec{k} \cdot \vec{r}} \frac{1}{E \pm i\epsilon - \frac{\hbar^2 k^2}{2m}} e^{-i\vec{k} \cdot \vec{r}'} \quad (\text{A.7})$$

Now, set  $\vec{x} = \vec{r} - \vec{r}'$ . The best way to solve above integral is using spherical coordinates where  $\theta$  is set to be the angle between  $\vec{k}$  and  $\vec{x}$ . Then one need only to solve

$$G_0(\vec{x} | E) = \frac{1}{(2\pi)^2} \int_0^\infty dk k^2 \int_0^\pi d\theta \sin(\theta) e^{ikx \cos(\theta)} \frac{1}{E \pm i\epsilon - \frac{\hbar^2 k^2}{2m}} \quad (\text{A.8})$$

The integral over  $\theta$  can be solved by substitution  $u = \cos(\theta)$  and one observes at this point already that the solution only depends on the magnitude of  $\vec{x}$

$$G_0(x | E) = -i \frac{2m}{x\hbar^2} \frac{1}{(2\pi)^2} \int_0^\infty dk \frac{k}{\frac{2mE}{\hbar^2} - k^2 \pm i\epsilon} (e^{ikx} - e^{-ikx}) \quad (\text{A.9})$$

The above integral can be simplified by substituting  $k \rightarrow -k$  in  $e^{-ikx}$

$$G_0(x | E) = -i \frac{2m}{x\hbar^2} \frac{1}{(2\pi)^2} \int_{-\infty}^\infty dk \frac{k}{\frac{2mE}{\hbar^2} - k^2 \pm i\epsilon} e^{ikx} \quad (\text{A.10})$$

The above integral vanishes for  $k \rightarrow \pm\infty$  and the integral can be written as a complex contour integral that is closed in the upper complex half plane, where it is further exponentially suppressed for positive complex numbers. Rewriting the denominator, using that  $\epsilon$  is an arbitrary small number

$$G_0(x|E) = i \frac{2m}{x\hbar^2} \frac{1}{(2\pi)^2} \oint dz \frac{z}{(z - \frac{\sqrt{2mE}}{\hbar} \pm i\epsilon)(z + \frac{\sqrt{2mE}}{\hbar} \pm i\epsilon)} e^{izx} \quad (\text{A.11})$$

The above integral contains two poles at  $z_1 = \frac{\sqrt{2mE}}{\hbar} \pm i\epsilon$  and  $z_2 = -(\frac{\sqrt{2mE}}{\hbar} \pm i\epsilon)$ . From this point it becomes clear that the sign of  $\epsilon$  determines which pole has to be taken. As the integral is closed in the upper complex plane, only the pole with a positive complex part has to be considered. In the case of the retarded Green's function that is  $z_1$  and for the advanced Green's function  $z_2$ .

Finally, applying the residue theorem, replacing  $x = |\vec{r} - \vec{r}'|$  and use the dispersion relation of the free Hamiltonian  $k = \sqrt{2mE}/\hbar$ , the two solutions for Eq.(A.3) are

$$G_0(\vec{r}, \vec{r}'|k) = -\frac{m}{2\pi\hbar^2} \frac{e^{ik|\vec{r}-\vec{r}'|}}{|\vec{r} - \vec{r}'|} \quad (\text{A.12})$$

$$G_0(\vec{r}, \vec{r}'|k) = -\frac{m}{2\pi\hbar^2} \frac{e^{-ik|\vec{r}-\vec{r}'|}}{|\vec{r} - \vec{r}'|} \quad (\text{A.13})$$

In scattering theory one is interested in waves that are radiating away from the target, therefore the retarded Green's function is the one that needs to be considered.

## A.2. Scattering theory for electromagnetic waves

The scattering theory valid for non-interacting and non-relativistic particles such as neutron is derived in the frame work of quantum mechanics as shown in Sec.2.3.1, but this work also focus heavily on X-ray scattering to study the structure of nanoparticles and their assemblies. Quantum electrodynamics gives the correct description of scattering for photons. However, the propagation of X-ray photons is well described by classical electrodynamics for all cases that are relevant in this work. In this appendix will be shown that classical electrodynamics leads to the same type of differential equation for the description of the propagation of X-ray photons, as the Schrödinger equation used for neutrons. In order to describe the general propagation of photons, the starting point is Maxwell's macroscopic equations [175].

$$\vec{\nabla} \times \vec{E} + \partial_t \vec{B} = 0 \quad (\text{A.14})$$

$$\vec{\nabla} \cdot \vec{B} = 0 \quad (\text{A.15})$$

$$\vec{\nabla} \cdot \vec{D} = \rho \quad (\text{A.16})$$

$$\vec{\nabla} \times \vec{H} - \partial_t \vec{D} = \vec{j} \quad (\text{A.17})$$

Where  $\rho$  and  $\vec{j}$  are the free charge and the current densities, respectively.  $\vec{E}$  and  $\vec{B}$  are the electric and the magnetic field induction, respectively.  $\vec{D}$  is the electric displacement field and  $\vec{H}$  is the magnetisation field.

The material equations are given as

$$\vec{D} = \epsilon_0 \vec{E} + \vec{P} \quad (\text{A.18})$$

$$\vec{B} = \mu_0 (\vec{H} + \vec{M}) \quad (\text{A.19})$$

Where  $\mu_0 = 4\pi \cdot 10^{-7} \text{NA}^{-2}$ ,  $\vec{P}$  is the polarization and  $\vec{M}$  is the magnetization describes macroscopically all the microscopic dipoles and ring currents within a material.

$\epsilon_0$  and  $\mu_0$  related to the light speed via the following relation

$$c = \frac{1}{\sqrt{\mu_0 \epsilon_0}} \quad (\text{A.20})$$

Generally,  $\vec{P}$  and  $\vec{M}$  are expressed in relation to  $\vec{E}$  and  $\vec{H}$

$$\vec{P} = \epsilon_0 \chi_e \vec{E} \quad (\text{A.21})$$

$$\vec{M} = \chi_m \vec{H} \quad (\text{A.22})$$

where  $\chi_e$  and  $\chi_m$  are the electric and magnetic susceptibilities tensors, respectively. Both are in general tensors of 2nd-order. Here, we assume that polarization and magnetization of the materials respond linearly and isotropic to the field. With

$$\epsilon_r = 1 + \chi_e \tag{A.23}$$

$$\mu_r = 1 + \chi_m \tag{A.24}$$

The material refractive index is defined as

$$n = \sqrt{\epsilon_r \mu_r} \tag{A.25}$$

The phase velocity of light inside a material is given by

$$c_p = \frac{1}{\sqrt{\epsilon_0 \mu_0 \epsilon_r \mu_r}} = \frac{c}{n} \tag{A.26}$$

substitute the previous definitions into Maxwell's equation

$$\vec{\nabla} \times \vec{E} + \partial_t \vec{B} = 0 \tag{A.27}$$

$$\vec{\nabla} \cdot \vec{B} = 0 \tag{A.28}$$

$$\epsilon_0 \epsilon_r \vec{\nabla} \cdot \vec{E} = \rho \tag{A.29}$$

$$\vec{\nabla} \times \vec{B} - \frac{1}{c_p^2} \partial_t \vec{E} = \mu_0 \mu_r \vec{j} \tag{A.30}$$

taking the curl on both sides of the first Maxwell's equation, and inserting the other equations

$$\vec{\nabla} \times \vec{\nabla} \times \vec{E} + \frac{1}{c_p^2} \partial_t^2 \vec{E} = -\mu_0 \mu_r \partial_t \vec{j} \quad (\text{A.31})$$

which finally transform with the general vector identity

$$\vec{\nabla} \times \vec{\nabla} \times \vec{A} = \vec{\nabla}(\vec{\nabla} \cdot \vec{A}) - \Delta \vec{A} \quad (\text{A.32})$$

The general wave equation for  $\vec{E}$  is given as

$$\Delta \vec{E} - \frac{1}{c_p^2} \partial_t^2 \vec{E} = \mu_0 \mu_r \partial_t \vec{j} + \frac{1}{\epsilon_0 \epsilon_r} \vec{\nabla} \rho \quad (\text{A.33})$$

The above differential equation, which is derived from Maxwell's equation describes, in general, the propagation of electromagnetic waves inside the material.

The time dependence of  $\vec{E}$  can be given as

$$\vec{E}(\vec{r}, t) = \vec{E}(\vec{r}) e^{-i\omega t} \quad (\text{A.34})$$

and the dispersion relation

$$\omega = ck \quad (\text{A.35})$$

then the wave equation (Eq.A.33) can be rewritten as

$$(\Delta + n^2 k^2) \vec{E} = \frac{1}{\epsilon_0 \epsilon_r} \left( \frac{n^2}{c^2} \partial_t \vec{j} + \vec{\nabla} \rho \right) \quad (\text{A.36})$$

As can be seen from the above equation which is known as inhomogeneous Helmholtz-equation, that the definition of the phase velocity was used on the right-hand side and it's interesting to mention here the closeness of this equation to the time-independent Schrödinger equation, which given with  $k^2 = \frac{2mE}{\hbar^2}$  in positional space as

$$(\Delta + k^2) \psi = \frac{2m}{\hbar^2} V \psi \quad (\text{A.37})$$

At this point it is nicely clear how the classical electrodynamics and quantum mechanics result in a similar description of different problems.

For a further explanation about the X-ray scattering process and how the X-ray photons interacts with matter, it is necessary to discuss the electric field generated by a single electron cloud oscillating in phase with an incoming field, which is given as

$$\vec{E}_i(\vec{r}, t) = \hat{e}_i E^0 e^{i(\vec{k}\cdot\vec{r}-\omega t)} \quad (\text{A.38})$$

Where  $\hat{e}_i$  is the unit vector defines the polarization direction of the electric field perpendicular to  $\vec{k}$ .

In this model, no free static charge is assumed, only a single moving cloud with density distribution of  $\rho_e(\vec{r})$  that oscillates with  $v(t)$

$$\rho(\vec{r}, t) = 0 \quad (\text{A.39})$$

$$\vec{j}(\vec{r}, t) = -e\rho_e(\vec{r})\vec{v}(t) \quad (\text{A.40})$$

Now, use Newton's law  $\vec{F} = m\vec{a}$  for a simplified model of an accelerated electron due to the electric field  $\vec{F} = q\vec{E}$  to write  $\partial_t \vec{j}$  in the wave equation (Eq.A.33) with

$$\partial_t \vec{v} = \vec{a} = -\frac{e}{m} \hat{e}_i E^0 e^{i(\vec{k}\cdot\vec{r}-\omega t)} \quad (\text{A.41})$$

Where  $\vec{a}$  is the acceleration, e and m are charge and the mass of the electron, respectively.

Then the Helmholtz equation for the electric field (Eq.A.36) can be written as

$$(\Delta + n^2 k^2) \vec{E} = \frac{n^2 e^2}{\epsilon_0 \epsilon_r c^2} \rho_e \hat{e}_i E^0 e^{i\vec{k}\cdot\vec{r}} \quad (\text{A.42})$$

As for x-rays n is close to 1,  $n^2$  can be approximated to 1.

In order to solve the above differential equation, the Green's function like in Sec.A.1 will be considered, which fulfils the relation

$$(\Delta + k^2)G(\vec{r}, \vec{r}') = \delta(\vec{r} - \vec{r}') \quad (\text{A.43})$$

The Green's function  $G(\vec{r}, \vec{r}')$  is given by [175]

$$G^\pm(\vec{r}, \vec{r}') = -\frac{1}{4\pi} \frac{e^{\pm ik|\vec{r} - \vec{r}'|}}{|\vec{r} - \vec{r}'|} \quad (\text{A.44})$$

Where  $G^+(\vec{r}, \vec{r}')$  for the outgoing spherical wave and  $G^-(\vec{r}, \vec{r}')$  for the inward going wave. It is necessary to mention again that in scattering only the outgoing solution is interesting to describe the radiation.

With the above Green's function the inhomogeneous Helmholtz equation (Eq.A.36) can be solved straight forward as a superposition of the homogeneous solution and the outgoing solution

$$\vec{E}(\vec{r}, t) = \vec{E}_i(\vec{r}, t) + \hat{e}_i \frac{e^2}{4\pi\epsilon_0 mc^2} E^0 \int dV' \frac{e^{ik|\vec{r} - \vec{r}'|}}{|\vec{r} - \vec{r}'|} \rho_e(\vec{r}') e^{i\vec{k} \cdot \vec{r}} \quad (\text{A.45})$$

Approximate  $|\vec{r} - \vec{r}'|$  and  $|\vec{r} - \vec{r}'|^{-1}$  as has been done in Sec. 2.3.1 and use the definition of the classical electron radius

$$r_e = \frac{e^2}{4\pi\epsilon_0 mc^2} \approx 2.8 \text{ fm} \quad (\text{A.46})$$

Then the electric field can be written as

$$\vec{E}(\vec{r}, t) = \vec{E}_i(\vec{r}, t) + \hat{e}_i E^0 \frac{e^{ikr}}{r} r_e \int dV' e^{-i\vec{q} \cdot \vec{r}'} \rho_e(\vec{r}') \quad (\text{A.47})$$

where the Fourier transform of the electron density (integrated part) is identified as the atomic form factor ( $f_a(\vec{q})$ ). Here, the scattering solution is identified as an integral of spherical waves generated at every point in space proportional to the electron density and proportional to the incoming wave which is equivalent to the case of the neutron scattering.

The differential cross-section is defined as

$$\frac{d\sigma}{d\Omega} = |\hat{e}_i \cdot \hat{e}_f|^2 r_e^2 |f_a(\vec{q})|^2 \quad (\text{A.48})$$

The above equation is known as Thomson scattering and it includes an additional polarization factor  $|\hat{e}_i \cdot \hat{e}_f|^2$ , where  $\hat{e}_f$  is the detection direction, where the experiment geometry and the source determine the polarization factor.

## **B. Preparation parameters of grating lines by Eulitha company**

### **Lithographie oxidmaske:**

- resist coating (WB 5) UV6
- in Dehydrieren at 413K for 90s
- cool down 60s
- UV6-06: 4000rpm (Prg4)
- relax resist for 60s
- soft bake at 413K for 60s
- Exposure Mask Aligner 3 (SUSS MA6)
- Mask Wash 5 in 0.2mJ/cm<sup>2</sup>

### **Development:**

- Post exposure bake: 413K for 90s
- immerse MF 24A for 60s

### **RIE oxide hard mask:**

- RIE 4: Ar/CHF<sub>3</sub> Oxid etch, endpoint by interferometer
- Resist stripping: DMSO/sylopentanone 15 min, Acetone 15 min, IPA 60s and DI 30s.

### **Dicing:**

- Protection resist: in dehydrieren 413K for 90s
- cool down 60s -AZ5214: 4000rpm (Prg 4)
- relax resist 60s
- soft bake at 384K for 60s
- peel of foil, remove resist: Ac+IPA+DI

## C. The EBL protocol and the preparation parameters of grating lines by HNF

Thermal oxidation 20-50nm  $SiO_2$

Spin-coating (4000rpm (prg 4)) of protection resist (AZ5214) on N-Si (110) silicon substrate:

- 90s 140°C Dehydration
- 60s cool down
- 60s relaxing
- 60s 110°C Soft bake

**Dicing:**

- 20mm\*20mm pieces

**Remove protective resist: Ac + IPA + DI**

Spin-coating (2000rpm) of E-beam resist (CSAR) on 20mm\*20mm silicon substrate ( $\Rightarrow$  140 nm):

- 90s 140°C Dehydration
- 60s cool down
- 60s relax resist
- 60s 110°C Soft Bake

**Exposure VISTEC EBPG 5000+**

- Dose test: 50 $\mu$ C to 250 $\mu$ C; 100 $\mu$ m\*100 $\mu$ m fields with lines and spaces (30nm, 50nm, 70nm).

**Development:**

- AR 600-546 developer for 60 s and in Isopropyl alcohol (IPA) for 30 s and in Deionized water (DI) for 30 s.

**RIE Oxid hard mask:**

- etching by Ar/ $CHF_3$  oxide

## D. Absolute calibration of SAXS measurements at GALAXI

The main aim of the absolute calibration of SAXS data:

- (i) To merge data obtained from two different detector distances to a single data set.
- (ii) To obtain the nanoparticles concentration in the solvent.

**Transmitted intensity at one detector channel at a given Q is:**

$$I(Q) = I_0 \Delta\Omega A D T \frac{d\Sigma}{d\Omega}(Q) \quad (\text{D.1})$$

Where  $I_0$  is the incoming flux,  $\Delta\Omega$  is the solid angle covered by the detector channel,  $A$  is the irradiated area,  $D$  is the thickness,  $T$  is the transmission and  $\frac{d\Sigma}{d\Omega}(Q)$  is the differential scattering cross section.

The solid angle can be found from the following relation:

$$\Delta\Omega = \frac{V}{L_{SD}^2} \quad (\text{D.2})$$

Where  $V$  is the size of the detecting channel and  $L_{SD}$  is the sample-to-detector distance.

**Sample transmitted intensity:**

$$I_{sample}(Q) = I_{sample+EC}(Q) - T_{sample} I_{EC}(Q) \quad (\text{D.3})$$

Where  $I_{sample+EC}(Q)$  is the measured intensity,  $T_{sample}$  is the sample transmission and  $I_{EC}(Q)$  is the empty cell transmission.

The sample transmission  $T_{sample}$  can be calculated from the following relation:

$$T_{sample} = \frac{T_{sample+EC}}{T_{EC}} \quad (\text{D.4})$$

In order to get the nanoparticles concentration in the solvent, the nanoparticle in the solvent and the solvent alone have to be measured and calibrated following the previous procedure. Therefore, the differential scattering cross section of the nanoparticle is given as:

$$\left(\frac{d\Sigma}{d\Omega}\right)_{NP} = \left(\frac{d\Sigma}{d\Omega}\right)_{NP+solvent} - (1 - C_{vol})\left(\frac{d\Sigma}{d\Omega}\right)_{solvent} \quad (D.5)$$

Where  $C_{vol}$  is the volume concentration of the particles in the solvent.

## E. Form Factors

### E.1. Spherical form factor

Typically spherical nanoparticles have a uniform scattering length density. For spherical NP with a core radius  $R$  the 1D scattering intensity is calculated in the following way:

$$I = \frac{scale}{V_{sphere}} \left[ 3V_{sphere}(\Delta\rho) \cdot \frac{\sin(qR) - qR \cos(qR)}{(qR)^3} \right]^2 + background \quad (E.1)$$

where  $scale$  is a volume fraction,  $V_{sphere}$  is the volume of the scatterer, NP volume,  $R$  is the radius of the sphere,  $background$  is the background level and  $\Delta\rho$  is the difference between the scattering length densities (SLDs) of the scatterer and the solvent.

Then the spherical form factor is given as:

$$F_{sphere}(q) = \begin{cases} 3\Delta\rho V_{sphere} \frac{\sin(qR) - qR \cos(qR)}{(qR)^3}, & q \neq 0 \\ \Delta\rho V_{sphere}, & q = 0 \end{cases} \quad (E.2)$$

### E.2. Spherical Core-Shell form factor

Usually, the nanoparticles are surrounded by surfactants like oleic acid. Therefore, the particles, in this case, can be assumed as two parts, the inner part known as "core" and the outer part known as "shell". For a spherical particle with radius  $R$  surrounded with an oleic acid with thickness  $a$  shown in Figure E.1, the best model explains the particles known as the "spherical core-shell" model which combines the contribution from both the sphere and the shell.

The scattering length density of core-shell particles can be given in spherical coordinates as:

$$\rho(\vec{r}) = \begin{cases} \rho_{core}, & 0 < r < R, \\ \rho_{shell}, & R < r < R + a, \\ \rho_s, & r > R + a \end{cases} \quad (E.3)$$

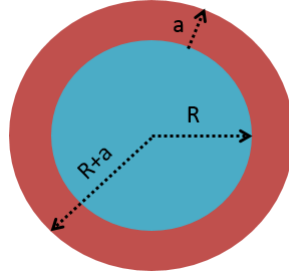


Figure E.1.: Schematic representation of core shell particles.

The form factor of a monodisperse spherical particle with a core-shell structure is described in the following equation.

$$F(\vec{q}) = \frac{3}{V_s} \left[ V_c(\rho_c - \rho_s) \frac{\sin(\vec{q}R) - \vec{q}R \cos(\vec{q}R)}{(\vec{q}R)^3} + V_s(\rho_s - \rho_{solv}) \frac{\sin(\vec{q}r_{Rs}) - \vec{q}r_{Rs} \cos(\vec{q}r_{Rs})}{(qr_{Rs})^3} \right] \quad (E.4)$$

Where  $V_s$  is the volume of the whole particles (core with shell),  $V_c$  is the core volume,  $r_{Rs}$  = core radius (R) + shell thickness (a), R is the core radius,  $\rho_c$ ,  $\rho_s$  and  $\rho_{solvent}$  are the scattering length density of the core, shell and the solvent respectively.

The core shell form factor can be assumed as a summation of two spheres form factors

$$F(q) = F_{sphere}(\vec{q}; R, \rho_c, \rho_s) + F_{sphere}(\vec{q}; R + a, \rho_s, \rho_{Rs}) \quad (E.5)$$

Where  $\rho_{Rs} = \rho_c - \rho_s$ , the difference between scattering length density of the core and the shell known as "contrast".

### E.3. Cubic form factor

Iron oxide nanocubes were used to study the influence of a regular structure in the assembly of the nanoparticles. For a cube of edge-length  $2R$ , the volume is

$$V = (2R)^3$$

The form factor amplitude of oriented cubes in Cartesian coordinates given as:

$$F_{cube}(\vec{q}) = \int_V e^{i\vec{q}\cdot\vec{r}} d\vec{r} \quad (\text{E.6})$$

Where  $\vec{q}$  in Cartesian coordinates given as  $(q_x, q_y, q_z)$ ,  $\vec{r}=(x, y, z)$  and  $\vec{q}\cdot\vec{r}=q_x x+q_y y+q_z z$ , therefore, the form factor amplitude becomes

$$F_{cube}(\vec{q}) = \int_{-R}^R e^{iq_x x} dx \int_{-R}^R e^{iq_y y} dy \int_{-R}^R e^{iq_z z} dz \quad (\text{E.7})$$

$$= V_{cube} \text{sinc}(q_x R) \text{sinc}(q_y R) \text{sinc}(q_z R) \quad (\text{E.8})$$

## F. 2D Ordered Arrays of Ferrimagnetic Cobalt Ferrite Nanodots

### F.1. Magnetic moment per nanoparticle in Bohr magneton ( $\mu_B$ / NP)

Here, full description of how to calculate the magnetic moment / nanoparticles is given. The calculation has been performed for the two-dimensional arrays of COF nanodots in Ch. 6.

Our system consists of hemispherical nanoparticles with a diameter of 23 nm and a height of 10 nm. These nanoparticles arranged into a hexagonal lattice with lattice constant 34 nm.

First we find the area of a regular hexagon by splitting it into six equilateral triangles,

$$A_{hexagon} = \frac{3\sqrt{3}}{2}a^2 \quad (F.1)$$

Where  $a$  is the lattice constant.

Each hexagon as shown in figure F.1 contains two full particles (i.e. 6 particles with a third of each inside the hexagon) and one full particle at the middle, then, the area of the hexagon corresponds to three particles,

$$6 \times \frac{1}{3} \left( \pi \left( \frac{d}{2} \right)^2 \right) + \pi \left( \frac{d}{2} \right)^2 = \frac{3}{4} \pi d^2 \quad (F.2)$$

Where  $d$  is the particle diameter.

Second, the number of particles on the substrate,

$$N_{NP} = \frac{A_{substrate}}{A_{3-particles}} = \frac{3 \times 3mm^2}{\frac{3}{4}\pi d^2} = 7.2243 \times 10^9 \quad (F.3)$$

Third, divide the magnetic moment (emu) value by the number of the particles. Fourth, to convert from emu / NP to  $\mu_B$  / NP,

$$1\text{emu}/NP = 1.0783 \times 10^{11} \mu_B/NP \quad (\text{F.4})$$

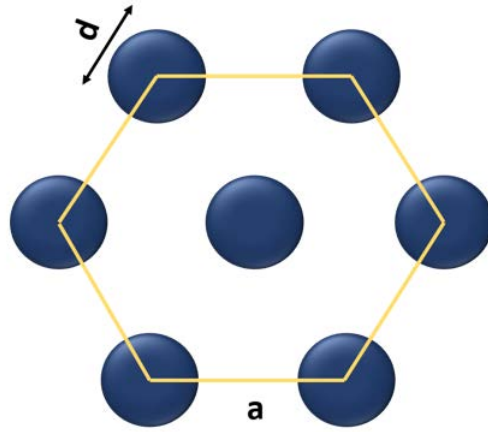


Figure F.1.: Schematic representation of a hexagon.

## F.2. Magnetization curves

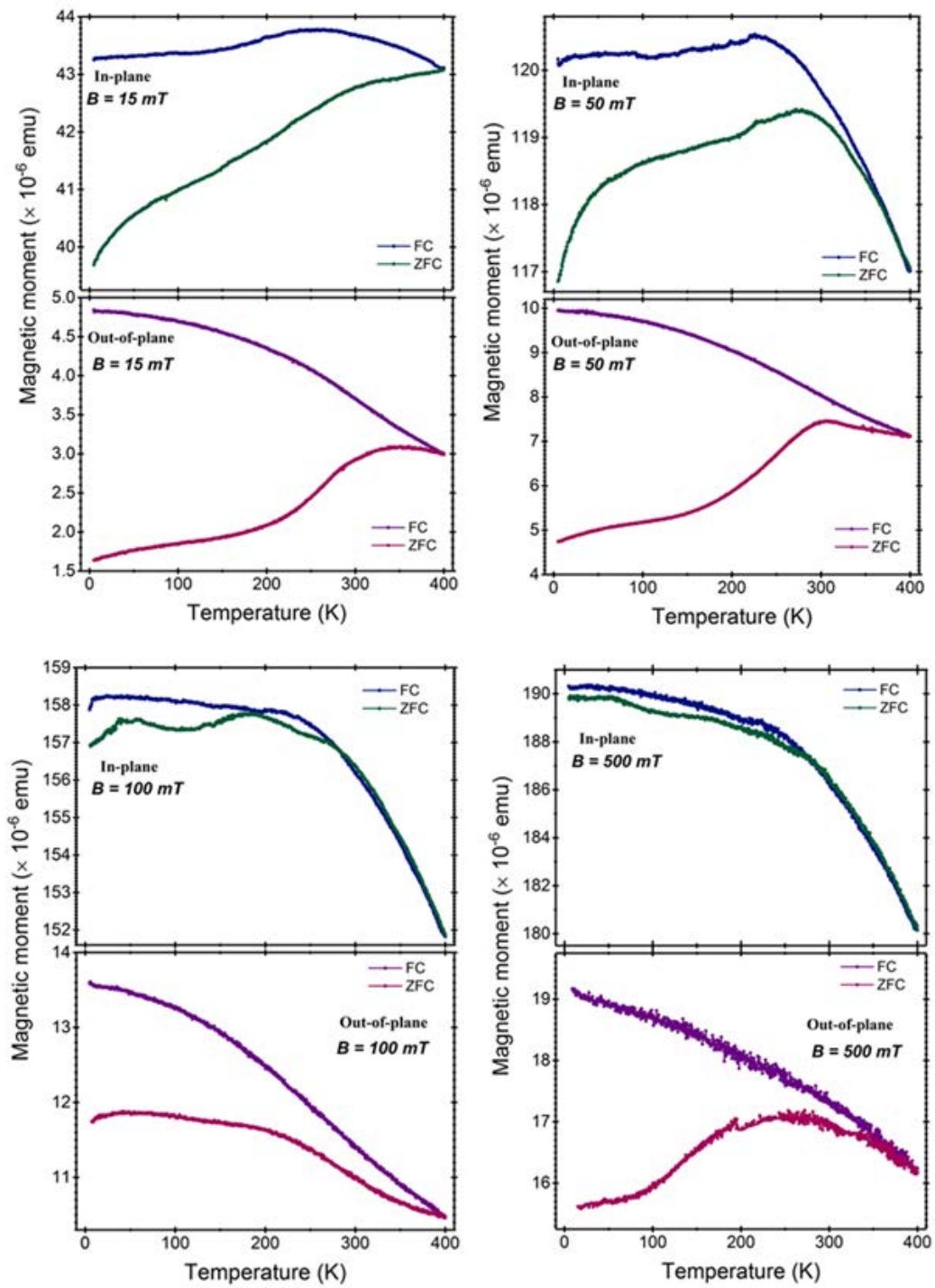


Figure F.2.: In-plane and out-of-plane temperature-dependent magnetization of the ordered  $\text{CoFe}_2\text{O}_4$  NP monolayers measured at various magnetic fields.

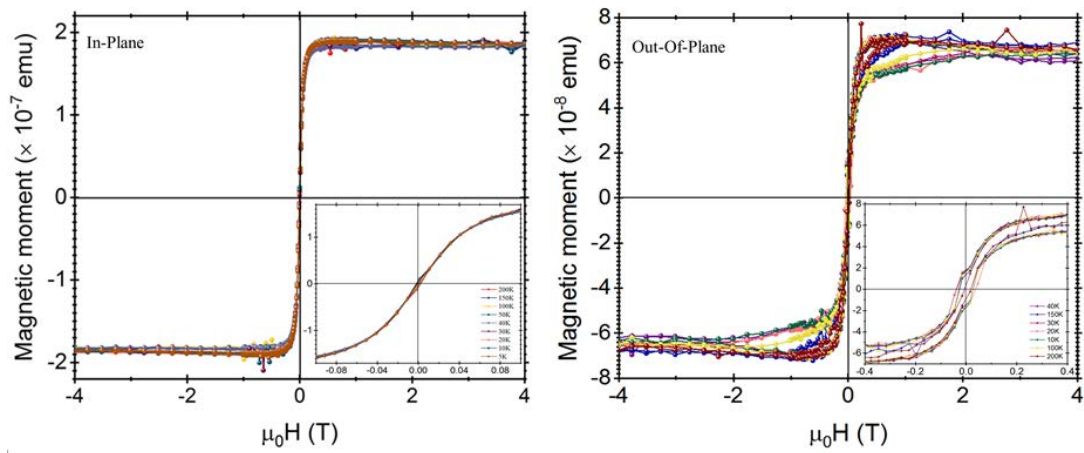


Figure F.3.: In-plane and out-of-plane hysteresis loops of the ordered  $\text{CoFe}_2\text{O}_4$  NP monolayers measured at various temperature. The downright insets is an expanded low-field curve.

### F.3. Neutron reflectometry

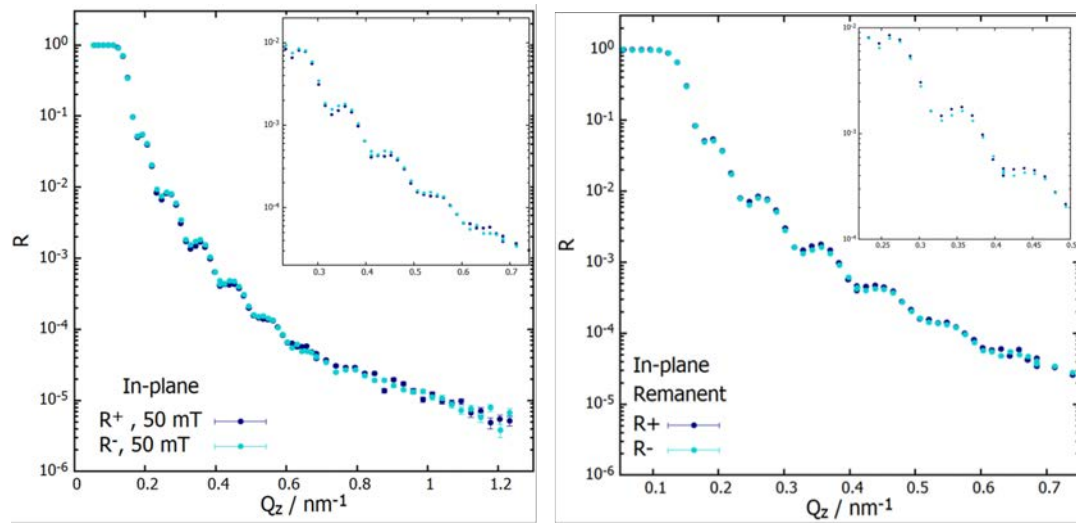


Figure F.4.: PNR measurements from COF nanodots onto a silicon substrate measured at 300 K with an applied In-plane field, (upper left) half polarized NR at 50 mT, (upper right) half polarized NR at remnant field.

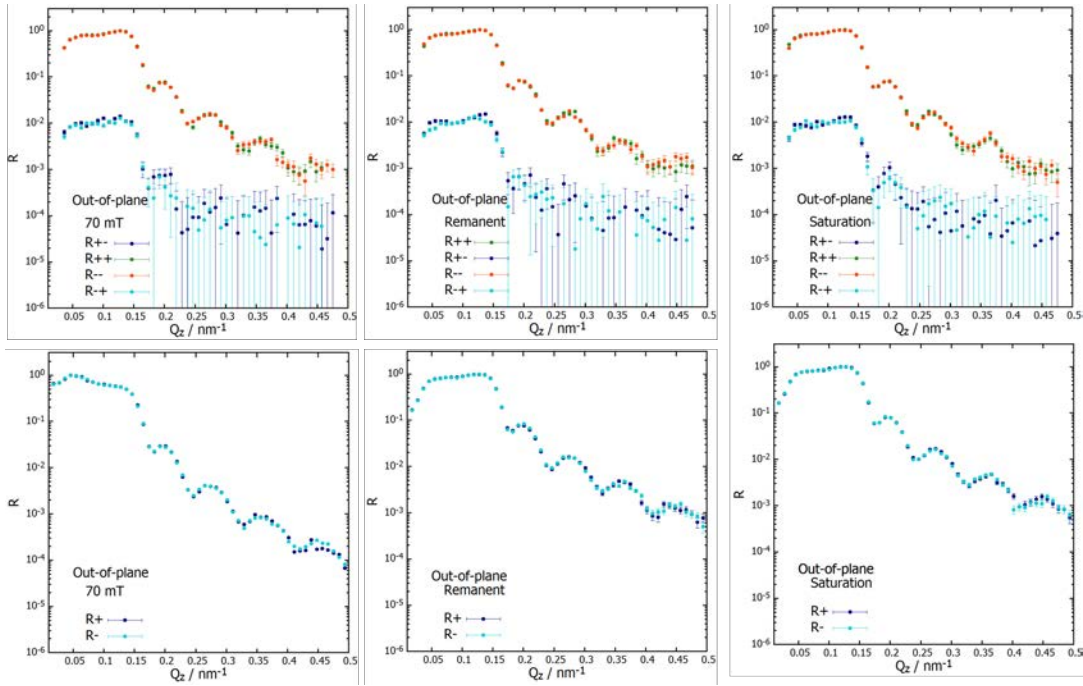


Figure F.5.: PNR measurements from COF nanodots onto a silicon substrate measured at 300 K with an applied Out-of-plane field. The upper plots show a full polarized NR measured at 70 mT, remnant and saturation, respectively. The bottom plots show a half polarized NR measured at 70 mT, remnant and saturation, respectively.

# Glossary

## Abbreviations

<b>DWBA</b>	distorted wave Born
<b>FC</b>	field cooled
<b>ZFC</b>	zero-field cooled
<b>fcc</b>	face-centered cubic
<b>hcp</b>	hexagonal close-packed
<b>1D</b>	One dimensional
<b>2D</b>	Two dimensional
<b>3D</b>	Three dimensional
<b>AF</b>	AntiFerromagnetic
<b>EB</b>	Exchange Bias
<b>FiM</b>	Ferrimagnetic
<b>mSLD</b>	magnetic Scattering Length Density
<b>nSLD</b>	nuclear Scattering Length Density
<b>NP</b>	Nanoparticle
<b>RSO</b>	Reciprocating Sample Option

## Experimental Methods

<b>GISANS</b>	Grazing-Incidence Small-Angle Neutron Scattering
<b>GISAXS</b>	Grazing-Incidence Small-Angle X-ray Scattering
<b>NR</b>	Neutron Reflectometry
<b>PNR</b>	Polarized Neutron Reflectometry
<b>SAXS</b>	Small-Angle X-ray Scattering
<b>SEM</b>	Scanning Electron Microscopy
<b>TEM</b>	Transmission Electron Microscopy
<b>AFM</b>	Atomic Force Microscopy
<b>MPMS</b>	Magnetic Property Measurement System
<b>XRR</b>	X-ray Reflectometry

## Instruments

<b>GALAXI</b>	Gallium anode low-angle x-ray instrument ((GI)SAXS/XRR)
---------------	---

instrument at the Forschungszentrum Jülich)

**MARIA** Magnetic reflectometer with high incident angle (neutron reflectometer at MLZ)

**SQUID** Superconducting Quantum Interference Device

## Magnetic Units Conversion to SI

**emu** for magnetic moments in the cgs system,  $1\text{emu} = 10^{-3} \text{Am}^2$

$\frac{\text{emu}}{\text{mL}}$  magnetization scaled to material volume,  $1\frac{\text{emu}}{\text{mL}} = \frac{\text{kA}}{\text{m}}$

## Scientific Facilities

**MLZ** Heinz Maier-Leibnitz Zentrum facility for neutron research in Garching, Germany

## Symbols

$a$	lattice constant
$\mathbf{a}_{p-p}$	interparticle distance
$\mathbf{A}$	area
$\alpha_i$	incident angle
$\vec{B}, \mu_0\vec{H}$	magnetic field, $\vec{B} = \mu_0(\vec{H} + \vec{M})$
$\mathbf{d}$	sample thickness
$\mathbf{E}$	energy
$\vec{k}$	wavevector
$k_B$	Boltzman constant
$\mathbf{K}$	magnetocrystalline anisotropy density
$L_{SDD}$	sample-to-detector distance
$\lambda$	wavelength
$\vec{M}$	Magnetization of a material
$\vec{\mu}$	magnetic moment
$\mathbf{N}$	number of particles
$\mathbf{n}$	number density
$\theta$	scattering angle
$\mathbf{p}(\mathbf{Q})$	form factor
$\vec{q}$	scattering vector

<b>r, R</b>	reflection magnitude, reflectivity
$\rho$	scattering length density
<b>S</b>	structure factor
<b>T</b>	temperature
<b>V</b>	volume

# Bibliography

- [1] Bharat Bhushan, ed. *Springer Handbook of Nanotechnology*. Springer Handbooks. Berlin, Heidelberg: Springer Berlin Heidelberg, 2010. ISBN: 978-3-642-02524-2. DOI: 10.1007/978-3-642-02525-9. URL: <http://link.springer.com/10.1007/978-3-642-02525-9>.
- [2] Vladimir Dyakonov Christoph Brabec , Ullrich Scherf, ed. *Organic Photovoltaics: Materials, Device Physics, and Manufacturing Technologies*. 2nd. 2016, p. 642. ISBN: 978-3-527-33225-0.
- [3] Eugenii Katz and Itamar Willner. “Integrated Nanoparticle-Biomolecule Hybrid Systems: Synthesis, Properties, and Applications”. In: *Angewandte Chemie International Edition* 43.45 (Nov. 2004), pp. 6042–6108. ISSN: 1433-7851. DOI: 10.1002/anie.200400651. URL: <http://doi.wiley.com/10.1002/anie.200400651>.
- [4] Guangli Che et al. “Metal-Nanocluster-Filled Carbon Nanotubes: Catalytic Properties and Possible Applications in Electrochemical Energy Storage and Production”. In: *Langmuir* 15.3 (Feb. 1999), pp. 750–758. ISSN: 0743-7463. DOI: 10.1021/la980663i. URL: <https://pubs.acs.org/doi/10.1021/la980663i>.
- [5] Elzbieta Frackowiak and François Béguin. “Carbon materials for the electrochemical storage of energy in capacitors”. In: *Carbon* 39.6 (May 2001), pp. 937–950. ISSN: 00086223. DOI: 10.1016/S0008-6223(00)00183-4. URL: <https://linkinghub.elsevier.com/retrieve/pii/S0008622300001834>.
- [6] Ketul Popat. *Nanotechnology in Tissue Engineering and Regenerative Medicine*. 2011, p. 302. ISBN: 9780367383329.
- [7] Nguyen TK Thanh. *Magnetic Nanoparticles From Fabrication to Clinical Applications* No Title. CRC Press, 2012. ISBN: 9780367507923.
- [8] Alfred W. Hübler and Onyema Osuagwu. “Digital quantum batteries: Energy and information storage in nanovacuum tube arrays”. In: *Complexity* (2010), NA–NA. ISSN: 10762787. DOI: 10.1002/cplx.20306. URL: <http://doi.wiley.com/10.1002/cplx.20306>.
- [9] Eric Shinn et al. “Nuclear energy conversion with stacks of graphene nanocapacitors”. In: *Complexity* 18.3 (Jan. 2013), pp. 24–27. ISSN: 10762787. DOI: 10.1002/cplx.21427. URL: <http://doi.wiley.com/10.1002/cplx.21427>.
- [10] R. Waser. *Nanoelectronics and Information Technology*. Wiley-VCH, 2012. ISBN: 978-3-527-40927-3.

- [11] Raúl José Martín-Palma Fernando Agullo-Rueda José Martínez-Duart. *Nanotechnology for Microelectronics and Optoelectronics*. Isevier, 206, p. 304. ISBN: 9780080445533.
- [12] S. Sun; C. B. Murray; D. Weller; L. Folks; and A. Moser. “Monodisperse FePt nanoparticles and ferromagnetic FePt nanocrystal superlattices”. In: *Science* 287 (2000). ISSN: 287(5460):1989-92.
- [13] C.M. Schneider S. Blügel, T. Brückel. “Magnetism goes Nano”. In: 36th IFF Spring School 2005, Forschungszentrum Jülich GmbH.
- [14] “Magnetic Nanoparticles: A Subject for Both Fundamental Research and Applications”. In: *Journal of Nanomaterials* 2013 (2013), pp. 1–22. ISSN: 1687-4110. DOI: 10.1155/2013/952540. URL: <http://www.hindawi.com/journals/jnm/2013/952540/>.
- [15] M. Sachan et al. “Field evolution of magnetic correlation lengths in -Co nanoparticle assemblies”. In: *Applied Physics Letters* 92.15 (Apr. 2008), p. 152503. ISSN: 0003-6951. DOI: 10.1063/1.2911736. URL: <http://aip.scitation.org/doi/10.1063/1.2911736>.
- [16] G. Binasch et al. “Enhanced magnetoresistance in layered magnetic structures with antiferromagnetic interlayer exchange”. In: *Physical Review B* 39.7 (Mar. 1989), pp. 4828–4830. ISSN: 0163-1829. DOI: 10.1103/PhysRevB.39.4828. URL: <https://link.aps.org/doi/10.1103/PhysRevB.39.4828>.
- [17] M. N. Baibich et al. “Giant Magnetoresistance of (001)Fe/(001)Cr Magnetic Superlattices”. In: *Physical Review Letters* 61.21 (Nov. 1988), pp. 2472–2475. ISSN: 0031-9007. DOI: 10.1103/PhysRevLett.61.2472. URL: <https://link.aps.org/doi/10.1103/PhysRevLett.61.2472>.
- [18] S. A. Wolf. “Spintronics: A Spin-Based Electronics Vision for the Future”. In: *Science* 294.5546 (Nov. 2001), pp. 1488–1495. ISSN: 00368075. DOI: 10.1126/science.1065389. URL: <https://www.sciencemag.org/lookup/doi/10.1126/science.1065389>.
- [19] Igor Žutić, Jaroslav Fabian, and S. Das Sarma. “Spintronics: Fundamentals and applications”. In: *Reviews of Modern Physics* 76.2 (Apr. 2004), pp. 323–410. ISSN: 0034-6861. DOI: 10.1103/RevModPhys.76.323. URL: <https://link.aps.org/doi/10.1103/RevModPhys.76.323>.
- [20] B D Terris and T Thomson. “Nanofabricated and self-assembled magnetic structures as data storage media”. In: *Journal of Physics D: Applied Physics* 38.12 (June 2005), R199–R222. ISSN: 0022-3727. DOI: 10.1088/0022-3727/38/12/R01. URL: <https://iopscience.iop.org/article/10.1088/0022-3727/38/12/R01>.
- [21] B. Yu; M. Meyyappan. “Nanotechnology: Role in emerging nanoelectronics”. In: *Solid-State Electronics* 50 (2006), pp. 536–544. DOI: 10.1016/j.sse.2006.03.028.

- 
- [22] M. Mitchell Waldrop. “The chips are down for Moore’s law”. In: *Nature* 530.7589 (Feb. 2016), pp. 144–147. ISSN: 0028-0836. DOI: 10.1038/530144a. URL: <http://www.nature.com/articles/530144a>.
- [23] A J Hill Hannink, Richard H. J., ed. *Nanostructure Control of Materials*. 1st. 2006, p. 368. ISBN: 9781855739338.
- [24] G. M. Whitesides and B. Grzybowski. “Self-assembly at all scales”. In: *Science* 17 (2002). DOI: 10.1126/science.1070821.
- [25] Stephen Whitelam et al. “The role of collective motion in examples of coarsening and self-assembly”. In: *Soft Matter* 5.6 (2009), pp. 1251–1262. ISSN: 1744-683X. DOI: 10.1039/B810031D. URL: <http://xlink.rsc.org/?DOI=B810031D>.
- [26] Alexander S. Powers et al. “Tracking Nanoparticle Diffusion and Interaction during Self-Assembly in a Liquid Cell”. In: *Nano Letters* 17.1 (Jan. 2017), pp. 15–20. ISSN: 1530-6984. DOI: 10.1021/acs.nanolett.6b02972. URL: <https://pubs.acs.org/doi/10.1021/acs.nanolett.6b02972>.
- [27] Elisabeth Josten et al. “Superlattice growth and rearrangement during evaporation-induced nanoparticle self-assembly”. In: *Scientific Reports* 7.1 (Dec. 2017), p. 2802. ISSN: 2045-2322. DOI: 10.1038/s41598-017-02121-4. URL: <http://www.nature.com/articles/s41598-017-02121-4>.
- [28] S. Blundell. *Magnetism in condensed matter*. Oxford University Press, Oct. 2001. ISBN: 9780198505914.
- [29] A. C. Berceanu. “Ferromagnetic Insulator State in Doped FeTiO<sub>3</sub>”. PhD thesis. 2008.
- [30] S. Bedanta and W. Kleemann. “Supermagnetism”. In: *Journal of Physics D: Applied Physics* 42.1 (Dec. 2008).
- [31] J. Osborn. “Demagnetizing factors of the general ellipsoid”. In: *Physical review* 67.11 (1945), p. 351.
- [32] J. M. D. Coey. *Magnetism and magnetic materials*. Cambridge University Press, Oxford, 2001. ISBN: 9780511845000. DOI: <https://doi.org/10.1017/CB09780511845000>.
- [33] W. H. Meiklejohn and C. P. Bean. “New magnetic anisotropy”. In: *physical review* 105 (1956). DOI: <https://doi.org/10.1103/PhysRev.105.904>.
- [34] Y. Fan et al. “Exchange bias of the interface spin system at the Fe/MgO interface”. In: *Nature Nanotechnology* 8.6 (June 2013), pp. 438–444. ISSN: 1748-3387. DOI: 10.1038/nnano.2013.94. URL: <http://www.nature.com/articles/nnano.2013.94>.
- [35] V. Skumryev; S. Stoyanov; Y. Zhang; G. Hadjipanayis; D. Givord; and J. Nogues. “Beating the superparamagnetic limit with exchange bias”. In: *nature* (2003). DOI: 10.1038/nature01687.

- [36] C.P.Bean. “Hysteresis Loops of Mixtures of Ferromagnetic Micropowders”. In: *Journal of Applied Physics* 26 (1955). DOI: <https://doi.org/10.1063/1.1721912>.
- [37] C.P.Bean and J.D. Livingstone. “Superparamagnetism”. In: *Journal of Applied Physics* 30 (1959). DOI: <https://doi.org/10.1063/1.2185850>.
- [38] O.Petracic. “Superparamagnetic nanoparticle ensembles”. In: *Superlattices and Microstructure* 47.5 (2010).
- [39] J. A. Mydosh. *Spin Glasses: An Experimental Introduction*. London: Taylor and Francis, May 1993. ISBN: 9780429080135. DOI: <https://doi.org/10.1201/9781482295191>.
- [40] J. L. Dormann; D. Fiorani; and E. Tronc. *Magnetic Relaxation in Fine-Particle Systems. Advances in Chemical Physics*. Ed. by I. Prigogine; S.A. Rice. John Wiley & Sons, Jan. 1997. ISBN: 9780470141571. DOI: 10.1002/9780470141571.
- [41] G. M. Whitesides and M. Boncheva. “Beyond molecules: Self-assembly of mesoscopic and macroscopic components”. In: *National Academy of Science* 99.8 (2002), pp. 4769–4774. DOI: <https://doi.org/10.1073/pnas.082065899>.
- [42] C. B. Murray; C. R. Kagan; and M. G. Bawendi. “Self-organization of CdSe nanocrystallites into three-dimensional quantum dot superlattices”. In: *American Association for the Advancement of Science* 270 (1995), pp. 1335–1338. ISSN: 1095-9203. DOI: 10.1126/science.270.5240.1335.
- [43] P. Poddar; T. T. Shafir; T. Fried; and G. Markovich. “Dipolar interactions in two- and three-dimensional magnetic nanoparticle arrays”. In: *Physical Review B* 18.196 (2002), p. 259. DOI: 10.1103/PhysRevB.66.060403.
- [44] C. T. Black; C. B. Murray; R. L. Sandstrom; and S. Sun. “Spin-dependent tunneling in self-assembled cobalt-nanocrystal superlattices”. In: *Science* 18.196 (2000). ISSN: 10;290(5494):1131-4.
- [45] D. Mishra; M. J. Benitez; O. Petracic; G. A. B. Confalonieri; P. Szary; F. Brüssing; K. Theis-Bröhl; A. Devishvili; A. Vorobiev; O. Konovalov. “Self-assembled iron oxide nanoparticle multilayer: x-ray and polarized neutron reflectivity”. In: *Nanotechnology* 23.055707 (2012). DOI: 10.1088/0957-4484/23/5/055707.
- [46] K. J. M. Bishop; C. E. Wilmer; S. Soh; and B. A. Grzybowski. “Nanoscale forces and their uses in self-assembly”. In: *small* 5.1600 (2009). DOI: 10.1002/smll.200900358.
- [47] J. Israelachvili. *Intermolecular and Surface Forces*. 2nd. Academic Press, London, 1994. ISBN: 9780123919335.
- [48] A.P. Hynninen and M. Dijkstra. “Phase diagram of dipolar hard and soft spheres: manipulation of colloidal crystal structures by an external field”. In: *Phys. Rev. Letts.* 94.4 (Apr. 2005), p. 138303. DOI: 10.1103/PhysRevLett.94.138303.

- [49] B. Nikoobakht; Z. L. Wang; and M. A. El-Sayed. “Self-assembly of gold nanorods”. In: *J. Phys. Chem. B* 36.104 (Aug. 2000).
- [50] S. Ahmed and K. M. Ryan. “Self-assembly of vertically aligned nanorod supercrystals using highly oriented pyrolytic graphite”. In: *nano Lett* 7.8 (2007). DOI: <https://doi.org/10.1021/nl071263v>.
- [51] A. R. G. Alig; M. Akbulut; Y. Golan; and J. Israelachvili. “Forces between surfactant-coated ZnS nanoparticles in dodecane: Effect of water”. In: *Adv. Funct. Mater* 37 (2006). DOI: <https://doi.org/10.1002/adfm.200500705>.
- [52] Y. Min; M. Akbulut; K. Kristiansen; Y. Golan; and J. Israelachvili. “The role of interparticle and external forces in nanoparticle assembly”. In: *Nature Materials* 36.37 (2008). DOI: 10.1038/nmat2206.
- [53] B. G. Prevo; D. M. Kuncicky; and O. D. Velev. “Engineered deposition of coatings from nano- and micro-particles: A brief review of convective assembly at high volume fraction”. In: *Colloids Surf. A* 37 (2007). DOI: 10.1016/j.colsurfa.2007.08.030.
- [54] *lectures notes of the 50<sup>th</sup> IFF spring school held at Forschungszentrum Jülich "Scattering! soft, functional and quantum material"*. Forschungszentrum Jülich GmbH, Jülich. 2019.
- [55] Z. Wang; Y. Liu; and Z. Zhang. *X-ray and Neutron Scattering (Handbook of Nanophase and Nanostructured Materials)*. Springer, Boston, MA, 2003. ISBN: 978-0-387-23814-2. DOI: [https://doi.org/10.1007/0-387-23814-X\\_12](https://doi.org/10.1007/0-387-23814-X_12).
- [56] J. Als-Nielsen and D. McMorrow. *Elements of modern x-ray physics*. 2nd. John Wiley sons Ltd., London, 2011.
- [57] V.F.Sears. “Neutronscatteringlengthsandcrosssections”. In: *Neutron News* 3 (1992), pp. 26–37. DOI: 10.1080/10448639208218770.
- [58] L. G. Parratt. “Surface studies of solids by total reection of x-rays”. In: *Physical Review* 95.359 (1954).
- [59] H. Zabel; K. Theis-Brohl; and B. P. Toperver. *Polarized neutron reectivity and scattering from magnetic nanostructures and spintronic materials (Handbook of Magnetism and Advanced Magnetic Materials)*. Ed. by H. Kronmuller and S. Parki. Vol. 3. John Wiley & Sons, New Yor, 2007. ISBN: 9780470022177. DOI: 10.1002/9780470022184.
- [60] J. Burl; C. Durniak; J. M. Fisher; M. Ganeva; G. Pospelov; W. Van Herck and J. Wuttke. “BornAgain: software for simulating and fitting grazing-incidence small-angle scattering”. In: *Journal of Applied Crystallography* 53.1 (Feb. 2020), pp. 262–276. DOI: 10.1107/S1600576719016789. URL: <https://doi.org/10.1107/S1600576719016789>.
- [61] S. D. Bader. “Colloquium: Opportunities in nanomagnetism”. In: *Reviews of Modern Physics* 78 (Jan. 2006), pp. 1–15. DOI: 10.1103/RevModPhys.78.1.

- [62] D. McMullan. “Scanning electron microscopy 1928-1965”. In: *Scanning* 17 (May 1995), pp. 175–185. DOI: 10.1002/sca.4950170309.
- [63] A. E. Vladar and M. T. Postek. *Handbook of Charged Particle Optics*. Ed. by Jon Orloff. CRC Press, 2009. DOI: 13:978-1-4200-4554-3.
- [64] C.Kittel. *Introduction to solid state physics(chapter 12, "superconductivity")*. 8th ed. John Wiley & Sons, 1986. ISBN: 047141526X.
- [65] Quantum Design. “Magnetic Property Measurement System MPMS XL”. In: *Reference Manual* (2005).
- [66] A. Kraft; C. Rupprecht; and Y. C. Yam. “Superconducting Quantum Interference Device (SQUID)”. In: *UBC Physics 502 project* (2017).
- [67] E.Kentzinger; M.Krutyeva; and U. Rucker. “GALAXI: Gallium anode low-angle x-ray instrument”. In: *large-scale research facilities* 2(61):1-5 (2016).
- [68] A. P. Hammersley. “FIT2D: a multi-purpose data reduction, analysis and visualization program”. In: *Journal of Applied Crystallography* 49.2 (Apr. 2016), pp. 646–652. DOI: 10.1107/S1600576716000455. URL: <https://doi.org/10.1107/S1600576716000455>.
- [69] Jülich Centre for Neutron Science. “MARIA: Magnetic reflectometer with high incident angle”. In: *large-scale research facilities* (2015). URL: <http://dx.doi.org/10.17815/jlsrf-1-29>.
- [70] H. Zabel. “X-ray and neutron reflectivity analysis of thin films and superlattices”. In: *Appl. Phys. A*, 58:159 (1994).
- [71] J. R. Levine; J. B. Cohen; Y. W. Chung; P. Georgopoulos. “Grazing-incidence small-angle X-ray scattering: new tool for studying thin film growth”. In: *Journal of Applied Crystallography* 22.6 (Dec. 1989), pp. 528–532. DOI: 10.1107/S002188988900717X. URL: <https://doi.org/10.1107/S002188988900717X>.
- [72] M. Tolan; W. Press; F. Brinkop and J.P. Kotthaus. “X-ray diffraction from laterally structured surfaces: Total external reflection”. In: *Phys. Rev. B* 51 (4 Jan. 1995), pp. 2239–2251. DOI: 10.1103/PhysRevB.51.2239. URL: <https://link.aps.org/doi/10.1103/PhysRevB.51.2239>.
- [73] T. Metzger; K.H. Haj; J. Peisl; M. Wendel; H. Lorenz; J. Kotthaus; and G.S. Cargill III. “Nanometer surface gratings on Si(100) characterized by x-ray scattering under grazing incidence and atomic force microscopy”. In: *Journal of Applied Physics* 81 (Feb. 1997), pp. 1212–1216. DOI: 10.1063/1.363864.
- [74] P. Mikulik; M. Jergel; T. Baumbach; E. Majková; E. Pincik; S. Luby; L. Ortega; R. Tucoulou; P. Hudek; I. Kostic. “Coplanar and non-coplanar x-ray reflectivity characterization of lateral W/Si multilayer gratings”. In: *Journal of Physics D: Applied Physics* 34.10A (May 2001), A188–A192. DOI: 10.1088/0022-3727/34/10a/339. URL: <https://doi.org/10.1088%20%2F0022-3727%2F34%2F10a%2F339>.

- [75] M. Yan; and A. Gibaud. “On the intersection of grating truncation rods with the Ewald sphere studied by grazing-incidence small-angle X-ray scattering”. In: *Journal of Applied Crystallography - J APPL CRYST* 40 (Dec. 2007), pp. 1050–1055. DOI: 10.1107/S0021889807044482.
- [76] M. Pflüger; V. Soltwisch; J. Probst; F. Scholze; M. Krumrey. “Grazing Incidence Small Angle X-Ray Scattering (GISAXS) on Small Targets Using Large Beams”. In: *IUCrJ* 4 (Mar. 2017). DOI: 10.1107/S2052252517006297.
- [77] D. Babonneau. “FitGISAXS: software package for modelling and analysis of GISAXS data using IGOR Pro”. In: *J. Appl. Cryst* 43 (July 2010), pp. 929–936.
- [78] S. T. Chourou; A. Sarje; X. S. Li; E. R. Chan; A. Hexemer. “HipGISAXS: a high-performance computing code for simulating grazing-incidence X-ray scattering data”. In: *J. Appl. Cryst* 46 (Nov. 2013), pp. 1781–1795.
- [79] J. Burle; C. Durniak; J. M. Fisher; M. Ganeva; G. Pospelov; W. Van Herck and J. Wuttke. “BornAgain – Software for simulating and fitting X-ray and neutron small-angle scattering at grazing incidence”. In: (2018). URL: <http://www.bornagainproject.org>.
- [80] R. Lazzari. “IsGISAXS: a program for grazing-incidence small-angle X-ray scattering analysis of supported islands”. In: *J. Appl. Cryst* 35 (2002), pp. 406–421. DOI: 10.1107/S0021889802006088.
- [81] A. L. Patterson. “A Direct Method for the Determination of the Components of Interatomic Distances in Crystals”. In: *Z. Für Krist. - Cryst. Mater* 90 (1935), pp. 517–542. DOI: 10.1524/zkri.1935.90.1.517.
- [82] H. H. Solak; C. Dais; and F. Clube. “Displacement talbot lithography: a new method for high-resolution patterning of large areas”. In: *Optics express* 19.11 (2011), p. 10686.
- [83] H. Solak; C. Dais; F. Clube and L. Wang. “Phase shifting masks in Displacement Talbot Lithography for printing nano-grids and periodic motifs”. In: *Microelectronic Engineering* 143 (Aug. 2015), pp. 74–80.
- [84] A. Kato and F. Scholze. “Effect of line roughness on the diffraction intensities in angular resolved scatterometry”. In: *Appl. Opt.* 49.31 (Nov. 2010), pp. 6102–6110.
- [85] F. Scholze; A. Kato; J. Wernecke; M. Krumrey. *EUV and x-ray scattering methods for CD and roughness measurement*. 2011. DOI: 10.1117/12.896847. URL: <https://doi.org/10.1117/12.896847>.
- [86] V. Soltwisch; J. Wernecke; A. Haase; J. Probst; M. Schoengen; M. Krumrey and F. Scholze. “Nanometrology on gratings with GISAXS: FEM reconstruction and Fourier analysis”. In: *Proc. SPIE. Metrology, Inspection, and Process Control for Microlithography XXVIII*. Vol. Vol. 9050. 2014, p. 905012. DOI: 10.1117/12.2046212.

- [87] V. Soltwisch; J. Wernecke; A. Haase; J. Probst; M. Schoengen; F. Scholze; J. Pomplun and S. Burger. "Determination of line profile on nanostructured surfaces using EUV and x-ray scattering". In: *Proc. SPIE. Photomask Technology*. Ed. by P. W. Ackmann and N. Hayashi. Vol. 9235. 2014, p. 92351D. DOI: 10.1117/12.2066165.
- [88] M. Tolan and W. Press. "X-ray diffraction from laterally structured surfaces: Total external reflection". In: *PHYSICAL REVIEW B* 51.4 (Jan. 1995).
- [89] B. L. Henke; E. M. Gullikson and J. C. Davis. "X-Ray Interactions: Photoabsorption, Scattering, Transmission, and Reflection at  $E = 50\text{--}30,000$  eV,  $Z = 1\text{--}92$ ". In: *Atomic Data and Nuclear Data Tables* 54 (1993), pp. 181–342. DOI: 10.1006/adnd.1993.1013.
- [90] H. S. Suh; X. Chen; P. A. Rincon-Delgadillo; J. Zhang; J. Strzalka; J. Wang; W. Chen; R. Gronheid; J. J. de Pablo; N. Ferrier; M. Doxastakis; P. F. Nealey. "Characterization of the shape and line-edge roughness of polymer gratings with grazing incidence small-angle X-ray scattering and atomic force microscopy". In: *Journal of Applied Crystallography* 49.3 (June 2016), pp. 823–834. DOI: 10.1107/S1600576716004453. URL: <https://doi.org/10.1107/S1600576716004453>.
- [91] Asma Qdemat et al. "Self assembled monolayer of silica nanoparticles with improved order by drop casting". In: *RSC Advances* 10.31 (2020), pp. 18339–18347. ISSN: 2046-2069. DOI: 10.1039/D0RA00936A. URL: <http://xlink.rsc.org/?DOI=D0RA00936A>.
- [92] R. H. J. Hannink; A. J. Hill. *Nanostructure Control of Materials*. CRC press, Feb. 2006. ISBN: 9781845691189.
- [93] T. Fried; G. Shemer; G. Markovich. "Ordered Two-Dimensional Arrays of Ferrite Nanoparticles". In: *Advanced Materials* 13.1158-1161 (2001). DOI: 10.1002/1521-4095(200108)13:15<1158::AID-ADMA1158>3.0.CO;2-6.
- [94] V. Ukleev; A. Khassanov; I. Snigireva; O. Konovalov; M. Dudnik; I. Dubitskiy; A. Vorobiev. "Self-assembly of a binary mixture of iron oxide nanoparticles in Langmuir film: X-ray scattering study". In: *Materials Chemistry and Physics* 202.31-39 (2017). DOI: 10.1016/j.matchemphys.2017.08.069.
- [95] M. Pauly; B. P. Pichon; P.-A. Albouy; S. Fleutot; C. Leuvrey; M. Trassin; J.-L. Gallani; S. Begin-Colin. "Monolayer and multilayer assemblies of spherically and cubic-shaped iron oxide nanoparticles". In: *J. Mater. Chem.* 21.16018 (2011). DOI: 10.1039/c1jm12012c.
- [96] N. D. Denkov; O. D. Velev; P. A. Kralchevsky; I. B. Ivanov; H. Yoshimura; and K. Nagayama. "Two dimensional crystallization". In: *Nature* 361 (1993).
- [97] M. Kondo; P. Sharifi; R. Brinkmann; and N. Mendive. "Opals: status and prospects". In: *Angewandte Chemi (International ed. in English)* 48.6212-33 (2009).

- [98] M. I. Bodnarchuk; M. V. Kovalenko; S. Pichler; G. Fritz-Popovski; G. Hesser; W. Heiss. “Large-Area Ordered Superlattices from Magnetic Wüstite/Cobalt Ferrite Core/Shell Nanocrystals by Doctor Blade Casting”. In: *ACS Nano* 4.423-431 (2010), pp. 423–431. DOI: 10.1021/nn901284f.
- [99] H. S. Kim; B. H. Sohn; W. Lee; J.-K. Lee; S. J. Choi; S. J. Kwon. “Multi-functional layer-by-layer self-assembly of conducting polymers and magnetics nanoparticles”. In: *Thin solid films* 419 (2002), pp. 173–177. DOI: 10.1016/S0040-6090(02)00779-4.
- [100] T. P. Bigioni; X.-M. Lin; T. T. Nguyen; E. I. Corwin; T. A. Witten; H. M. Jaeger. “Kinetically driven self assembly of highly ordered nanoparticle monolayers”. In: *Nature Materials* 5 (2006), pp. 265–270. DOI: 10.1038/nmat1611.
- [101] Y. Xia; B. Gates; Y. Yin; and Y. Lu. “Monodispersed colloidal spheres: old materials with new applications”. In: *Advanced materials* 12.10 (2000), pp. 693–713.
- [102] A. T. Heitsch; R. N. Patel; B. W. Goodfellow; D.-M. Smilgies; B. A. Korgel. “GISAXS Characterization of Order in Hexagonal Monolayers of FePt Nanocrystals”. In: *Phys. Chem. C* (2010), pp. 14427–14432. DOI: 10.1021/jp1047979.
- [103] A. Vorobiev; A. Khassanov; V. Ukleev; I. Snigireva; O. Konovalov. “Substantial Difference in Ordering of 10, 15, and 20 nm Iron Oxide Nanoparticles on a Water Surface: In Situ Characterization by the Grazing Incidence X-Ray Scattering”. In: *Langmuir* 31 (2015), pp. 11639–11648. DOI: 10.1021/acs.langmuir.5b02644.
- [104] T. Wen; S. A. Majetich. “Ultra-Large-Area Self-Assembled Monolayers of Nanoparticles”. In: *ACS Nano* 11 (2011), pp. 8868–8876. DOI: 10.1021/nn2037048.
- [105] M. Kondo; K. Shinozaki; L. Bergstrom and N. Mizutani. “Preparation of Colloidal Monolayers of Alkoxylated Silica Particles at the Air-Liquid Interface”. In: *Langmuir* 11 (1995), pp. 394–397. DOI: 10.1021/1a00002a003.
- [106] N. D. Denkov; O. D. Velev; P. A. Kralchevsky; I. B. Ivanov; H. Yoshimura; and K. Nagayama. “Two-dimensional crystallization”. In: *Nature* 361.26 (1993). DOI: <https://doi.org/10.1038/361026a0>.
- [107] W. Han; Z. Lin. ““Learning from “Coffee Rings”: Ordered Structures Enabled by Controlled Evaporative Self-Assembly”. In: *Angew. Chem.* 51 (2012), pp. 1534–1536. DOI: 10.1002/anie.201104454.
- [108] R. D. Deegan; O. Bakajin; T. F. Dupont; G. Huber; S. R. Nagel; T. A. Witten. “Capillary flow as the cause of ring stains from dried liquid drops”. In: *Nature* 389 (1997), pp. 827–829. DOI: 10.1038/39827.
- [109] M. Anyfantakis; Z. Geng; M. Morel; S. Rudiuk; D. Baigl. “Modulation of the Coffee-Ring Effect in Particle/Surfactant Mixtures: the Importance of Particle-Interface Interactions”. In: *Langmuir* 31 (2015), pp. 4113–4120. DOI: 10.1021/acs.langmuir.5b00453.

- [110] M. G. Basavaraj V. R. Dugyala. “Control over Coffee-Ring Formation in Evaporating Liquid Drops Containing Ellipsoids”. In: *Langmuir* 30 (2014), pp. 8680–8686. DOI: 10.1021/la500803h.
- [111] A. K. Geim; S.V. Dubonos; I.V. Grigorieva; et al. “Microfabricated adhesive mimicking gecko foot- hair”. In: *Nat Mater* 2.461 (2003).
- [112] Y. Wang; L. Chen; H. Yang; Q. Guo; W. Zhou; M. Tao. “Large-area self assembled monolayers of silica microspheres formed by dip coating”. In: *Materials Science- Poland* 28.12 (2010), pp. 467–478.
- [113] T. Oge; L. B. Modesto-Lopez; F. Iskandar; K. Okuyama. “Fabrication of a large area monolayer of silica particles on a sapphire substrate by a spin coating method”. In: *Colloids and surfaces A* 297 (Apr. 2007), pp. 71–78.
- [114] S. S. Shinde; S. Park; and J. Shin. “Spin synthesis of monolayer of SiO<sub>2</sub> thin films”. In: *Journal of Semiconductors* 36.4 (Apr. 2015).
- [115] M. Szekeres; O. Kamalin; R.A. Schoonheydt; K. Wostyn; K. Clays; A. Persoons; I. Dekany. “Ordering an optical properties of monolayers and multilayers of silica spheres deposited by the Langmuir–Blodgett method”. In: *Chem. Mater* 12 (2002), pp. 3268–3274.
- [116] T. Okubo; S. Chujo; S. Maenosono; Y. Yamaguchi. “Microstructure of silica particle monolayer films formed by capillary immersion force”. In: *Nanopart. Res* 5 (2003), pp. 111–117.
- [117] T. Ogi; L. B. Modesto-Lopez; F. Iskandar; et al. “Fabrication of a large area monolayer of silica particles on a sapphire substrate by a spin coating method”. In: *Coll Surf A: Physicochem Eng Aspects* 297.71 (2007).
- [118] H. Bohidar; K. Rawat; H. B. Bohidar. *Design of Nanostructures: Self-Assembly of Nanomaterials*. Wiley-Vch, Oct. 2017. ISBN: 9783527343331.
- [119] F. J. Arriagada; K. Osseo-Asare. “Synthesis of nanosize silica in a nonionic water-in-oil microemulsion: Effects of the water/surfactant molar ratio and ammonia concentration”. In: *journal of colloid and interface science* 211.2 (MAR 15 1999), 210–220. ISSN: 0021-9797. DOI: {10.1006/jcis.1998.5985}.
- [120] F. J. Arriagada; K. OsseoAsare. “Phase and dispersion stability effects in the synthesis of silica nanoparticles in a nonionic reverse microemulsion”. In: *colloids and surfaces* 69.2-3 (DEC 11 1992), 105–115. ISSN: 0166-6622. DOI: {10.1016/0166-6622(92)80221-M}.
- [121] K. OsseoAsare; F.J. Arriagada. “Preparation of SiO<sub>2</sub> nanoparticles in a nonionic reverse micellar system”. In: *colloids and surfaces* 50 (NOV 12 1990), 321–339. ISSN: 0166-6622. DOI: {10.1016/0166-6622(90)80273-7}.
- [122] A. K. van Helden; J. W. Jansen; and A. Vrij. “Dispersion polarization in organic media”. In: *Coll.interface.Sci* 81.354 (1981).
- [123] D. Mishra et al. “Self-assembled iron oxide nanoparticle multilayer: x-ray and polarized neutron reflectivity”. In: *Nanotechnology* 23 (2012).

- [124] D. Mishra; et al. “Self-assembled iron oxide nanoparticle multilayer: x-ray and polarized neutron reflectivity”. In: *Nanotechnology* 23.5 (2012).
- [125] A. Moser; K. Takano; D. T. Margulies; M. Albrecht; Y. Sonobe; Y. Ikeda; S. Sun; and E. E. Fullerton. “Magnetic recording: advancing into the future”. In: *Phys. D: Appl. Phys* 35 (2002), R157–R167. URL: [stacks.iop.org/JPhysD/35/R157](https://stacks.iop.org/JPhysD/35/R157).
- [126] S. Guo; F. Xu; B. Wang; N. Wang; H. Yang; P. Dhanapal; F. Xue; J. Wang; R. W. Li. “2D Magnetic Mesocrystals for Bit Patterned Media”. In: *Adv. Mater. Interfaces* 5.1800997 (Aug. 2018). URL: <https://doi.org/10.1002/admi.201800997>.
- [127] C. A. Ross. “Patterned Magnetic Recording Media”. In: *Annu. Rev. Mater. Res* 31 (2001), pp. 203–235. URL: <https://doi.org/10.1146/annurev.matsci.31.1.203>.
- [128] F. Liu; C.A. Ross. “Size-dependent magnetic properties of 100–500nm diameter IrMn/NiFe disks made by a two-step deposition process”. In: *Applied Physics* 116.194307 (2014). URL: <https://doi.org/10.1063/1.4902080>.
- [129] C. N. Chinnasamy; M. Senoue; B. Jeyadevan; O. Perales-Perez; K. Shinoda; K.J. Tohji. “Microstructural development of cobalt ferrite ceramics and its influence on magnetic properties”. In: *Colloid Interface Sci* 19 (2003), pp. 1209–1213. DOI: 10.1007/s12540-013-6009-8.
- [130] A. R. Bueno; M.L. Gregori; MCS. Nóbrega. “Effect of Mn substitution on the microstructure and magnetic properties of  $\text{Ni}_{0.50x}\text{Zn}_{0.50x}\text{Mn}_{2x}\text{Fe}_2\text{O}_4$  ferrite prepared by the citrate–nitrate precursor method”. In: *Mater Chem Phys* 105 (2007), pp. 229–233.
- [131] E. Tirosh; G. Shemer; and G. Markovich. “Optimizing Cobalt Ferrite Nanocrystal Synthesis Using a Magneto-optical Probe”. In: *Chemistry of Materials* 18 (2006), pp. 465–470. URL: <https://doi.org/10.1021/cm052401p>.
- [132] Z. Iatridi; K. Vamvakidis; I. Tsougos; K. Vassiou; C. Dendrinou-Samara and G. Bokias. “Multifunctional Polymeric Platform of Magnetic Ferrite Colloidal Superparticles for Luminescence, Imaging, and Hyperthermia Applications”. In: *ACS Appl. Mater. Interfaces* 8.51 (2016). URL: <https://doi.org/10.1021/acsami.6b13161>.
- [133] H. Gu; K. Xu; Z. Yang; C. K. Chang; and B. Xu. “Synthesis and cellular uptake of porphyrin decorated iron oxide nanoparticles—a potential candidate for bimodal anticancer therapy”. In: *Chem. Commun* (34 2005), pp. 4270–4272. DOI: 10.1039/B507779F. URL: <http://dx.doi.org/10.1039/B507779F>.
- [134] U. Luders; A. Barthelemy; M. Bibes; K. Bouzehouane; S. Fusil; E. Jacquet; J. P. Contour; J. F. Bobo; J. Fontcuberta; and A. Fert. “ $\text{NiFe}_2\text{O}_4$ : A Versatile Spinel Material Brings New Opportunities for Spintronics”. In: *Advanced materials* 18 (2006), pp. 1733–1736. URL: <https://doi.org/10.1002/adma.200500972>.

- [135] G. Baldi; D. Bonacchi; C. Innocenti ; G. Lorenzi; and C. Sangregorio. “Cobalt ferrite nanoparticles: The control of the particle size and surface state and their effects on magnetic properties”. In: *Magnetism and Magnetic Materials* 311 (2007), pp. 10–16. URL: <https://doi.org/10.1016/j.jmmm.2006.11.157>.
- [136] M. Georgescu; M. Klokkenburg; B. H. Ern e; P. Liljeroth; D. Vanmaekelbergh; E. P. A. Zeijlmans. “Flux closure in two-dimensional magnetite nanoparticle assemblies”. In: *Phys. Rev. B* 73 (18 May 2006), p. 184415. DOI: 10.1103/PhysRevB.73.184415. URL: <https://link.aps.org/doi/10.1103/PhysRevB.73.184415>.
- [137] Denis; LA. Ponomarenko; M. G. Mikheev; M. Beltran; Y. Khodorkovsky; A. Tishin Y. Koksharov; S. P. Gubin; I. B. Kosobudsky; G. Y. Yurkov; D. A. Pankratov. “Electron paramagnetic resonance spectra near the spin-glass transition in iron oxide nanoparticles”. In: *Phys. Rev. B* 63 (Dec. 2000). DOI: 10.1103/PhysRevB.63.012407.
- [138] V. Russier. “Calculated magnetic properties of two-dimensional arrays of nanoparticles at vanishing temperature”. In: *Applied Physics* 89 (2001), pp. 1287–1294. DOI: 10.1063/1.1333034.
- [139] V.Pillai; D.O.Shah. “Synthesis of high-coercivity cobalt ferrite particles using water-in-oil microemulsions”. In: *Journal of Magnetism and Magnetic Materials* 163 (Oct. 1996), pp. 243–248. DOI: [https://doi.org/10.1016/S0304-8853\(96\)00280-6](https://doi.org/10.1016/S0304-8853(96)00280-6).
- [140] K.Maaza; A. Mumtaza; S.K.Hasanaina; A. Ceylan. “Synthesis and magnetic properties of cobalt ferrite (CoFe<sub>2</sub>O<sub>4</sub>) nanoparticles prepared by wet chemical route”. In: *Journal of Magnetism and Magnetic Materials* 308 (2007), pp. 289–295. DOI: <https://doi.org/10.1016/j.jmmm.2006.06.003>.
- [141] J.S. Jung; J.H. Lim. “CoFe<sub>2</sub>O<sub>4</sub> nanostructures with high coercivity”. In: *Applied Physics* 97 (2005). DOI: 10.1063/1.1852851.
- [142] A. V. Ramos; M. J. Guittet; J. B. Moussy; R. Mattana; C. Deranlot; F. Petroff; C. Gatel. “Room temperature spin filtering in epitaxial cobalt-ferrite tunnel barriers”. In: *Applied Physics Letters* 91.122107 (2007). DOI: 10.1063/1.2787880.
- [143] A. Goldman. *Handbook of Modern Ferromagnetic Materials*. Springer Science+Business Media, 1999.
- [144] L. D. Tung; V. Kolesnichenko; D. Caruntu; N. H. Chou; C. J. O’Connor; and L. Spinu. “Magnetic properties of ultrafine cobalt ferrite particles”. In: *Applied physics* 93 (2003). DOI: 10.1063/1.1540145.
- [145] D.J. Craik. *Magnetic Oxides*. John Wiley & Sons, London, 1975. URL: <https://doi.org/10.1002/bbpc.19760800218>.
- [146] M. Tachiki. “Origin of the Magnetic Anisotropy Energy of Cobalt Ferrite”. In: *Progress of Theoretical Physics* 23 (1960), pp. 1055–1071. DOI: 10.1143/PTP.23.1055.

- [147] A. H. Morrish G. A. Sawatzky F. van der Woude. “Cation Distributions in Octahedral and Tetrahedral Sites of the Ferrimagnetic Spinel  $\text{CoFe}_2\text{O}_4$ ”. In: *Applied Physics* 39 (1968), pp. 1204–1206. DOI: 10.1063/1.1656224.
- [148] G. A. Sawatzky; F. van der Woude; A. H. Morrish. “Mössbauer Study of Several Ferrimagnetic Spinels”. In: *Physical Review* 187 (1969), pp. 747–757. DOI: 10.1103/PhysRev.187.747.
- [149] G. Muscas; N. Yaacoub; G. Concas; F. Sayed; R. S. Hassan; J. Greneche; C. Cannas; A. Musinu; V. Foglietti; S. Casciardi; C. Sangregoria; D. Peddis. “Evolution of the magnetic structure with chemical composition in spinel iron oxide nanoparticles”. In: *Nanoscale* 7 (2015), pp. 13576–13585.
- [150] A. Repko; J. Vejpravová; T. Vacková; D. Zákutná; D. Niznanský. “Oleate-based hydrothermal preparation of  $\text{CoFe}_2\text{O}_4$  nanoparticles, and their magnetic properties with respect to particle size and surface coating”. In: *Magnetism and Magnetic Materials* 390 (2015), pp. 142–151. DOI: 10.1016/j.jmmm.2015.04.090.
- [151] D. Peddis; M. V. Mansilla; S. Morup; C. Cannas; A. Musinu; G. Piccaluga; F. D’Orazio; F. Lucari; D. Fiorani. “Spin-Canting and Magnetic Anisotropy in Ultrasmall  $\text{CoFe}_2\text{O}_4$  Nanoparticles”. In: *Phys. Chem. B* 112 (2008), pp. 8507–8513. DOI: 10.1021/jp8016634.
- [152] C. P. Bean and I. S. Jacobs. “Magnetic Granulometry and Super-Paramagnetism”. In: *Journal of Applied Physics* 27.1448 (May 2004). URL: <https://doi.org/10.1063/1.1722287>.
- [153] E.V. Gopalan; P. A. Joy; I. A. Al-Omari; D. S. Kumar; Y. Yoshida; M. R. Anantharaman. “On the structural, magnetic and electrical properties of sol-gel derived nanosized cobalt ferrite”. In: *Journal of Alloys and Compounds* 485.1-2 (Oct. 2009), pp. 711–717. DOI: 10.1016/j.jallcom.2009.06.033.
- [154] B. Kale; S. Watawe S. Khot; N. Shinde; B. Ladgaonkar. “Magnetic and structural properties of Magnesium Zinc Ferrites synthesized at different temperature”. In: *Adv. Appl. Sci. Res.* 2 (Jan. 2011).
- [155] X. Jin; V. Justin; P. Giuseppe; L. Alessandro; M. Jamo; S. Ali; A. H. Jeroen; R. Petra; J. K. Bart; N. Beatriz; and L. Katja. “Chemical Solution Deposition of Ordered 2D Arrays of Room-Temperature Ferrimagnetic Cobalt Ferrite Nanodots”. In: *polymer* 11.10 (2019), p. 1598. DOI: 10.3390/polym11101598.
- [156] A. M Zysler R. D; Fiorani. D; Testa. “Investigation of magnetic properties of interacting  $\text{Fe}_2\text{O}_3$  nanoparticles”. In: *Magnetism and Magnetic Materials* 224.1 (2001), pp. 5–11. DOI: 10.1016/S0304-8853(00)01328-7.
- [157] A. Fujishima; S. i. Ohkoshi; S. Y. Osamu Sato; T. Iyoda and K. Hashimoto. “Photoinduced magnetic pole inversion in a ferro–ferrimagnet”. In: *Applied Physics Letters* 70.8 (1997). DOI: 10.1063/1.118475.

- [158] H. Lee; A. M. Purdon; V. Chu; and R. M. Westervelt. “Controlled Assembly of Magnetic Nanoparticles from Magnetotactic Bacteria Using Microelectromagnets Arrays”. In: *Nano Lett* 4.5 (2004), pp. 995–998.
- [159] Y. Sun; M. B. Salamon; K. Garnier; and R. S. Averback. “Memory y Effects in an Interacting Magnetic Nanoparticle System”. In: *Phys. Rev. Lett* 91.167206 (2003).
- [160] K. Theis-Bröhl; D. Mishra; B. P. Toperverg; H. Zabel; B. Vogel; A. Regtmeier; and A. Hütten. “Self-organization of magnetic nanoparticles: A polarized grazing incidence small angle neutron scattering and grazing incidence small angle x-ray scattering study”. In: *Appl.Phys* 110.102207 (2011).
- [161] Dr. R. M. Cornell; Prof. em. Dr. Dr. h.c. U. Schwertmann. *The Iron Oxides: Structure; Properties; Reactions; Occurences and Uses; Second Edition*. Wiley-VCH Verlag GmbH & Co. KGaA, 2003. ISBN: 9783527602094. DOI: 10.1002/3527602097.
- [162] D. Dunlop; Ö. Özdemir. *Rock Magnetism: Fundamentals and Frontiers*. Cambridge University Press, July 2010. ISBN: 9780511612794. DOI: <https://doi.org/10.1017/CB09780511612794>.
- [163] R. C. O’Handley. *Modern Magnetic Materials Principles and Applications*. John Wiley & Sons, 2000. ISBN: 978-0-471-15566-9.
- [164] G. F. Goya; T. S. Berquo; F. C. Fonseca; M. P. Morales. “Static and dynamic magnetic properties of spherical magnetite nanoparticles”. In: *Appl. Phys* 94.3520 (2003). DOI: 10.1063/1.1599959.
- [165] L. R. Bickford; J. M. Brownlow; R. F. Penoyer. “Magnetocrystalline anisotropy in cobalt-substituted magnetite single crystals”. In: *Proc. IEEE*. Vol. 104. 238. 1956. DOI: 10.1049/pi-b-1.1957.0038.
- [166] C. Medrano; M. Schlenker; J. Espeso; Y. Miyamoto. “Domains in the low-temperature phase of magnetite from synchrotron-radiation x-ray topographs”. In: *Physical Review B* 59 (1999), pp. 1185–1195. DOI: 10.1103/PhysRevB.59.1185.
- [167] K. Momma and F. Izumi. “VESTA 3 for three-dimensional visualization of crystal, volumetric and morphology data”. In: *Journal of Applied Crystallography* 44.6 (Dec. 2011), pp. 1272–1276. DOI: 10.1107/S0021889811038970. URL: <https://doi.org/10.1107/S0021889811038970>.
- [168] T. Hyeon. “Chemical synthesis of magnetic nanoparticles”. In: *Chem. Commun.* (8 2003), pp. 927–934. DOI: 10.1039/B207789B. URL: <http://dx.doi.org/10.1039/B207789B>.
- [169] Dominique Dresen. “Collective Magnetism in Long-Range Ordered Structures of Magnetic Nanoparticles”. PhD thesis. Universität zu Köln, 2019.

- [170] Ulrich; F. Zheng; H. L. Peng; X. K. Wei; R. E. D. Borkowski L. Wang; A. Qdemat; O. Petracic; E. Kentzinger; U. Rücker and T. Brückel. “Manipulation of dipolar magnetism in low-dimensional iron oxide nanoparticle assemblies”. In: *Phys. Chem. Chem. Phys.* 21 (11 2019), pp. 6171–6177. DOI: 10.1039/C9CP00302A. URL: <http://dx.doi.org/10.1039/C9CP00302A>.
- [171] K Šliužienė ; V Lisauskas; R Butkutė; B Vengalis ; S Tamulevicius and M Andrulevicius. “Growth and investigation of p-n structures based on Fe<sub>3</sub>O<sub>4</sub> thin films”. In: *Journal of Physics: Conference Series* 100.8 (Mar. 2008), p. 082028. DOI: 10.1088/1742-6596/100/8/082028. URL: <https://doi.org/10.1088/1742-6596/100/8/082028>.
- [172] A. Mitra; J. Mohapatra; S. S. Meena; C. V. Tomy; M. Aslam. “Verwey Transition in Ultrasmall-Sized Octahedral Fe<sub>3</sub>O<sub>4</sub> Nanoparticles”. In: *J. Phys. Chem. C* 118.33 (July 2014), pp. 19356–19362. DOI: [org/10.1021/jp501652e](https://doi.org/10.1021/jp501652e).
- [173] M. Benitez; D. Mishra; P. Szary; G. B. Confalonieri; M. Feyen; A. Lu; L. Agudo; G. Eggeler; O. Petracic; and H. Zabel. “Structural and magnetic characterization of self-assembled iron oxide nanoparticle arrays”. In: *Physics: Condensed Matter* 23.12 (2011), p. 126003.
- [174] R. A. Bromley. “The lattice vibrations of the MoS<sub>2</sub> structure”. In: *The Philosophical Magazine: A Journal of Theoretical Experimental and Applied Physics* 23.186 (1971), pp. 1417–1427. DOI: 10.1080/14786437108217011. eprint: <https://doi.org/10.1080/14786437108217011>. URL: <https://doi.org/10.1080/14786437108217011>.
- [175] J. D. Jackson. *Classical Electrodynamics*. 3rd ed. John Wiley & Sons, 1999.
- [176] Th. Brückel; D. Richter; G. Roth; A. Wischnewski; and R. Zorn; editor. *Neutron scattering : lectures of the JCNS laboratory course held at Forschungszentrum Jülich and at the Heinz Maier-Leibnitz Zentrum Garching ; in cooperation with RWTH Aachen and University of Münster*. Forschungszentrum Jülich GmbH, Jülich. 2015.
- [177] D.S. Sivia. *Elementary Scattering Theory, For X-ray and neutron users*. Oxford University Press, Oxford, 2011.
- [178] G. L. Squires. *Introduction to the Theory of Thermal Neutron Scattering*. Dover Publications, New York, 1997.
- [179] S. W. Lovesey. *Theory of Neutron Scattering from Condensed Matter Volume II: Polarization Effects and Magnetic Scattering*. Clarendon Press, Oxford, 1987.
- [180] H.P. Klug; and L. E. Alexander. *X-Ray Diffraction Procedures: For Polycrystalline and Amorphous Materials*. 2nd. Wiley, May 1974. ISBN: 978-0-471-49369-3.
- [181] M. Tolan. *X-ray scattering from soft-matter thin films*. Springer (Springer tracts in modern physics), Berlin, 1999. ISBN: 978-3-662-14218-9.

- [182] R. W. James. *The Optical Principles of the Diffraction of X-Rays*. OxBow Press, Woodbridge Connecticut, 1962.
- [183] D. B. Williams and C. B. Carter. *Transmission electron microscopy*. Springer, New York, 1996. ISBN: 9780387765013. DOI: 10.1007/978-0-387-76501-3.
- [184] Y. Sahoo; M. Cheon; S. Wang; H. Luo; E. Furlani; and P. Prasad. “Fielddirected self-assembly of magnetic nanoparticles”. In: *The Journal of Physical Chemistry B* 108.11 (2004), pp. 3380–2004.
- [185] C. Liu and Z. J. Zhang. “Size-dependent superparamagnetic properties of mn spinel ferrite nanoparticles synthesized from reverse micelles”. In: *Chemistry of Materials* 13.6 (2001), p. 2092.

# Acknowledgements

**Can't believe I am nearing the end of my time as a PhD student.**

After many late nights and early mornings, I can finally conclude that the thesis is finished.

The time I spent on pursuing my PhD degree was one of the most exciting, impressive and difficult journeys in my academic career. Writing this PhD thesis has been both difficult and fun to do and it is the output of the effort and support of several people to whom I am extremely grateful. It is time to thank everybody who has contributed in some way to the completion of this thesis.

First and foremost, my deep sense of gratitude and profound respect to my research supervisor **Prof. Dr. Thomas Bruückel** for his continuous support, encouragement and guidance during my PhD study. He is a constant source of motivation and full of positive energy, which helped me a lot during many difficult periods. I thank him for introducing me to the world of scattering. Also, I would like to especially thank him for providing me the opportunities to present my work at different national and international conferences. Big thanks for his responsiveness that brought me to Germany and allowed me to accomplish my PhD thesis in JCNS-2 at the Forschungszentrum Jülich. It was a great experience for me working in a comfortable atmosphere with all kind colleagues.

Furthermore gratitude is spoken to **Prof. Dr. Joachim Mayer** for agreeing to be the second referee of my thesis.

I would like to speak a large thank you to my supervisor **Dr. Emmanuel Kentzinger** for helping and guiding me in all possible ways during this journey. I would like to thank him for many valuable advice and suggestions, which helped in improving the thesis to its present form. The discussions with him on different aspects of physics in general and in particular scattering was a learning experience for me, he has been a tremendous mentor for me. It has been a privilege for me to work with him and I sincerely hope I continue to have opportunities to interact with him for the rest of my research career. I am extremely grateful to him.

I would especially like to thank **Dr. Johan Buitenhuis** (ICS-3) for providing me with nanoparticles and for the nice work we had together. Many thanks

for your warm support when I needed most.

I thank **Prof. Giuseppe Portale** from the University of Groningen for providing samples for cobalt ferrite nanodots chapter.

The collaboration from the **Helmholtz Nano Facility (HNF)** is thanked for providing samples: Wolfgang Albrecht, Irina Kempf, Georg Mathey, Juergen Moers.

Also, the collaboration from the **University of Cologne** is thanked for providing nanoparticles: Sabrina Disch, Dominique Dresen.

I thank **Berthold Schmitz** for his technical support during the measurements at MPMS.

**Dr. Oleg Petravic** is thanked for discussions on magnetism.

I would like to thanks **Dr. Karen Friese** for fruitful discussion sometimes.

**Dr. Stefan Mattauch** for the scientific support during the neutron reflectivity measuerment performed at MARIA in MLZ.

I would like to thank **Jochen Friedrich** (PGI-7) for providing us the opportunity to use their SEM.

Thank you to **Dr. Ulrich Rücker** for the help using GALAXI.

A Great acknowledgment to the **BornAgain** team particularly **Marina Ganeva** for the help with the simulation. **Dr. Paul Zakalek**, many thanks for helping and for scentific discussion most of the time.

Financial support from **Brain Gain** for the first PhD year is gratefully acknowledged.

**Paul Diego, Nileena Nandakumaran**, many thanks for the fun we had together. It was a great pleasure to share the office with you. Keep up with your great work.

Furthermore, all colleagues of the institute JCNS-2 is thanked for the inspiring environment to work and have fun. Thanks for the good times and all the discussions we had over the last years. Wish you all the best.

Special thanks to **Mrs. Barbara Daegener** for all the good work and help you've done for me.

I thank **Prof. Salman Salman** from Al-Quds University, for his attention and his support when I needed most.

**Thaer** my life partner, my love... thank you very much for being by my side for 4 years (and counting)! Could not have done it without you.

**Celia**, you are the splitting image of me, you are everything to me. I can't imagine my life without you. You make me smile, happy and proud. You have become my best friend and I love you more than anything. Sorry because I couldn't be with you most of the time when you were baby, you will grow and you will understand and you will be proud of your mother.

I want to thank a special person **Mohammad Abdul Qavi** who was and still in my life, too pity his soul left life before sharing me this day. I know you were waiting for this day. Your memory will be with me always. I will be ever grate-

ful for your assistance, support and advice during whole my academic journey. At last but not least, I would like to express my deepest love to my family members and all my relatives, particularly my father for the encouragement, my mother and my mother in law for their patience. I respect them for their love and care. Their encouragement has brought me through some difficult times in my study.

## Statutory declaration

I declare that this thesis represents my own work and have been prepared by myself, except where due acknowledgment is made, and that it has not been previously included in a thesis, or report submitted to this University or to any other institution for a degree, diploma or other qualifications. I am aware of the provisions of the doctoral degree regulations. The dissertation I submitted was looked after by Prof. Dr. Thomas Brückel.

---

(Place, date)

---

Signature

# Personal Bibliography

## Journal articles

**05.2020:** Qdemat, Asma Kentzinger, Emmanuel Buitenhuis, Johan Rücker, Ulrich Ganeva, Marina Brückel, Thomas. (2020). *"Self assembled monolayer of silica nanoparticles with improved order by drop casting"*. RSC Advances. 10. 18339-18347. 10.1039/D0RA00936A.

**07.2020:** Hanbali, Ghadeer Jodeh, Shehdeh Hamed, Othman Bol, Roland Khalaf, Bayan Qdemat, Asma Samhan, S. (2020). *"Enhanced Ibuprofen Adsorption and Desorption on Synthesized Functionalized Magnetic Multiwall Carbon Nanotubes from Aqueous Solution"*. Materials. 13. 3329. 10.3390/ma13153329.

**07.2020:** Hanbali, Ghadeer Jodeh, Shehdeh Hamed, Othman Bol, Roland Khalaf, Bayan Qdemat, Asma Samhan, S. Dagdag, Omar. (2020). *Magnetic Multiwall Carbon Nanotube Decorated with Novel Functionalities: Synthesis and Application as Adsorbents for Lead Removal from Aqueous Medium*. Processes. 8. 10.3390/pr8080986.

**02.2019:** Wang, Liming Qdemat, Asma Petracic, Oleg Kentzinger, Emmanuel Rücker, Ulrich Zheng, Fengshan Lu, Penghan Wei, Xiankui Dunin-Borkowski, Rafal Brückel, Thomas. (2019). *"Manipulation of dipolar magnetism in low-dimensional iron oxide nanoparticle assemblies"*. Physical Chemistry Chemical Physics. 21. 10.1039/C9CP00302A.

# Curriculum Vitae

Date / place of birth      12/05/1991 in Jerusalem, Palestine  
Nationality                      Palestinian

**02/2016 - 12/2020 : Dissertation** in physics at RWTH Aachen University,  
*"Nanoparticle assemblies: Order by self-organization and collective magnetism"*  
with Prof. Dr. Thomas Bruückel

**01/2014 - 01/2016 : Master's degree** in physics at Al-Quds University-  
Jerusalem/ Jülich center of neutron science at Forschungszentrum Jülich -Germany,  
*"Ordering Phenomena in Magnetic Nanoparticle Assemblies"* with Prof. Dr.  
Thomas Brückel and Prof. Salman M. Salman.

**02/2010 - 02/2012: Bachelor's degree** in physics at Al-Quds University-  
Jerusalem.

**08/2009 : High School Diploma** at Kharas Secondary School Hebron, Pales-  
tine